Metal-Oxides (M_xO_y, where M = Ti, Al, Fe, Ta and W): Synthesis, Fabrication, Surface Functionalization and Applications in Catalysis

THESIS

Submitted in partial fulfilment

of the requirements for the degree of

DOCTOR OF PHILOSOPHY

By

NAGARJUNA RAVI KIRAN

ID. No. 2014PHXF0008H

Under the Supervision of

PROF. RAMAKRISHNAN GANESAN

BIRLA INSTITUTE OF TECHNOLOGY AND SCIENCE, PILANI

2019

BIRLA INSTITUTE OF TECHNOLOGY AND SCIENCE, PILANI

CERTIFICATE

This is to certify that the thesis entitled **"Metal-Oxides (M_xO_y, where M = Ti, Al, Fe, Ta and W): Synthesis, Fabrication, Surface Functionalization and Applications in Catalysis"** submitted by NAGARJUNA RAVI KIRAN, ID No 2014PHXF0008H for the award of Ph. D. of the institute embodies original work done by him under my supervision.

Signature of the Supervisor:

Name: **Prof. Ramakrishnan Ganesan**

Designation: **Associate Professor**

Institute: **Department of Chemistry**

BITS-Pilani, Hyderabad Campus.

Date:

Acknowledgements

It is a pride moment to show the gratification with a sense of pleasure at the long travelled journey, to be able to recapture some of the fine moments and to be able to thank some of whom were with me from the beginning, some who joined me at some stage during the journey, whose rally round kindness, love, and blessings have brought me to this day. I wish to thank each and every one of them with all my heart.

Foremost, I owe thanks to a very special person, my supervisor, Prof. Ramakrishanan Ganesan for his continuous support of my Ph.D. study and research, for his enormous patience, motivation, enthusiasm, and immense knowledge. I consider myself fortunate to be associated with him who gave a decisive turn and a significant boost to my career. His valuable guidance helped me in all the time of my research and writing of this thesis.

I would like to thank many people who helped me in this entire tenure of my Ph.D. with their valuable time, suggestions and encouragement. I am thankful to acknowledge my doctoral advisory committee (DAC) members, Prof. N. Rajesh and Prof. Sounak Roy for their tremendous support and encouragement during this period. I thank DRC convener Dr. Durba Roy and former DRC convenor Prof. Jayanthi Subbalakshmi for their valuable suggestions.

I am thankful to Head of the Department (HOD), Prof. Manab Chakravarty and entire chemistry department faculty members for their valuable interaction and discussions throughout the journey. I sincerely acknowledge Dr. Balaji Gopalan for his remarkable support and inputs to carry out the research. I am grateful to Prof. Jayathi Ray Dutta for the collaboration in the field of biological sciences.

I am grateful to former vice-chancellor Prof. Bijendra Nath Jain, vice-chancellor Prof. Souvik Bhattacharyya of BITS Pilani, former director Prof. V. S. Rao and Prof. G Sundar, present director of BITS Pilani Hyderabad Campus for giving me an opportunity to pursue and to carry out my Doctoral research work.

I would like to express my sincere thanks to Prof. V. V. Vamshi Krishna, Dean, Academic-Graduate Studies and Research Division (Ph.D. Programme) and former dean Prof. Vidya Rajesh for their continuous support and encouragement during my research work. And I extend my thanks to Mr. Praveen, AGSRD for his help and information to complete the course formalities in time.

My sincere thanks to Department of Science and technology (DST), Government of India, New Delhi, for providing financial assistance in the form of project fellowship. I would

also thank BITS-Pilani, Hyderabad Campus for providing institute fellowship for their financial support without which it would have been very difficult to carry out my research work.

I am truly grateful to my dearest friend, Dr. Ranga Santosh, who brought me to the research work and encouraged me all the times. I would like to thank my lab mate Swapna Challagulla for her continuous support and other lab mates Dinabandhu Patra, Aniket Balapure, and Soumitra Payra for their constant help. I thank my friends Srinivasa Rao, Swetha, Shivani, Sathvika, Imran, Uday Kumar, Zubair, Suresh Amaroju and Saisudhakar for their encouragement. I sincerely acknowledge the research scholars in chemistry and other departments for the time they had spent for me and making my stay at campus a memorable one. I take this opportunity to thank one and all who helped me directly or indirectly.

I thank chemistry department non-teaching staff and Central Analytical Lab (CAL) technicians for their excellent cooperation throughout my research work.

My heart felt regards goes to my parents Papa Chary and Kalamma who have given their blessings for the great desire to see me succeed and get the highest degree in education. I must specially thank my wife Srivani for the support and encouragement which helped me in keeping my morale high and daughter Advika Bhashini for giving joyful environment. I would like to do that by dedicating this thesis to my family. Special thanks to my brother Uday Kiran, sister Sushma, brother-in-law Ravi and nephews Rishik and Vyomik who standing beside me with their love and unconditional support. I really consider myself the luckiest in the world to have such a lovely and caring family.

I thank the Almighty, The Lord Krishna for giving me the strength and patience to work through all these years.

As much as my doctoral research work has been a personal pursuit, the story would not have been completed without the efforts and help from my co-workers, friends and well-wishers who have been an integral part of this saga for the last five years. My heartfelt thanks and deep sense of appreciation to all the people mentioned here and others whose names I might have omitted unwittingly.

Date **Nagarjuna Ravi Kiran**

Abstract

In the modern day scenario, utilization of nanomaterials in diverse fields has become obligatory to resolve the needs and desires. Owing to their optical, electronic and catalytic properties, the preparation of nanomaterials has been given a greater significance. Especially, the nano-sized metal oxides are well-intentioned for various applications including sensors, solar cells, photocatalysis, storage devices, anti-reflection coatings, optical waveguides, environmental remediation, and biological applications. The size, shape and performance of the metal oxide nanoparticles can also be dictated by the synthetic method by which they have been made. Numerous preparative methods are reported such as combustion, solid state, sol–gel, hydrothermal, vapor deposition (physical and chemical), mechanochemical synthesis etc. Sol–gel method is a cost-effective and most common synthetic approach among all, due to its simplicity and flexibility. The existing sol–gel procedure is limited by reaction time, scalability and ease of doping. Therefore, an improved, general and versatile synthetic approach is required, which can be used to tune the material property and thereby to enhance the performance.

In the first chapter, various synthetic procedures for the preparation of metal oxide nanomaterials are discussed. This emphasises the importance of the polymerizable sol–gel approach towards the synthesis of supported metal oxide nanomaterials and fabrication of metal oxide micro and nanostructures. The properties and the different characterization techniques to analyze the prepared materials are also mentioned. A brief description on the applications of the metal oxides micro/nanostructures are given at the end of this chapter.

In the chapter 2, the reagents and chemicals used for the synthesis and applications are given. Various analytical instruments that were utilized for the characterization of materials have also been listed in this chapter.

In the chapter 3, a polymerizable sol-gel method has been employed to synthesize tailored TiO_2 supported zeolite-4A. The synthetic procedure was optimized by using FTIR, TGA and DSC to prepare various TiO_2 loading ranging from 10 to 30 wt% on the support. The as-synthesized materials were characterized thoroughly and found that the polymerizable sol-gel approach yields highly dispersed nano-crystalline TiO_2 on the zeolite-4A support. The tailored materials exhibited high rate of photocatalytic degradation of methylene blue at alkaline pH. The used catalysts were subjected to recyclability investigations, which demonstrated highly stable surface of these materials. As the material has proven for its

properties and activity, this has further improved by combining with reduced graphene oxide. This bifunctional nanocomposite photocatalyst that possesses high photocatalytic activity as well as enhanced adsorption capability was developed. The adsorption component, graphene oxide was synthesized following an improved oxidation method from graphite flakes; while the photoactive component, TiO_2 was synthesized by the polymerizable sol–gel route. The as-synthesized graphene oxide was partially photo-reduced, and got anchored as reduced graphene oxide onto TiO_2. This reduced-graphene oxide/TiO_2 was dispersed over the zeolite-4A and this nanocomposite hybrid system exhibited remarkable adsorption capability as well as high photocatalytic degradation efficiency for methylene blue.

In chapter 4, we have demonstrated the photoreduction of Cr(VI) in aqueous medium as it is hazardous for the human being and aquatic life. Fe_3O_4 is chosen as the magnetically recoverable support, onto which, 10, 20, 30 and 50% of TiO_2 have been dispersed following the polymerizable sol–gel approach. With 5 mM of oxalic acid as the hole-scavenger, the TiO_2/Fe_3O_4 materials have demonstrated superior activity to the non-supported bulk TiO_2 towards Cr(VI) photoreduction under UV irradiation in aerobic atmosphere. The 30% TiO_2/Fe_3O_4 catalyst has also demonstrated good recoverability as well as recyclability. This work was extended by using non semiconducting support, alumina and $Fe_3O_4@Fe_2O_3$ as active catalyst. Core-shell type $Fe_3O_4@Fe_2O_3$ was dispersed over nano Al_2O_3 support using aqueous medium co-precipitation method. The Fe_3O_4 core offers magnetic recoverability, while the shell Fe_2O_3, due to its optimal band gap, provides photocatalytic activity in the visible light region. The synthesized materials were studied for Cr(VI) visible light photoreduction. The 40% $Fe_3O_4@Fe_2O_3/Al_2O_3$ catalyst showed magnetic recoverability and the catalytic efficiency was stable up to 4 cycles. Along with the reported supported catalyst systems, a non-supported metal oxide, WO_3 was also synthesized and used for the Cr(VI) photoreduction in visible light. A W-containing sol–gel resin is formulated and subjected to thermally induced free radical polymerization followed by calcination at three different temperatures such as 450, 650 and 850 °C. The calcination temperature has been found to be crucial in tuning the crystallinity and non-stoichiometry of the materials. The higher photocatalytic efficiency was achieved with of WO_3-450. This could be attributed to the nano-crystalline nature, which lead to the formation of high surface area material. The synthesized catalysts have been explored for the efficiency of Cr(VI) photoreduction in aqueous medium under visible light and the results are correlated with the structural and electronic properties of the materials.

Palladium is one of the widely used precious metals towards catalysis, energy and environmental applications. Efficient recovery and reusability of palladium from the spent catalysts is not only highly desirable for sustainable industrial processing, but also for preventing environmental contamination. In chapter 5, we have presented a facile citrate-mediated amine-functionalization of alumina nanopowder in aqueous medium. The amine-functionalized sorbent is thoroughly studied for its vital palladium-sorption parameters such as amount of adsorbent, pH, adsorption capacity, thermodynamics, and kinetics. The palladium adsorption over amine-functionalized alumina nanopowder is further characterized with XRD, and XPS. IR analysis of palladium adsorbed over polyethyleneimine is performed to elucidate the mechanistic insight on the role of nitrogen in capturing palladium. The amine-functionalized sorbent after adsorbing palladium is studied for the catalytic reduction of 4-nitrophenol and Cr(VI), and hydrogen generation from ammonia borane, which demonstrated its excellent catalytic activity and reusability towards energy and environmental applications. The environmentally benign materials and all-aqueous reactions employed in this work demonstrate the potential of the strategy for efficient and economical industrial transformations and waste stream management.

After successful achievement of supported metal oxide nanostructures and their catalytic performances with polymerizable sol–gel method, this approach has been extended to fabricate as thin films using UV-nanoimprint lithography (UV-NIL). UV-NIL is a promising technique for direct fabrication of functional oxide nanostructures. Since it is mostly carried out in aerobic conditions, the free radical polymerization during imprinting is retarded due to the radical scavenging ability of oxygen. Therefore, it is highly desirable to have an oxygen-insensitive photo-curable resin that not only alleviates the requirement of inert conditions but also enables patterning without making substantial changes in the process. In chapter 6, we presented the formulation of metal-containing resins that employ oxygen-insensitive thiol-ene photo-click chemistry. Allyl acetoacetate (AAAc) has been used as a bifunctional monomer of ene group and pentaerythritol tetrakis(3-mercaptopropionate) (PETMP), a four-arm thiol derivative, is used as a crosslinker as well as an active component in the thiol-ene photo-click chemistry. The FT-IR analyses on the metal-free and metal-containing resin formulations revealed that the optimum ratio of alkene to thiol is 1:0.5 for an efficient photo-click chemistry. The thiol-ene photo-click chemistry has been successfully demonstrated for direct imprinting of oxides by employing TiO_2 and Ta_2O_5 as candidate systems. The imprinted films of metal-containing resins were subjected to calcination to

obtain the corresponding patterned metal oxides. This technique can potentially be expanded to other oxide systems as well. This approach is further augmented with other promising oxygen insensitive and photocurable materials such as epoxy based resists. The second part of this chapter deals with the materials consisting epoxy and oxetane functional groups. TiO_2 thin films have been made using epoxy acetoacetate as monomer. The cross-linking between epoxy groups occurs through cationic polymerization and presence of air does not affect the polymerization.

In summary, the synthesis of metal oxide micro/nanostructures using polymerizable sol–gel and their functionalization is described. The approach adopted for the synthesis is method. Since it is suitable for the fabrication of micro/nano metal oxide structures, UV-NIL have been employed to imprint the TiO_2 thin films. In conclusion, the approaches demonstrated in this thesis show high potential for the synthesis and fabrication of functional oxide materials as solids and thin films.

The conclusions of this work and the future scope of the present work are discussed in chapter 7.

Table of content

Abbreviations

eV	Electron volt
KeV	Kilo electron volts
V	Volts
nm	Nanometre
µm	Micrometre
cm	Centimetre
m	Metre
µL	Microliter
mL	Millilitre
L	Litre
mg	Milligram
g	Gram
mmol	Millimole
mol	Mole
sec	Seconds
min	Minutes
hr	Hours
Å	Angstroms
M	Molar
mM	Millimolar
W	Watt
%	Percentage
ppm	Parts per million
ppb	Parts per billion
R	Reflectance
K	Kbelka-Munk factor
Oe	Oersted (Ampere/meter)

List of schemes

List of figures

List of tables

Chapter 1

Introduction

Chapter 1: Introduction

1.1 Introduction to metal oxide nanomaterials

The use of the nanomaterials in different areas of daily life has become essential to resolve the needs and technological advances.[1] Therefore, metal oxides are at their high demand in various research fields of science, due to their robustness, availability and efficiency.[2] The metal oxides in bulk as well as in nano-size are predominantly taking the part to achieve the requirements. Particularly, the metal oxide nanomaterials are the most and commonly used constituents in the fields of sensors,[3] solar cells,[4] photocatalysis,[5,6] storage devices,[7] anti-reflection coatings,[8] optical waveguides,[9] environmental remediation,[10] and biological applications.[11,12] Because of the nano-size, the particles may acquire different properties such as chemical, mechanical, optical and magnetic properties. Hence, the synthesis and applications related to these materials grabbed the attention of the chemical society. Ocean of study is being employed every year in different aspects associated to the metal oxides.

1.2 Properties of metal oxide nanomaterials

1.2.1 Chemical properties

Metal oxides are known to exhibit different chemical properties like acid/base, redox properties. These properties make the material to participate in many organic and inorganic reactions. Many organic transformation reactions involve bulk and nano-sized metal oxide materials like CuO, ZnO and MgO as heterogeneous and homogeneous catalysts.[13,14] The surface of the material plays an important role in the heterogeneous catalysis. The important characteristics of the surface of the catalysts are the coordination environment of surface atoms, redox properties and the oxidation state at surface layer. Due to redox nature of the materials, they can participate in electrophilic and nucleophilic reactions such as oxidation of hydrocarbons. The activity of the surface can also be decided by acid/base character of the material. This character is useful for adsorption-desorption phenomena, which is the key step of heterogeneous catalysis. Surface acidity and basicity can be determined using ζ-potential measurements. These surface properties can be improved by surface functionalization by deploying required functional groups, molecules or forming alloys of the nanoparticles on the surfaces.[15] Hence, the metal oxides chemically take part in various oxidation, reduction, hydrolysis and elimination reactions either as a support or active material.[16]

1.2.2 Electronic properties

Metal oxide materials can show ionic or mixed ionic/electronic conductivity and it has been experimentally well recognized that both can be influenced by the structure and geometry of the material. These properties vary from bulk to nano size metal oxides.[17] The electronic conduction occurs through two types of hopping mechanism. Those are, n- and p-hopping cause by electrons and holes respectively. The number of 'free' electrons/holes of an oxide can be enhanced by introducing non-stoichiometry and are balanced by the much less mobile oxygen/cation vacancies.[18] The number of electronic charge carriers in a metal oxide is a function of the band-gap. The nanostructure of the material leads to produce confinement effect, which in turn affects the band gap of the metal oxide. As the particle size decreases, the band gap increases due to the formation of discrete electronic states,[19, 20] whereas the bulk materials show overlapping of the electronic states that minimize the band gap. Therefore, the electronic property and size of the metal oxides are related to each other. Thus, the metal oxide materials in the nano regime are significantly utilized for sensing,[21] photovoltaic and photodynamic therapeutic applications.[22]

1.2.3 Optical properties

The interaction of the material with light leads to show different optical characters to it, such as absorption, reflection, refraction, transmittance, diffraction, photoluminescence and polarization etc.[23,24] For nanocrystalline semiconductors, both linear (one exciton per particle) and nonlinear optical (multiple excitons) properties arise because of transitions between electron and hole discrete or quantized electronic levels. These optical properties can be tuned by tailoring the morphology of the metal oxide nanoparticles, and designing hybrid metal oxide nanoparticles for the required application.[25] Metal oxides are good support for the plasmonic metallic nanoparticles to localize light into deep sub wavelength regime and can be applied in sensors and photo catalysis. This kind of systems is highly useful to change the absorption regime of the metal oxide (e.g. TiO_2) from the UV to visible regime which in turn is highly useful for the solar cell technologies to harness maximum solar power.[26] Transparent nanoparticles such as indium oxide are highly useful for the transparent conductive electrodes, solar cells and photovoltaic devices.[27]

1.2.4 Mechanical properties

Mechanical properties like softness, hardness, sinterability, super plasticity and ductility can be showed by metal oxides. These properties are useful for the fabrication of different

micro/nanostructures of metal oxides. Due to such properties the metal oxide transparent thin films are highly useful in electronic industry.[28-30] The addition of inorganic nanoparticles can enhance the mechanical properties of polymer thin films. The presence of TiO_2 and SiO_2 nanoparticles in epoxy resin improved the thermal properties and etch resistance.[31]

1.3 Synthetic procedures to prepare metal oxide micro/nanostructures

The synthesis of the desired metal oxide nanomaterials is of paramount of importance in realizing the desired applications. The size, shape and performance of the metal oxide nanoparticles are dictated by the synthetic method by which they have been made. Numerous preparative methods are reported such as combustion, solid state, sol–gel, hydrothermal, vapor deposition (physical and chemical) and mechanochemical synthesis etc.

1.3.1 Solution combustion synthesis

In this method, a suitable metal precursor solution with low vapour pressure is taken and heated in a furnace. The precursor is considered as oxidiser and it undergoes combustion in presence of fuel to form condensed metal oxide. The precursors are usually metal nitrates and fuels include urea, glycine and hydrazides.[32] This method is simple to operate and produces porous nanostructures with high surface area. Metal oxides including $LaFeO_3$, TiO_2, Fe_3O_4 and Fe_2O_3 were prepared following this route.[33-36] It has limitations such as production of huge gases and interference from the external components.

1.3.2 Hydrothermal synthesis

This process involves the heating of the metal precursor solution above the solvent's boiling point in a closed hydrothermal bomb. The reaction progresses in pressurized atmosphere to yield the corresponding metal oxide. The energy of the reaction can be supplied as direct heat or microwave radiation. Several reports are available for the hydrothermal synthesis of Fe_2O_3, NiO, Co_3O_4, CeO_2, MgO, CuO, ZnO hollow spheres and NiO, Co_3O_4 nanoarrays.[37-39] Microwave assisted synthesis of ZnO, CuO and TiO_2 were also reported.[33,40] This method yields porous and crystalline metal oxides; nevertheless it is costly and limits by uncontrollable pressures inside the hydrothermal reactor.

1.3.3 Vapour deposition

This procedure is classified into two classes, (a) physical vapor deposition (PVD) and (b) chemical vapor deposition (CVD). In PVD, the material will be directly evaporated and coated onto the substrate. While in CVD the reactive precursors are first made into gaseous state to react and then the oxides are deposited on the substrate. Both of these methods are

suitable for thin film coating applications. Thin films of $YBa_2Cu_3O_7$, TiO_2, SiO_2 were prepared through PVD[41,42] and ZnO–TiO_2, Co_3O_4, HfO_2, MnO_2 were made by CVD.[43-47] This technique produces good quality of thin films on substrates, but requires high temperatures (>900 °C) for the evaporation of materials.

1.3.4 Solid state decomposition

The solid state precursors are mixed thoroughly and subjected to heating to decompose into the requisite metal oxide. This process is further classified into 3 types: thermal decomposition, microwave-assisted and photochemical decomposition. The metal precursors can be hydroxides, oxalates, citrates, hydroxyl carbonates and sulphates. Vast range of metal oxides has been synthesized like α-Fe_2O_3, NiO, $BaTiO_3$, Al_2TiO_5, Ca_2FeO_3 and $CaCo_2O_4$.[48-52] This process operates at low cost and high productivity. The difficulties associate with this method is non-homogeneous mixing of precursors in solid state and the agglomeration of the particles during decomposition.

1.3.5 Co-precipitation synthesis

The oxides will be precipitated from salt solutions of metal in aqueous or non-aqueous solvents. This is a room temperature and pH dependent process. For instance, magnetite (Fe_3O_4) can be synthesised using $FeSO_4$ and $FeCl_3$ as precursors in this method.[53] Various other metal oxides and mixed metal oxide nanomaterials including ZrO_2-CeO_2, ZnO, $MgCr_2O_4$, $MgFe_2O_4$ and $MgNiO_2$ are synthesized using this approach.[54, 55] It is a simple and low cost method. The limitations of this process are solubility, pH and ionic strength.

1.3.6 Sol–gel approach

Sol–gel method is a cost-effective and most common synthetic approach among all, due to its simplicity and flexibility. In conventional sol–gel method, inorganic metal salts or metal alkoxides are used as precursors for the synthesis of corresponding metal oxides. The process involves two steps of reactions.[56] First, the sol formation by hydroxylation of the precursor material. Later on, condensation occurs between hydroxyl moieties to form oxide network. The oxide network is called as gel. The gel leads to form corresponding metal oxide on subsequent heat treatment. Fig. 1.1 shows the representative procedure involved in the Sol–gel approach. This approach is advantageous due to the formation of homogeneous metal oxides. The method involves the use of alkoxide precursors appeared to be adaptable, because of better control over the size and structure of the metal oxide. Several metal oxides have been synthesized using alkoxide-based sol–gel method.[57-59]

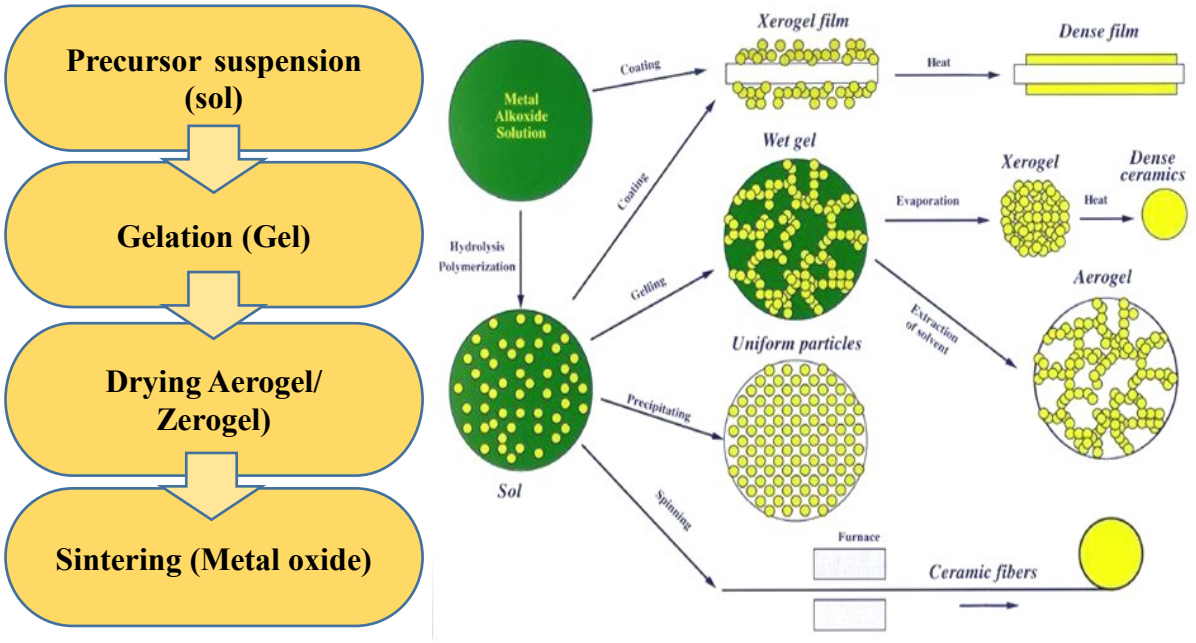

Figure 1.1: Schematic representation of the sol–gel process.

Several semiconductor oxides such as TiO_2, ZnO, WO_3 etc. find extensive applications in various fields such as photocatalysis, solar energy harvesting and hydrogen evolution reaction. The sol–gel method has been well-studied and developed due to its potential to synthesize functional materials.[56] One of the major applications of metal oxides is in photocatalysis. To increase the photocatalytic behaviour it is required to minimize the exciton electron-hole recombination. To achieve this, doping of metals like Ag, Au, W, and Cu etc. are used.[60] Unlike other synthetic procedures, sol–gel method facilitates facile synthesis of nanocrystalline metal oxides of high purity under mild reaction conditions.[61] For instance, a uniform tetragonal single crystal structured TiO_2 nanowires have been fabricated within the pores of anodic aluminium oxide template by cathodically induced sol–gel method.[62] Abbasi et al.,[63] have synthesized CeO_2 nanopowder via sol–gel by taking cerium nitrate as a precursor and used for the oxidation of toluene. Several reports are available on the synthesis of supported metal oxides through sol–gel approach. Some of these include, thermally stable alumina supported metal oxides such as MgO, CaO, TiO_2 and Cr_2O_3 prepared by using self-assembly of a metal precursor and aluminium *iso*propoxide in presence of a triblock copolymer.[64] Palanisamy and co-workers,[65] have synthesized mesoporous Fe_2O_3/TiO_2 by sol–gel method and shown photosensitization in solar light for the degradation of 4-chlorophenol. Kim et al.,[66] have synthesized several zirconia supported metal oxides such as $ZnO–TiO_2–Nd_2O_3/ZrO_2$, $ZnO–Yb_2O_3–SiO_2/ZrO_2$, $ZnO–SiO_2/ZrO_2$ by sol–gel approach. According to Sharma et al.,[67] sol–gel synthesized TiO_2-CoO supported

with reduced graphene oxide (RGO) has shown 98.2% photodegradation of 2-chlorophenol under visible light. Tang et al.,[68] have synthesized magnetic TiO_2-graphene hybrid photocatalyst using tetra-n-butyl titanate as precursor by sol–gel method and the catalyst has shown efficient removal of 2,4-dichlorophenoxy acetic acid from real waste water. TiO_2 supported Beta zeolite has been prepared by taking titanium isopropoxide as a precursor in sol–gel route and used for methanol conversion.[69]

The activity of these materials is generally enhanced by band engineering, in which the semiconductor oxides are doped and/or dispersed over a support. The existing sol–gel procedure to synthesize supported or doped oxides is limited by reaction time, scalability and ease of doping. Therefore, an improved, general and versatile synthetic approach is required, which can be used to tune the material property and thereby enhance the performance. In this context, a new polymerizable sol–gel precursor mediated approach has recently been developed to fabricate metal oxide nanostructures.[70] This method has been shown promising for the fabrication of various metal oxides onto substrates as thin films. This combines both sol–gel and acrylate-based polymerization synthetic methods (Fig. 1.2).

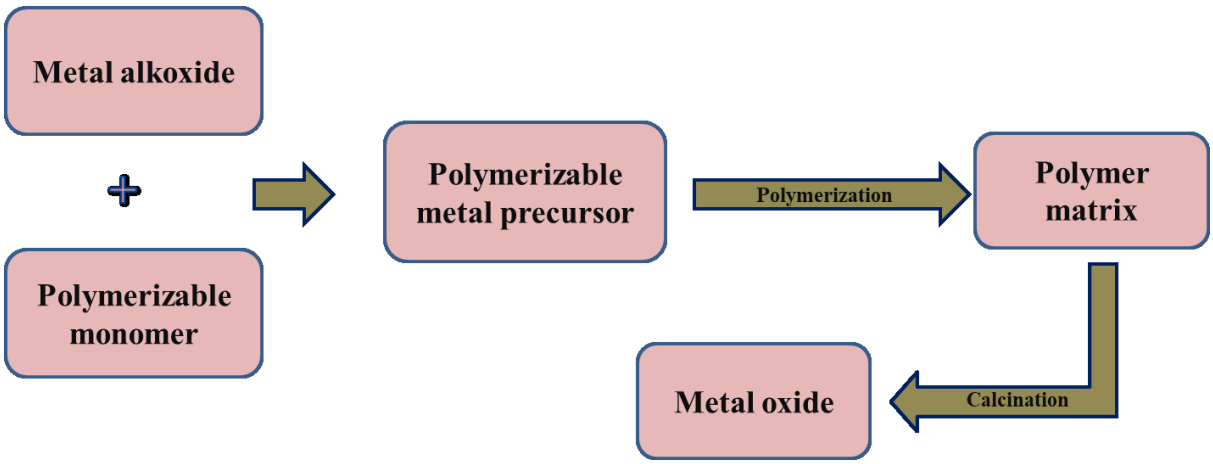

Figure 1.2: Schematic represents the polymerizable sol–gel synthetic approach.

In this approach, acrylate groups participate in the *in situ* free radical polymerization. TiO_2 was successfully patterned by nanoimprinting lithography using this polymerizable titanium metacrylate precursor.[71] Since many metal-methacrylates are highly prone to hydrolysis, an improvised method using metal-methacrylate acetoacetates was introduced. Using this approach patterning of several metal oxides (~15) have been demonstrated effectively by Ganesan et al.[72] This method facilitates the homogeneous dispersion of metal inside a polymeric matrix through *in situ* polymerization of metal-containing polymerizable precursors. The resultant polymer is subjected to calcination to yield the corresponding metal

oxide. This approach allows one to carry out easy doping. The photocurable metal-containing precursors are suitable to fabricate oxide nanopatterns by lithography. Several metal oxides are effectively patterned by this route including TiO_2, ZrO_2, HfO_2, Nb_2O_5, Ta_2O_5, V_2O_5, WO_3, SnO_2, B_2O_3, In_2O_3 and Y_2O_3 etc.[73]

This method has high potential to be extended for the fabrication of supported metal oxides, which can find huge applications in catalysis, photovoltaic devices, sensors etc. In this work several supported metal oxides have been synthesized based on this approach and their potential for photocatalysis have been explored.

1.4 Characterization of metal oxides

The materials have to be thoroughly characterized during and after the synthetic process. It is important to develop the synthetic procedure and to prove the formation of the desired material. Following are the instrumentation techniques that have been used in our work.

1.4.1 Thermo-analytical techniques

The processing parameters can be optimized using thermal analytical measurements such as differential scanning calorimetry (DSC) and thermogravimetric analysis (TGA). In DSC heat flow as a function of temperature can be measured to find whether the reaction is endo or exothermic. It also provides the information regarding melting (t_m), glass transition (t_g), and crystallization temperature etc. TGA executes the decomposition of material as a function of temperature. This technique shows the percentage mass loss, which is useful to optimize the reaction conditions like polymerization and calcination.

1.4.2 Fourier transmission infrared spectroscopy (FT-IR)

FT-IR is one of the efficient tools to get the chemical functional groups of the material. The interaction of infrared radiation with molecular bonds leads to vibrational fluctuations such as bending, wagging and stretching in the molecule. Different vibrational frequencies correspond to different functional groups can indicate the structure. The technique can therefore be used to monitor the changes in functional group signature peaks as a function of reaction progress.

1.4.3 Raman spectroscopy

This is a spectroscopic technique based on the Raman scattering. As the radiation interacts with the molecule, there are two possible scattering phenomena. One is elastic scattering, also known as Reyleigh scattering and the other is inelastic scattering, known as Raman

scattering. Raman scattering is composed of stokes and anti-stokes lines. The intensity of these scattered radiations can be measured and plotted against wavenumber of the radiation. This technique is complementary to FT-IR and is useful for the material identification. In addition, the characteristic vibrational modes of the crystals allow one to identify the phase of the material and thus the technique complements X-ray diffraction in some cases.

1.4.4 X-ray diffraction (XRD)

This is another efficient tool for the characterization of the solid materials. X-ray is the electromagnetic radiation with the wavelength in the range 0.5-2.5Å occupying the region between the gamma and extreme ultraviolet rays of the electromagnetic spectrum. The scattering of X-rays from the surface gives rise to constructive and destructive interference. When Bragg's law ($n\lambda = 2d\sin\theta$) is satisfied, the scattering results in a constructive interference and gives a signal at the corresponding 2θ values, which are used to gain the structural information of the crystalline materials. Thus, this technique is regularly used for the phase identification, phase quantification, crystallite size, cell parameter calculation, and for the textural studies of the crystalline materials. Scherrer formula ($a = \frac{K\lambda}{(\beta cos\theta)}$) can be used to calculate the crystallite size, where β is full width at half maxima (FWHM) and θ is angle of the major intense peak of the pattern. K represents shape factor which has a typical value of about 0.9, but it differs with the actual shape of the crystallite.

1.4.5 X-ray photoelectron spectroscopy (XPS)

XPS is a highly useful instrumentation tool to acquire detailed analysis of the surface at atomic level to understand the elemental composition. This technique was initially known as the Electron Spectroscopy for Chemical Analysis (ESCA), which works based on photoelectric effect ($KE = h\nu - BE$). XPS is used to find the binding energy of the atoms except hydrogen and helium in the periodic table. From the binding energy values obtained from the surface of the material, one would be able to identify the elemental composition and their oxidation states.

1.4.6 X-ray fluorescence spectroscopy (XRF)

X-ray fluorescence is an emission phenomenon of the secondary X-rays that come from the element when it is bombarded with high energy radiation. Sodium to uranium can be easily detected from sub-ppm level to percentage level with the help of XRF. Elements with higher atomic number are easier for the detection as compared to the elements with lower atomic

number. Hence, the technique is highly useful for studying the composition of metal oxides, doped samples and composite materials. Doping concentration, composition of the composite materials can be easily calculated using this simple non-destructive technique. XRF compares the spectral intensity of unknown samples to the standard samples.

1.4.7 Diffuse reflectance spectroscopy (DRS)

The solid samples can partially absorb, transmit and scatter the incident light. The reflected light intensity is measured in % of reflectance against the wavelength of the radiation. This reflected energy is converted into a function called Kubelka-Munk function ($K = \frac{(1-R)2}{2R}$). It is used to determine the band gap and electronic structure of the metal oxide materials.

1.4.8 Field emission scanning electron microscopy (FE-SEM)

The scanning electron microscopy is an important characterization technique that uses a focused electron beam . In FE-SEM secondary electrons are emitted from the solid sample, which are collected to create an area map of the secondary emission. The technique is used to determine the surface morphology (texture) and chemical composition (in energy dispersive spectroscopy mode) of the material samples.

1.4.9 High resolution transmission electron microscopy (HR-TEM)

In this technique, high energy electron beams are utilized to transmit through the sample of interest. Using the contrast between transmitted and untransmitted e^- beams, the image is created. This technique provides very high resolution image to the extent of 0.2 Å. One would be able to measure the inter-planar distance for the crystalline materials using this technique.

1.4.10 Brunauer–Emmett–Teller (BET) surface area measurements

This measurement works on the basis of physical adsorption of the gaseous molecules on the solids (BET theory). According to the BET theory, the gaseous molecules adsorb on the surface of the adsorbent as monolayer. The monolayer adsorption and desorption of the gas will be carried out and surface area, pore volume and pore diameter can be calculated using BET formula.

1.5 Applications of metal oxides

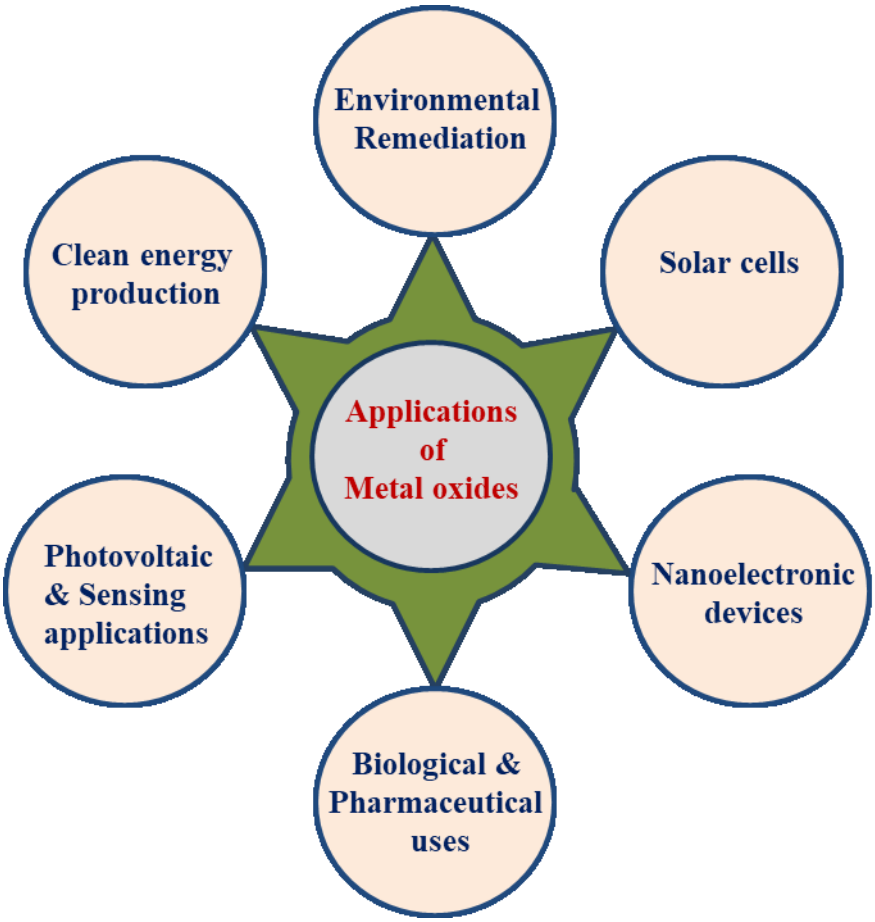

Figure 1.3: Pictorial representation depicting applications of metal oxides in various avenues.

1.5.1 Environmental remediation: Photocatalytic applications

Owing to the versatile electronic and optical properties, metal oxides are considered for various photocatalytic applications as potential photocatalysts. Particularly, the semiconducting metal oxides are having eminent role in the photocatalysis of the pollutants. Mainly for heterogeneous photocatalysis, the materials with suitable band gap, appropriate morphology, high surface area, stability and reusability are considered to be the best catalysts.[5,74,75] Many semiconducting metal oxides including ZnO, V_2O_5, TiO_2, SnO_2, CeO_2 and Fe_2O_3 have the stated properties and successfully used for the application. In general, the photocatalytic phenomena proceeds through light induced charge separation mechanism which occurs in the catalyst. The light is either UV or visible radiation depending on the materials' band gap. As an electron gets excited to the conduction band from the valence band, it forms an electron-hole (e^-/h^+) pair as shown in Fig. 1.4. The photogenerated pair can oxidize or reduce the substance which is adsorbed on the surface of the catalyst. Catalytic

oxidation is assumed to continue via direct attack of adsorbed species on the catalytic surface by photogenerated holes (in valence band) or to be indirectly mediated by radicals, such as ·OH, generated from adsorbed water, oxygen, and hydroxyl groups on the catalyst surface. In this way, hazardous organic compounds can be completely mineralized. Organic substances like dyes, antibiotics, biological waste can be degraded in this manner.[76-78] While in catalytic reduction, the photoexcited electrons can be transferred to a species/compound to reduce it. **c**The Cr(VI) reduction to Cr(III) is an example for such a photoreduction.[79,80]

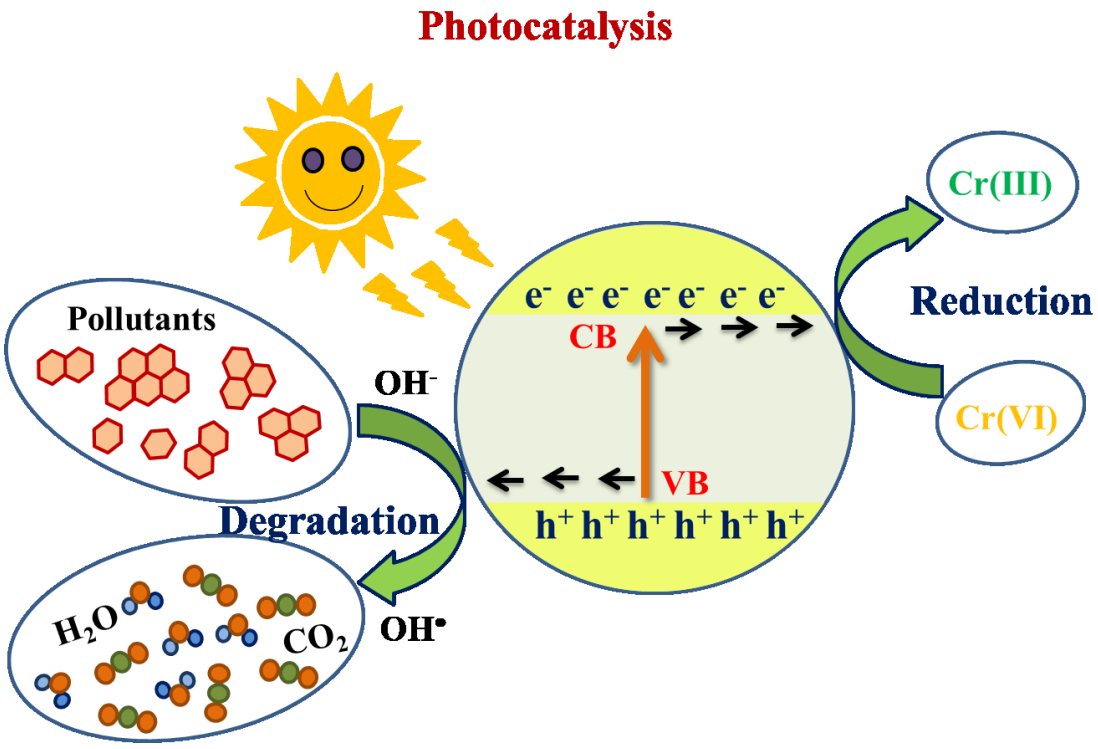

Figure 1.4: Schematic representation of a typical photocatalytic phenomenon.

1.5.2 Solar cells

Due to the increased energy demands and depleting fossil fuels, renewable energy approaches such as solar cells have become increasingly popular. Briefly, the solar cell is an electrical device that can convert the electromagnetic radiation into electric energy. This device contains semiconducting material and works based on photovoltaic effect. The classes of solar cells are organic photovoltaics (OPVs), dye-sensitized solar cells (DSSCs), quantum-dot solar cells (QDSCs), oxide-based solar cells (OSCs) and perovskite solar cells (PSC). Since many metal oxides contain excellent semiconducting properties, they have been used extensively in this field.[81,82]

1.5.3 Clean energy production

Due to the limited availability of the conventional energy sources, the new generation energy boon is hydrogen gas. The benefits associated with hydrogen gas burning are no-harmful gas production and 100% energy conversion. So, the research is going in the direction of production and storage of hydrogen gas. Hydrogen gas can be produced from methane reforming, partial oxidation of hydrocarbons and coal gasification.[83] Water splitting reaction also produces the hydrogen gas through electrochemical and photochemical mechanism. Methods such as hydrolysis of ammonia borane and sodium borohydride can also have the potential to generate hydrogen, since they possess properties like low molecular weight, easily transportable solid, safe and high gravimetric hydrogen storage. Several metal oxides such as Co_3O_4, Fe_2O_3, CuO, Cu_2O, MoO_3 and V_2O_5 have been used to produce hydrogen from ammonia borane hydrolysis.[84]

1.5.4 Micro/nano-electronic devices

Enormous applications are associated with micro/nano-electronic devices using nanotechnology such as memory storage, displays, optoelectronic devices, quantum computers, energy production, and medical diagnosis. Thus, development of materials for the fabrication of functional devices like transistor, capacitor, and resistor is interesting and challenging aspect. The use of metal oxide nanomaterials for such applications is remarkable. Metal oxides covering TiO_2, SiO_2, HfO_2, $LaAlO_3$ and $SrTiO_3$ are found to be highly useful in electronic devices due to their semiconducting properties.[85] Another important characteristic of this branch is the fabrication of micro/nano-electronic device. The fabrication of the devices through lithographic techniques is one of the simple methods which produce the required systems in high throughput. Several technical implementations such as nanoimprint lithography (NIL), electron-beam lithography (EBL), atomic force microscopy (AFM) and dip-pen nanolithography (DPN) are studied for the processing of materials.[86-88] Among them, NIL has appeared as a possible substitute to traditional lithography techniques because of its simplicity, versatility, low cost, high-resolution, and potential for achieving high throughput.[70]

Along with the above mentioned applications, metal oxides find several many other applications in sensing,[89-94] biological[95] and pharmaceutical fields.[96-99]

1.6 References

1. Fernandez-Garcia, M.; Rodriguez, J. A., Metal oxide nanoparticles. *Encyclopedia of Inorganic and Bioinorganic Chemistry* **2011**.

2. Khan, M. M.; Adil, S. F.; Al-Mayouf, A., Metal oxides as photocatalysts. *Elsevier*: 2015.

3. Comini, E., Metal oxide nano-crystals for gas sensing. *Analytica Chimica Acta* **2006,** *568* (1-2), 28-40.

4. Qi, J.; Dang, X.; Hammond, P. T.; Belcher, A. M., Highly efficient plasmon-enhanced dye-sensitized solar cells through metal@ oxide core–shell nanostructure. *ACS Nano* **2011,** *5* (9), 7108-7116.

5. Hisatomi, T.; Kubota, J.; Domen, K., Recent advances in semiconductors for photocatalytic and photoelectrochemical water splitting. *Chemical Society Reviews* **2014,** *43* (22), 7520-7535.

6. Wang, H.; Zhang, L.; Chen, Z.; Hu, J.; Li, S.; Wang, Z.; Liu, J.; Wang, X., Semiconductor heterojunction photocatalysts: design, construction, and photocatalytic performances. *Chemical Society Reviews* **2014,** *43* (15), 5234-5244.

7. Arico, A. S.; Bruce, P.; Scrosati, B.; Tarascon, J. M.; Van Schalkwijk, W., Nanostructured materials for advanced energy conversion and storage devices. In *Materials For Sustainable Energy: A Collection of Peer-Reviewed Research and Review Articles from Nature Publishing Group*, World Scientific: **2011**,148-159.

8. Chen, D., Anti-reflection (AR) coatings made by sol–gel processes: a review. *Solar Energy Materials and Solar Cells* **2001,** *68* (3-4), 313-336.

9. Yoshida, M.; Prasad, P. N., Sol−gel-processed SiO_2/TiO_2/poly(vinylpyrrolidone) composite materials for optical waveguides. *Chemistry of Materials* **1996,** *8* (1), 235-241.

10. Hua, M.; Zhang, S.; Pan, B.; Zhang, W.; Lv, L.; Zhang, Q., Heavy metal removal from water/wastewater by nanosized metal oxides: a review. *Journal of Hazardous Materials* **2012,** *211*, 317-331.

11. Diez-Pascual, A. M.; Diez-Vicente, A. L., Effect of TiO_2 nanoparticles on the performance of polyphenylsulfone biomaterial for orthopaedic implants. *Journal of Materials Chemistry B* **2014,** *2* (43), 7502-7514.

12. Fiedler, T.; Belova, I.; Murch, G.; Roether, J.; Boccaccini, A., Tailoring elastic properties of PLGA/TiO_2 biomaterials. *Computational Materials Science* **2012,** *61*, 283-286.

13. Griffiths, C.; O'Horo, M.; Smith, T., The structure, magnetic characterization, and oxidation of colloidal iron dispersions. *Journal of Applied Physics* **1979,** *50* (11), 7108-7115.

14. Xu, P.; Zeng, G. M.; Huang, D. L.; Feng, C. L.; Hu, S.; Zhao, M. H.; Lai, C.; Wei, Z.; Huang, C.; Xie, G. X., Use of iron oxide nanomaterials in wastewater treatment: a review. *Science of the Total Environment* **2012,** *424*, 1-10.

15. Stoimenov, P. K.; Klinger, R. L.; Marchin, G. L.; Klabunde, K. J., Metal oxide nanoparticles as bactericidal agents. *Langmuir* **2002,** *18* (17), 6679-6686.

16. Rani, M.; Shanker, U., Degradation of traditional and new emerging pesticides in water by nanomaterials: recent trends and future recommendations. *International Journal of Environmental Science and Technology* **2018,** *15* (6), 1347-1380.

17. Roduner, E., Size matters: why nanomaterials are different. *Chemical Society Reviews* **2006,** *35* (7), 583-592.

18. Lavik, E.; Kosacki, I.; Tuller, H.; Chiang, Y.; Ying, J., Nonstoichiometry and electrical conductivity of nanocrystalline $CeO_{\{2-x\}.}$ *Journal of Electroceramics* **1997,** *1* (1), 7-14.

19. Canham, L. T., Silicon quantum wire array fabrication by electrochemical and chemical dissolution of wafers. *Applied Physics Letters* **1990,** *57* (10), 1046-1048.

20. Lehmann, V.; Gosele. U., Porous silicon formation: A quantum wire effect. *Applied Physics Letters* **1991,** *58*, 856.

21. Franke, M. E.; Koplin, T. J.; Simon, U., Metal and metal oxide nanoparticles in chemiresistors: does the nanoscale matter? *Small* **2006,** *2* (1), 36-50.

22. Peng, Y.; Lu, B.; Wu, F.; Zhang, F.; Lu, J. E.; Kang, X.; Ping, Y.; Chen, S., Point of anchor: impacts on interfacial charge transfer of metal oxide nanoparticles. *Journal of the American Chemical Society* **2018,** *140* (45), 15290-15299.

23. Yoffe, A., Semiconductor quantum dots and related systems: electronic, optical, luminescence and related properties of low dimensional systems. *Advances in Physics* **2001,** *50* (1), 1-208.

24. Flores-Gonzalez, M.; Louis, C.; Bazzi, R.; Ledoux, G.; Lebbou, K.; Roux, S.; Perriat, P.; Tillement, O., Elaboration of nanostructured Eu^{3+}-doped Gd_2O_3 phosphor fine

spherical powders using polyol-mediated synthesis. *Applied Physics A* **2005,** *81* (7), 1385-1391.

25. Zhang, L.; Jing, H.; Boisvert, G.; He, J. Z.; Wang, H., Geometry control and optical tunability of metal–cuprous oxide core–shell nanoparticles. *ACS Nano* **2012,** *6* (4), 3514-3527.

26. Misra, S.; Li, L.; Jian, J.; Huang, J.; Wang, X.; Zemlyanov, D.; Jang, J. W.; Ribeiro, F. H.; Wang, H., Tailorable Au nanoparticles embedded in epitaxial TiO_2 thin films for tunable optical properties. *ACS Applied Materials & Interfaces* **2018,** *10* (38), 32895-32902.

27. Siedl, N.; Gugel, P.; Diwald, O., Synthesis and aggregation of In_2O_3 nanoparticles: impact of process parameters on stoichiometry changes and optical properties. *Langmuir* **2013,** *29* (20), 6077-6083.

28. Tjong, S.; Chen, H., Nanocrystalline materials and coatings. *Materials Science and Engineering: R: Reports* **2004,** *45* (1-2), 1-88.

29. Soto-Figueroa, C.; Vicente, L.; Martinez-Magadan, J. M.; Rodriguez-Hidalgo, M. D. R., Self-organization process of ordered structures in linear and star poly(styrene)−poly(isoprene) block copolymers: Gaussian models and mesoscopic parameters of polymeric systems. *The Journal of Physical Chemistry B* **2007,** *111* (40), 11756-11764.

30. Lu, L.; Li, S.; Lu, K., An abnormal strain rate effect on tensile behavior in nanocrystalline copper. *Scripta Materialia* **2001,** *45* (10), 1163-1169.

31. Wu, C. C.; Hsu, S. L. C., Preparation of epoxy/silica and epoxy/titania hybrid resists via a sol−gel process for nanoimprint lithography. *The Journal of Physical Chemistry C* **2010,** *114* (5), 2179-2183.

32. Manukyan, K. V.; Cross, A.; Roslyakov, S.; Rouvimov, S.; Rogachev, A. S.; Wolf, E. E.; Mukasyan, A. S., Solution combustion synthesis of nano-crystalline metallic materials: mechanistic studies. *The Journal of Physical Chemistry C* **2013,** *117* (46), 24417-24427.

33. Challagulla, S.; Nagarjuna, R.; Ganesan, R.; Roy, S., TiO_2 synthesized by various routes and its role on environmental remediation and alternate energy production. *Nano-Structures & Nano-Objects* **2017,** *12*, 147-156.

34. Roy, S.; Hegde, M.; Ravishankar, N.; Madras, G., Creation of redox adsorption sites by Pd^{2+} ion substitution in nanoTiO_2 for high photocatalytic activity of CO oxidation, NO reduction, and NO decomposition. *The Journal of Physical Chemistry C* **2007,** *111* (23), 8153-8160.

35. Roy, S.; Marimuthu, A.; Hegde, M.; Madras, G., High rates of CO and hydrocarbon oxidation and NO reduction by CO over $Ti_{0.99}Pd_{0.01}O_{1.99}$. *Applied Catalysis B: Environmental* **2007,** *73* (3-4), 300-310.

36. Toniolo, J.; Takimi, A. S.; Andrade, M. J.; Bonadiman, R.; Bergmann, C. P., Synthesis by the solution combustion process and magnetic properties of iron oxide (Fe_3O_4 and α-Fe_2O_3) particles. *Journal of Materials Science* **2007,** *42* (13), 4785-4791.

37. Titirici, M. M.; Antonietti, M.; Thomas, A., A generalized synthesis of metal oxide hollow spheres using a hydrothermal approach. *Chemistry of Materials* **2006,** *18* (16), 3808-3812.

38. Yu, J.; Yu, X., Hydrothermal synthesis and photocatalytic activity of zinc oxide hollow spheres. *Environmental Science & Technology* **2008,** *42* (13), 4902-4907.

39. Yang, Q.; Lu, Z.; Liu, J.; Lei, X.; Chang, Z.; Luo, L.; Sun, X., Metal oxide and hydroxide nanoarrays: Hydrothermal synthesis and applications as supercapacitors and nanocatalysts. *Progress in Natural Science: Materials International* **2013,** *23* (4), 351-366.

40. Faraji, S.; Ani, F. N., Microwave-assisted synthesis of metal oxide/hydroxide composite electrodes for high power supercapacitors–a review. *Journal of Power Sources* **2014,** *263*, 338-360.

41. Humphreys, R.; Satchell, J.; Chew, N.; Edwards, J.; Goodyear, S.; Blenkinsop, S.; Dosser, O.; Cullis, A., Physical vapour deposition techniques for the growth of $YBa_2Cu_3O_7$ thin films. *Superconductor Science and Technology* **1990,** *3* (1), 38-52.

42. Gonzalez-Garcia, L.; Lozano, G.; Barranco, A.; Míguez, H.; González-Elipe, A. R., TiO_2–SiO_2 one-dimensional photonic crystals of controlled porosity by glancing angle physical vapour deposition. *Journal of Materials Chemistry* **2010,** *20* (31), 6408-6412.

43. Barreca, D.; Comini, E.; Ferrucci, A. P.; Gasparotto, A.; Maccato, C.; Maragno, C.; Sberveglieri, G.; Tondello, E., First example of ZnO−TiO_2 nanocomposites by

chemical vapor deposition: structure, morphology, composition, and gas sensing performances. *Chemistry of Materials* **2007,** *19* (23), 5642-5649.

44. Bahlawane, N.; Rivera, E. F.; Kohse-Hoinghaus, K.; Brechling, A.; Kleineberg, U., Characterization and tests of planar Co_3O_4 model catalysts prepared by chemical vapor deposition. *Applied Catalysis B: Environmental* **2004,** *53* (4), 245-255.

45. Smith, R. C.; Ma, T.; Hoilien, N.; Tsung, L. Y.; Bevan, M. J.; Colombo, L.; Roberts, J.; Campbell, S. A.; Gladfelter, W. L., Chemical vapour deposition of the oxides of titanium, zirconium and hafnium for use as high-k materials in microelectronic devices. A carbon-free precursor for the synthesis of hafnium dioxide. *Advanced Materials for Optics and Electronics* **2000,** *10* (3-5), 105-114.

46. Reichelt, K.; Jiang, X., The preparation of thin films by physical vapour deposition methods. *Thin Solid Films* **1990,** *191* (1), 91-126.

47. Choy, K., Chemical vapour deposition of coatings. *Progress in Materials Science* **2003,** *48* (2), 57-170.

48. Xu, X.; Wolfus, Y.; Shaulov, A.; Yeshurun, Y.; Felner, I.; Nowik, I.; Koltypin, Y.; Gedanken, A., Annealing study of Fe_2O_3 nanoparticles: magnetic size effects and phase transformations. *Journal of Applied Physics* **2002,** *91* (7), 4611-4616.

49. Salavati-Niasari, M.; Mohandes, F.; Davar, F.; Mazaheri, M.; Monemzadeh, M.; Yavarinia, N., Preparation of NiO nanoparticles from metal-organic frameworks via a solid-state decomposition route. *Inorganica Chimica Acta* **2009,** *362* (10), 3691-3697.

50. Buscaglia, M. T.; Bassoli, M.; Buscaglia, V.; Alessio, R., Solid-state synthesis of ultrafine $BaTiO_3$ powders from nanocrystalline $BaCO_3$ and TiO_2. *Journal of the American Ceramic Society* **2005,** *88* (9), 2374-2379.

51. Freudenberg, B.; Mocellin, A., Aluminum titanate formation by solid-state reaction of fine Al_2O_3 and TiO_2 powders. *Journal of the American Ceramic Society* **1987,** *70* (1), 33-38.

52. Vidyasagar, K.; Gopalakrishnan, J.; Rao, C., A convenient route for the synthesis of complex metal oxides employing solid-solution precursors. *Inorganic Chemistry* **1984,** *23* (9), 1206-1210.

53. Iida, H.; Takayanagi, K.; Nakanishi, T.; Osaka, T., Synthesis of Fe_3O_4 nanoparticles with various sizes and magnetic properties by controlled hydrolysis. *Journal of Colloid and Interface Science* **2007,** *314* (1), 274-280.

54. Singh, A., Structure, synthesis, and application of nanoparticles. *Singh AK. Engineered Nanoparticles-Structure, Properties and Mechanisms of Toxicity* **2016**, 19-76.

55. Yagi, S.; Ichikawa, Y.; Yamada, I.; Doi, T.; Ichitsubo, T.; Matsubara, E., Synthesis of binary magnesium–transition metal oxides via inverse coprecipitation. *Japanese Journal of Applied Physics* **2013,** *52* (2R), 025501.

56. Corriu, R.; Leclercq, D.; Lefevre, P.; Mutin, P. H.; Vioux, A., Preparation of monolithic binary oxide gels by a nonhydrolytic sol-gel process. *Chemistry of Materials* **1992,** *4* (5), 961-963.

57. Kakihana, M., Invited review "sol–gel" preparation of high temperature superconducting oxides. *Journal of Sol-Gel Science and Technology* **1996,** *6* (1), 7-55.

58. Pflitsch, C.; Siddiqui, R. A.; Eckert, C.; Atakan, B., Sol–gel deposition of chromium doped aluminium oxide films (ruby) for surface temperature sensor application. *Chemistry of Materials* **2008,** *20* (8), 2773-2778.

59. Goswami, Y.; Kumar, V.; Rajaram, P.; Ganesan, V.; Malik, M. A.; O'Brien, P., Synthesis of SnO_2 nanostructures by ultrasonic-assisted sol–gel method. *Journal of Sol–Gel Science and Technology* **2014,** *69* (3), 617-624.

60. McFarland, E. W.; Metiu, H., Catalysis by doped oxides. *Chemical Reviews* **2013,** *113* (6), 4391-4427.

61. Livage, J.; Henry, M.; Sanchez, C., Sol–gel chemistry of transition metal oxides. *Progress in Solid State Chemistry* **1988,** *18* (4), 259-341.

62. Miao, Z.; Xu, D.; Ouyang, J.; Guo, G.; Zhao, X.; Tang, Y., Electrochemically induced sol−gel preparation of single-crystalline TiO_2 nanowires. *Nano Letters* **2002,** *2* (7), 717-720.

63. Abbasi, Z.; Haghighi, M.; Fatehifar, E.; Rahemi, N., Comparative synthesis and physicochemical characterization of CeO_2 nanopowder via redox reaction, precipitation and sol–gel methods used for total oxidation of toluene. *Asia-Pacific Journal of Chemical Engineering* **2012,** *7* (6), 868-876.

64. Morris, S. M.; Fulvio, P. F.; Jaroniec, M., Ordered mesoporous alumina-supported metal oxides. *Journal of the American Chemical Society* **2008,** *130* (45), 15210-15216.

65. Palanisamy, B.; Babu, C.; Sundaravel, B.; Anandan, S.; Murugesan, V., Sol–gel synthesis of mesoporous mixed Fe_2O_3/TiO_2 photocatalyst: application for degradation of 4-chlorophenol. *Journal of Hazardous Materials* **2013,** *252*, 233-242.

66. Kim, M.; DiMaggio, C.; Salley, S. O.; Ng, K. S., A new generation of zirconia supported metal oxide catalysts for converting low grade renewable feedstocks to biodiesel. *Bioresource Technology* **2012,** *118*, 37-42.

67. Sharma, A.; Lee, B. K., Rapid photo-degradation of 2-chlorophenol under visible light irradiation using cobalt oxide-loaded TiO_2/reduced graphene oxide nanocomposite from aqueous media. *Journal of Environmental Management* **2016,** *165*, 1-10.

68. Tang, Y.; Zhang, G.; Liu, C.; Luo, S.; Xu, X.; Chen, L.; Wang, B., Magnetic TiO_2-graphene composite as a high-performance and recyclable platform for efficient photocatalytic removal of herbicides from water. *Journal of Hazardous Materials* **2013,** *252*, 115-122.

69. Lafjah, M.; Djafri, F.; Bengueddach, A.; Keller, N.; Keller, V., Beta zeolite supported sol–gel TiO_2 materials for gas phase photocatalytic applications. *Journal of Hazardous Materials* **2011,** *186* (2-3), 1218-1225.

70. Ganesan, R.; Lim, S. H.; Saifullah, M.; Hussain, H.; Kwok, J. X.; Ryan, L.; Bo, H. A.; Low, H. Y., Direct nanoimprinting of metal oxides by in situ thermal co-polymerization of their methacrylates. *Journal of Materials Chemistry* **2011,** *21* (12), 4484-4492.

71. Ganesan, R.; Dumond, J.; Saifullah, M. S.; Lim, S. H.; Hussain, H.; Low, H. Y., Direct patterning of TiO_2 using step-and-flash imprint lithography. *ACS Nano* **2012,** *6* (2), 1494-1502.

72. Ganesan, R.; Dinachali, S. S.; Lim, S. H.; Saifullah, M.; Chong, W. T.; Lim, A. H.; Yong, J. J.; San Thian, E.; He, C.; Low, H. Y., Direct nanoimprint lithography of Al_2O_3 using a chelated monomer-based precursor. *Nanotechnology* **2012,** *23* (31), 315304.

73. Dinachali, S. S.; Saifullah, M. S.; Ganesan, R.; Thian, E. S.; He, C., A universal scheme for patterning of oxides via thermal nanoimprint lithography. *Advanced Functional Materials* **2013,** *23* (17), 2201-2211.

74. Pelizzetti, E.; Minero, C., Metal oxides as photocatalysts for environmental detoxification. *Comments on Inorganic Chemistry* **1994,** *15* (5-6), 297-337.

75. Hoffmann, M. R.; Martin, S. T.; Choi, W.; Bahnemann, D. W., Environmental applications of semiconductor photocatalysis. *Chemical Reviews* **1995,** *95* (1), 69-96.

76. Konstantinou, I. K.; Albanis, T. A., TiO_2-assisted photocatalytic degradation of azo dyes in aqueous solution: kinetic and mechanistic investigations: a review. *Applied Catalysis B: Environmental* **2004,** *49* (1), 1-14.

77. Xue, J.; Ma, S.; Zhou, Y.; Zhang, Z.; He, M., Facile photochemical synthesis of Au/Pt/g-C_3N_4 with plasmon-enhanced photocatalytic activity for antibiotic degradation. *ACS Applied Materials & Interfaces* **2015,** *7* (18), 9630-9637.

78. Elmolla, E. S.; Chaudhuri, M., Photocatalytic degradation of amoxicillin, ampicillin and cloxacillin antibiotics in aqueous solution using UV/TiO_2 and UV/H_2O_2/TiO_2 photocatalysis. *Desalination* **2010,** *252* (1-3), 46-52.

79. Nagarjuna, R.; Challagulla, S.; Ganesan, R.; Roy, S., High rates of Cr(VI) photoreduction with magnetically recoverable nano-Fe_3O_4@Fe_2O_3/Al_2O_3 catalyst under visible light. *Chemical Engineering Journal* **2017,** *308*, 59-66.

80. Challagulla, S.; Nagarjuna, R.; Ganesan, R.; Roy, S., Acrylate-based polymerizable sol–gel synthesis of magnetically recoverable TiO_2 supported Fe_3O_4 for Cr(VI) photoreduction in aerobic atmosphere. *ACS Sustainable Chemistry & Engineering* **2016,** *4* (3), 974-982.

81. Shaikh, J. S.; Shaikh, N. S.; Mali, S. S.; Patil, J. V.; Pawar, K. K.; Kanjanaboos, P.; Hong, C. K.; Kim, J. H.; Patil, P. S., Nanoarchitectures in dye-sensitized solar cells: metal oxides, oxide perovskites and carbon-based materials. *Nanoscale* **2018,** *10* (11), 4987-5034.

82. Mishra, A.; Bauerle, P., Small molecule organic semiconductors on the move: promises for future solar energy technology. *Angewandte Chemie International Edition* **2012,** *51* (9), 2020-2067.

83. Fan, L. S.; Li, F., Chemical looping technology and its fossil energy conversion applications. *Industrial & Engineering Chemistry Research* **2010,** *49* (21), 10200-10211.

84. Lapin, N.; D'yankova, N. Y., Hydrogen evolution kinetics during transition metal oxide-catalyzed ammonia borane hydrolysis. *Inorganic Materials* **2013,** *49* (10), 975-979.

85. Cen, C.; Thiel, S.; Mannhart, J.; Levy, J., Oxide nanoelectronics on demand. *Science* **2009,** *323* (5917), 1026-1030.

86. Snow, E.; Campbell, P., Fabrication of Si nanostructures with an atomic force microscope. *Applied Physics Letters* **1994,** *64* (15), 1932-1934.

87. Chou, S. Y.; Krauss, P. R.; Renstrom, P. J., Nanoimprint lithography. *Journal of Vacuum Science & Technology B: Microelectronics and Nanometer Structures Processing, Measurement, and Phenomena* **1996,** *14* (6), 4129-4133.

88. Piner, R. D.; Zhu, J.; Xu, F.; Hong, S.; Mirkin, C. A., " Dip-pen" nanolithography. *Science* **1999,** *283* (5402), 661-663.

89. Madler, L.; Roessler, A.; Pratsinis, S. E.; Sahm, T.; Gurlo, A.; Barsan, N.; Weimar, U., Direct formation of highly porous gas-sensing films by in situ thermophoretic deposition of flame-made Pt/SnO_2 nanoparticles. *Sensors and Actuators B: Chemical* **2006,** *114* (1), 283-295.

90. Sahm, T.; Madler, L.; Gurlo, A.; Barsan, N.; Pratsinis, S. E.; Weimar, U., Flame spray synthesis of tin dioxide nanoparticles for gas sensing. *Sensors and Actuators B: Chemical* **2004,** *98* (2-3), 148-153.

91. Li, Y.; Liang, J.; Tao, Z.; Chen, J., CuO particles and plates: synthesis and gas-sensor application. *Materials Research Bulletin* **2008,** *43* (8-9), 2380-2385.

92. Garzella, C.; Comini, E.; Tempesti, E.; Frigeri, C.; Sberveglieri, G., TiO_2 thin films by a novel sol–gel processing for gas sensor applications. *Sensors and Actuators B: Chemical* **2000,** *68* (1-3), 189-196.

93. Kida, T.; Nishiyama, A.; Yuasa, M.; Shimanoe, K.; Yamazoe, N., Highly sensitive NO_2 sensors using lamellar-structured WO_3 particles prepared by an acidification method. *Sensors and Actuators B: Chemical* **2009,** *135* (2), 568-574.

94. Fernandez, A. C.; Sakthivel, P.; Jesudurai, J., Semiconducting metal oxides for gas sensor applications. *Journal of Materials Science: Materials in Electronics* **2018,** *29* (1), 357-364.

95. Figueiredo Borgognoni, C.; Kim, J. H.; Zucolotto, V.; Fuchs, H.; Riehemann, K., Human macrophage responses to metal-oxide nanoparticles: a review. *Artificial Cells, Nanomedicine, and Biotechnology* **2018**, 1-10.

96. Laurent, S.; Saei, A. A.; Behzadi, S.; Panahifar, A.; Mahmoudi, M., Superparamagnetic iron oxide nanoparticles for delivery of therapeutic agents: opportunities and challenges. *Expert Opinion on Drug Delivery* **2014,** *11* (9), 1449-1470.

97. Jangra, S. L.; Stalin, K.; Dilbaghi, N.; Kumar, S.; Tawale, J.; Singh, S. P.; Pasricha, R., Antimicrobial activity of zirconia (ZrO_2) nanoparticles and zirconium complexes. *Journal of Nanoscience and Nanotechnology* **2012,** *12* (9), 7105-7112.

98. Mangalaraj, D.; Devi, D. N., Ag/TiO_2 (metal/metal Oxide) core shell nanoparticles for biological applications. In *Recent Trends in Materials Science and Applications*, Springer: 2017; 9-17.

99. Li, K.; Xie, Y.; You, M.; Huang, L.; Zheng, X., Plasma sprayed cerium oxide coating inhibits H_2O_2-induced oxidative stress and supports cell viability. *Journal of Materials Science: Materials in Medicine* **2016,** *27* (6), 100.

Chapter 2

Materials and characterization methods

Chapter 2: Materials and characterization methods

2.1 Materials

Titanium (IV) *iso*propoxide (TIPO), titanium (IV) ethoxide, tantalum (V) ethoxide, tungsten (V) ethoxide, methacrylic acid (MAA), 2-(methacryloyloxy)ethyl acetoacetate (MAEAA), ethylene glycol dimethacrylate (EDMA), allyl acetoacetate (AAAc), pentaerythritol tetrakis(3-mercaptopropionate) (PETMP), 2-hydroxy-2-methylpropiophenone (HMP), glycidol, *tert*-butyl acetoacetate (t-BAA), 3-methyl-3-oxetane methanol, diphenyliodonium hexafluorophosphate (DPHFP), 1H,1H,2H,2H–perfluorodecyltrichlorosilane, benzoyl peroxide (BPO), alumina nano powder, Fe_3O_4, sodium citrate (SC), acetic acid, polyethylenimine (branched, M_w ~800), 1-ethyl-3-(3-dimethylaminopropyl) carbodiimide (EDC), and *N*-hydroxysuccinimide (NHS) acetone, graphite flakes, and methylene blue (MB), potassium dichromate ($K_2Cr_2O_7$) and toluene were purchased from Sigma Aldrich and used as received unless otherwise specified.

Conc. H_2SO_4, H_3PO_4, $KMnO_4$, H_2O_2, HCl, ethanol, oxalic acid, ammonium oxalate, potassium periodate 1,5-diphenylcarbazide (DPC), iron (II) sulfate ($FeSO_4.7H_2O$), iron (III) chloride anhydrous ($FeCl_3$), ammonia solution (25%), sodium borohydride, 4-nitrophenol (4-NP) and sodium hydroxide were procured from SD Fine Chemicals, India Ltd.

Industrial grade Zeolite-4A was generously offered by Ion Exchange Pvt. Ltd., India. Alumina nanopowder (AO) of ~80 nm in average size was procured from Nanoshel Inc. and used as-received. Palladium chloride was procured from Himedia, India.

Polydimethylsiloxane (PDMS) stamps were fabricated from Sylgard 184 purchased from Sigma Aldrich. Ammonia borane (AB) was synthesized following the literature procedure.[1]

2.2 Characterization

The synthesized materials were thoroughly characterized for their chemical, structural and morphological characteristics. Functional group analyses and chemical changes of the samples were performed by making pellets with KBr and characterized with FTIR studies in the transmission mode by using Shimadzu (FTIR-8400S) with the resolution of 4 cm^{-1}. Differential scanning calorimetry (DSC) (Shimadzu DSC-60) and thermogravimetric analysis (TGA) (Perkin-Elmer/ Shimadzu DTG-60) measurements were obtained at a scanning rate of 10 °C/min. Diffuse reflectance spectroscopy (Varian, Cary 5000/ JASCO V-670) was measured to analyze the band gap of the catalysts. X-ray diffraction (XRD) patterns of the

powders were recorded with Bruker AXS D8 Advance/ Rigaku Ultima IV with Cu K_α radiation (λ = 1.5418 Å) at a scan rate of 1°/min. Raman spectroscopy (Horiba Jobin-Yvon, LabRAM/UniRAM 3300) studies were carried out to corroborate the XRD phase analyses. The Brunauer-Emmett-Teller (BET) surface area of the catalysts was determined using nitrogen adsorption/desorption studies with BET apparatus (Smart Sorb 93/Micromeritics ASAP 2020). Scanning Electron Microscope (SEM) (Hitachi S3400/Carl-Zeiss ULTRA-55/FEI Apreo S) fitted with Energy Dispersive Spectroscopy (EDS) unit was employed to analyze the surface morphology and composition of the synthesized catalysts. High resolution transmission electron microscopy (TEM) (Jeol, JEM 2100) was used to analyze the dispersion of the active material over the support. X-ray photoelectron spectroscopy (XPS) (PHI 5000 Versa Prob II (FEI Inc.)) was used to measure the oxidation state of elements present in the materials. Energy dispersive X–ray fluorescence (ED-XRF) spectra were collected using PANalytical (Epsilon 1) to analyze the composition of the synthesized catalysts. Magnetic properties of the synthesized catalysts were analyzed with Lakeshore Vibrating sample magnetometer (VSM) model 665. The synthesized epoxy and oxetane monomers were characterized using Bruker Ascend (400 MHz) nuclear magnetic resonance (NMR) spectrophotometer.

A UV-Vis spectrophotometer (JASCO V-650) was used to measure the concentration of MB and Cr(VI) solutions to follow photodegradation and photoreduction, respectively. Atomic absorption spectroscopy (AAS) (Shimadzu AA-7000) was used to quantify the total chromium and palladium content in the solution.

Zetasizer Nano-ZS (Malvern) was employed to measure the particle size as well as surface zeta potential, wherein the test samples were taken in the form of 20 μg/mL aqueous suspensions.

2.3 Reference

1. Ramachandran, P. V.; Gagare, P. D., Preparation of ammonia borane in high yield and purity, methanolysis, and regeneration. *Inorganic Chemistry* **2007,** *46* (19), 7810-7817.

Chapter 3

Polymerizable sol-gel precursor mediated synthesis of TiO_2/zeolite-4A and RGO/TiO_2/zeolite-4A, their application towards photodegradation of methylene blue

Chapter 3: Polymerizable sol-gel precursor mediated synthesis of TiO_2/zeolite-4A and RGO/TiO_2/zeolite-4A, their application towards photodegradation of Methylene blue

3.1. Introduction

Owing to the enormous potential for environmental remediation, there is a persistent quest for the design and development of new efficient photocatalytic materials. Several semiconducting materials such as TiO_2, $BaTiO_3$, $SrTiO_3$, Bi_2WO_6 etc. have shown significant photocatalytic properties.[1-9] Among them, TiO_2 is by far the most popular candidate, on which, numerous works have been carried out such as tuning the band gap by doping, supporting onto different materials etc. so as to improve its efficiency.[10-16] Due to its optimal and tunable semiconducting properties, TiO_2 has been used for vast range of applications including sensors,[17] solar cells,[18] photocatalysis,[19-23] memory devices,[24] anti-reflection coatings,[25] optical waveguides[26] and environmental remediation.[27-29] It is considered to be a non-toxic material and therefore used in several bio-applications too.[30,31] Plenty of literature is available as TiO_2 being studied as the high-potential heterogeneous photocatalyst for mineralization of the environmental pollutants.[32-34] Studies of electronic and charge–transfer processes occurring during the heterogeneous photocatalysis on TiO_2 is well documented.[35-37] The heterogeneous photocatalysis generally involves formation of an electron–hole pair. Catalytic oxidation is assumed to proceed via direct attack of adsorbed species on the catalytic surface by photogenerated holes (in valence band) or to be indirectly mediated by radicals, such as $^{\bullet}OH$, generated from adsorbed water, oxygen, and hydroxyl groups on the catalyst surface. In this way, hazardous organic compounds can be completely mineralized. Structurally TiO_2 has mainly three polymorphs, namely anatase, rutile and brookite. Rutile is thermodynamically stable at room temperature, and anatase is kinetically stable. The low rate of electron–hole recombination over anatase TiO_2 proved to be better catalyst compared to the rutile phase.[38] TiO_2 is a wide band gap material having a band gap in the range of ~3.2 – 3.7 eV.[39] This energy corresponds to <390 nm wavelength of light and thus TiO_2 generates electron-hole pair by absorbing radiation below 390 nm. Since this wavelength lies at near UV region, several studies have been devoted to bring down the band gap.[40-44] The mode of synthesis of TiO_2 also influences the photocatalytic activity of the catalyst (i.e., band gap, bounded hydroxyl species, crystallinity and particle size). The anatase phase nano-TiO_2

prepared by the solution combustion method has been reported to have better photocatalytic activity compared to the commercial Degussa P-25 catalyst.[45,46]

Synthesis of TiO_2 serves as a fundamental requisite to realize the potential applications and therefore various synthetic approaches have been explored.[47,48] Conventionally majority of the TiO_2 photocatalysts have been synthesized via sol-gel route.[49] Titanium alkoxide and titanium tetrachloride are the most common choices of starting materials for sol-gel based TiO_2 synthesis. Vapor phase (chemical and physical vapor deposition) synthesis of TiO_2 has also been reported by taking titanium tetrachloride as the starting compound.[50] Typically these precursors upon hydrolysis produce titanium hydroxide that upon further calcinations at above 400 °C generate crystalline phases of TiO_2 such as anatase, rutile and brookite. For photocatalytic applications, it is preferred to utilize supported-TiO_2 as the supports can synergistically participate in the photodegradation either by altering the band gap or by offering adsorption sites, where the pollutants are first attracted and then degraded by the catalyst.[51-55] In addition, the supports disperse the active materials on its surface and thereby yield large surface area of the catalyst.

In this effort, we first report a facile synthesis of zeolite-4A-supported TiO_2, mediated by free radical polymerization of methacrylate-functionalized titanium-containing precursor. This route offers facile and scalable synthesis of various oxides.[56] To the best of our knowledge, this is the first report using this free radical polymerizable sol-gel route to synthesize supported-TiO_2 photocatalyst and its usage for photodegradation of dyes. We utilized polymerizable methacrylate-functionalized titanium-containing precursor, which was polymerized in the presence of zeolite-4A support by inducing free radical thermal polymerization. Upon further calcination, we obtained zeolite-4A-supported TiO_2. Methylene blue was chosen as the model dye in this work, as it is one of the most common dyes used in industries. Industrial grade zeolite-4A was chosen for this study, as it is known that particles having less than 500 nm size possess higher degree of leaching into the water system and thereby yielding secondary contamination.[57-59] Therefore, for practical applications it is desirable that the supports and/or catalysts must have particle size greater than 500 nm. The industrial grade zeolite-4A chosen in this study has an average size of 1 μm. Catalysts prepared in this work were used to study the photodegradation of methylene blue as a potential application. Zeolite-4A was found to enhance the adsorption of the methylene blue on its surface, thus enabled TiO_2 to degrade the dye effectively.

To enhance the adsorption ability further, we then looked upon graphene oxide (GO) as a potential candidate. A plethora of literature is available on GO exhibiting remarkable adsorption characteristics due to the presence of a large amount of oxidized functional groups such as hydroxyl, aldehyde, and carboxylic.[60-65] One of the most popular methods of synthesizing GO from graphite is popularly known as modified Hummer's method. Recently, an improved oxidizing method was re-ported by Marcano et al.[62] In this improved method, in addition to $KMnO_4$ and H_2SO_4, H_3PO_4 was used as opposed to $NaNO_3$ that has been used in modified Hummer's method. This modified oxidation approach yielded highly oxidized GO with higher yield. The extensive oxidation is desired because the higher the functional groups in graphene, the higher the adsorption capability. Therefore, we choose to synthesize GO by this improved oxidation method in order to obtain maximum oxidation. However, the challenge is to anchor the GO onto TiO_2 or Zeolite-4A surface. Recently, Williams et al. showed the synthesis of reduced-graphene oxide (RGO) from GO by photoreduction with TiO_2.[63] During the photoreduction process, it was demonstrated that the RGO got anchored onto the TiO_2 surface. In this current work, we envisaged to enhance the adsorption capability of TiO_2/zeolite-4A by incorporating RGO on its surface. Such a strategy would yield a bifunctional material that would possess higher adsorption ability as well as higher photocatalytic activity.[64,65] Methylene blue (MB) was chosen as the model pollutant in this work, as it is one of the most common dyes used in industries. The synthesized RGO/TiO_2/zeolite-4A nanocomposite was thoroughly characterized and used to study its efficiency for adsorption and photodegradation of methylene blue. In such a way, two catalytic systems TiO_2/zeolite-4A and RGO/TiO_2/zeolite-4A are discussed.

3.2. TiO_2/zeolite-4A

3.2.1 Experimental section

(i) Methods

Titanium methacrylate was synthesized in a similar fashion reported in the literature. In a typical experiment, 6 mmol of methacrylic acid was added drop wise into a vial containing 3 mmol of titanium (IV) *iso*propoxide stirred under an inert atmosphere. An immediate color change of the solution from colorless to yellow indicated the formation of methacrylate substituted titanium complex. About 2-wt% of BPO (with respect to MAA) in 100 µL of acetone was added into this titanium complex to formulate a polymerizable precursor solution. Calculated amount of zeolite-4A support was then added into the precursor solution

as prepared above. About 50 µL of water was added into this mixture and shaken vigorously in a shaker, which resulted in gelation in about 15 min (*vide infra*). The obtained gel was heated to 125 °C for 30 min to carry out free radical polymerization that yielded a powdery product. This powder was calcined at 450 °C for 4 hrs to obtain TiO_2 supported zeolite-4A. By varying the Ti-methacrylate to zeolite-4A ratio, catalysts containing different weight fractions of supported TiO_2 were prepared (see Table 3.1).

Table 3.1: Feed compositions of precursors

Sample	Amount of TiPO (g)	Amount of MAA (g)	Amount of zeolite-4A (g)
Unmodified TiO_2	1.0	0.605	0
10 % TiO_2/zeolite-4A	0.873	0.53	2.304
15 % TiO_2/zeolite-4A	1.313	0.795	2.175
20 % TiO_2/zeolite-4A	1.91	1.16	2.0
30 % TiO_2/zeolite-4A	2.626	1.595	1.79

The point of zero charge (PZC) has been found from the plot of ΔpH (pH_{intial} - pH_{final}) *vs* pH_{intial}, following batch equilibrium technique.[61,66] For this, 100 mg of sample was soaked in a 50 mL of 0.1 M KNO_3 solution at different initial pH (between 3 and 9) adjusted by addition of 0.1 M HNO_3/NaOH and stirred for 24 h at 27 °C. The intersection of linear fitting of the points at the X-axis ($pH_{initial}$) was taken as the PZC.

(ii) Photocatalytic evaluation

Photodegradation studies were carried out using a cylindrical annular batch photoreactor fitted with a medium pressure mercury vapor lamp of 125 W. The lamp radiated predominantly at 365 nm (3.4 eV). The average energy of the light emitted was 3.5 eV with a corresponding photon flux of 5.86×10^{-6} mol of photons/s. The photoreactor consisted of a double-walled borosilicate immersion well that is placed inside the reaction vessel. Water was circulated around the lamp to keep the reaction at room temperature. The water circulation also helped stopping the IR radiation from the lamp. All degradations were performed in an open system with an open air circulation to provide enough oxygen for the oxidative degradation of pollutants. The catalyst amount for a particular batch reaction (with 100 mL of 10 ppm methylene blue) was varied between 25 mg and 200 mg of 20%

TiO_2/zeolite-4A catalyst (see supporting information). Since, 50 mg of the catalyst showed considerable time window for photodegradation, further studies were carried out using 50 mg of the catalysts. During irradiation, ~1 to 2 mL of the suspension was collected in regular time interval and the progress of photodegradation was monitored by observing the disappearance of the absorption peak of methylene blue at 663.5 nm the UV-visible absorption spectra in a Shimadzu UV-spectrometer.

3.2.2 Results and discussion

(i) Materials

The synthetic strategy of supported TiO_2 catalyst entails zeolite-4A mixed with a polymerizable Ti-containing precursor. Scheme 3.1 depicts the pictorial representation of the synthetic strategy. Polymerization is induced in a homogeneously mixed precursor and the support so as to yield Ti-containing polymer coated onto the support. Upon calcination this would lead to the formation of TiO_2 supported on zeolite-4A. In a first attempt, titanium *tetra*methacrylate was synthesized by adding four equivalent of methacrylic acid to one equivalent of titanium (IV) *iso*propoxide. This yielded titanium *tetra*methacrylate as the four *iso*propoxy groups of titanium are replaced by the methacrylate groups. As soon as the vigorous shaking of the added zeolite-4A support in the above formulated solution was ceased (*vide supra*), the support got settled down at the bottom of the container, leaving majority of the precursor solution residing on top. In order to obtain a uniform coating, it is required to have a homogeneous dispersion of the support in the precursor matrix. Hence, in the second attempt, to circumvent the precipitation of the zeolite support, *di*methacrylate substituted Ti-containing precursor was synthesized by adding two equivalent of methacrylic acid to one equivalent of titanium (IV) *iso*propoxide. This on average is envisaged to replace two *iso*propoxy groups of titanium (IV) *iso*propoxide with methacrylate group, sparing the remaining two *iso*propoxy groups that are vulnerable for rapid hydrolysis. This strategy is employed because the remaining *iso*propoxy groups undergo easy hydrolysis to yield titanium hydroxide that would precipitate as a gel, entrapping the support, and thereby result in a homogeneous dispersion (*vide* Scheme 3.1).

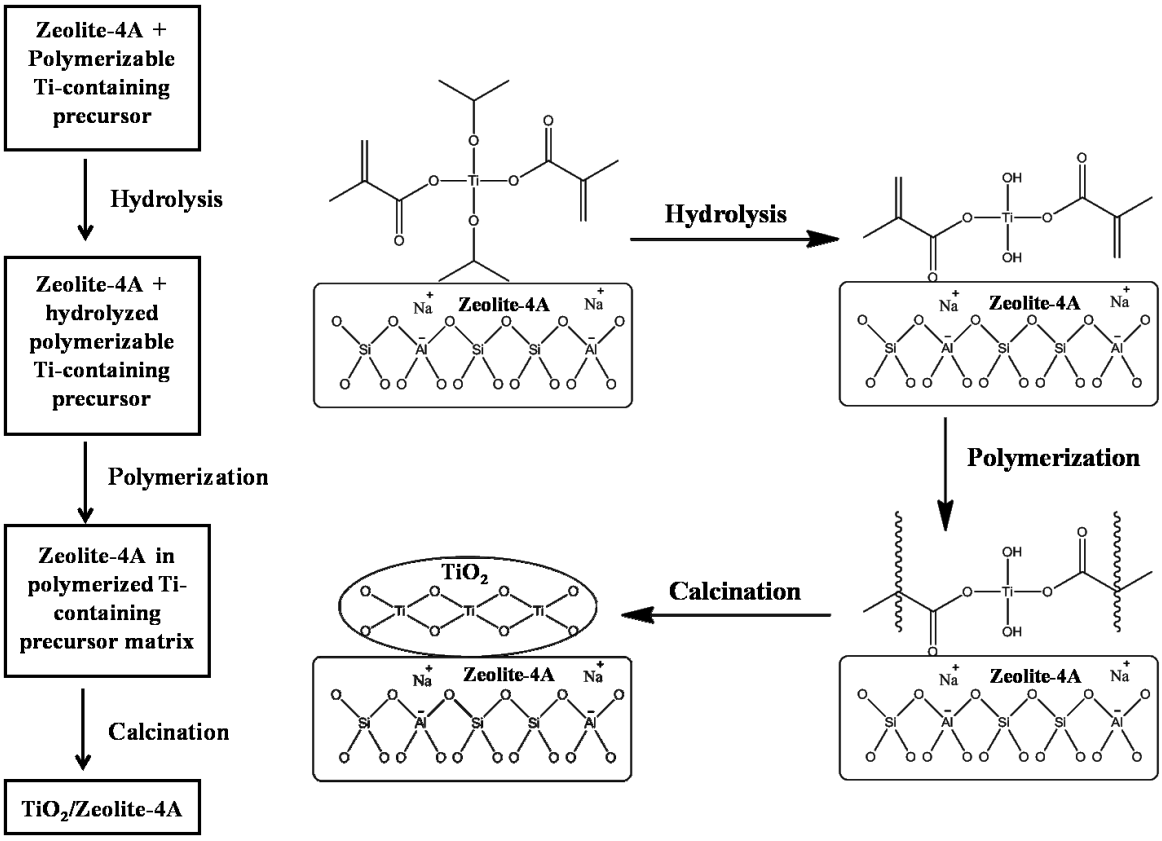

Scheme 3.1: Synthetic strategy of TiO_2/zeolite-4A catalysts *via* polymerizable sol-gel approach.

The chemical changes during the catalyst synthesis were monitored by IR spectroscopy. Fig. 3.1 shows the IR spectra of the prehydrolyzed, hydrolyzed, polymerized and calcined sample of Ti-*di*methacrylate *diiso*propoxide/zeolite-4A. Before hydrolysis, peaks are observed at 1644, 1555 and 1422 cm^{-1} that correspond to carbon-carbon double bond stretching of methacrylate and asymmetric and symmetric stretching of metal-complexed carbonyl groups, respectively. A small peak at 1699 cm^{-1} is also observed that may probably correspond to carbonyl stretching of free methacrylic acid. After hydrolysis, the IR spectrum vastly remains unchanged, except an increase in the peak area correspond to the hydroxyl group. This could be attributed to the formation of isopropanol that is a byproduct of hydrolysis as well as the presence of water. It is noteworthy that the peaks at 1555 and 1422 cm^{-1} are preserved even after hydrolysis, which confirms that the chelation of methacrylic acid to the metal center remain unaffected. These peaks remain unaffected even after polymerization, indicating that the titanium metal is trapped in the polymer matrix that is uniformly coated over the zeolite-4A support. Considerable decrease in the methacrylate carbon-carbon double bond peak intensity at 1644 cm^{-1} is seen after the polymerization step, confirming the occurrence of polymerization. The small residual peak of the methacrylate

double bond after polymerization indicates that not all methacrylate groups have participated in the reaction. Despite the incomplete reaction, polymerization converts the wet gel into a dry powdery substance. After calcination, due to the burning off of organics, the IR spectrum did not contain any bands of organic functional groups. The finger print region below 1000 cm^{-1} is crowded due to the overlapping signals from TiO_2 and zeolite-4A.

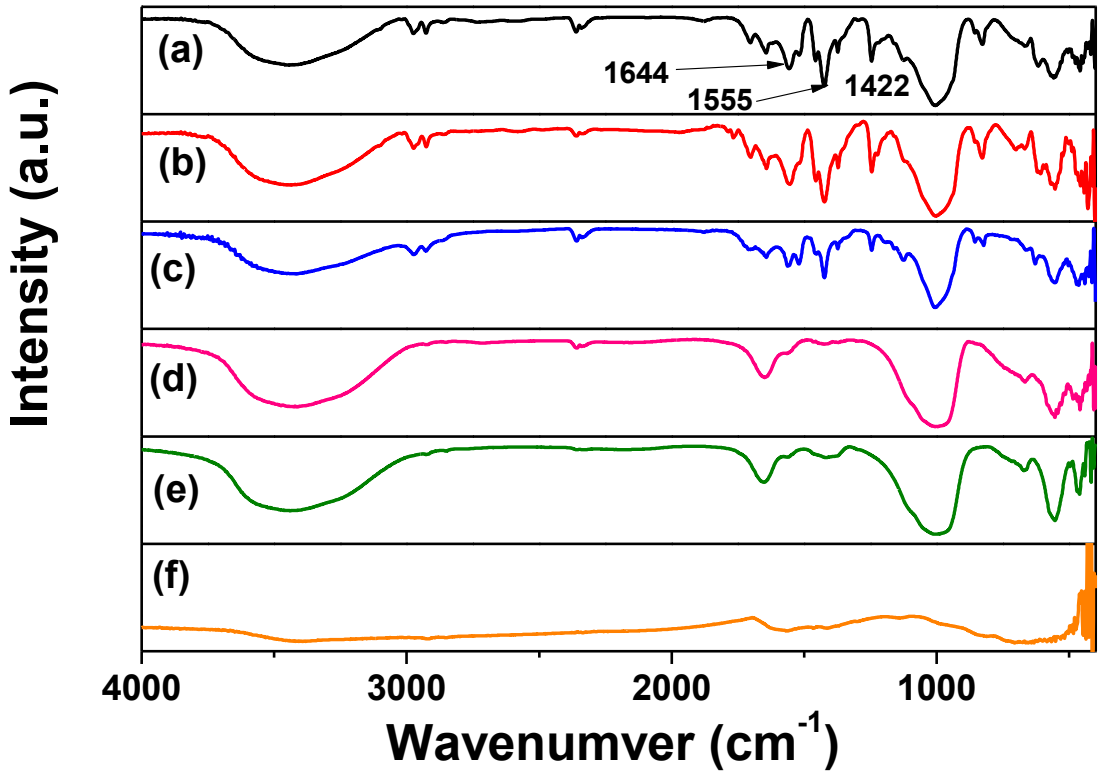

Figure 3.1: Infrared spectra of (a) prehydrolyzed precursor/zeolite-4A, (b) hydrolyzed precursor/zeolite-4A, (c) polymerized precursor/zeolite-4A, (d) calcined TiO_2/zeolite-4A, (e) unmodified zeolite-4A and (f) calcined TiO_2.

Thermal analyses such as DSC and TGA were performed in order to evaluate the polymerization condition and thermal decomposition of precursor/zeolite-4A. Fig. 3.2 (a) shows the DSC scan result of 20 wt% TiO_2 precursor/zeolite-4A. The DSC scan reveals an exothermic peak at about 125 °C, indicating the occurrence of free-radical polymerization at this temperature. This temperature is therefore used for all the polymerization reactions in this work. TGA studies of the polymerized precursor/zeolite-4A samples in air atmosphere are shown in Fig. 3.2 (b). Irrespective of the different feed amount of precursor, a two-step thermal degradation pattern was observed. The first step, up to 250 °C, is attributed to the loss of low volatile components such as water, isopropanol, unreacted methacrylic acid monomer etc. The second step mass loss between 250 and 450 °C corresponds to the

degradation of organics from the Ti-containing precursor polymer coated on the surface of zeolite-4A. An increasing weight loss was observed with increasing TiO_2 loading, which is due to more organic content from the Ti-containing precursor. Above 450 °C, a near flat line was observed. Therefore, 10, 15, 20 and 30 wt% TiO_2/zeolite-4A catalysts were prepared by calcining the polymerized samples at 450 °C.

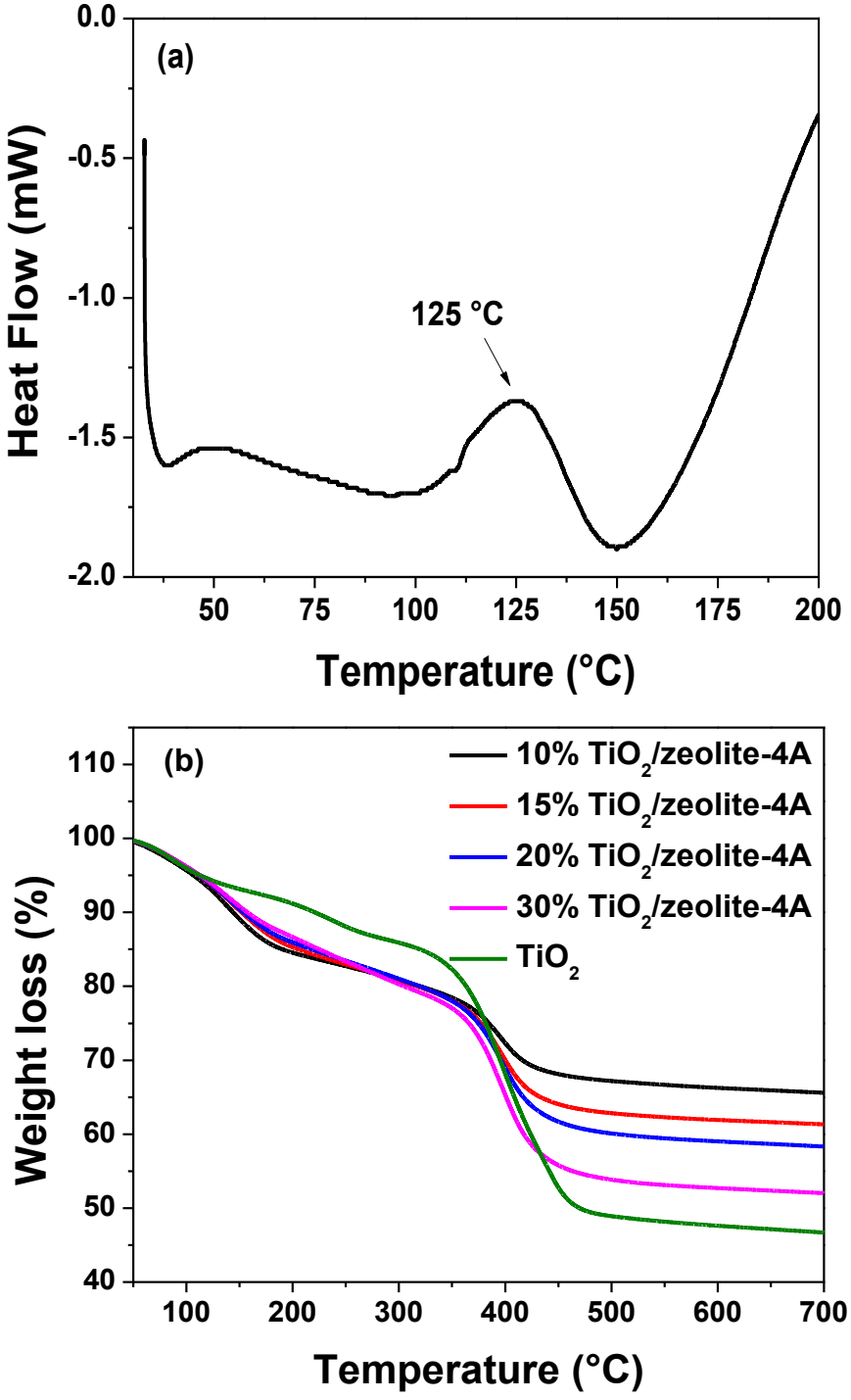

Figure 3.2: (a) DSC of 20% TiO_2 precursor/zeolite-4A; (b) TGA of TiO_2 precursor/zeolite-4A and TiO_2 precursor.

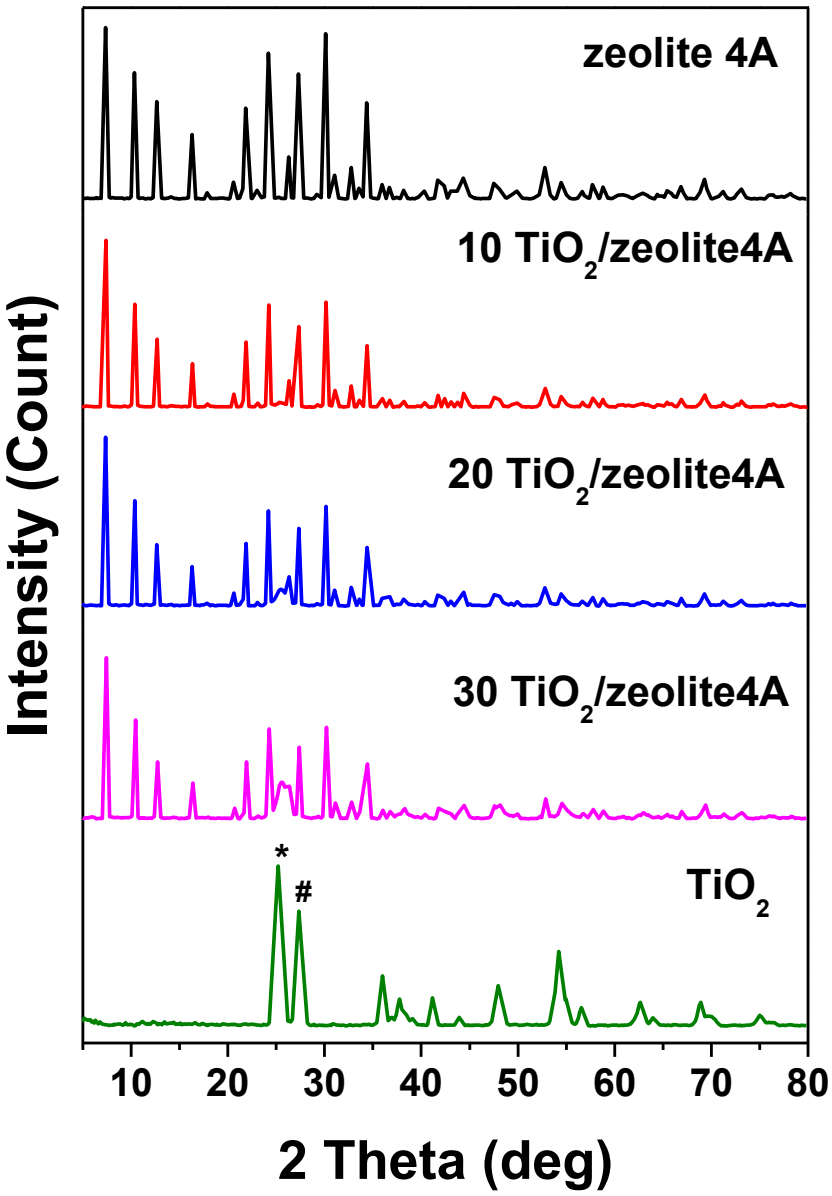

Figure 3.3: XRD of zeolite-4A, 10, 20 and 30 wt% TiO_2/zeolite-4A, and TiO_2. * and # indicates the anatase and rutile phases, respectively.

XRD patterns of the unmodified zeolite-4A, TiO_2 and 10, 20 and 30 % TiO_2/zeolite-4A powders are plotted in Fig. 3.3. The supplied zeolite-4A showed highly crystalline structure. On the other hand the polymerizable sol-gel synthesized TiO_2 peaks were broad indicating nano crystallinity. The pure TiO_2 made by this procedure crystallized in anatase as well as rutile structure. The anatase to rutile ratio is roughly about 1.5:1. When 10% TiO_2 was incorporated in zeolite-4A, the XRD pattern did not change much from that of unmodified zeolite-4A. There was no observable TiO_2 peak in 10% TiO_2/zeolite-4A catalyst, which signifies that the TiO_2 particles could be very small in size and highly dispersed in zeolite surface. When the TiO_2 loading was increased to 20%, there was significant peak of anatase

TiO_2. Interestingly, with the increment in loading of TiO_2, the TiO_2 peaks showed higher crystallinity indicating bigger crystallite size.

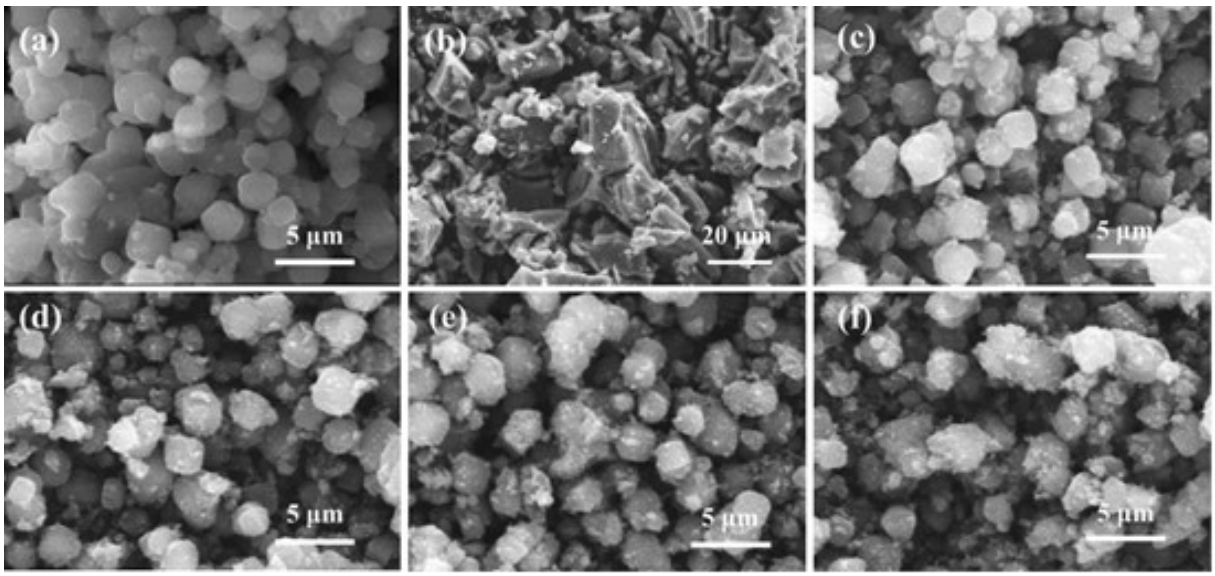

Figure 3.4: Composite SEM images of (a) zeolite-4A, (b) TiO_2, and (c-f) 10, 15, 20 and 30 wt% TiO_2/zeolite-4A, respectively.

SEM was employed to visualize the morphology of the samples and the images are shown in Fig. 3.4. The unmodified zeolite-4A was seen to have cubic shapes with the size ranging from 0.5 µm to 2 µm. The surface of the zeolite-4A is observed to be smooth with well-defined edges. On the other hand, the unmodified TiO_2 was seen to have irregular shapes with particle size ranging from 3 µm to 20 µm. There is a clear trend seen in the SEM images of the catalysts with increasing amount of TiO_2 from 10 wt% to 30 wt%. The 10 % TiO_2/zeolite-4A catalyst showed distinct bright particles on the surface of the zeolite-4A. With increasing the TiO_2 content, greater amount of bright particles were observed in the zeolite-4A surface. In case of 20 % TiO_2/zeolite-4A, the zeolite-4A support was seen to have slightly smoothened edges, which was more pronounced in case of 30 % TiO_2/zeolite-4A. This confirms that most of the TiO_2 were anchored onto the zeolite-4A surface. The TiO_2 particle sizes in the supported catalyst were in the range of 50-300 nm. A few larger particles were also seen, particularly so in 20 % and 30 % TiO_2/zeolite-4A, which may be fused 'TiO_2-zeolite' particles along with a small amount of unanchored TiO_2 particles. A qualitative energy dispersive spectroscopic (EDS) analysis confirmed the presence as well as a clear trend of increase in TiO_2 content with increasing the feed ratio of Ti-precursor (Fig 3.5). The successful anchoring of TiO_2 on zeolite-4A confirmed by SEM also shows the potential of

the polymerizable sol-gel route for easy fabrication of doped as well as multicomponent oxides on various supports.[13,67-70]

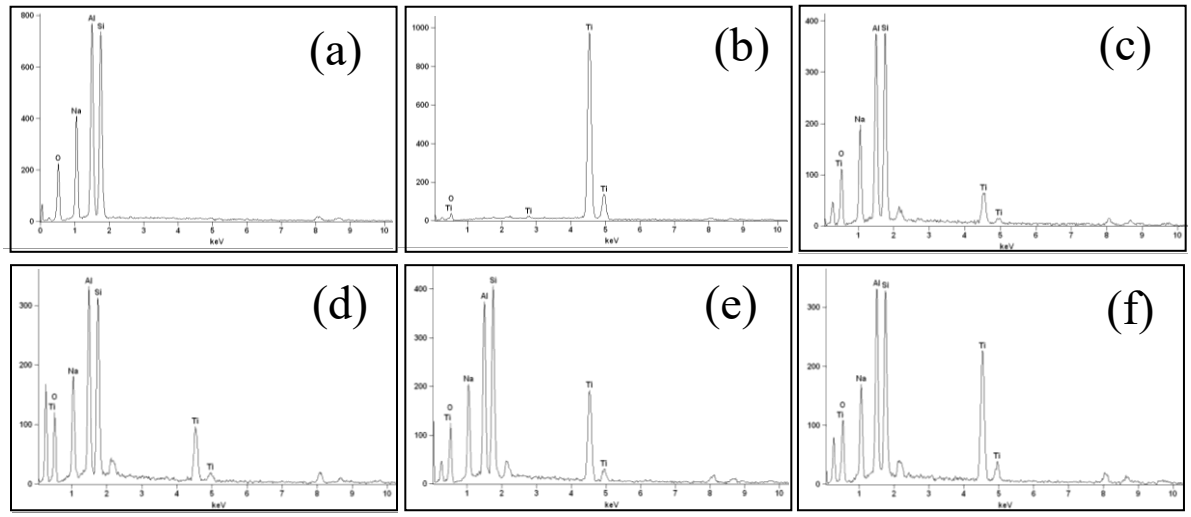

Figure 3.5: Composite EDS images of (a) zeolite-4A, (b) TiO_2, and (c-f) 10, 15, 20 and 30 wt% TiO_2/zeolite-4A, respectively.

Table 3.2: Surface area analysis

Sample	Specific Surface area (m^2/g)*
Pristine zeolite-4A	1.24
Pristine TiO_2	38.48
10 % TiO_2/zeolite-4A	11.48
15 % TiO_2/zeolite-4A	14.98
20 % TiO_2/zeolite-4A	21.35
30 % TiO_2/zeolite-4A	24.33
20 % TiO_2/zeolite-4A – Physical blend	8.56

* Determined from nitrogen adsorption isotherms (BET method) with 98 % confidence level.

Surface area measurements were carried out by using Brunauer–Emmett–Teller (BET) method and the results are listed in Table 3.2. The surface area of unmodified zeolite-4A was found to be 1.24 m^2/g and that of unmodified TiO_2 was found to be 38.48 m^2/g. For comparison, a physical blend of sol-gel synthesized TiO_2 and zeolite-4A was prepared. In case of the catalysts, the surface area was found to be increasing with increase in TiO_2 content. The physical blend of 20 % TiO_2 and 80 % zeolite-4A was found to have the surface

area of 8.56 m^2/g, which is in good agreement with the additive value of the respective unmodified components' surface area. Interestingly, the 20 % TiO_2/zeolite-4A catalyst showed a surface area of 21.35 m^2/g (~2.5 times than the physical blend). Such an increase in surface area may be attributed to the reason that the TiO_2 nanoparticles are highly dispersed and anchored onto the zeolite-4A surface. Since the pore diameter of the zeolite-4A (0.4 nm) is much smaller, the TiO_2 nanoparticles cannot be encapsulated in the cages or channels of the zeolite-4A. Thus, it is largely presumed that the TiO_2 nanoparticles are supported onto the zeolite-4A surface.

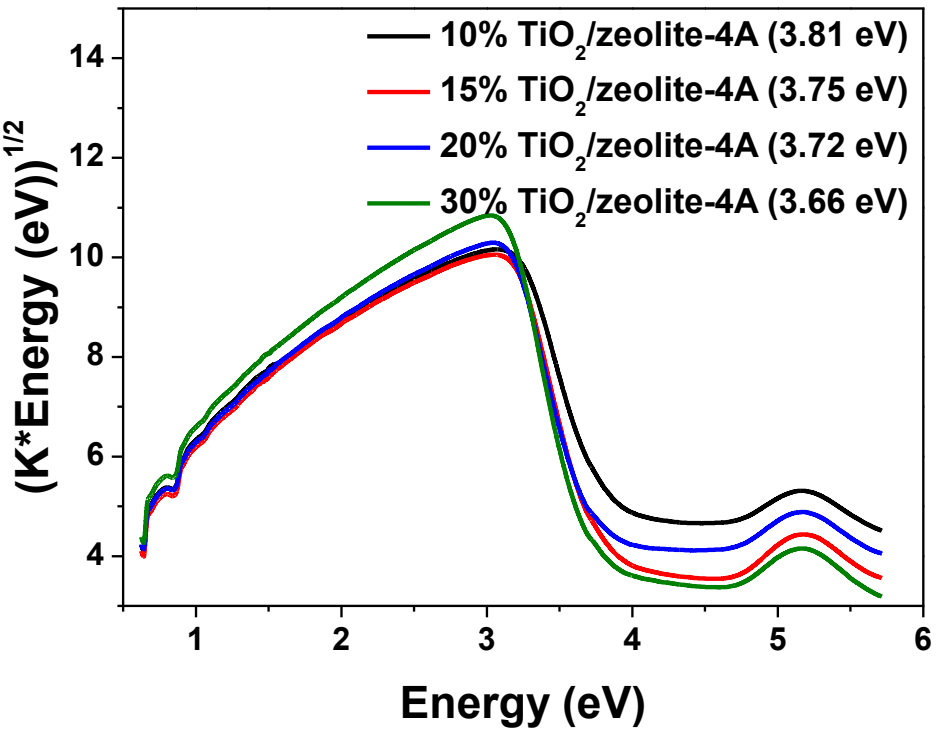

Figure 3.6: Plot of (Kubelka Munk factor (K)*Energy)$^{1/2}$ vs Energy obtained from diffuse reflectance spectra of the catalysts.

Direct band gap of the catalysts were obtained from the Kubelka Munk function. The Kubelka Munk factor (K) was calculated by using $K = (1-R)^2/2R$, where R is the % reflectance. In the (K × energy)$^{1/2}$ vs energy plot, intersection of the extrapolated linear portion of the curve with the energy axis yields the direct band gap of the material. In Fig. 3.6, (K × energy)$^{1/2}$ was plotted against energy to obtain the band gap from the diffuse reflectance spectra for the 10, 15, 20 and 30 wt% TiO_2/zeolite-4A powders.[71] The 10% TiO_2/zeolite-4A had a band gap of around 3.81 eV, which went down with the increment of TiO_2 loading in zeolite-4A. The 15, 20 and 30 % TiO_2/zeolite-4A had the band gap of 3.75, 3.72 and 3.66 eV, respectively. The powder XRD and the electron microscopy showed that

with lower loading of TiO_2 in zeolite-4A the crystallite sizes of TiO_2 became smaller. The change in crystallite size with TiO_2 loading could be nicely corroborated with the band gap obtained from diffuse reflectance spectra. The increasing band gap with decreasing TiO_2 loading (*vis a vis* smaller crystallites) could be attributed to the quantum confinement.

The PZC of unmodified zeolite-4A, as-synthesized TiO_2, as-synthesized 20 wt% TiO_2/zeolite-4A catalyst and used-catalyst (pre-treated for overnight at pH 5.0) is found to be 5.6, 5.5, 7.5 and 6.4, respectively. The PZC of TiO_2 synthesized by our method (5.5) is found to be in the same range to that of TiO_2 synthesized by other methods.[72] A little decrease in PZC of used-catalyst compared to the as-synthesized catalyst was observed. This could be due to the overnight pre-treatment of the as-synthesized catalyst at acidic pH that could have altered the surface charge.[73]

(ii) Catalytic degradation

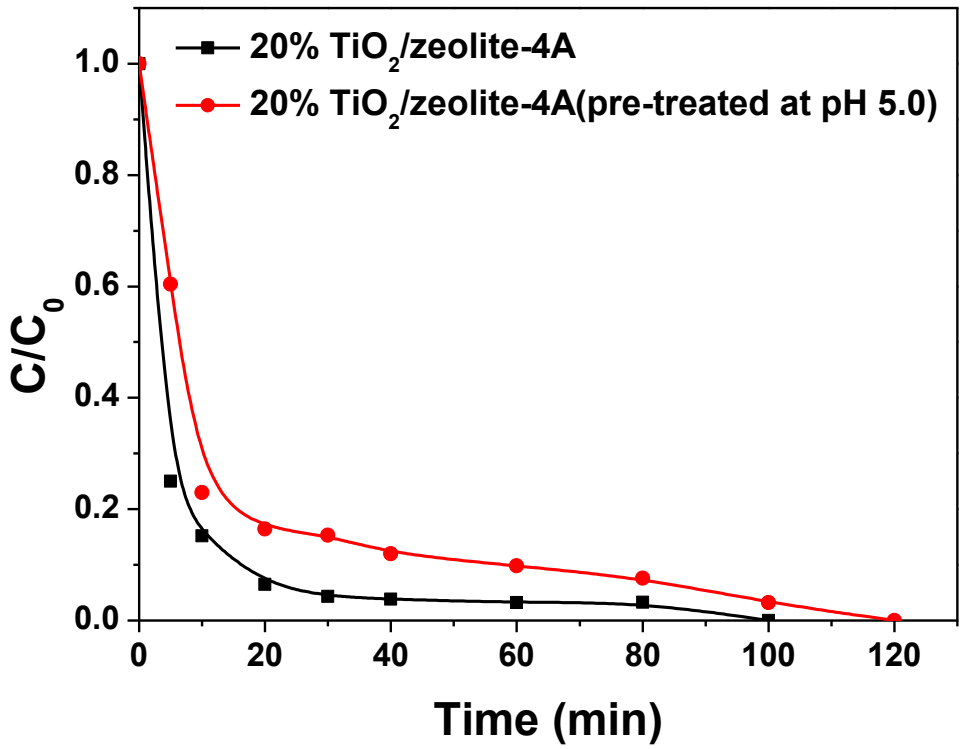

Figure 3.7: Comparison of the catalytic performance of methylene blue degradation with 50 mg of as-prepared and acid pre-treated 20 % TiO_2/zeolite-4A.

Photodegradation efficiency of the synthesized catalysts were studied by choosing methylene blue as a model dye, as this is widely used in industries and known to contaminate the environment. Moreover, methylene blue has been chosen as a model dye for photodegradation studies with numerous catalysts and thus serves as a reference compound.

It is known from the literature that methylene blue due to its cationic nature adsorbs well onto basic substrates and therefore the optimum pH for its photodegradation is in the range of 8 to 9.[74] To corroborate this adsorption phenomenon, we pretreated our as-prepared 20% TiO_2/zeolite-4A catalyst with pH 5.0 for overnight to make the surface acidic. This affected the adsorption of methylene blue as evidenced from Fig 2.7.[53,75] Though there is no significant difference in catalytic performances, however, the initial adsorption of methylene blue is quite different on both the surfaces. This could be attributed to the acidic surface of zeolite-4A on which the adsorption of cationic dye is poor.

In our study, for a comparison, we carried out photodegradation studies at two different pH values, namely pH 8.5 and pH 6.0. Fig. 3.8 (a) shows the photocatalytic degradation of methylene blue with 50 mg of 20% TiO_2/zeolite-4A catalyst at pH 8.5 and Fig. 3.8 (b) shows the same with pH 6. Interestingly, the UV absorbance graphs of photodegradation at these two different pH values looked distinctly different. For the degradation at pH = 8.5, the main peak of methylene blue at 663.5 nm gradually decreased with time along with a significant blue shift of the peak. The other major peak of methylene blue at 292 nm initially decreased however after 30 minutes of degradation, absorbance pattern changed completely. On the other hand when the photocatalytic degradation was carried out at pH = 6; there was no peak shift of the two major peaks of methylene blue. It may be due to the reason that the degradation pathway could be different at acidic and basic conditions, which is not addressed in the existing literature to the best of our knowledge. Since the scope of the current work is not to explore the mechanism, further mechanistic investigation was not carried out.

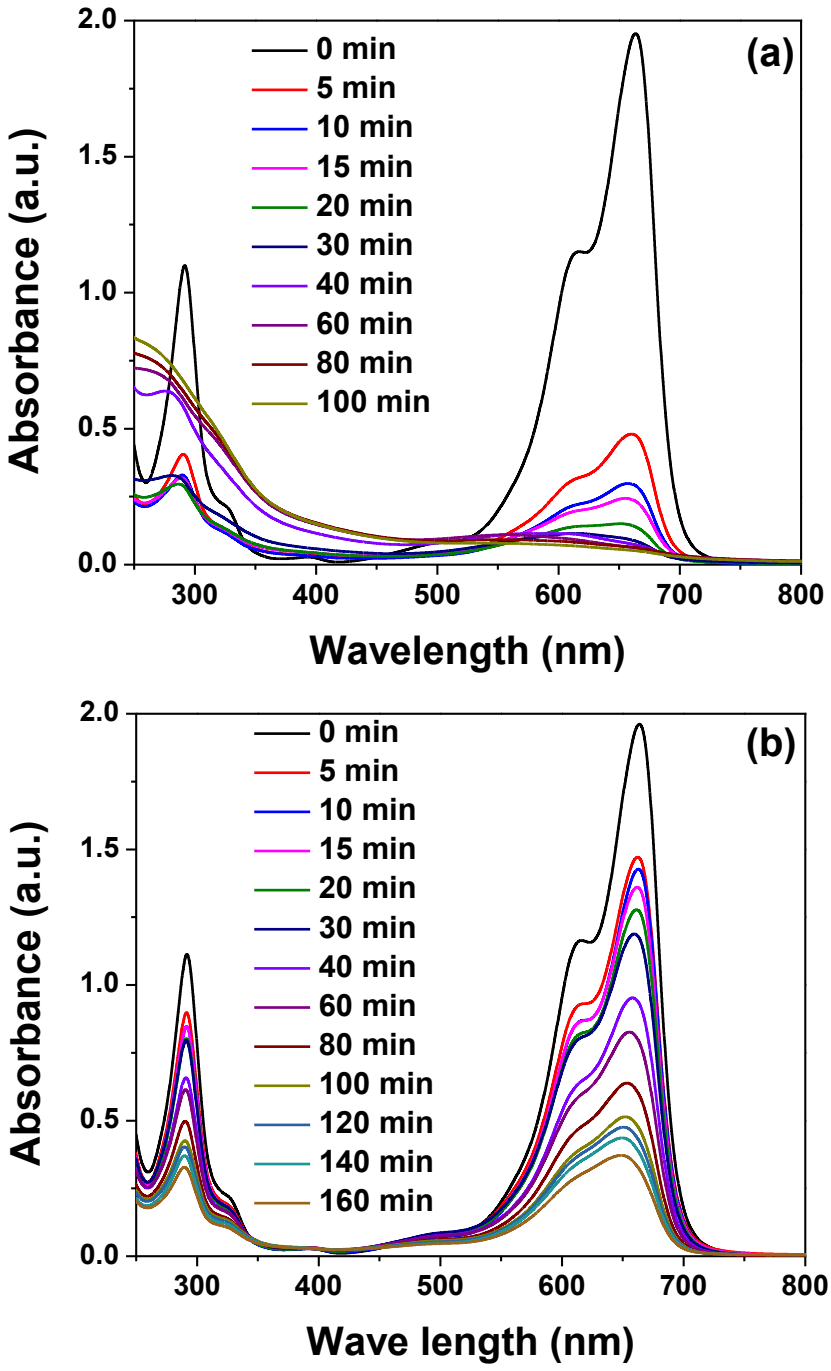

Figure 3.8: UV-Vis absorbance spectra of methylene blue as a function of degradation time with 20% TiO_2/zeolite-4A at (a) pH = 8.5 and (b) pH = 6.

The kinetics of degradation of the dye in acidic and basic medium was also different. Fig. 3.9 shows the degradation of methylene blue with time in acidic and basic medium with 20 % TiO_2/zeolite-4A. The photoabatement rate of methylene blue in basic pH was faster than that in acidic pH. Further studies were carried out to optimize rate of photodegradation with TiO_2 loading. In basic medium with initial increment of TiO_2 loading the degradation was faster; the fastest degradation was achieved in basic medium was with 20% TiO_2/zeolite-

4A catalyst. With more TiO_2 loading like 30 %, however, the degradation was poorer than that of 20% TiO_2/zeolite-4A catalyst. This could be due to relatively larger size and agglomerated TiO_2 particles.

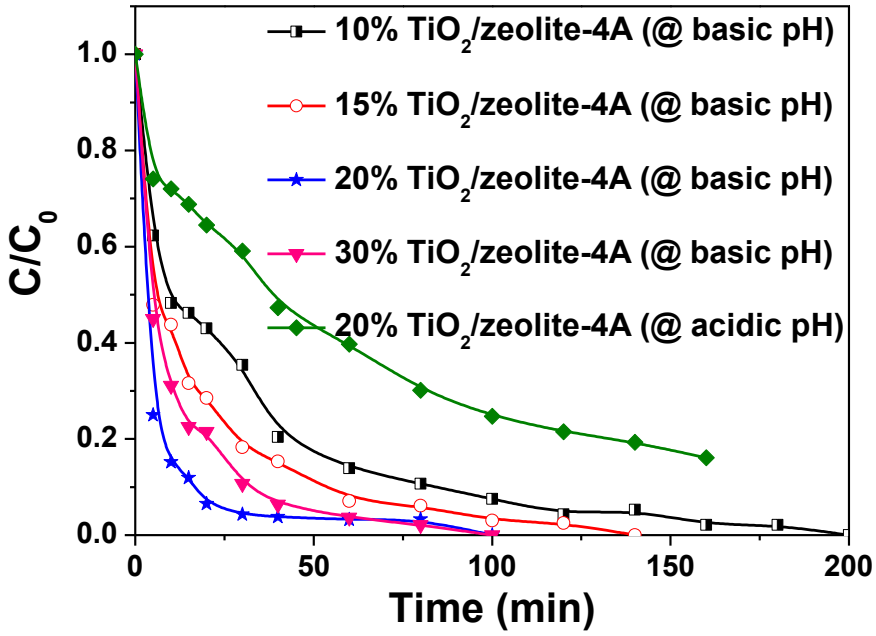

Figure 3.9: Photocatalytic degradation of methylene blue with different loading of 50 mg of TiO_2/zeolite-4A in acidic and basic medium.

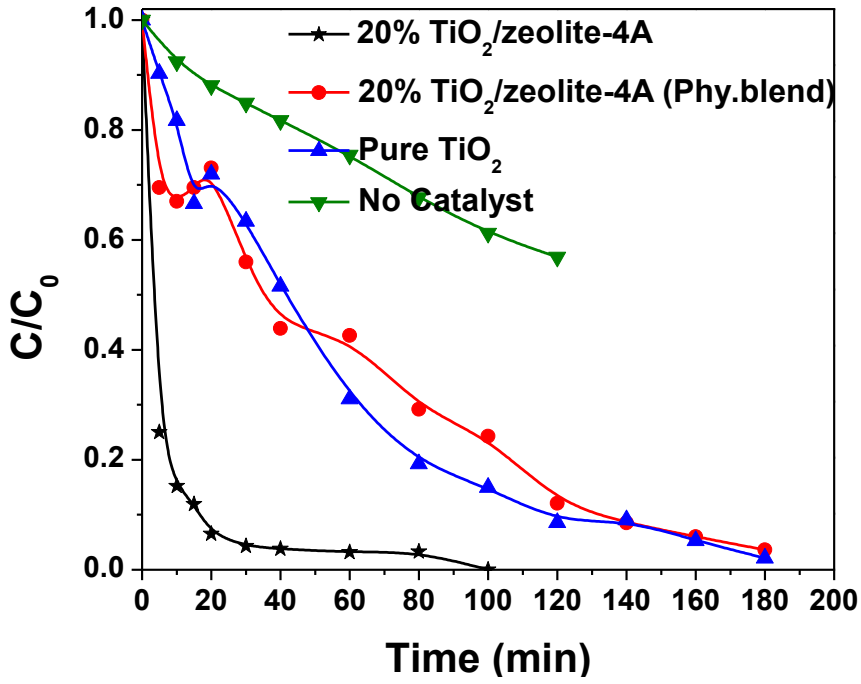

Figure 3.10: Photocatalytic degradation of methylene blue without catalyst and with 50 mg of TiO_2/zeolite-4A (sol–gel synthesized), TiO_2/zeolite-4A (physical blend) and 10 mg of TiO_2 in basic medium (@ pH = 8.5).

Fig. 3.10 shows the difference in catalytic activity of the polymerizable sol–gel synthesized 20 % TiO_2/zeolite-4A, physical blend of TiO_2 with zeolite-4A and the TiO_2 powder without support. Without catalyst only up to 40% of photodegradation of methylene blue was achieved in 120 minutes. The synthesized catalyst outperformed the catalytic activity of the physical blend. Interestingly, the degradation profile of the physical blend and the TiO_2 powder without support look similar. On the other hand, the completely different degradation profile observed with the polymerizable sol–gel synthesized 20 % TiO_2/zeolite-4A indicates a clear difference in surface morphology of the synthesized one from the physical blend. The high performance of the synthesized catalysts is attributed to the highly dispersed active site-support interaction. The recyclability of the catalyst was further explored. After each cycle, the exhausted catalyst was regenerated by calcining the catalyst at 400 °C for 30 minutes. The recyclability of the performance of the catalysts was carried out up to 5 cycles of performance, which showed a very stable behaviour (data not shown).

3.3 RGO/TiO_2/zeolite-4A

3.3.1. Experimental section

(i) Synthesis and characterization of materials

In a typical GO synthesis process, a 1:6 (wt. ratio) mixture of graphite flakes and $KMnO_4$ was slowly added to a 9:1 mixture of concentrated H_2SO_4/H_3PO_4. The reaction mixture was heated to 55 °C and stirred continuously for 12 h in a water bath. The reaction mixture was cooled down to room temperature and poured into an ice water bath containing 30% H_2O_2. The final suspension was centrifuged and washed with excess of water, 30% HCl solution and ethanol, sequentially. The obtained powder after washing was dried at 60 °C for 48 h.

TiO_2 and TiO_2/Zeolite-4A were synthesized by following our previously reported procedure.[76] Photoreduction of GO was done as in a similar fashion reported by Williams et al.[63] About 10 wt.% (with respect to TiO_2) of GO was added to TiO_2 and TiO_2/zeolite-4A in isopropyl alcohol (IPA) and stirred well. The obtained suspensions were irradiated with UV light (125 W Hg vapor lamp) under continuous bubbling of nitrogen gas for 60 min. The resultant RGO-anchored TiO_2 (RGO/TiO_2) and RGO/TiO_2/zeolite-4A were centrifuged, collected, and dried at 60 °C.

(ii) Adsorption and catalysis

The batch adsorption studies were carried out with various photo-catalytic materials like TiO_2, zeolite 4A, RGO/TiO_2, TiO_2/zeolite-4A, and RGO/TiO_2/zeolite-4A without the presence of any light source. For each adsorption study, the TiO_2 content was kept constant at 20 mg and 100 mL of 25 ppm aqueous MB solution was used. To follow the adsorption kinetics, investigations were carried out with 30 mg of RGO/TiO_2/zeolite-4A material in 30 mL of different concentrations of MB solution (10, 25, 40, 60 and 80 ppm) in the dark. The solutions were stirred to be equilibrated and 1 mL of aliquot was drawn out from each stock solution at different time intervals to measure the equilibrium concentration of MB. The amount of MB adsorbed on RGO/TiO_2/zeolite-4A (mg/g) at equilibrium (q_e) was calculated by using the following equation: $q_e = \frac{(Co-Ce)V}{W}$, where Co and Ce are the initial and final (equilibrium) MB concentrations (mg/L), V is the amount of solvent (L) and W is the weight of adsorbent (g) taken. The degradation studies of MB by various photocatalytic materials under irradiation of UV light were carried out in a photoreactor fitted with a 125 W mercury vapor lamp having maximum intensity at 365 nm. The reaction vessel was fitted with a double walled borosilicate immersion well with water circulation to carry out the reaction at room temperature and also to prevent IR radiation. All the photodegradation experiments were done under aerobic condition. In a typical photodegradation study, 100 mL of 25 ppm aqueous MB solution was added with 20 mg of TiO_2 (in the case of Zeolite-containing catalysts it is 100 mg) at a pH of ~8.5. During the photocatalysis, 1 mL of the suspension was withdrawn at regular time intervals and centrifuged to remove the catalyst and the supernatant solution was used to measure the absorbance.

2.4.2. Results and discussion

(i) Materials

Fig. 2.11 shows the XRD profile of GO, TiO_2, 20% TiO_2/zeolite-4A, 10% RGO/TiO_2 and 10% RGO–20% TiO_2/zeolite-4A. The XRD profile of GO in Fig. 3.11 indicates the high crystallinity of the material. The sharp peak at $2\theta = 10.4°$ corresponds to the interplanar spacing of ~ 7.5 Å between the (002) planes. The interplanar spacing of the materials is proportion-al to the degree of oxidation due the presence of oxygen functionalities. The significant interplanar spacing of GO synthesized by the improved oxidation method indicates the extent of high oxidation of graphite flakes. The peak at $2\theta = 42.2°$ could be due to the turbostratic band of the disordered carbon materials. The TiO_2 synthesized by the

polymerizable sol–gel route crystallized in anatase as well as in rutile phase. The significant TiO_2 peaks appeared in the profile at 2θ = 25.3° (for anatase) and at 27.6° (for rutile). The anatase to rutile ratio is roughly about 1.5:1. When GO was photoreduced by TiO_2, an RGO/ TiO_2 nanocomposite was formed. The XRD profile of RGO/TiO_2 shows that the characteristic first peak of GO (originally at 2θ = 10.4°) is lowered slightly in intensity and also shifted to 2θ = 12.1°. This indicates that the photoreduction was able to partially reduce the oxygen functionalities of GO, thus lowering the interplanar spacing. Also, broadening of the 12.1° peak indicates lower crystallinity of the RGO. TiO_2 anchored with Zeolite-4A shows highly crystalline zeolite-4A peaks. The presence of anatase TiO_2 is observed at 2θ = 25.3°, however the rutile phase was obscured. The XRD profile of RGO/TiO_2/zeolite-4A in Fig. 2.11 also showed the existence of the anatase TiO_2 phase. The RGO was only 2% of zeolite-4A in RGO/TiO_2/zeolite-4A, therefore no significant RGO peak was observed.

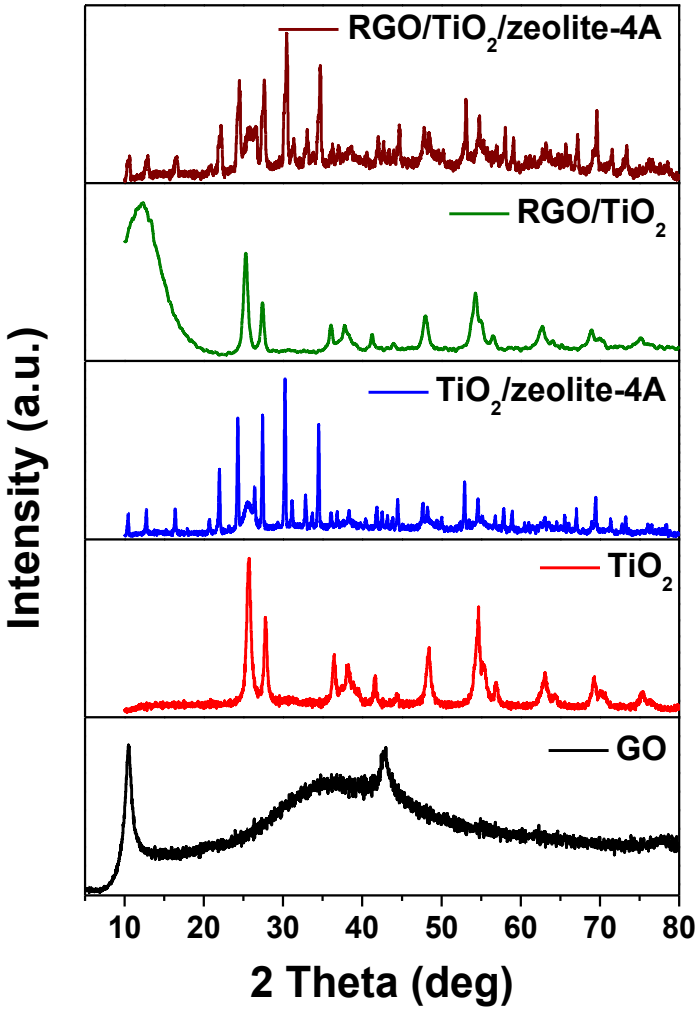

Figure 3.11: XRD profile of GO, TiO_2, 20% TiO_2/zeolite-4A, 10% RGO/TiO_2 and 10% RGO/20% TiO_2/zeolite-4A.

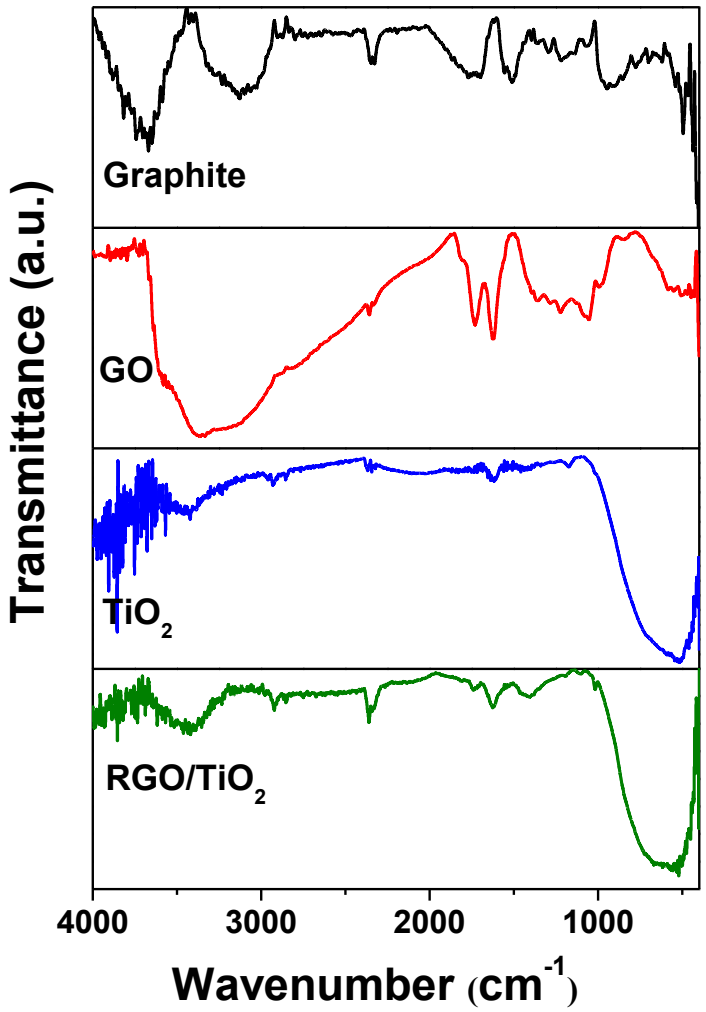

Figure 3.12: FTIR spectra of pristine graphite, GO, TiO_2 and 10% RGO/TiO_2.

The FTIR spectra of pristine graphite, GO, TiO_2 and RGO/TiO_2 are shown in 3.12. It can be clearly seen from the spectra that the pristine graphite exhibits feeble peaks below 1700 cm^{-1}, indicating the absence of any oxidized carbon. After oxidation, GO exhibits characteristic stretching peaks of carbonyl group at ~1725 cm^{-1}, carbon–carbon double bond at ~ 1670 cm^{-1} and hydroxyl group at ~ 3400 cm^{-1}. On the other hand, the stretching frequencies of TiO_2 are concentrated only in the finger print region and appeared as a broad peak. The RGO/TiO_2 showed a spectrum that contained both the characteristic stretching frequencies of TiO_2 as well as GO. It is noteworthy that the RGO/TiO_2 showed a small shoulder at ~1725 cm^{-1}, which confirms that the GO is not fully reduced and hence retaining most of the oxidized species. To corroborate this observation, we further performed Raman spectroscopy investigations (Fig. 3.13). It is well known that the G band of graphite was observed at around 1580 cm^{-1} in Raman spectroscopy. This band corresponds to the ordered graphitic domain of sp^2 hybridized carbon. In the case of GO, in addition to this G band, a

characteristic D band peak at 1350 cm^{-1} was observed that corresponds to the disordered (oxidized) domain of graphene sheet.[55] The ratio of intensity of D band to G band (I_D/I_G) indicates the extent of oxidation in the graphene sheet. In our case, the I_D/I_G of GO synthesized by the improved oxidation method was observed to be 0.94. The I_D/I_G of 10 wt.% RGO/TiO_2 was observed to be 0.87, which clearly indicates the partial decrease in the disordered domain and enhancement in the ordered domain. This additionally confirms that the reduction of graphene oxide was moderate and therefore a good amount of carbon remains oxidized.

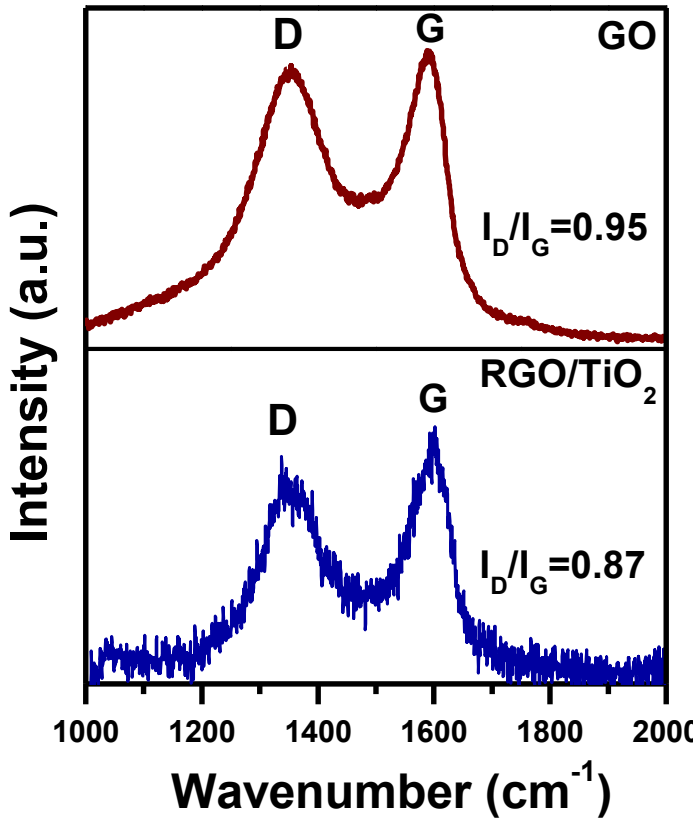

Figure 3.13: Raman Spectra of GO and 10% RGO/TiO_2.

To quantify the amount of RGO anchored onto TiO_2, thermogravimetric analysis (TGA) was performed on 10 wt.% RGO/TiO_2 under nitrogen atmosphere (Fig. 3.14). Pristine TiO_2 served as a control in the analysis. The pristine TiO_2 showed a mass loss of ~ 1 wt.% in the temperature range of 150 to 550 °C, which may be attributed to the presence of residual carbon. On the other hand, 10 wt.%-RGO/TiO_2 showed a mass loss corresponding to ~ 7.5 wt.% in the temperature range between 200 and 500 °C, beyond which the mass was stable, indicating that no further mass loss has occurred beyond this temperature. This has proved that the major portion of the feed GO got anchored onto TiO_2. Therefore, this method of

anchoring of GO onto TiO_2 was extrapolated to synthesize 10 wt.% RGO/TiO_2/zeolite-4A, which was further used for adsorption and degradation of MB.

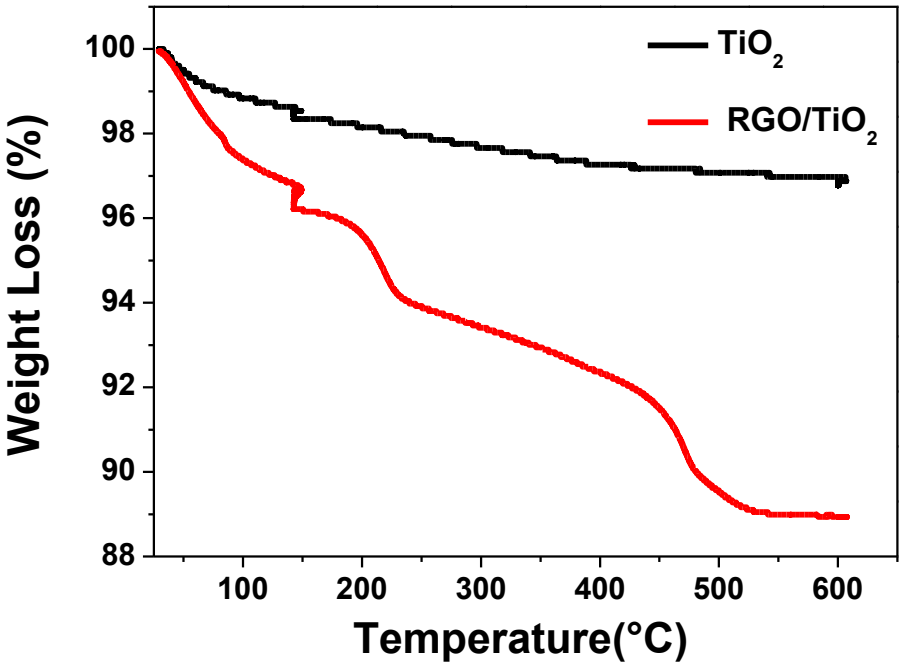

Figure 3.14: TGA of TiO_2 and 10% RGO/TiO_2.

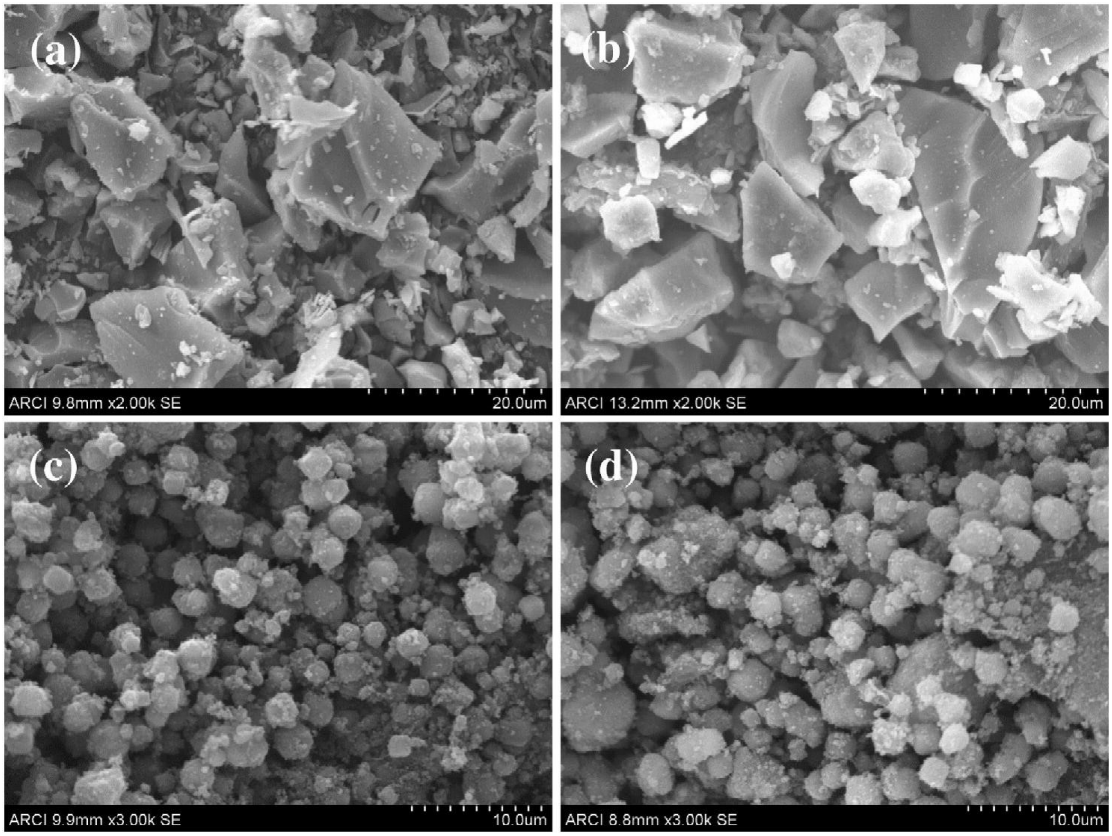

Figure 3.15: SEM images of (a) TiO_2, (b) 10%RGO/TiO_2, (c) 20% TiO_2/zeolite-4A and (d) 10% RGO/20% TiO_2/zeolite-4A.

These results successfully demonstrate the partial reduction of GO and its subsequent anchoring onto TiO_2. SEM was employed to visualize the synthesized materials before and after partial reduction of GO on TiO_2 and TiO_2/zeolite-4A (Fig. 3.15). Pristine TiO_2 was found to be crystal-line having irregular shapes, with the size ranging from 2–20 μm. Also, the size distribution was found to be huge. On the other hand, TiO_2/zeolite-4A was found to possess finely dispersed TiO_2 micro/nanoparticles on 500 nm–2 μm size cubic-shaped zeolite-4A support. In this case, the size distribution was found to be narrower than that of pristine TiO_2. After anchoring of RGO on these materials, the SEM of the resultant products looked similar. This shows that the photoreduction step did not affect TiO_2 and TiO_2/zeolite-4A during the anchoring of GO.

Surface area measurements were additionally carried out by using the Brunauer–Emmett–Teller (BET) method and the results are presented in Table 3.3. In line with our previous report, the surface area of zeolite-4A and pristine TiO_2 was found to be 1.2 and 36.3 m^2/g, respectively. The TiO_2/zeolite-4A obtained by the polymerizable sol–gel route possessed a surface area of 20.8 m^2/g. When partially reduced GO was introduced onto TiO_2 and TiO_2/zeolite-4A, the surface areas were found to be 30.3 and 19.8 m^2/g. Thus, the introduction of RGO onto the catalytic materials did not result in significant changes in surface area.

Table 3.3: Surface area of synthesized materials.

Sample	Specific Surface area (m^2/g)*
zeolite-4A	1.2
Pristine TiO_2	36.3
20 % TiO_2/zeolite-4A	20.8
10% RGO/TiO_2	30.3
10% RGO/20% TiO_2/zeolite-4A	19.8

* Determined from nitrogen adsorption isotherms (BET method) with 95 % confidence level.

Several works have been reported, in which TiO_2 has been doped with graphene or RGO in order to tune the electronic properties so as to improve the photocatalytic activity of the TiO_2 catalyst.[54,55,71,77-81] To investigate this, the direct band gap of the catalyst materials was calcu-lated from plotting the Kubelka Munk function against energy in Fig. 3.16. The

Kubelka Munk factor (K) was calculated by using $K = (1 - R)^2/2R$, where R is the % reflectance. In the plot, the intersection of the extrapo-lated linear portion of the curve with the energy axis yields the direct band gap of the material. The as-synthesized TiO_2 showed a band gap of 3.28 eV, which was reduced a little to 3.23 eV when RGO was incor-porated onto it. The RGO has a very little role in tuning the band gap of the material. When TiO_2 was dispersed on Zeolite-4A, the band gap was higher (3.7 eV) than that of pristine TiO_2. The same trend was also observed in our previous report.[76] The particle sizes become smaller due to dispersion on the support and the subsequent increase in band gap was attributed to the quantum confinement. When RGO was incorporated in the TiO_2/zeolite-4A, there was no change in the band gap of the material (E_g of RGO/TiO_2/zeolite-4A = 3.7 eV). This was not surprising as the RGO got anchored only onto the surface and therefore the crystal structure of TiO_2 was not altered.

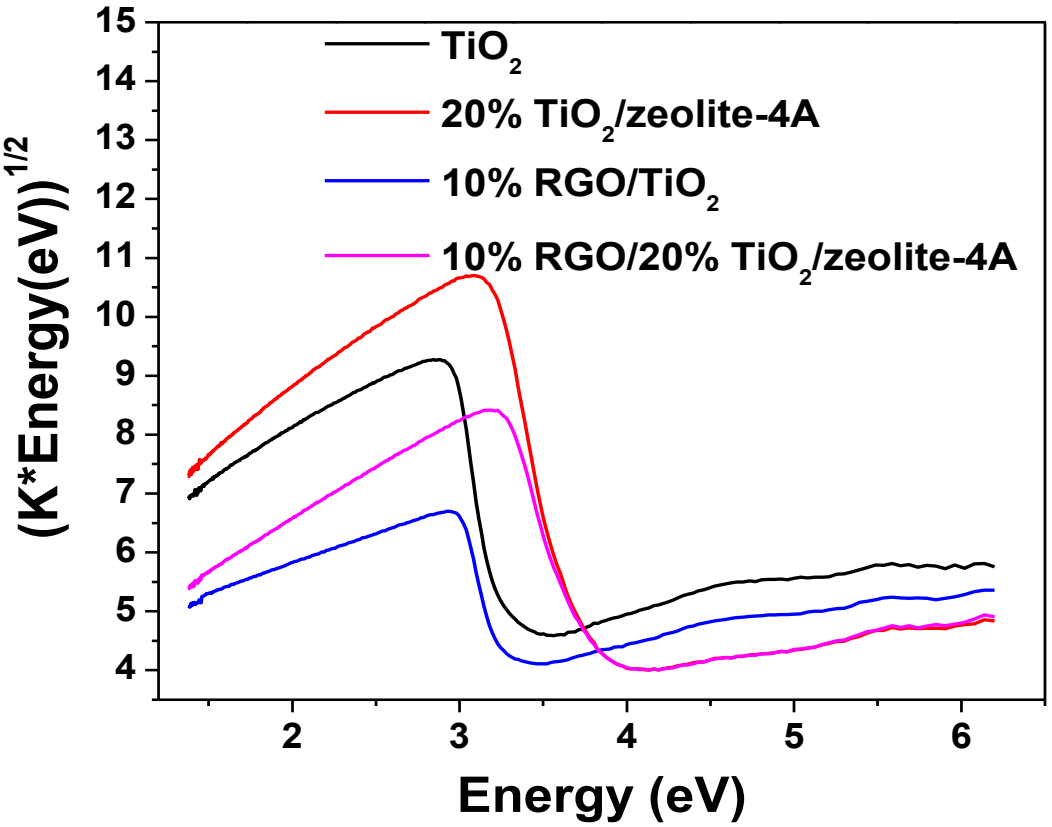

Figure 3.16: Solid state UV-Vis of TiO_2, 10%RGO/TiO_2, 20% TiO_2/zeolite-4A and 10% RGO/20% TiO_2/zeolite-4A.

(ii) Adsorption and catalytic degradation

Batch adsorption studies were carried out with 25 ppm of MB at pH 8.5 over different materials, like pure TiO_2, zeolite 4A, RGO/TiO_2, TiO_2/zeolite-4A, and RGO/TiO_2/zeolite-4A

in the dark for 2 h of duration (Fig. 3.17). The pure TiO_2 as well as the pure zeolite-4A both showed a very poor adsorption capability (~10%). However, when RGO was anchored onto TiO_2 or TiO_2 was dispersed on zeolite-4A, in both cases the MB ad-sorption increased up to 30%. When RGO/TiO_2/zeolite-4A was used for adsorption in the specified condition, in less than 20 min the equilibrium was attained and the adsorption showed the highest value of around 80%. Since the RGO incorporation onto the catalysts did not result in significant changes in the surface area as indicated by the BET measurements, the profound enhancement in adsorption onto the bi-functional catalysts could be due to the presence of chemical functionalities in the RGO.

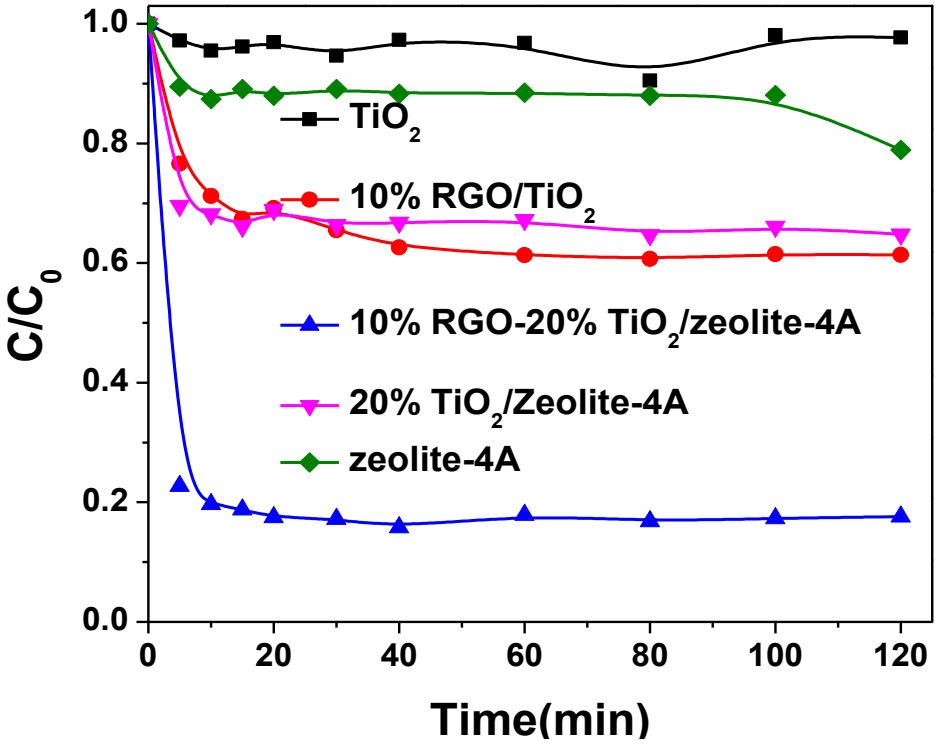

Figure 3.17: Adsorption of aqueous MB solution over TiO_2, 10% RGO/TiO_2, 10% RGO/20% TiO_2/zeolite-4A, 20% TiO_2/zeolite-4A and zeolite-4A against time.

Therefore, further detailed investigations were carried out with RGO/TiO_2/zeolite-4A for MB adsorption. Fig. 3.18 shows the ad-sorption of MB against time with various initial concentrations of MB. The Langmuir isotherm fits nicely with the experimental observation indicating that the MB could get adsorbed onto RGO/TiO_2/zeolite-4A ac-cording to the Langmuir isotherm model (Fig. 3.19). The kinetics were analyzed through the pseudo first, and pseudo second order rate equations. The value of regression coefficient (R^2) for the pseudo first order adsorption model was almost unity (Fig. 3.20). Hence, the pseudo first

order kinetic model is more suitable to describe the kinetic behaviour of MB adsorption onto RGO/TiO_2/zeolite-4A surface.

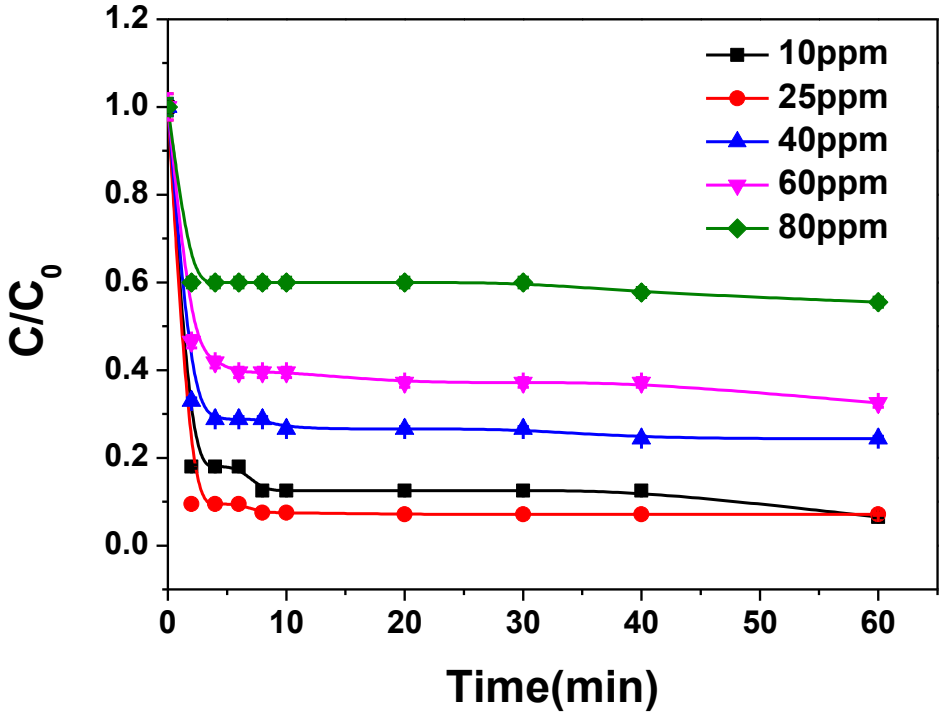

Figure 3.18: Adsorption of different concentration of MB over 10% RGO/20% TiO_2/zeolite-4A against time.

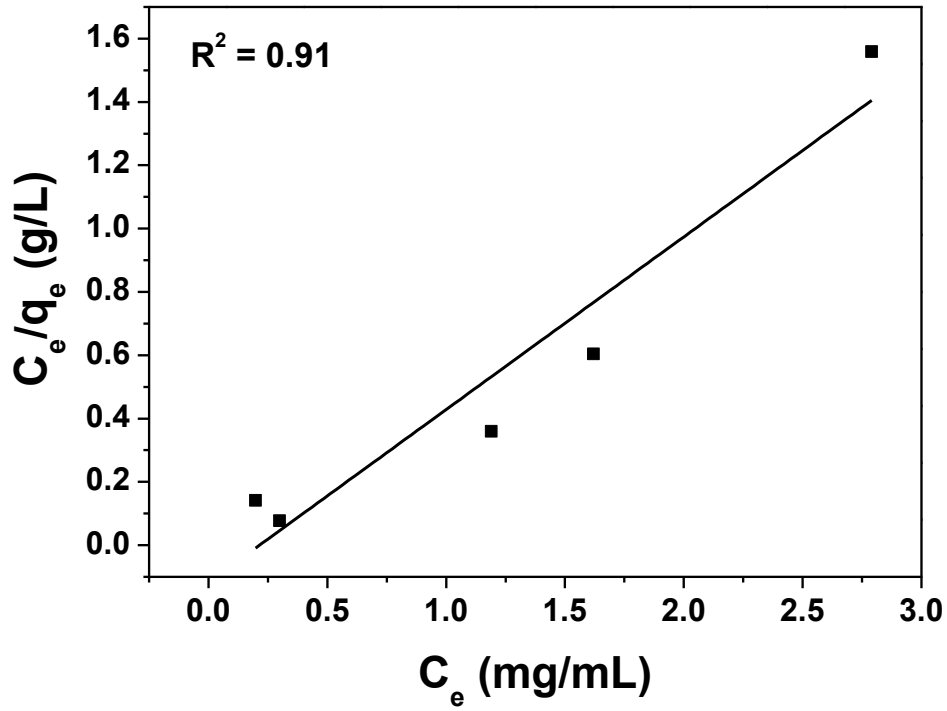

Figure 3.19: Langmuir isotherm model of MB adsorption over 10% RGO/20% TiO_2/zeolite-4A.

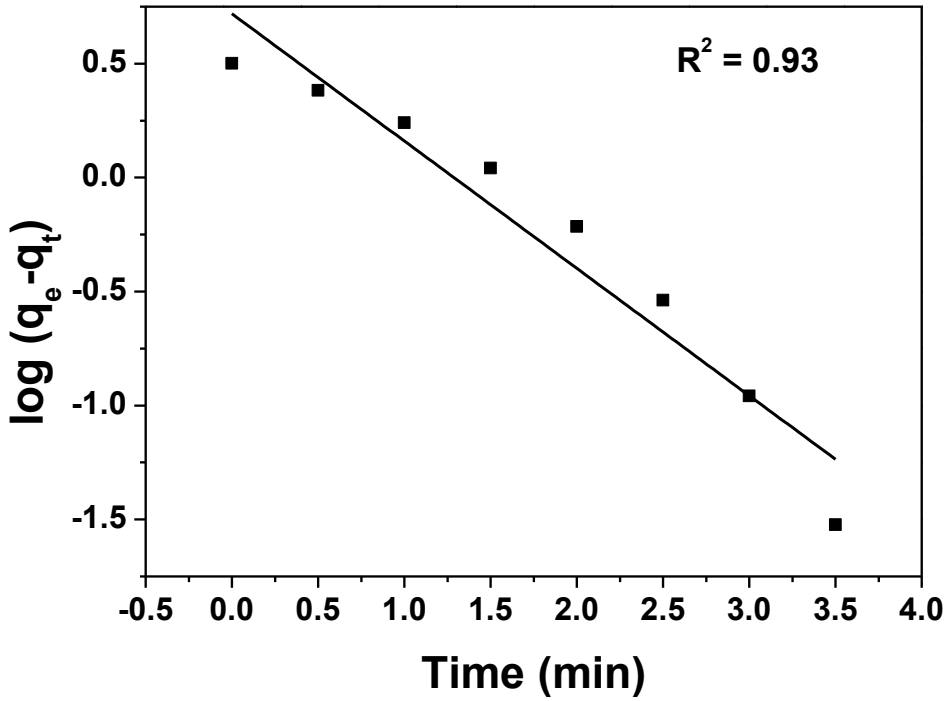

Figure 3.20: Kinetic plot obtained from the pseudo first-order equation for MB adsorption on to 10% RGO/20% TiO_2/zeolite-4A.

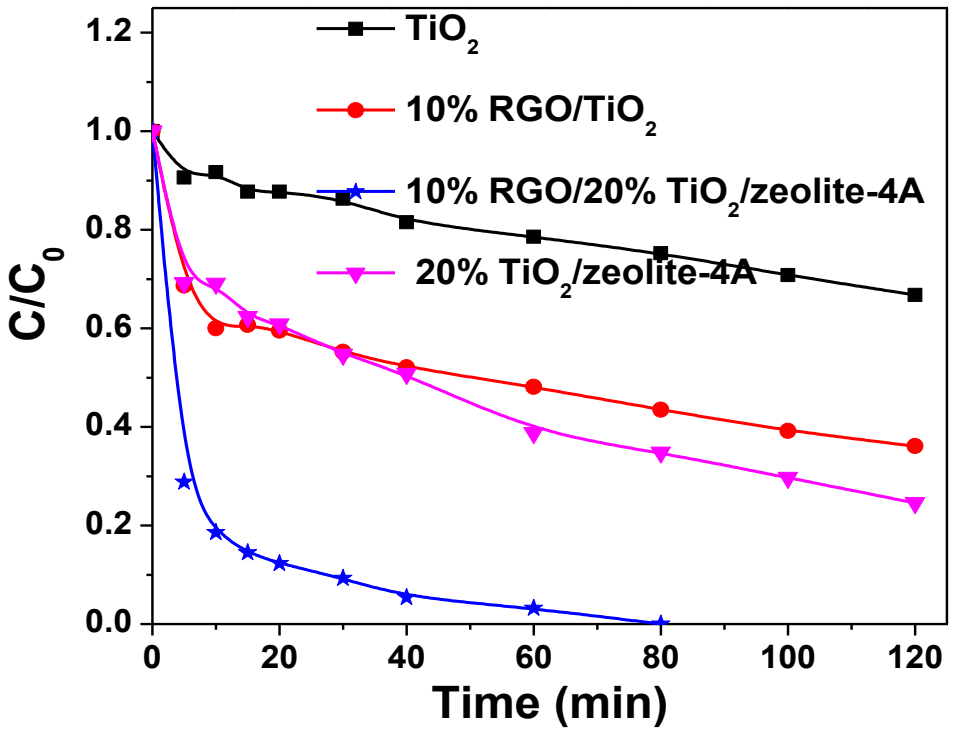

Figure 3.21: Photocatalytic degradation of MB with TiO_2, 10% RGO/TiO_2, 20% TiO_2/zeolite-4A and 10% RGO/20% TiO_2/zeolite-4A.

Photocatalytic degradation of MB over various catalysts was studied and plotted in Fig. 3.21. The catalytic reaction was carried out for 2 h of duration. The as-synthesized pure TiO_2 showed the poorest activity among the lot. Only, 20% of MB was catalytically degraded with pristine TiO_2. One should note that the adsorption capability of pure TiO_2 was also very poor (see Fig. 3.17). MB adsorption was increased significantly with RGO/TiO_2 and TiO_2/zeolite-4A, and that trend reflects the catalytic degradation activity also. After 2 h of UV light irradiation, ~40% of MB was degraded with RGO/TiO_2 and TiO_2/zeolite-4A. The zeolite-4A or RGO helps in adsorbing the MB better, and this provides more contact time for the active sites of TiO_2 to catalytically react with the pollutant.

2.4 Conclusions

TiO_2 supported zeolite-4A was successfully synthesized by customized polymerizable sol-gel method. The hydrolysis of the precursor blend of Ti-*di*methacrylate *diiso*propoxide and the industrial grade zeolite-4A under vigorous shaking produced a homogeneously mixed polymerizable gel in the zeolite matrix. Upon inducing the free radical polymerization at 125°C, this gel produced a polymer coating on the top of the support. Further calcination at 450 °C for 4 hours yielded highly dispersed TiO_2 anchored on the zeolite-4A. Diffuse reflectance spectroscopy revealed a clear trend in decreasing the band gap from 3.81 to 3.66 eV when TiO_2 content in the matrix was increased from 10 to 30 wt% indicating the nano crystallinity of TiO_2 particle. Surface area measurement disclosed an enhancement of surface area by ~2.5 times for the customized sol-gel synthesized 20 % TiO_2/zeolite-4A than that of the physical blend of 20 % TiO_2 and zeolite-4A. The photocatalytic activities of the catalysts were studied by measuring the photodegradation of methylene blue. The catalysts showed pH dependence, and the rate was faster in alkaline medium. The polymerizable sol-gel synthesized catalyst was found to have superior catalytic activity to the physical blend of TiO_2 and zeolite-4A. To improve the adsorption capacity of the catalyst, GO was anchored on to TiO_2 and zeolite-4A. This investigation deals in detail with the synthesis of GO by an improved oxidation method from graphite flakes, and pure TiO_2 by the polymerizable sol–gel route. The GO was partially photoreduced in alcoholic medium in the presence of TiO_2 and in the process; the RGO was anchored onto the TiO_2 surface. The RGO/TiO_2 was dispersed on zeolite-4A for better adsorption efficiency. The partial reduction of GO to RGO over TiO_2 was evidenced from XRD, FT-IR and Raman spectroscopy. TGA confirmed that ~75% of the feed GO got anchored onto TiO_2. No significant band gap alteration was found from diffuse reflectance spectroscopy study on the RGO anchored materials. The adsorption of methylene

blue over RGO/TiO_2/zeolite-4A was found to be following the Langmuir isotherm model. The adsorption kinetics was fitted well with the pseudo first order kinetic model. The high adsorption as well as photocatalytic degradation efficiency of RGO/TiO_2/zeolite-4A towards MB paves the way for new advanced bifunctional materials for environmental applications.

2.5. References

1. Martinez-Rubio, M.; Ireland, T.; Fern, G.; Silver, J.; Snowden, M., A new application for microgels: novel method for the synthesis of spherical particles of the Y_2O_3: Eu phosphor using a copolymer microgel of NIPAM and acrylic acid. *Langmuir* **2001,** *17* (22), 7145-7149.

2. Yang, J.; Wang, X.; Zhao, X.; Dai, J.; Mo, S., Synthesis of uniform Bi_2WO_6-reduced graphene oxide nanocomposites with significantly enhanced photocatalytic reduction activity. *The Journal of Physical Chemistry C* **2015,** *119* (6), 3068-3078.

3. Mukherjee, B.; Wilson, W.; Subramanian, V. R., TiO_2 nanotube (TNT) surface treatment revisited: Implications of ZnO, $TiCl_4$, and H_2O_2 treatment on the photoelectrochemical properties of TNT and TNT–CdSe. *Nanoscale* **2013,** *5* (1), 269-274.

4. Sambandam, B.; Surenjan, A.; Philip, L.; Pradeep, T., Rapid synthesis of C-TiO_2: tuning the shape from spherical to rice grain morphology for visible light photocatalytic application. *ACS Sustainable Chemistry & Engineering* **2015,** *3* (7), 1321-1329.

5. Torres-Martínez, L. M.; Moctezuma, E.; Ruiz-Gomez, M. A.; Juarez-Ramirez, I.; Figueroa-Torres, M. Z., Sol–gel synthesis of Sm_2InTaO_7 and its photocatalytic activity on degradation of crystal violet dye and reduction of Cr(VI) ions. *Research on Chemical Intermediates* **2013,** *39* (4), 1533-1544.

6. Zhang, Y.; Xu, Y. J., Bi_2WO_6: a highly chemoselective visible light photocatalyst toward aerobic oxidation of benzylic alcohols in water. *RSC Advances* **2014,** *4* (6), 2904-2910.

7. Peng, R.; Wu, C. M.; Baltrusaitis, J.; Dimitrijevic, N. M.; Rajh, T.; Koodali, R. T., Ultra-stable CdS incorporated Ti-MCM-48 mesoporous materials for efficient photocatalytic decomposition of water under visible light illumination. *Chemical Communications* **2013,** *49* (31), 3221-3223.

8. Eswar, N. K.; Katkar, V. V.; Ramamurthy, P. C.; Madras, G., Novel AgBr/Ag_3PO_4 decorated ceria nanoflake composites for enhanced photocatalytic activity toward dyes and bacteria under visible light. *Industrial & Engineering Chemistry Research* **2015,** *54* (33), 8031-8042.

9. Adhikari, S.; Sarkar, D.; Madras, G., Highly efficient WO_3–ZnO mixed oxides for photocatalysis. *RSC Advances* **2015,** *5* (16), 11895-11904.

10. Wu, Q.; Zhao, J.; Qin, G.; Wang, C.; Tong, X.; Xue, S., Photocatalytic reduction of Cr(VI) with TiO_2 film under visible light. *Applied Catalysis B: Environmental* **2013,** *142*, 142-148.

11. Rasalingam, S.; Wu, C. M.; Koodali, R. T., Modulation of pore sizes of titanium dioxide photocatalysts by a facile template free hydrothermal synthesis method: implications for photocatalytic degradation of rhodamine B. *ACS Applied Materials & Interfaces* **2015,** *7* (7), 4368-4380.

12. Yurdakal, S.; Tek, B. S.; Alagoz, O. U.; Augugliaro, V.; Loddo, V.; Palmisano, G.; Palmisano, L., Photocatalytic selective oxidation of 5-(hydroxymethyl)-2-furaldehyde to 2,5-furandicarbaldehyde in water by using anatase, rutile, and brookite TiO_2 nanoparticles. *ACS Sustainable Chemistry & Engineering* **2013,** *1* (5), 456-461.

13. Lim, J.; Murugan, P.; Lakshminarasimhan, N.; Kim, J. Y.; Lee, J. S.; Lee, S. H.; Choi, W., Synergic photocatalytic effects of nitrogen and niobium co-doping in TiO_2 for the redox conversion of aquatic pollutants under visible light. *Journal of Catalysis* **2014,** *310*, 91-99.

14. Liang, K.; Tay, B. K.; Kupreeva, O. V.; Orekhovskaya, T. I.; Lazarouk, S. K.; Borisenko, V. E., Fabrication of double-walled titania nanotubes and their photocatalytic activity. *ACS Sustainable Chemistry & Engineering* **2014,** *2* (4), 991-995.

15. Park, J. J.; Kim, D. Y.; Lee, J.-G.; Cha, Y. H.; Swihart, M. T.; Yoon, S. S., Supersonic aerosol-deposited TiO_2 photoelectrodes for photoelectrochemical solar water splitting. *RSC Advances* **2014,** *4* (17), 8661-8670.

16. Leelavathi, A.; Madras, G.; Ravishankar, N., Ultrathin Au nanowires supported on rGO/TiO_2 as an efficient photoelectrocatalyst. *Journal of Materials Chemistry A* **2015,** *3* (33), 17459-17468.

17. Bai, J.; Zhou, B., Titanium dioxide nanomaterials for sensor applications. *Chemical Rreviews* **2014,** *114* (19), 10131-10176.

18. Foong, T. R. B.; Chan, K. L.; Hu, X., Structure and properties of nano-confined poly (3-hexylthiophene) in nano-array/polymer hybrid ordered-bulk heterojunction solar cells. *Nanoscale* **2012,** *4* (2), 478-485.

19. Han, F.; Kambala, V. S. R.; Srinivasan, M.; Rajarathnam, D.; Naidu, R., Tailored titanium dioxide photocatalysts for the degradation of organic dyes in wastewater treatment: a review. *Applied Catalysis A: General* **2009,** *359* (1-2), 25-40.

20. Hegde, M.; Nagaveni, K.; Roy, S., Synthesis, structure and photocatalytic activity of nano TiO 2 and nano $Ti_{1-x}M_xO_{2-\delta}$ (M= Cu, Fe, Pt, Pd, V, W, Ce, Zr). *Pramana* **2005,** *65* (4), 641-645.

21. Palmisano, G.; Yurdakal, S.; Augugliaro, V.; Loddo, V.; Palmisano, L., Photocatalytic selective oxidation of 4-methoxybenzyl alcohol to aldehyde in aqueous suspension of home-prepared titanium dioxide catalyst. *Advanced Synthesis & Catalysis* **2007,** *349* (6), 964-970.

22. Khataee, A.; Kasiri, M. B., Photocatalytic degradation of organic dyes in the presence of nanostructured titanium dioxide: influence of the chemical structure of dyes. *Journal of Molecular Catalysis A: Chemical* **2010,** *328* (1-2), 8-26.

23. Subramanian, V.; Wolf, E.; Kamat, P. V., Semiconductor−metal composite nanostructures. To what extent do metal nanoparticles improve the photocatalytic activity of TiO_2 films? *The Journal of Physical Chemistry B* **2001,** *105* (46), 11439-11446.

24. Kwon, D. H.; Kim, K. M.; Jang, J. H.; Jeon, J. M.; Lee, M. H.; Kim, G. H.; Li, X.-S.; Park, G.-S.; Lee, B.; Han, S., Atomic structure of conducting nanofilaments in TiO_2 resistive switching memory. *Nature Nanotechnology* **2010,** *5* (2), 148.

25. Kesmez, O.; Camurlu, H. E.; Burunkaya, E.; Arpac, E., Sol–gel preparation and characterization of anti-reflective and self-cleaning SiO_2–TiO_2 double-layer nanometric films. *Solar Energy Materials and Solar Cells* **2009,** *93* (10), 1833-1839.

26. Yoshida, M.; Prasad, P. N., Sol−gel-processed SiO_2/TiO_2/poly(vinylpyrrolidone) composite materials for optical waveguides. *Chemistry of Materials* **1996,** *8* (1), 235-241.

27. Yang, G.; Jiang, Z.; Shi, H.; Xiao, T.; Yan, Z., Preparation of highly visible-light active N-doped TiO_2 photocatalyst. *Journal of Materials Chemistry* **2010,** *20* (25), 5301-5309.

28. Li, X.; Wang, J.; Rykov, A. I.; Sharma, V. K.; Wei, H.; Jin, C.; Liu, X.; Li, M.; Yu, S.; Sun, C., Prussian blue/TiO_2 nanocomposites as a heterogeneous photo-fenton catalyst for degradation of organic pollutants in water. *Catalysis Science & Technology* **2015,** *5* (1), 504-514.

29. Munoz-Batista, M.; Kubacka, A.; Fernández-Garcia, M., Effect of g-C_3N_4 loading on TiO_2-based photocatalysts: UV and visible degradation of toluene. *Catalysis Science & Technology* **2014,** *4* (7), 2006-2015.

30. Diez-Pascual, A. M.; Diez-Vicente, A. L., Effect of TiO_2 nanoparticles on the performance of polyphenylsulfone biomaterial for orthopaedic implants. *Journal of Materials Chemistry B* **2014,** *2* (43), 7502-7514.

31. Fiedler, T.; Belova, I.; Murch, G.; Roether, J.; Boccaccini, A., Tailoring elastic properties of PLGA/TiO_2 biomaterials. *Computational Materials Science* **2012,** *61*, 283-286.

32. Arbuj, S. S.; Hawaldar, R. R.; Mulik, U. P.; Wani, B. N.; Amalnerkar, D. P.; Waghmode, S. B., Preparation, characterization and photocatalytic activity of TiO_2 towards methylene blue degradation. *Materials Science and Engineering: B* **2010,** *168* (1-3), 90-94.

33. Subramanian, V. R.; Sarker, S.; Yu, B.; Kar, A.; Sun, X.; Dey, S. K., TiO_2 nanotubes and its composites: Photocatalytic and other photo-driven applications. *Journal of Materials Research* **2013,** *28* (3), 280-293.

34. Tayade, R. J.; Natarajan, T. S.; Bajaj, H. C., Photocatalytic degradation of methylene blue dye using ultraviolet light emitting diodes. *Industrial & Engineering Chemistry Research* **2009,** *48* (23), 10262-10267.

35. Hoffmann, M. R.; Martin, S. T.; Choi, W.; Bahnemann, D. W., Environmental applications of semiconductor photocatalysis. *Chemical Reviews* **1995,** *95* (1), 69-96.

36. Martin, S. T.; Herrmann, H.; Choi, W.; Hoffmann, M. R., Time-resolved microwave conductivity. Part 1—TiO_2 photoreactivity and size quantization. *Journal of the Chemical Society, Faraday Transactions* **1994,** *90* (21), 3315-3322.

37. Konstantinou, I. K.; Albanis, T. A., TiO_2-assisted photocatalytic degradation of azo dyes in aqueous solution: kinetic and mechanistic investigations: a review. *Applied Catalysis B: Environmental* **2004,** *49* (1), 1-14.

38. Linsebigler, A.; Lu, G., Yates, J. T., Photocatalysis on TiO_2 surfaces: principles, mechanisms, and selected results *Chemical Reviews.* **1995,** *95* (3), 735-758.

39. Serpone, N., Is the band gap of pristine TiO_2 narrowed by anion-and cation-doping of titanium dioxide in second-generation photocatalysts? *ACS Publications*: **2006**, 24287-24293.

40. Zaleska, A., Doped-TiO_2: a review. *Recent Patents on Engineering* **2008,** *2* (3), 157-164.

41. Wilson, W.; Manivannan, A.; Subramanian, V. R., Heterogeneous photocatalytic degradation of recalcitrant pollutants over CdS–TiO_2 nanotubes: Boosting effect of TiO_2 nanoparticles at nanotube–CdS interface. *Applied Catalysis A: General* **2012,** *441*, 1-9.

42. Abdullah, M.; Chong, F. K., Preparation and characterization of tungsten-loaded titanium dioxide photocatalyst for enhanced dye degradation. *Journal of Hazardous Materials* **2010,** *176* (1-3), 451-458.

43. Franco, A.; Neves, M.; Carrott, M. R.; Mendonça, M.; Pereira, M.; Monteiro, O., Photocatalytic decolorization of methylene blue in the presence of TiO_2/ZnS nanocomposites. *Journal of Hazardous Materials* **2009,** *161* (1), 545-550.

44. Huang, T.; Mao, S.; Yu, J.; Wen, Z.; Lu, G.; Chen, J., Effects of N and F doping on structure and photocatalytic properties of anatase TiO_2 nanoparticles. *RSC Advances* **2013,** *3* (37), 16657-16664.

45. Nagaveni, K.; Sivalingam, G.; Hegde, M.; Madras, G., Solar photocatalytic degradation of dyes: high activity of combustion synthesized nano TiO_2. *Applied Catalysis B: Environmental* **2004,** *48* (2), 83-93.

46. Sivalingam, G.; Nagaveni, K.; Hegde, M.; Madras, G., Photocatalytic degradation of various dyes by combustion synthesized nano anatase TiO_2. *Applied Catalysis B: Environmental* **2003,** *45* (1), 23-38.

47. Macwan, D.; Dave, P. N.; Chaturvedi, S., A review on nano-TiO_2 sol–gel type syntheses and its applications. *Journal of Materials Science* **2011,** *46* (11), 3669-3686.

48. Chen, X.; Mao, S. S., Titanium dioxide nanomaterials: synthesis, properties, modifications, and applications. *Chemical Reviews* **2007,** *107* (7), 2891-2959.

49. Yu, J.; Zhao, X.; Du, J.; Chen, W., Preparation, microstructure and photocatalytic activity of the porous TiO_2 anatase coating by sol-gel processing. *Journal of sol-gel Science and Technology* **2000,** *17* (2), 163-171.

50. Kumar, M. K.; Krishnamoorthy, S.; Tan, L. K.; Chiam, S. Y.; Tripathy, S.; Gao, H., Field effects in plasmonic photocatalyst by precise SiO_2 thickness control using atomic layer deposition. *ACS Catalysis* **2011,** *1* (4), 300-308.

51. You-ji, L.; Wei, C., Photocatalytic degradation of Rhodamine B using nanocrystalline TiO_2–zeolite surface composite catalysts: effects of photocatalytic condition on degradation efficiency. *Catalysis Science & Technology* **2011,** *1* (5), 802-809.

52. Gomez, S.; Marchena, C. L.; Pizzio, L.; Pierella, L., Preparation and characterization of TiO2/HZSM-11 zeolite for photodegradation of dichlorvos in aqueous solution. *Journal of Hazardous Materials* **2013,** *258*, 19-26.

53. Wang, C. C.; Lee, C. K.; Lyu, M. D.; Juang, L. C., Photocatalytic degradation of CI Basic Violet 10 using TiO_2 catalysts supported by Y zeolite: An investigation of the effects of operational parameters. *Dyes and Pigments* **2008,** *76* (3), 817-824.

54. Zhang, H.; Lv, X.; Li, Y.; Wang, Y.; Li, J., P25-graphene composite as a high performance photocatalyst. *ACS Nano* **2009,** *4* (1), 380-386.

55. Gao, Y.; Pu, X.; Zhang, D.; Ding, G.; Shao, X.; Ma, J., Combustion synthesis of graphene oxide–TiO_2 hybrid materials for photodegradation of methyl orange. *Carbon* **2012,** *50* (11), 4093-4101.

56. Dinachali, S. S.; Saifullah, M. S.; Ganesan, R.; Thian, E. S.; He, C., A universal scheme for patterning of oxides via thermal nanoimprint lithography. *Advanced Functional Materials* **2013,** *23* (17), 2201-2211.

57. Klaine, S. J.; Alvarez, P. J.; Batley, G. E.; Fernandes, T. F. Handy, R. D.; Lyon, D. Y.; Mahendra, S.; McLaughlin, M. J.; Lead, J. R., Nanomaterials in the environment: behavior, fate, bioavailability, and effects. *Environmental Toxicology and Chemistry* **2008,** *27* (9), 1825-1851.

58. Musee, N., Nanowastes and the environment: Potential new waste management paradigm. *Environment International* **2011,** *37* (1), 112-128.

59. Nowack, B.; Ranville, J. F.; Diamond, S.; Gallego-Urrea, J. A.; Metcalfe, C.; Rose, J.; Horne, N.; Koelmans, A. A.; Klaine, S. J., Potential scenarios for nanomaterial release and subsequent alteration in the environment. *Environmental Toxicology and Chemistry* **2012,** *31* (1), 50-59.

60. Yuan, Y.; Zhang, G.; Li, Y.; Zhang, G.; Zhang, F.; Fan, X., Poly(amidoamine) modified graphene oxide as an efficient adsorbent for heavy metal ions. *Polymer Chemistry* **2013,** *4* (6), 2164-2167.

61. Barathi, M.; Kumar, A. S. K.; Kumar, C. U.; Rajesh, N., Graphene oxide–aluminium oxyhydroxide interaction and its application for the effective adsorption of fluoride. *Rsc Advances* **2014,** *4* (96), 53711-53721.

62. Marcano, D. C.; Kosynkin, D. V.; Berlin, J. M.; Sinitskii, A.; Sun, Z.; Slesarev, A.; Alemany, L. B.; Lu, W.; Tour, J. M., Improved synthesis of graphene oxide. *ACS Nano* **2010,** *4* (8), 4806-4814.

63. Williams, G.; Seger, B.; Kamat, P. V., TiO_2-graphene nanocomposites. UV-assisted photocatalytic reduction of graphene oxide. *ACS Nano* **2008,** *2* (7), 1487-1491.

64. Sun, J. C.; Cheng, J. Fan, H.; Ai, S. Y. In Bifunctional Ag/AgCl/α-$Co(OH)_2$ nanocomposite with selective adsorption and photocatalytic properties for dyes removal, *Advanced Materials Research, Trans Tech Publ.* **2013,** 496-500.

65. Fang, J.; Shi, F.; Bu, J.; Ding, J.; Xu, S.; Bao, J.; Ma, Y.; Jiang, Z.; Zhang, W.; Gao, C., One-step synthesis of bifunctional TiO_2 catalysts and their photocatalytic activity. *The Journal of Physical Chemistry C* **2010,** *114* (17), 7940-7948.

66. Ofomaja, A. E.; Ho, Y. S., Effect of temperatures and pH on methyl violet biosorption by Mansonia wood sawdust. *Bioresource Technology* **2008,** *99* (13), 5411-5417.

67. Feng, L. L.; Zou, X.; Zhao, J.; Zhou, L. J.; Wang, D. J.; Zhang, X.; Li, G. D., Nanoporous Sr-rich strontium titanate: a stable and superior photocatalyst for H_2 evolution. *Chemical Communications* **2013,** *49* (84), 9788-9790.

68. Lin, Y.; Geng, Z.; Cai, H.; Ma, L.; Chen, J.; Zeng, J.; Pan, N.; Wang, X., Ternary graphene–TiO_2–Fe_3O_4 nanocomposite as a recollectable photocatalyst with enhanced durability. *European Journal of Inorganic Chemistry* **2012,** *2012* (28), 4439-4444.

69. Ismail, I. M.; Aslam, M.; Almeelbi, T.; Chandrasekaran, S.; Hameed, A., Ce^{3+} impregnated ZnO: a highly efficient photocatalyst for sunlight mediated mineralization. *RSC Advances* **2014,** *4* (31), 16043-16046.

70. Joshi, U. A.; Darwent, J. R.; Yiu, H. H.; Rosseinsky, M. J., The effect of platinum on the performance of WO_3 nanocrystal photocatalysts for the oxidation of methyl orange and iso-propanol. *Journal of Chemical Technology & Biotechnology* **2011,** *86* (8), 1018-1023.

71. Zhang, Y.; Tang, Z. R.; Fu, X.; Xu, Y. J., TiO_2−graphene nanocomposites for gas-phase photocatalytic degradation of volatile aromatic pollutant: is TiO_2−graphene truly different from other TiO_2−carbon composite materials? *ACS Nano* **2010,** *4* (12), 7303-7314.

72. Kosmulski, M., The significance of the difference in the point of zero charge between rutile and anatase. *Advances in Colloid and Interface Science* **2002,** *99* (3), 255-264.

73. Chou, J. C.; Liao, L. P., Study on pH at the point of zero charge of TiO_2 pH ion-sensitive field effect transistor made by the sputtering method. *Thin Solid Films* **2005,** *476* (1), 157-161.

74. Houas, A.; Lachheb, H.; Ksibi, M.; Elaloui, E.; Guillard, C.; Herrmann, J. M., Photocatalytic degradation pathway of methylene blue in water. *Applied Catalysis B: Environmental* **2001,** *31* (2), 145-157.

75. Matsui, M.; Kiyozumi, Y.; Yamamoto, T.; Mizushina, Y.; Mizukami, F.; Sakaguchi, K., Selective adsorption of biopolymers on zeolites. *Chemistry–A European Journal* **2001,** *7* (7), 1555-1560.

76. Nagarjuna, R.; Roy, S.; Ganesan, R., Polymerizable sol–gel precursor mediated synthesis of TiO_2 supported zeolite-4A and its photodegradation of methylene blue. *Microporous and Mesoporous Materials* **2015,** *211*, 1-8.

77. Compton, O. C.; Nguyen, S. T., Graphene oxide, highly reduced graphene oxide, and graphene: versatile building blocks for carbon-based materials. *Small* **2010,** *6* (6), 711-723.

78. Wang, Z. l.; Xu, D.; Huang, Y.; Wu, Z.; Wang, L. M.; Zhang, X. B., Facile, mild and fast thermal-decomposition reduction of graphene oxide in air and its application in high-performance lithium batteries. *Chemical Communications* **2012,** *48* (7), 976-978.

79. Xu, C.; Yuan, Y.; Yuan, R.; Fu, X., Enhanced photocatalytic performances of TiO_2-graphene hybrids on nitro-aromatics reduction to amino-aromatics. *RSC Advances* **2013,** *3* (39), 18002-18008.

80. Du, J.; Lai, X.; Yang, N.; Zhai, J.; Kisailus, D.; Su, F.; Wang, D.; Jiang, L., Hierarchically ordered macro−mesoporous TiO_2−graphene composite films: improved mass transfer, reduced charge recombination, and their enhanced photocatalytic activities. *ACS Nano* **2010,** *5* (1), 590-596.

81. Wang, Y.; Shi, R.; Lin, J.; Zhu, Y., Significant photocatalytic enhancement in methylene blue degradation of TiO_2 photocatalysts via graphene-like carbon in situ hybridization. *Applied Catalysis B: Environmental* **2010,** *100* (1-2), 179-183.

Chapter 4

Synthesis of TiO_2/Fe_3O_4, $Fe_3O_4@Fe_2O_3/Al_2O_3$, WO_3 and their photocatalytic applications towards Cr(VI) reduction

Chapter 4: Synthesis of TiO_2/Fe_3O_4, $Fe_3O_4@Fe_2O_3/Al_2O_3$, WO_3 and their photocatalytic applications towards Cr(VI) reduction

4.1 Introduction

In the backdrop of increasing environmental concern, water treatment has been considered as one of the frontier research areas.[1-3] Water is mainly contaminated by the presence of various matters like dyes, active pharmaceutical ingredients, organic industrial effluents, and also heavy metals.[4-6] Photocatalytic removal of organics and heavy metals is a promising approach as it offers several advantages.[7,8] Some of them include easy recoverability of the photocatalyst, room temperature process and efficient energy management. For heavy metals, the hazardous metal ions are either reduced or oxidized and converted into non-hazardous species. One such example is chromium, whose most stable oxidation states are reported to be VI and III. Cr(VI), which is a thermodynamically stable state of chromium.[9] Chromium is widely used in several industrial processes such as metal plating, leather tanning, mining, paint making and others.[10, 11] The untreated industrial effluents contains Cr(VI), which is potentially carcinogenic and also may cause pulmonary congestions, and liver damage.[12,13] It possesses acute toxicity as carcinogen and mutagen to the living being.[14] It is also reported that Cr(VI) can easily penetrate the placenta and affect the fetus.[15,16] Because of its high noxious nature, Cr(VI) has been designated as one of the most 'priority pollutants' to be removed, and WHO has recommended the permissible limit of Cr(VI) in drinking water as 0.05 ppm.[17,18] On the contrary, Cr(III) is environmentally benign and also a necessary trace element for human health by regulating the insulin function.[9,19,20] Photocatalytic reduction of Cr(VI) to Cr(III), is therefore an attractive strategy as it converts highly hazardous Cr(VI) into an essential and non-harmful species.[20-22]

Therefore, reducing Cr(VI) to Cr(III) is considered to be an important and environmentally coveted process. Among various methods of chemically reducing Cr(VI), the photocatalytic reduction with semiconducting materials is recently regarded as an attractive technology because of its low cost, high efficiency, no production of secondary pollutants and non-usage of any harsh reducing agents. Various semiconducting catalysts such as TiO_2, WO_3, ZnO, ZnS, CdS, $ZnIn_2S_4$, and $La_2Ti_2O_7$ have been used for Cr(VI) photoreduction.[23-33] For example, He et al., reported photocatalytic reduction of Cr(VI) with TiO_2 nanosheets.[34] They have used the facets of surface fluorinated anatase TiO_2 in aqueous suspension to reduce Cr(VI). The approach of anchoring an active photocatalytic material

like TiO_2 on a support disperses the active material on its surface and thereby increases the active sites. As discussed earlier, the TiO_2 supported zeolite-4A was synthesized in polymerizable sol–gel approach and demonstrated its application for dye degradation and nitroarenes reduction.[35-37] Therefore, in this current work, we have extrapolated this polymerizable sol–gel approach to synthesize TiO_2/Fe_3O_4 catalysts. Fe_3O_4 is chosen as the support since it is a magnetically recoverable and non-toxic material. Due to its biocompatibility, Fe_3O_4 has also been used in sensors and drug delivery. For sustainability and recyclability, such an easily recoverable support would be highly desirable. The recent trends show that a variety of functional materials has been anchored onto Fe_3O_4 in order to enhance the recyclability.[38-40] A recent report by Yang et al., describes a three-component Fe_3O_4@rGO@TiO_2 photocatalytic system, wherein, the role of Fe_3O_4@rGO to take up the photogenerated electrons in the conduction band (CB) of TiO_2 is discussed.[41] Such a phenomenon of electron hopping from the CB of one semiconducting material to that of another semiconducting material would minimize the electron-hole pair recombination, which could enhance the photocatalytic efficiency of the overall system.[42] In a CdS/α-Fe_2O_3 system, Zhang et al., have reported the synergistic role of heterojunctions towards the enhancement in photocatalytic activity.[43] Thus, the Fe_3O_4 support chosen in this work is also aimed at enhancing the photocatalytic activity of TiO_2 by minimizing the electron-hole pair recombination. This current work describes the synthesis and characterization of TiO_2/Fe_3O_4 catalysts and their application for photoreduction of Cr(VI) that is considered to be an important environmental issue.

The reduction potential for Cr(VI)/Cr(III) with respect to NHE is 1.33 V. If the chosen catalytic material's CB edge is above 1.33 V, the electron, which is in the CB may photocatalytically reduce Cr(VI) to Cr(III). However, the major impediments with respect to photocatalytic materials and technology are (i) UV energy requirement to excite the photoelectron, (ii) complexity in synthesis and the associated cost of the catalytic materials, (iii) lesser catalytic efficiency due to phenomenon like electron-hole recombination, and (iv) tedious recoverability of the catalytic materials (especially for nano-particles) and therefore lower recyclability. Therefore, there is a persistent quest for advanced materials, which can meet the above mentioned requirements.

Recently, Fe_2O_3 has gained considerable attention among the researchers working in the field of energy and environment.[10,20,43-46] For instance, Fe_2O_3 has been widely regarded as an efficient photoanode material for photoelectrochemical cell towards water splitting.[47,48] In

addition, it has also shown the potential for visible light photodegradation of organic environmental pollutants. The abundance and versatility in the synthetic approaches of Fe_2O_3 make the material low cost and attractive. Fe_2O_3 having a band gap (E_g) of ~ 2.2 eV, is suitable for visible light applications. The CB energy edge position of Fe_2O_3 is ~ - 4.8 eV with respect to the absolute vacuum scale or ~ 0.3 eV with respect to NHE, which is comfortably above the reduction potential of Cr(VI)/Cr(III).[49,50] Therefore, Fe_2O_3 could be regarded as a material of choice for Cr(VI) photoreduction. Further, to enhance the photoactivity of the semiconducting material, dispersing it onto a support as well as lowering the particle size to the nanoscale is the lucrative options. However, the recoverability of nano-Fe_2O_3 is a potential challenge that may affect the reusability of the material. This is due to the reason that as the diameter of the particle decreases the sedimentation velocity also decreases greatly. As a consequence, one requires performing centrifugation for a longer time and at higher rotation speed. On the other hand, magnetic recoverability of nanomaterials is getting increasingly popular over centrifugation approach. Magnetite (Fe_3O_4) is one of the most popular choices of materials for magnetic recoverability of various catalysts.[51-54] In this line, we synthesized magnetic Fe_3O_4@semiconducting Fe_2O_3 dispersed over the high surface area and highly thermally stable nano Al_2O_3 as support and discussed in chapter 4.3. The core-shell type of Fe_3O_4@Fe_2O_3 dispersed over Al_2O_3 support is referred hereafter as Fe_3O_4@Fe_2O_3/Al_2O_3. The Fe-loading was varied with respect to Al_2O_3 and the obtained materials were characterized and studied for their visible light photoreduction efficiency of Cr(VI) and magnetic recoverability.

A continuous search was carried out to find some additional catalysts that can work under visible light. The non-toxic and chemically stable WO_3 with a narrow band gap (2.7 to 3.1 eV) and suitable position of conduction band, has been regarded as a workhorse photocatalyst to harvest substantial portion of the solar spectrum towards photochemical reactions.[55-57] Structurally, WO_3 adopts various distinct crystallographic phases like monoclinic ($P2_1/n$, $P2_1/c$), triclinic ($P\bar{1}$), orthorhombic (Pmnb, Pbcn), and tetragonal (P4/nmm, P4/ncc) at different temperatures.[58-60] It belongs to a class of materials that can tolerate deviations from stoichiometry by adjustment of oxygen octahedral using shear mechanisms. The corner sharing WO_6 octahedron shears into edge sharing one without formation of oxygen vacancies, which leads to interesting electronic properties.[61-66] Due to these properties, WO_3 finds extensive applications in gas sensors, photochromic,

gasochromic and electrochromic devices.[67-70] It is also considered to be a promising anode material for oxygen evolution reaction in the photoelectrochemical water splitting.[71-73]

The surface morphologies as well as electronic properties vary due to different crystallographic structures, which in turn are governed by the synthetic approaches.[74] Various synthetic strategies such as precipitation, sol–gel, solution-combustion, hydrothermal method etc. have been employed to produce WO_3.[75-84] Several review articles describe the advances in the synthesis and applications of WO_3.[85,86] Lu *et al.*, utilized colloidal tungstenic oxide blended with polyvinylpyrrolidone to obtain electrospun nanowires that were converted to WO_3 nanowires through calcination.[87] Wang *et al.*, synthesized WO_3 nanorods through surfactant-free hydrothermal method and studied their electrochromic behavior.[88] Houx *et al.*, demonstrated the effect of heating rate on the nanoparticles' size through solvothermal synthesis in microwave and resistive heating.[89] Meng *et al.*, followed gas evaporative technique, in which a tungsten filament was subjected to resistive heating under oxygen atmosphere at low pressure to obtain WO_3 particles from nanosize to micron-size that were studied for NO_2 gas sensing.[90] They found that the WO_3 particles exhibiting nanocrystalline morphology was possessing the highest sensitivity towards gas sensing.[90] Zhang *et al.*, reported the beneficial role of using excess of nitric acid in the hydrothermal synthesis of WO_3 nanoplates that have shown fast response and distinct sensing selectivity for acetone gas.[91] Cruz *et al.*, utilized precipitation method to obtain WO_3 particles possessing various surface morphologies and studied their efficacy in visible light organic dye degradation.[92] Ahmadi *et al.*, reported hydrothermal synthesis of WO_3 nanoparticles using acidified sodium tungstate solution.[93] Hariharan *et al.*, synthesized nanocrystalline WO_3 through polyethylene glycol assisted microwave synthesis and demonstrated its utility towards electrochemical biosensing.[94] Considerable attention has also been given to tune the electronic properties of WO_3 through doping with various metals such Pt, Hf, Cu, Pd etc[78,95-98] as well as creating heterojunctions with other semiconductors such as TiO_2, ZnO, AgBr etc.[99-101]

As discussed earlier the polymerizable sol–gel (PSG) approach has been demonstrated for its capability in synthesizing supported catalysts and creating heterojunctions.[35,37,102] Little known with WO_3 for fabricating thin films through this approach. Here, we augment the potential of the PSG approach to synthesize WO_3 powders for the first time, which reserves the potential of bulk scale production of supported oxides.[35,37] In this work, the chemical changes, calcination temperature, structural evolution and surface morphology of WO_3 powders obtained through this approach have been explored. By tuning the calcination

temperature, we show the formation of WO_3 possessing a wide range of crystallinity and non-stoichiometry. The synthesized WO_3 materials have been utilized to study the photoreduction of a model priority pollutant Cr(VI) under visible light.[103] The photoreduction efficiency of Cr(VI) has been explored here against the crystallinity and non-stoichiometry of the PSG synthesized WO_3.

4.2 TiO_2/Fe_3O_4

4.2.1 Methods

(i) Synthesis of TiO_2 and TiO_2/Fe_3O_4 catalysts

TiO_2 supported Fe_3O_4 catalysts were synthesized by acrylate–based polymerizable sol–gel approach, analogous to our previous report.[35] Briefly, a polymerizable Ti-methacrylate complex was obtained by dropwise addition of MAA (2 eqvt.) to neat TiPO (1 eqvt.) that was kept stirring under inert atmosphere. Instantaneous yellow coloration was observed upon addition of MAA, indicating the formation of titanium *di*methacrylate *di*isopropoxide complex. To formulate the polymerizable precursor solution, a 2 wt% of BPO (w.r.to MAA) in 50 µL of acetone was added to the Ti-methacrylate complex. Free-radical thermal polymerization at 110 °C of this polymerizable precursor solution and subsequent calcination at 450 °C yielded pristine TiO_2. To synthesize TiO_2/Fe_3O_4 catalysts, calculated amount of Fe_3O_4 nanoparticles were added as a support material to the polymerizable precursor solution as prepared above. About 50 µL of water was introduced to this mixture and shaken vigorously until it formed a homogeneous gel, inside which the Fe_3O_4 support was homogeneously dispersed. This gel was subjected to polymerization and calcination as mentioned above to obtain TiO_2/Fe_3O_4 catalysts. Depending on the loading of Ti-methacrylate complex, catalysts containing different amount of TiO_2 such as 10, 20, 30 and 50 wt% supported onto Fe_3O_4 were prepared.

(ii) Photocatalytic studies

A cylindrical annular batch photoreactor fitted with a medium pressure mercury vapor lamp of 125 W was used for the photoreduction of Cr(VI). The lamp mainly had a broadband from 250 nm to 450 nm with useful maxima at 254, 312, and 365 nm for the photocatalytic reactions. The lamp was surrounded with a double-walled borosilicate immersion well and the set up was fitted inside a reaction vessel. To prevent IR radiation and to maintain constant temperature, water was constantly circulated around the lamp through the double-walled well. For each experiment, 100 mL of 20 ppm potassium dichromate solution and 30 mg of

catalyst were taken in the reaction vessel. The pH of the solution was brought to 3.0 at the beginning of each experiment. Prior to the irradiation, the solution was incubated with the catalyst in dark for 15 minutes to attain adsorption-desorption equilibrium. The aliquots were collected at regular time intervals during the photoreduction. The samples were analysed for Cr(VI) by complexing with DPC and the concentration was measured at 540 nm. The overall rate of the reaction was calculated below 10% conversion of Cr(VI).

4.2.2 Results and discussion

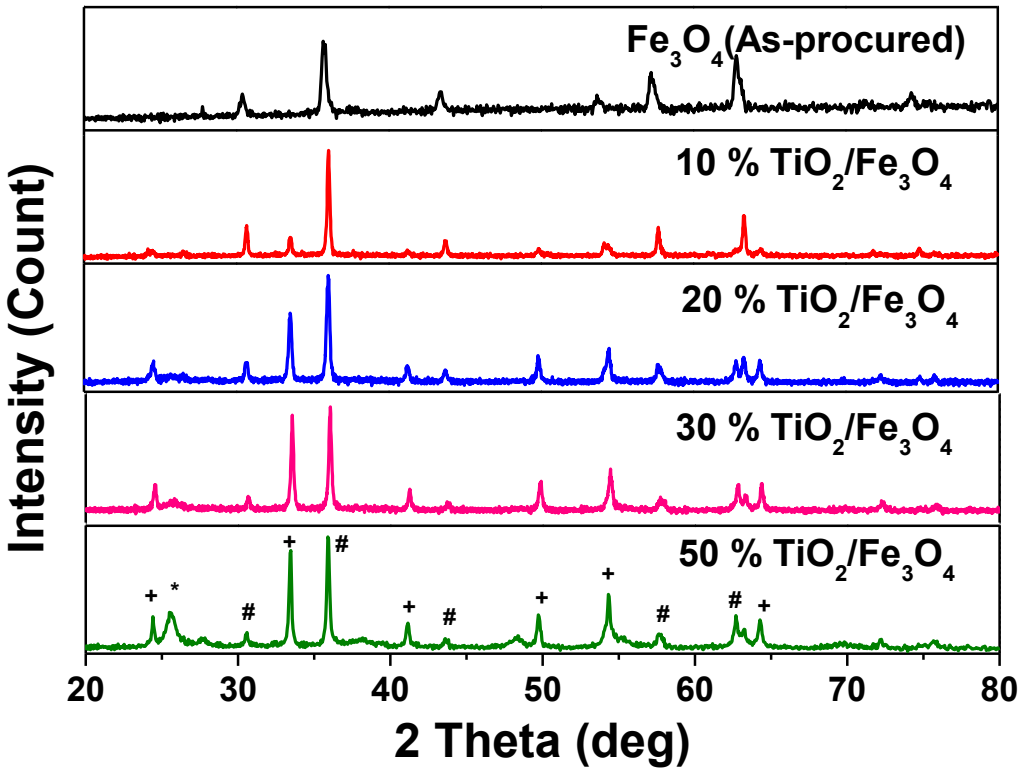

Figure 4.1: XRD of Fe_3O_4, 10, 20, 30 and 50% polymerizable sol–gel synthesized TiO_2/Fe_3O_4 catalysts. In 50% TiO_2/Fe_3O_4, the anatase TiO_2 (*), α-Fe_2O_3 (+) and Fe_3O_4 (#) phases are visible.

The pristine TiO_2 and TiO_2/Fe_3O_4 were synthesized using the acrylate–based polymerizable sol–gel route as per our previous reports.[35-37] XRD was employed to characterize the as-procured Fe_3O_4, and 10, 20, 30 and 50% TiO_2 supported Fe_3O_4 (Fig. 4.1). The XRD profile of as-procured Fe_3O_4 corresponds to the inverse spinel phase with the space group $Fd\bar{3}m$ (JCPDS No. 82-1533). When lower (10 and 20%) amount of TiO_2 is dispersed on Fe_3O_4, a prominent TiO_2 phase was not visible. However, when the TiO_2 loading was increased to 30-50%, the anatase peak of TiO_2 at 2θ=25.5° was noticeable. The broad anatase peak indicates the formation of highly dispersed nanocrystalline TiO_2 over the Fe_3O_4 support.

In all the TiO_2/Fe_3O_4 catalysts, peaks correspond to α-Fe_2O_3 were observed (JCPDS No. 89-8103, and 89-8104). Interestingly, with the increase in the TiO_2 loading, the intensity of the 2θ peaks correspond to α-Fe_2O_3 was also increased. We speculate that this could be due to the TiO_2-mediated thermal oxidation of Fe_3O_4. Also, the synthesized TiO_2/Fe_3O_4 catalysts were found to be brown in color, as opposed to the original black colored Fe_3O_4. Thus, we can conclude that TiO_2 shares a heterojunction with α-Fe_2O_3, which is generated on the surface of Fe_3O_4 during the calcination step.

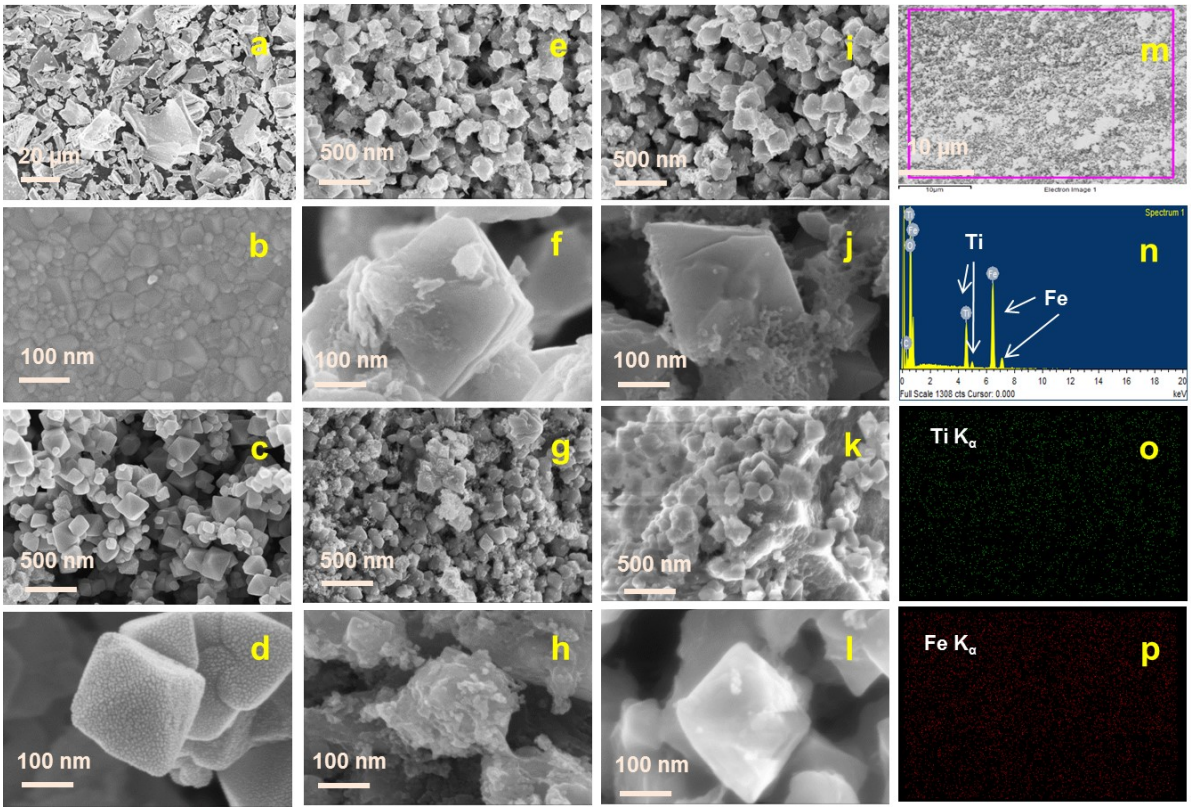

Figure 4.2: Composite FESEM images of TiO_2 (a, b), as-procured Fe_3O_4 (c, d), 10% TiO_2/Fe_3O_4 (e, f), 20% TiO_2/Fe_3O_4 (g, h), 30% TiO_2/Fe_3O_4 (i, j), and 50% TiO_2/Fe_3O_4 (k, l) photocatalysts. EDS analysis of 30% TiO_2/Fe_3O_4 (n), and elemental mapping of Ti and Fe (o, p) from the selected area of (m).

FE-SEM was studied to analyze the morphology of the synthesized materials and the corresponding images are shown in Fig. 4.2 (a-l). The pristine TiO_2 was found to be having irregular shapes and the size of the particles was mostly in the range of 5 to 30 µm. A closer look at the particles revealed the polycrystalline nature of TiO_2 and the crystallite domains were observed to be in the size range of 10 to 50 nm. The commercial Fe_3O_4 particles were in octahedral shape, having the edges in the range of 200 to 300 nm. The tiny islands found on the surface of Fe_3O_4 in Fig. 4.2 (d) are due to the sputtered Au-Pt alloy and hence the

TiO_2/Fe_3O_4 catalysts were imaged without any metal sputtering to avoid this clustering. With increasing TiO_2 loading from 10-50%, there is a clear increasing trend of TiO_2 coated over the Fe_3O_4 support. At higher loadings, however, in addition to this coating, free TiO_2 particles were also found. EDS and elemental mapping were performed on 30% TiO_2/Fe_3O_4 to gain further insight on the elemental composition as well as dispersion, the results of which are shown in Fig. 4.2 (m-p). The EDS spectrum revealed that the Ti:Fe ratio in the catalyst matches closely to that of feed ratio (Fig. 4.2 (n)), while the elemental mapping analysis demonstrated a high dispersion of TiO_2 over the Fe_3O_4 support (Fig. 4.2 (o, p)).

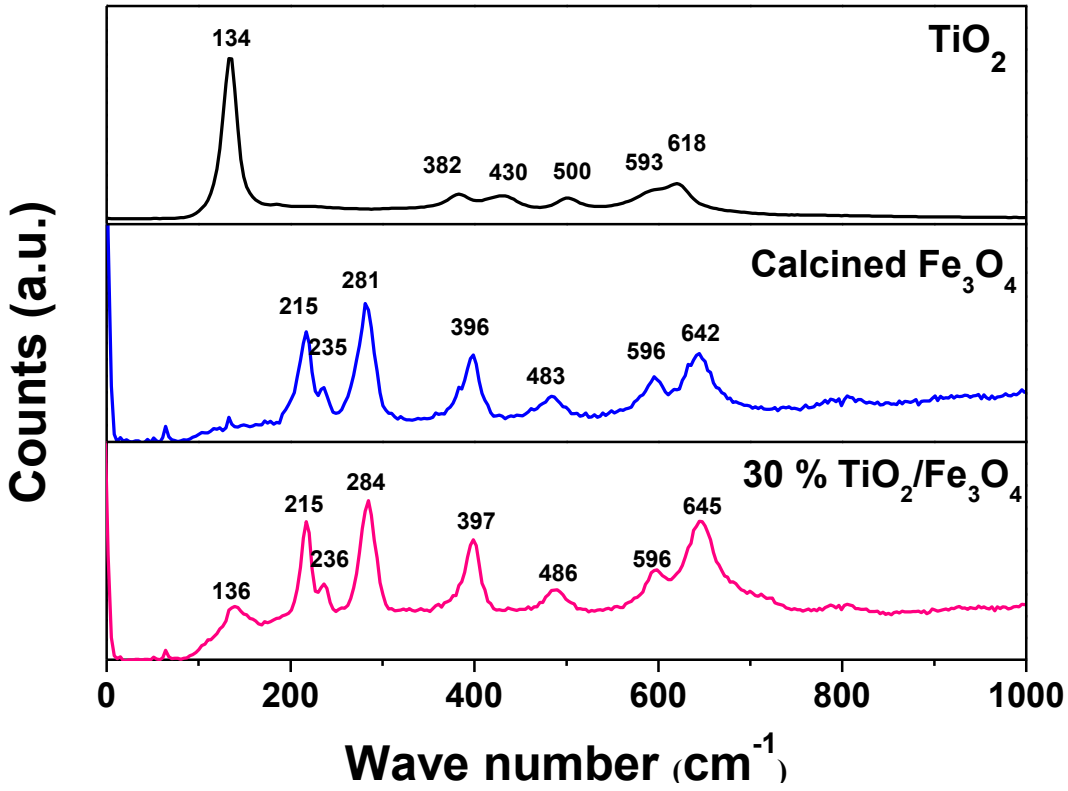

Figure 4.3: Raman spectra of pristine TiO_2, calcined Fe_3O_4 and 30% TiO_2/Fe_3O_4 synthesized by polymerizable sol–gel approach.

Raman spectroscopy was employed to analyze the pristine TiO_2, calcined Fe_3O_4, and as-synthesized 30% TiO_2/Fe_3O_4 (Fig. 4.3). A prominent peak at 134 cm^{-1} and weak peaks at 382, 500, and 618 cm^{-1} were observed in case of pristine TiO_2 that correspond to the Raman-active modes of anatase phase with the symmetries of E_g, B_{1g}, A_{1g}, and E_g, respectively.[104] Two more weak bands were observed at 430 and 593 cm^{-1}, that can be assigned to the E_g and A_{1g} Raman-active modes of rutile phase. This is in accordance with the XRD analysis of pristine TiO_2 that revealed the presence of both anatase as well as rutile phases. The calcined Fe_3O_4 support exhibited peaks at 215, 235, 281, 396, 483, 596, and 642 cm^{-1}, which can be

indexed to the Fe_2O_3 Raman-active modes of $A_{1g}(1)$, $E_g(1)$, $E_g(1)$, $E_g(1)$, $A_{1g}(2)$, $E_g(1)$, and E_u, respectively.[105,106] The 30% TiO_2/Fe_3O_4 composite catalyst possessed both the characteristic peaks of TiO_2 as well as Fe_2O_3, which is again in accordance with the XRD observation that TiO_2 shared an effective heterojunction with Fe_2O_3.

Fig. 4.4 shows the survey spectra of as-synthesized 30% TiO_2/Fe_3O_4 and its core level photoelectron spectra of Ti(2p) and Fe(2p). The survey scan reveals the presence of constituent elements such as Ti, Fe and O.[107-109] The $Ti(2p_{3/2})$ and $Ti(2p_{1/2})$ peaks were observed at 458.6 and 464.4 eV, respectively. This indicates the presence of Ti^{4+} in the catalytic material. The peaks at 710.7 and 724.3 eV were due to $Fe(2p_{3/2})$ and $Fe(2p_{1/2})$, respectively, which corresponds to Fe^{3+}. The satellite peak of $Fe(2p_{3/2})$ at ~718 eV further confirms that the iron on the surface is predominantly Fe^{3+}, which is in accordance with XRD and Raman analyses.

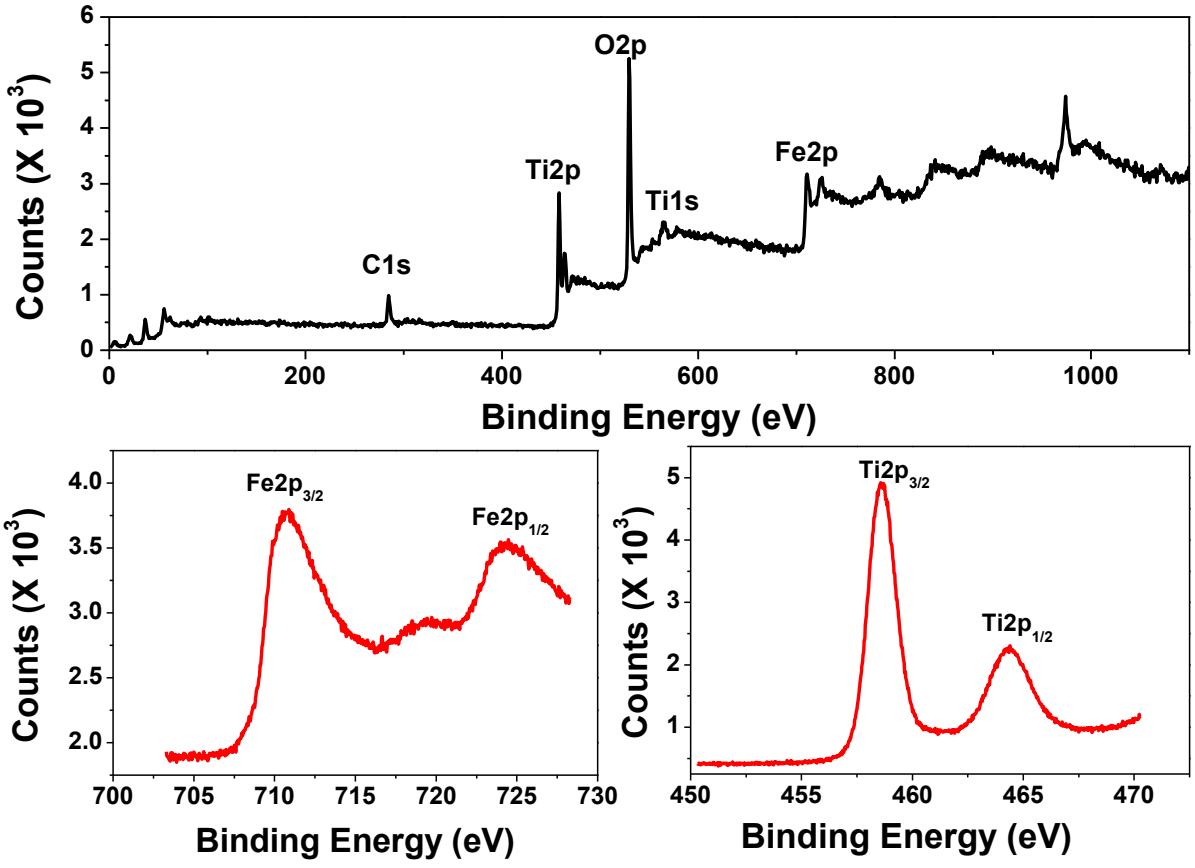

Figure 4.4: Survey scan and core level photoelectron spectra of Fe(2p) and Ti(2p) of as-synthesized 30% TiO_2/Fe_3O_4 catalyst.

$(K*E)^{1/2}$ vs E plots, derived from diffuse reflectance spectra of pristine TiO_2, 10, 20, 30, and 50% TiO_2/Fe_3O_4, calcined Fe_3O_4 and as-procured Fe_3O_4 are shown in Fig. 4.5. Kubelka-Munk factor (K) is calculated by using the formula, $K = (1-R)^2/2R$, where R

represents the % reflectance and E stands for energy of the incident radiation. The sol–gel synthesized TiO_2 shows the semiconducting band gap (E_g) of 3.2 eV. The as-procured Fe_3O_4 did not show any defined bandgap. The calcined Fe_3O_4, on the other hand, showed an E_g of 2.2 eV, which agrees well with the E_g of α-Fe_2O_3.[110,111] In addition to the 2.2 eV, a shoulder is observed at ~1.9 eV. These transitions could be due to metal to ligand, ligand to metal charge transfers, and magnetically coupled Fe^{3+} adjacent site transitions.[112] The 10-30% TiO_2/Fe_3O_4 samples showed profiles exactly similar to that of α-Fe_2O_3. We did not observe any signature of TiO_2 band gap in these samples. This could be attributed to the fine dispersion of TiO_2 and large presence of α-Fe_2O_3. However, in 50% TiO_2/Fe_3O_4, the spectrum clearly showed a shoulder at ~3.2 eV corresponding to E_g of TiO_2, in addition to the E_g = 2.2 eV of α-Fe_2O_3.

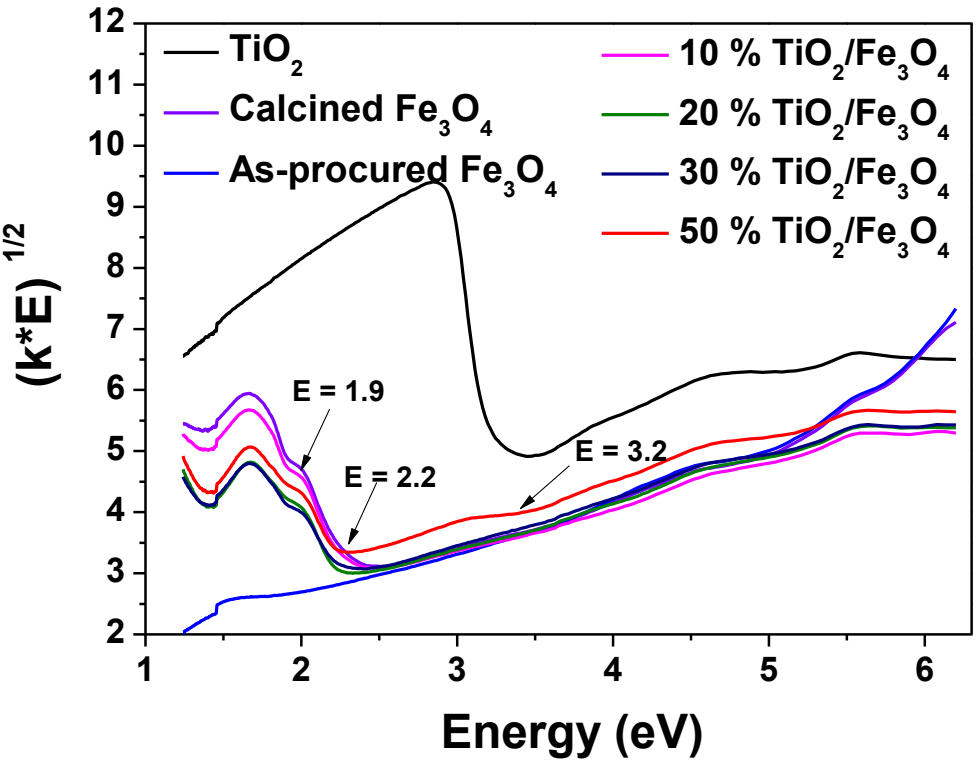

Figure 4.5: Plot of (Kubelka Munk factor (K) * Energy)$^{1/2}$ vs Energy obtained from diffuse reflectance spectra of the catalysts.

Table 4.1 shows the BET surface area measurements of the synthesized catalysts. The surface area of the pristine TiO_2 was found to be 35.1 m^2/g, while that of the calcined Fe_3O_4 was found to be 7.3 m^2/g. With the increase in TiO_2 loading from 10 to 50%, the surface area was found to be increasing from 10.9 m^2/g to 59.3 m^2/g. Such a remarkable increase in the surface area demonstrates the high dispersion of the active material over the support, which is in line with the XRD observation. To gain further clarity, the surface area of 30% TiO_2 and

Fe_3O_4 physical blend was compared with 30% TiO_2/Fe_3O_4 supported catalyst. The results revealed ~3 fold increase (11.9 m^2/g to 32.6 m^2/g) in surface area when TiO_2 was anchored over the Fe_3O_4 support. Thus, the polymerizable sol–gel approach clearly enhances the dispersion of the active material over the support.

Table 4.1: Nitrogen adsorption isotherm (BET method) analysis of the photocatalysts

Sample	Specific Surface area (m^2/g)[#]
Pristine TiO_2	35.1
Calcined Fe_3O_4	7.3
10% TiO_2/Fe_3O_4	10.9
20% TiO_2/Fe_3O_4	19.3
30% TiO_2/Fe_3O_4	32.6
50% TiO_2/Fe_3O_4	59.3
30% TiO_2-Fe_3O_4 physical blend	11.9

[#] Data obtained with 95 % confidence level.

Photocatalytic reduction of Cr(VI) by sol–gel synthesized pristine TiO_2 with various hole scavengers under inert and aerobic conditions is plotted in Fig. 4.6 (a) and 4.6 (b), respectively. Ammonium oxalate, oxalic acid and ethanol have been chosen as the hole scavengers in this study. In all the photocatalytic reduction experiments, the Cr(VI) was incubated with the catalyst in dark for 15 min to equilibrate the adsorption/desorption process before the light was turned on. Irrespective of the reaction atmosphere, the initial adsorption of Cr(VI) on TiO_2 was negligible when oxalic acid was used as the hole scavenger, whereas the same was found to be in the range of 25 to 35% when ammonium oxalate and ethanol were used as the hole scavengers. As seen in Fig. 4.6 (a), the rate of photoreduction of Cr(VI) under nitrogen atmosphere was comparatively faster with oxalic acid, and ammonium oxalate, than that with ethanol. Complete photoreduction of Cr(VI) with oxalic acid, and ammonium oxalate was achieved in 75 min. On the other hand, the photoreduction of Cr(VI) with ethanol as the hole scavenger resulted in only ~70% of conversion in 120 min.

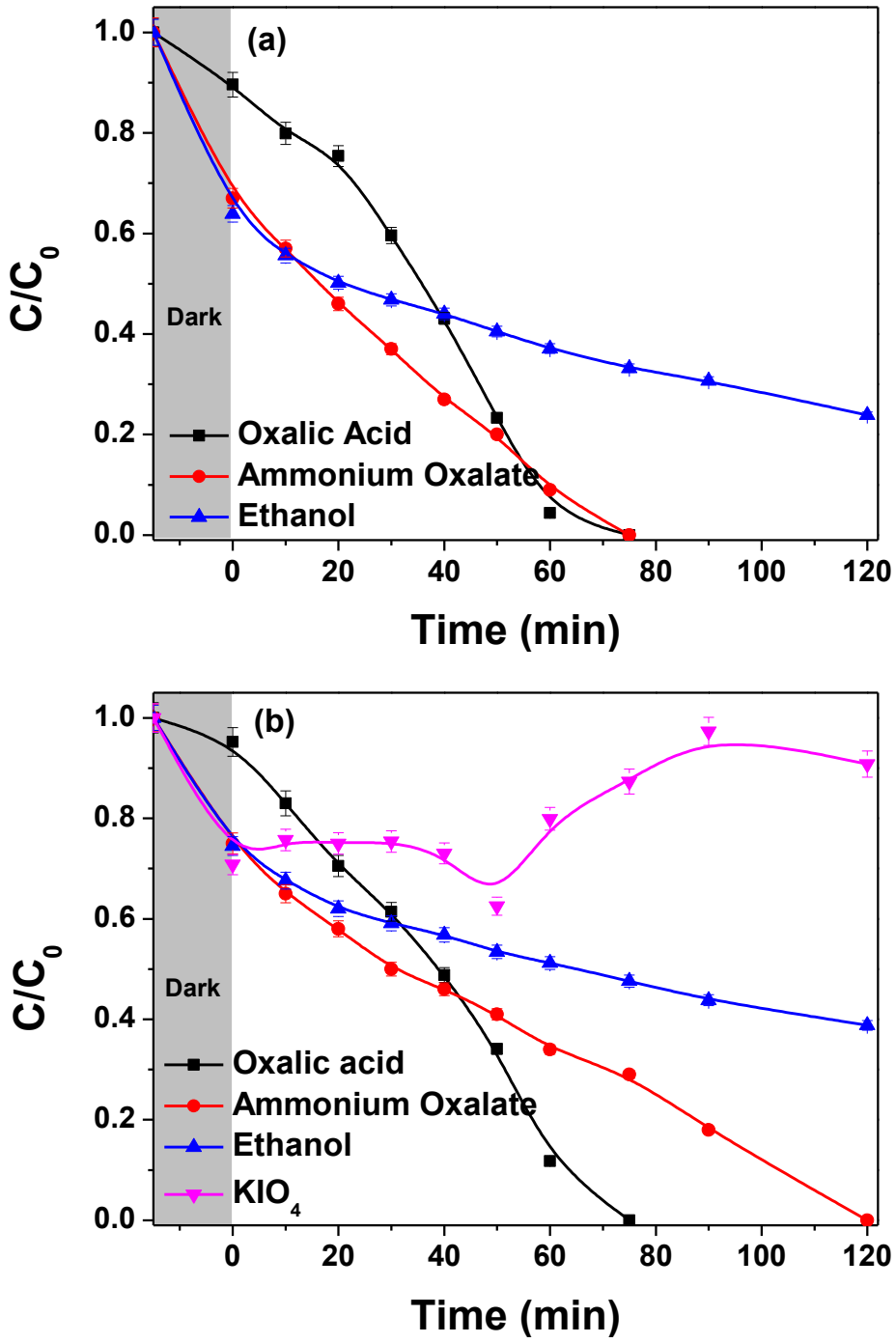

Figure 4.6: Photocatalytic reduction of Cr(VI) with various hole and electron scavenger(s) under (a) inert and (b) aerobic conditions with polymerizable sol–gel synthesized TiO_2.

The trend was slightly different when the photoreduction experiments were carried out under aerobic atmosphere (Fig. 4.6 (b)). In this case, the complete photoreduction of Cr(VI) was accomplished in 75 min with oxalic acid, and 120 min with ammonium oxalate. With ethanol as the hole scavenger, the conversion after 120 min was found to be ~ 55%. TiO_2 generates electrons in its CB and holes in its valence band (VB) when irradiated with suitable

wavelength of light. The hole scavengers scavenge the holes from the VB and thereby making the electrons in the CB available for photoreduction. When oxygen is present, it scavenges the electrons to get converted into superoxide radicals and thereby minimizing the availability of electrons for the photoreduction, which slows down the Cr(VI) reduction. To prove this further, we performed an additional experiment in aerobic atmosphere by taking an additional electron scavenger, IO_4^-. The presence of iodate has resulted in further slowing down the reaction rate (see Fig. 4.6 (b)), which has proven that the availability of photogenerated electrons in the CB of the semiconducting catalytic material is crucial to reduce the Cr(VI).

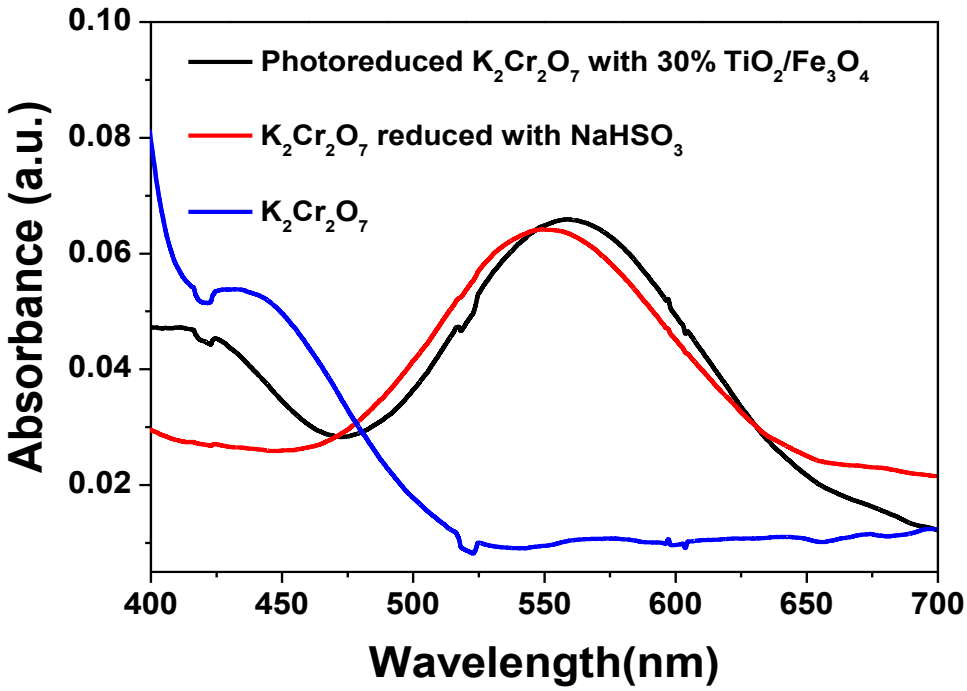

Figure 4.7: UV-visible spectra of PDCA treated solutions of $K_2Cr_2O_7$, $K_2Cr_2O_7$ reduced with $NaHSO_3$, and photoreduced $K_2Cr_2O_7$ with 30% TiO_2/Fe_3O_4.

Total chromium concentration was quantified before and after photoreduction using AAS (data not shown). The analysis revealed that the total chromium concentration did not change after the photoreduction, thus confirming that the reduced species remained in the solution. To identify the oxidation state of chromium after photoreduction, we treated the photoreduced product sample solution with 2,6-pyridine dicarboxylic acid (PDCA) that is known to specifically form a characteristic complex with Cr(III).[113] A positive control sample was prepared wherein $K_2Cr_2O_7$ was reduced by using $NaHSO_3$, followed by heating with PDCA for 30 min. Both the solutions exhibiting a light violet color were subjected to UV-visible analysis (Fig. 4.7). It was observed that both photoreduced as well as $NaHSO_3$

reduced samples exhibited light absorption in the range of 550-555 nm. However, a negative control of non-reduced $K_2Cr_2O_7$ did not show any absorption in this wavelength range after treating with PDCA. These results confirmed the successful conversion of Cr(VI) to Cr(III) under the photoreduction conditions.

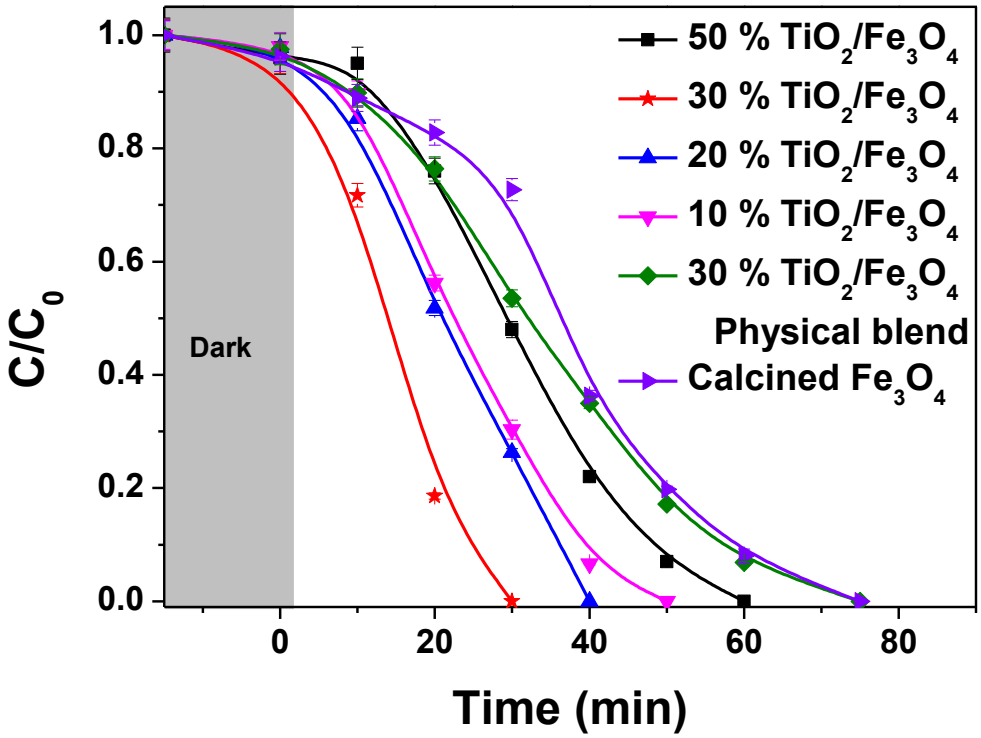

Figure 4.8: Photoreduction of Cr(VI) with 10-50% TiO_2/Fe_3O_4 , and calcined Fe_3O_4 catalysts under UV light irradiation in aerobic condition.

As the photoreduction under aerobic conditions has practical significance and also there was not much difference between aerobic and inert atmosphere, further photoreduction of Cr(VI) studies were carried out under aerobic conditions. To understand the chemistry of dispersed TiO_2 over a semiconducting magnetic support, TiO_2/Fe_3O_4 was employed for aerobic photoreduction of Cr(VI). Since oxalic acid possessed the maximum hole scavenging ability, it was used for further photoreduction studies. Fig. 4.8 shows the Cr(VI) photoreduction with 10-50% TiO_2/Fe_3O_4 catalysts under UV light irradiation. Calcined Fe_3O_4, and 30% TiO_2-calcined Fe_3O_4 physical blend were used as controls. As seen in the figure, the 10, 20, 30, and 50% TiO_2/Fe_3O_4 catalysts reduced the Cr(VI) completely in 50, 40, 30, and 60 min, respectively. Whereas both the controls, calcined Fe_3O_4, and 30% TiO_2-Fe_3O_4 physical blend, reduced the Cr(VI) in 75 min. For pristine TiO_2, and calcined Fe_3O_4 the rate of Cr(VI) photoreduction was found to be 0.43, and 0.24 ppm g^{-1} min^{-1}, respectively. When TiO_2 was anchored onto Fe_3O_4, the reaction rates have been found to be 0.5, 0.59,

0.91, and 0.24 ppm g^{-1} min^{-1} for 10, 20, 30, and 50% TiO_2/Fe_3O_4, respectively. The dispersion of the active sites clearly shows significant acceleration of the reaction rates up to 30% of TiO_2 loading, beyond which the reaction rate has decreased. Although 50% TiO_2/Fe_3O_4 has possessed roughly twice the surface area of 30% TiO_2/Fe_3O_4, the decrease in the photocatalytic activity indicates the role of effective heterojunction between TiO_2 and Fe_3O_4 support.

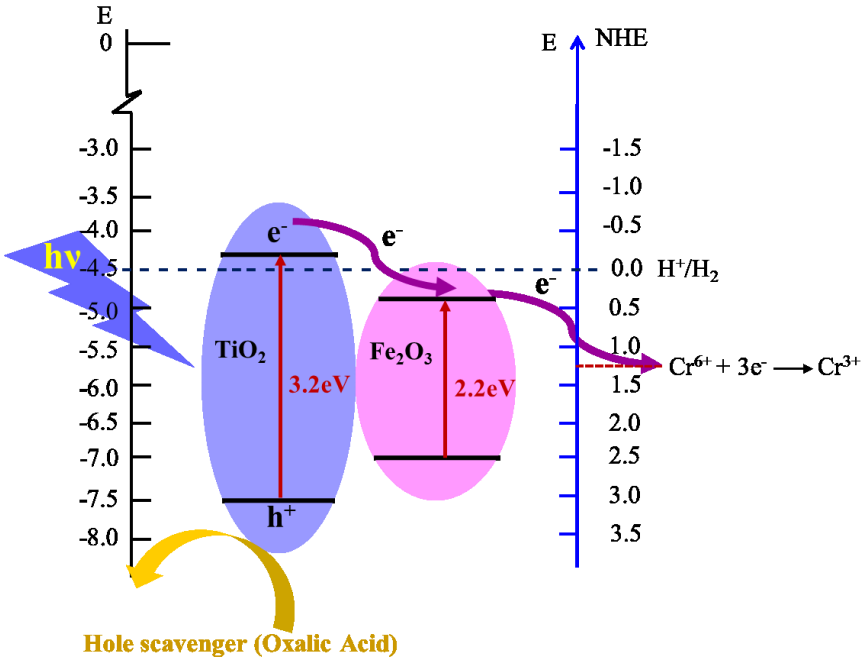

Figure 4.9: Schematic illustration of the proposed mechanism for the Cr(VI) photoreduction using TiO_2/Fe_3O_4 catalyst under UV light irradiation.

In addition to the high dispersion, there is a significant synergistic role of the CBs of TiO_2 and Fe_2O_3 towards the photocatalysis. In Fig. 4.9, the E_g between VB and CB of TiO_2 as well as Fe_2O_3 obtained from the diffuse reflectance spectra is merged with the standard reduction potential of Cr(VI)/Cr(III). Upon irradiation of UV light, the electrons move from the VB of TiO_2 to its CB leaving the holes behind. The CB of Fe_2O_3 is slightly energetically lower than that of TiO_2. The electron, therefore, may move downhill from the CB of TiO_2 to CB of Fe_2O_3, which in turn could significantly reduce the electron-hole recombination in TiO_2. The available electron in the CB of Fe_2O_3 can reduce the Cr(VI) to Cr(III) efficiently. Therefore, we observe a high rate of photoreduction with the sol–gel synthesized composite catalyst. However, when TiO_2 was physically mixed with calcined Fe_3O_4, the TiO_2-Fe_2O_3 interfaces were not so conducive for the effective hopping of electron from the CB of TiO_2 to CB of Fe_2O_3. The optimum concentration for this effective band overlap was observed with

30% loading of TiO_2 over Fe_3O_4, which could be due to the reason that the effective heterojunction between TiO_2 and Fe_3O_4 is formed at this loading.

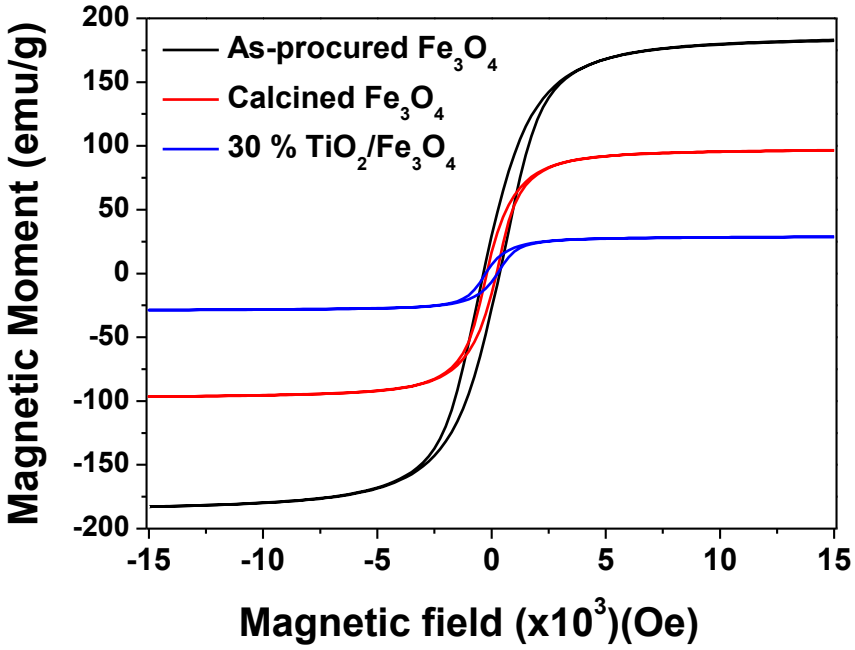

Figure 4.10: Magnetic hysteresis plot of as-procured Fe_3O_4, calcined Fe_3O_4 and 30% TiO_2/Fe_3O_4 catalysts.

In order to successfully recycle the composite catalysts, it is important to understand the magnetic recoverability. The saturation magnetization (M_s) was measured on Fe_3O_4, calcined Fe_3O_4 and 30% TiO_2/Fe_3O_4 by using vibrating sample magnetometer (VSM) and the corresponding hysteresis loops are shown in Fig. 4.10. The commercial Fe_3O_4 exhibited a M_s value of 174 emu/g, which came down to 95 emu/g after calcination. This is due to the surface oxidation of Fe_3O_4 to α-Fe_2O_3 during the calcination. The 30% TiO_2/Fe_3O_4 exhibited a normalized M_s value of 37.6 emu/g, which additionally confirmed the coating of TiO_2 over Fe_3O_4. It is noteworthy that despite the decrease in value, the M_s of the final catalyst is acceptable for easy magnetic recovery of the catalyst, and the value is comparable to those Fe_3O_4-based catalysts found in the literature.[41,114]

Recyclability of the catalyst for photoreduction of Cr(VI) was carried out with 30% TiO_2/Fe_3O_4 up to 4 cycles (Fig. 4.11 (a)). There was no decrease in the photocatalytic efficiency up to 4 cycles and ~84% of the catalyst was recovered at the end of the fourth cycle. The catalyst was recovered using a magnet at the end of each cycle (Fig. 4.11 (b)).

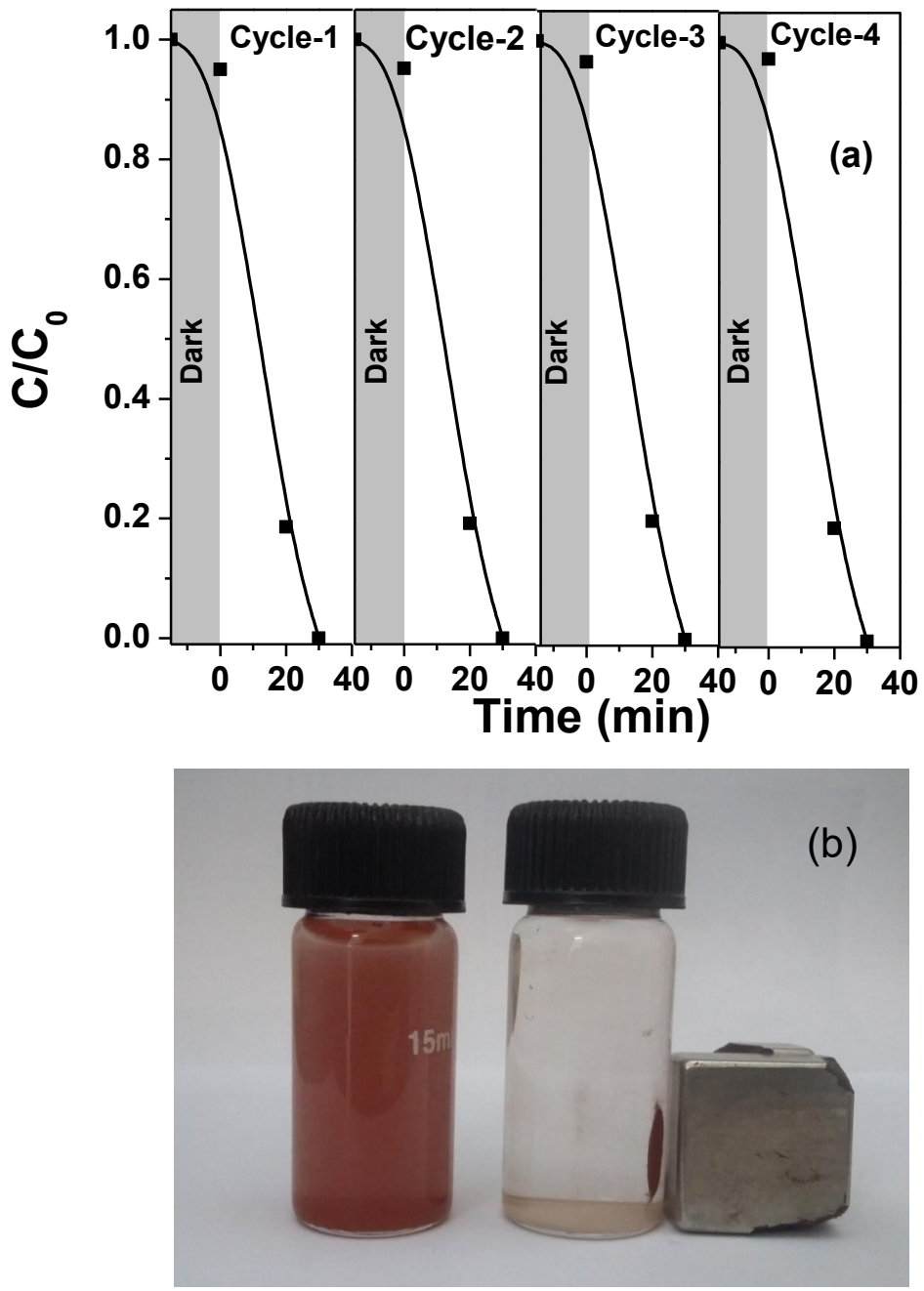

Figure 4.11: (a) Recyclability of 30% TiO_2/Fe_3O_4 for Cr(VI) photoreduction up to 4 cycles, (b) photograph showing the magnetic recoverability of the catalyst.

To further probe the stability of the photocatalyst, we performed XRD, Raman spectroscopy, and SEM-EDS analysis of the 30% TiO_2/Fe_3O_4 recovered catalyst after 4 cycles of photoreduction (Fig. 4.12). The XRD pattern was found to be the same as that of as-synthesized catalyst and thus confirmed that there is no change in the crystal structure before and after photoreduction. The SEM image as well as EDS analysis also revealed that the

morphology and elemental composition of the catalyst remain unchanged even after 4 cycles of photoreduction. The same trend was observed in case of Raman spectral analysis as well. These results have proven the high stability of the catalyst under the reaction conditions and also the magnetic recoverability.

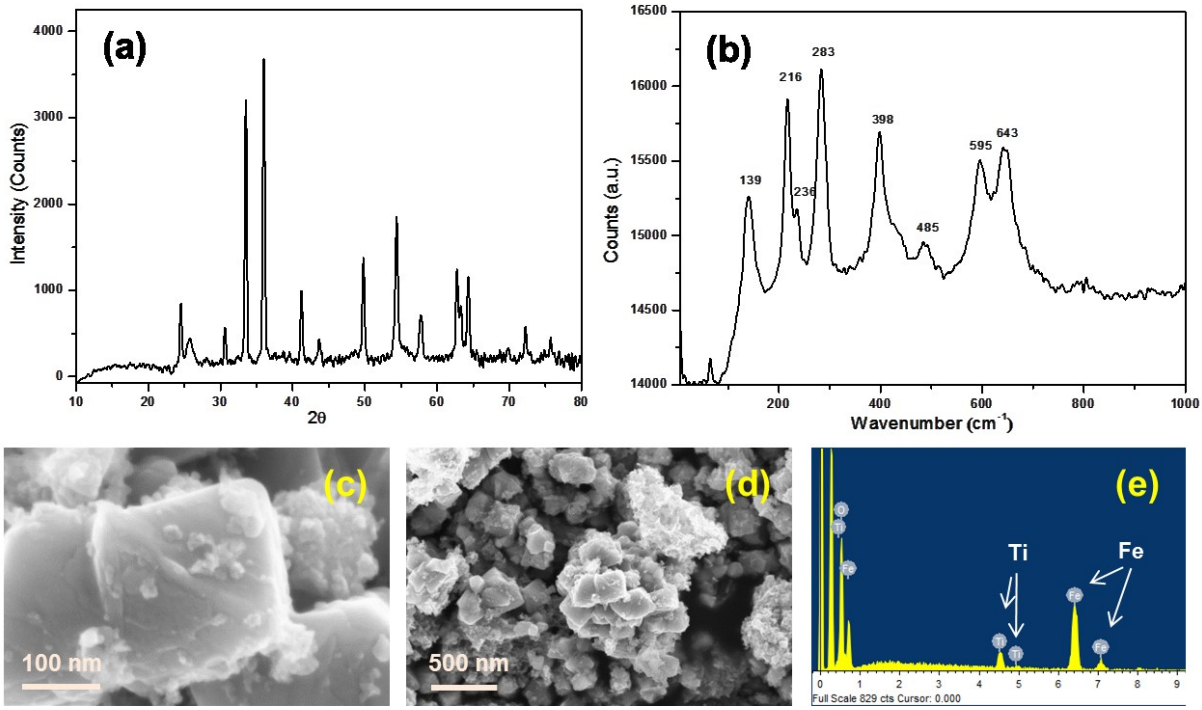

Figure 4.12: XRD (a), Raman spectrum (b), SEM (c, d), and EDS (e) data of 30% TiO_2/Fe_3O_4 recovered catalyst after 4 cycles of photoreduction.

4.3 Fe_3O_4@Fe_2O_3/Al_2O_3

4. 3.1 Experimental

(i) Synthesis of Fe_3O_4@Fe_2O_3/Al_2O_3

Fe_3O_4@Fe_2O_3/Al_2O_3 catalysts were synthesized by customized co-precipitation method.[115] $FeSO_4.7H_2O$ and $FeCl_3$ in 1:2 molar ratio were dissolved in 50 mL of acid-water (pH ~ 1.5). Varied amounts of Al_2O_3 nano powder were added to the above solution and sonicated for 10 min. The resultant suspension was continuously stirred with dropwise addition of ammonia solution (25%) until complete precipitation of Fe_3O_4/Al_2O_3 composite was obtained. With this approach, different loading of Fe_3O_4 such as 5, 10, 20, 40 wt % supported onto Al_2O_3 were prepared. The as-synthesized catalysts were subjected to calcination at 400 °C for 1 hr in order to oxidize the surface of Fe_3O_4 to Fe_2O_3. In addition, this calcination step has also

helped to stabilize the interface between Fe_3O_4 and Al_2O_3. In a similar way, the unsupported Fe_3O_4@Fe_2O_3 was also synthesized.

(ii) Photocatalytic Studies

The photocatalytic experiments were studied under simulated visible light using HPS 250 visible lamp of 250 W. To compare the activity, the photoreduction was also carried out under day light. For every experiment, 100 mL of 50 ppm Cr(VI) solution containing 10 mM of oxalic acid as hole scavenger was taken in a 500 mL beaker. The pH of the solution was adjusted to 3 using NaOH and HCl. A catalyst amount of 30 mg was added to the solution and was shaken in an orbital shaker at 200 rpm. Initially, the solution was shaken in dark for 15 min to reach adsorption-desorption equilibrium of Cr(VI) over the catalyst. This was followed by irradiation of visible light under aerobic condition. The aliquots were collected in a regular interval during photoreduction. The residual Cr(VI) concentration was determined by UV-Vis spectrophotometry at 540 nm after complexation with DPC.

4.3.2 Results and discussion

(i) Synthesis and compositional analysis

One of the popular methods to synthesize Fe_3O_4 nano particles is via co-precipitation method.[116, 117] In this route, Fe(II) and Fe(III) precursors are taken in 1:2 molar ratio as present in an inverse spinel form of $[Fe^{2+}Fe^{3+}]_{Td}[Fe^{3+}]_{Oh}O_4$, where T_d and O_h are tetrahedral and octahedral holes, respectively. In our customized synthesis, Fe(II) and Fe(III) precursors were co-precipitated in the presence of high surface area Al_2O_3 nano powder in order to anchor as well as disperse the Fe-oxide over the support. We observed that during synthesis, the black Fe_3O_4 was precipitated along with the Al_2O_3 nano powder. The obtained materials were subjected to calcination in order to stabilize the interface between Fe_3O_4 and Al_2O_3 and also to partially oxidize the surface of Fe_3O_4 to Fe_2O_3. The color of the catalysts was observed to have changed from black to brown indicating the formation of Fe_2O_3 on the surface. Table 4.2 summarises the yield and the BET surface area of the composite catalysts possessing varied loading of the active material. Up to 20% loading of the active material, the obtained yield was found to be ~ 90%. However, with 40% loading of the active material, the yield was substantially increased to 98%. The pristine Al_2O_3 nanopowder and the synthesized Fe_3O_4@Fe_2O_3 possessed a surface area of 57.3 and 88.8 $m^2\ g^{-1}$, respectively. When 5% of Fe_3O_4@Fe_2O_3 was dispersed over Al_2O_3 support, the surface area significantly increased to 102.5 $m^2\ g^{-1}$. In case of 10 and 20% Fe_3O_4@Fe_2O_3/Al_2O_3, the surface area was saturated at

~107 m^2 g^{-1}. On the contrary, the physical blend of 10% Fe_3O_4@Fe_2O_3 and Al_2O_3 possessed a surface area of ~86 m^2 g^{-1}. This shows the fine dispersion of the active material in the synthesized composite catalysts. When the loading of active material was increased to 40%, the surface area decreased to ~80 m^2 g^{-1}. This could be attributed to the formation of bigger Fe_3O_4 nanoparticles anchored over the support.

Table 4.2: Surface area of materials

No.	Catalyst	Yield (%)	Surface Area m^2/g
1	Fe_3O_4@Fe_2O_3	--	57.3
2	Al_2O_3	--	88.8
3	5% Fe_3O_4@Fe_2O_3/Al_2O_3	90	102.6
4	10% Fe_3O_4@Fe_2O_3/Al_2O_3	89	107.6
5	20% Fe_3O_4@Fe_2O_3/Al_2O_3	90	106.2
6	40% Fe_3O_4@Fe_2O_3/Al_2O_3	98	79.9
7	10% Fe_3O_4@Fe_2O_3-Al_2O_3 (Physical blend)	--	86.2

Table 4.3: Composition analysis of co-precipitated and physical blend catalysts by ED-XRF

Composition	Co-precipitated Catalyst	Physical blend
	Fe_3O_4@Fe_2O_3 : Al_2O_3	**Fe_3O_4@Fe_2O_3 : Al_2O_3**
5% Fe_3O_4@Fe_2O_3/Al_2O_3	5.8 : 94.2	4.5 : 95.5
10% Fe_3O_4@Fe_2O_3/Al_2O_3	10.1 : 89.9	8.7 : 91.3
20% Fe_3O_4@Fe_2O_3/Al_2O_3	18.8 : 81.2	14.5 : 85.5
40% Fe_3O_4@Fe_2O_3/Al_2O_3	33.8 : 66.2	32.9 : 67.1

Table 4.3 shows the ED-XRF compositional analysis of the co-precipitated and the physical blend catalysts. The observed values are at per with the theoretical loadings in both the cases. However, at any composition, the intensities of the active material in the co-precipitated catalysts were found to be little higher than that in the physical blend. This could be attributed to the higher dispersion of the active material in the co-precipitated catalysts.

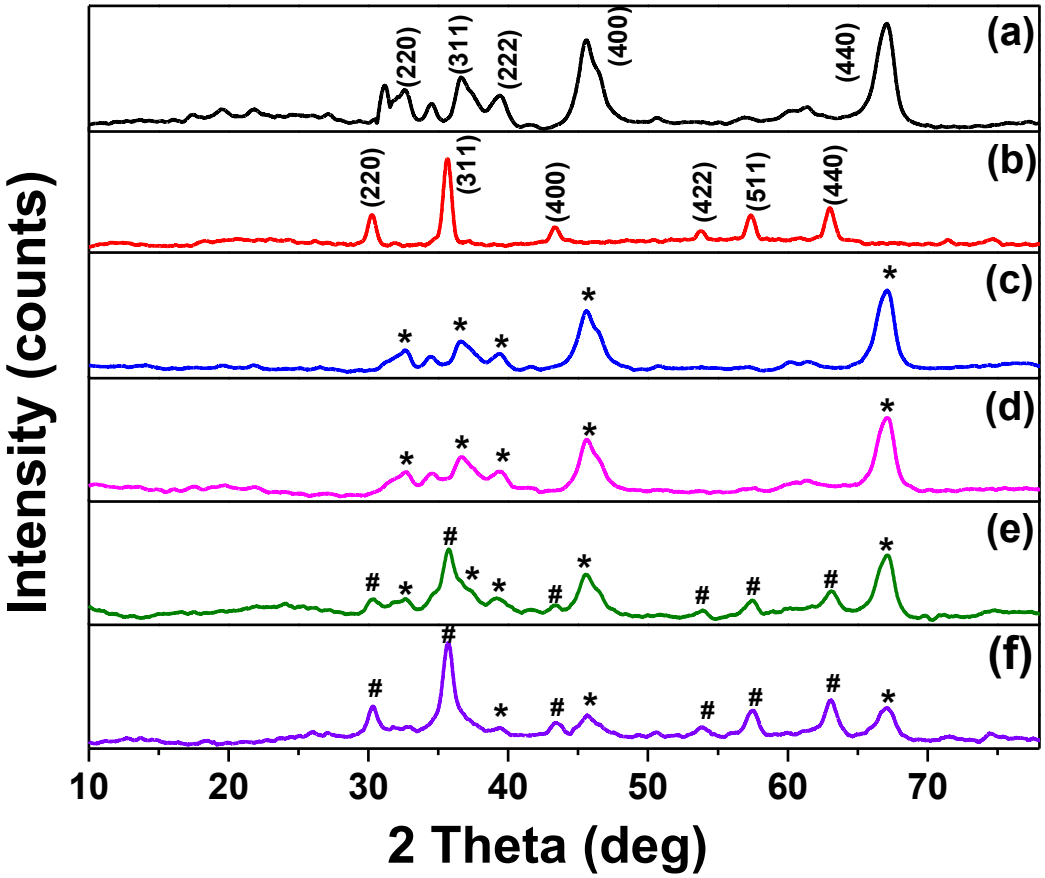

Figure 4.13: XRD patterns of (a) Al_2O_3, (b) Fe_3O_4@Fe_2O_3, (c) 5% Fe_3O_4@Fe_2O_3/Al_2O_3, (d) 10% Fe_3O_4@Fe_2O_3/Al_2O_3, (e) 20% Fe_3O_4@Fe_2O_3/Al_2O_3, and (f) 40% Fe_3O_4@Fe_2O_3/Al_2O_3. (* and # indicates phases of Al_2O_3 and Fe_3O_4 respectively).

Fig. 4.13 shows the XRD patterns of (a) Al_2O_3 (b) Fe_3O_4@Fe_2O_3 and (c-f) 10-40 % Fe_3O_4@Fe_2O_3. The commercially bought Al_2O_3 shows broad peaks confirming its nano size. The crystallite size measured for Al_2O_3 by Debye Scherrer's formula is ~ 6.2 nm. The Al_2O_3 was found to be in the γ-phase (JCPDS # 50-0741). Fe_3O_4@Fe_2O_3 after calcination of Fe_3O_4 in Fig. 4.13 (b) exhibits the characteristic peaks at 2θ = 30.78, 35.88, 43.58, 54.18, 57.79, 63.10° confirming that the calcined Fe_3O_4 crystalizes in inverse spinel phase (JCPDS # 89-4319). The crystallite size of Fe_3O_4 in Fe_3O_4@Fe_2O_3 measured was ~10.7 nm. Up to 10% of

Fe_3O_4@Fe_2O_3 loading over Al_2O_3, no significant peak corresponding to Fe_3O_4 was observed. This could be due to the high dispersion and lower amount of Fe_3O_4 loading over nano-Al_2O_3. When, Fe_3O_4 loading was increased to 20% and above, the characteristic peaks of Fe_3O_4 were visible. It should be noted that in all cases any characteristic peak corresponding to Fe_2O_3 was obscured.

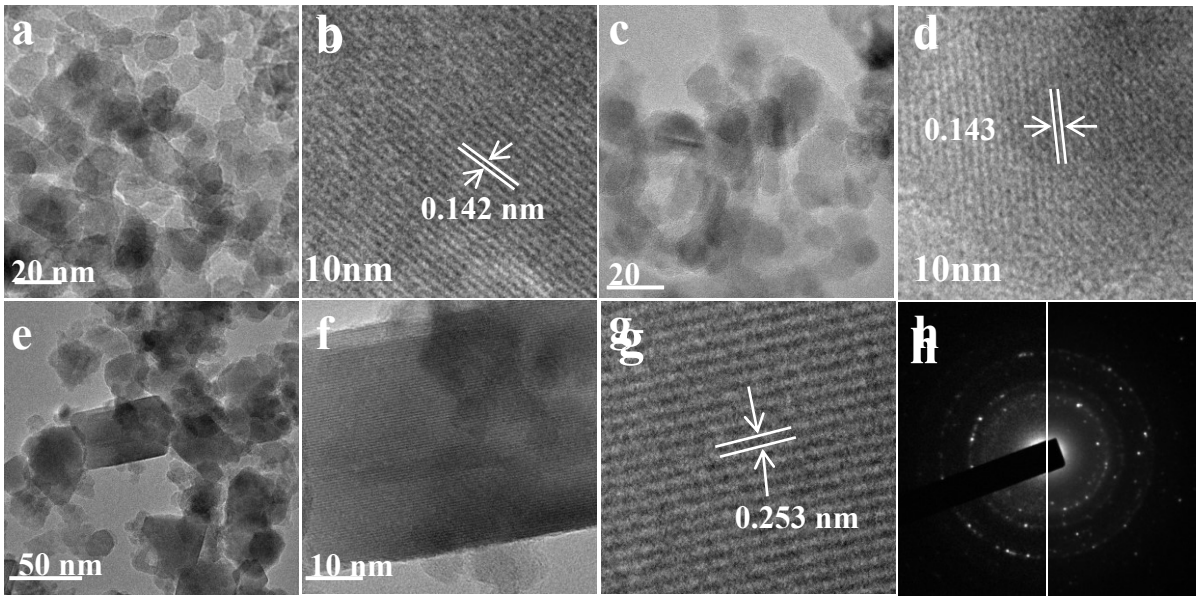

Figure 4.14: HR-TEM images of (a-b) Al_2O_3, (c-d) 10% Fe_3O_4@Fe_2O_3/Al_2O_3, (e-g) 40% Fe_3O_4@Fe_2O_3/Al_2O_3 and (h) comparison of electron diffraction patterns of Al_2O_3 (left) and 40% Fe_3O_4@Fe_2O_3/Al_2O_3 (right).

The detailed structural information of commercial alumina and synthesized Fe_3O_4@Fe_2O_3/Al_2O_3 (10 and 40%) photocatalysts was demonstrated by HR-TEM analysis. Fig. 4.14 shows the HR-TEM images of Al_2O_3 (a-b), 10 % (c-d) and 40 % Fe_3O_4@Fe_2O_3/Al_2O_3 (e-g). The pristine Al_2O_3 nanopowder was found to contain particles in the size range of 10 to 15 nm. It is observed from Fig. 3.14b that the lattice fringes with d-spacing of 0.142 nm corresponds to (440) plane of Al_2O_3. The HR-TEM image of 10 % Fe_3O_4@Fe_2O_3/Al_2O_3 (Fig. 3.14 (d)) has also shown the lattice fringes with d-spacing of 0.143 nm, which is due to the major component Al_2O_3 in the composite catalyst. No lattice fringes correspond to Fe_3O_4 was observed, indicating that the minor component (active material) is well dispersed and therefore did not form any significant crystalline domain. In case of 40 % Fe_3O_4@Fe_2O_3/Al_2O_3, along with the Al_2O_3 nanopowder, few bigger particles with a lateral dimension of ~30 to 40 nm were found (Fig. 4.14 (e) and 4.14 (f)). The high-resolution imaging of one such domain revealed the lattice fringes with d-spacing of 0.253 nm (Fig.

4.14 (g)), which agrees well with the (311) plane of Fe_3O_4. This confirms the formation of Fe_3O_4 nanoparticles over Al_2O_3 support. The comparison of electron diffraction rings between Al_2O_3 and 40 % Fe_3O_4@Fe_2O_3/Al_2O_3, additionally shows that the intensity of Al_2O_3 rings have diminished and the prominent Fe_3O_4 rings have started to appear in the case of latter (Fig. 4.14 (h)). It is noteworthy that there was no clear information on the presence of Fe_2O_3 at the surface of Fe_3O_4 nanoparticles.

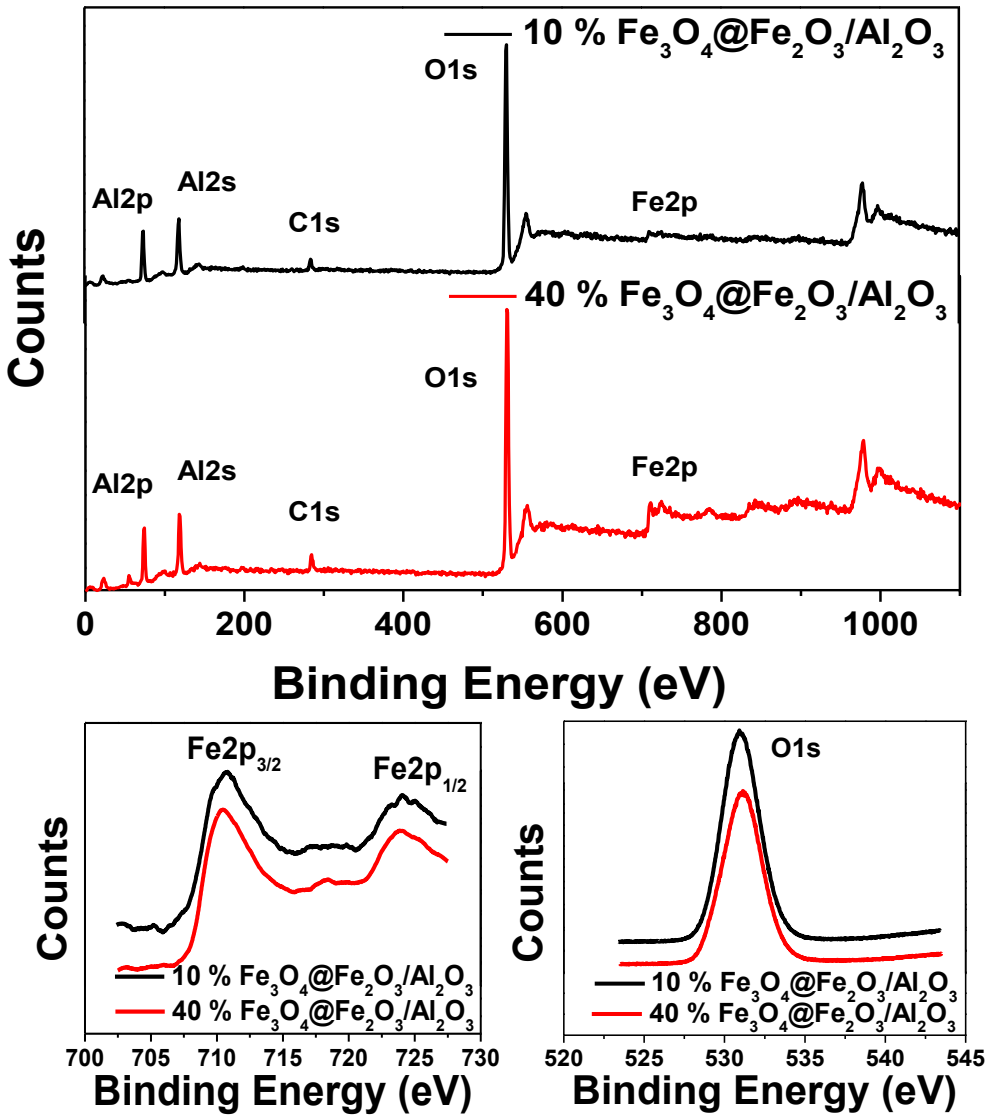

Figure 4.15: X-ray photoelectron survey spectra of 10% Fe_3O_4@Fe_2O_3/Al_2O_3 and 40% Fe_3O_4@Fe_2O_3/Al_2O_3 and their corresponding core level spectra of Fe(2*p*) and O(1*s*).

In order to gain further insight on the surface oxidation of Fe_3O_4, XPS was employed. Fig. 4.15 represents the X-ray photoelectron survey spectra of 10 and 40% Fe_3O_4@Fe_2O_3/Al_2O_3 and their corresponding core level spectra of Fe(2*p*) and O(1*s*). In the survey scan the characteristic elemental peaks of Al, Fe and O were observed, confirming the

composite nature of the catalyst. No significant difference, except a little increase in intensity of Fe (2*p*) peak was observed in 40% Fe_3O_4@Fe_2O_3/Al_2O_3 compared to 10% Fe_3O_4@Fe_2O_3/Al_2O_3. This can be attributed to the higher loading of Fe in 40% Fe_3O_4@Fe_2O_3/Al_2O_3. The core level spectra showed a very broad Fe($2p_{3/2}$) and Fe($2p_{1/2}$) peaks at 710.5 and 724 eV, respectively, confirming the mixed oxidation states of Fe as in Fe_3O_4. The characteristic satellite peak at ~ 718 eV in 40% Fe_3O_4@Fe_2O_3/Al_2O_3 reveals that the very surface is more oxidized to Fe^{3+}[102]. This indicates that higher loading of Fe_3O_4 produces detectable amount of Fe_2O_3 in the surface of Fe_3O_4. The O(1*s*) core level spectra is mildly higher in binding energy for 40% Fe_3O_4@Fe_2O_3/Al_2O_3 compared to that of 10% Fe_3O_4@Fe_2O_3/Al_2O_3. This may additionally support that the surface Fe is more oxidized to Fe_2O_3 in 40% Fe_3O_4@Fe_2O_3/Al_2O_3.

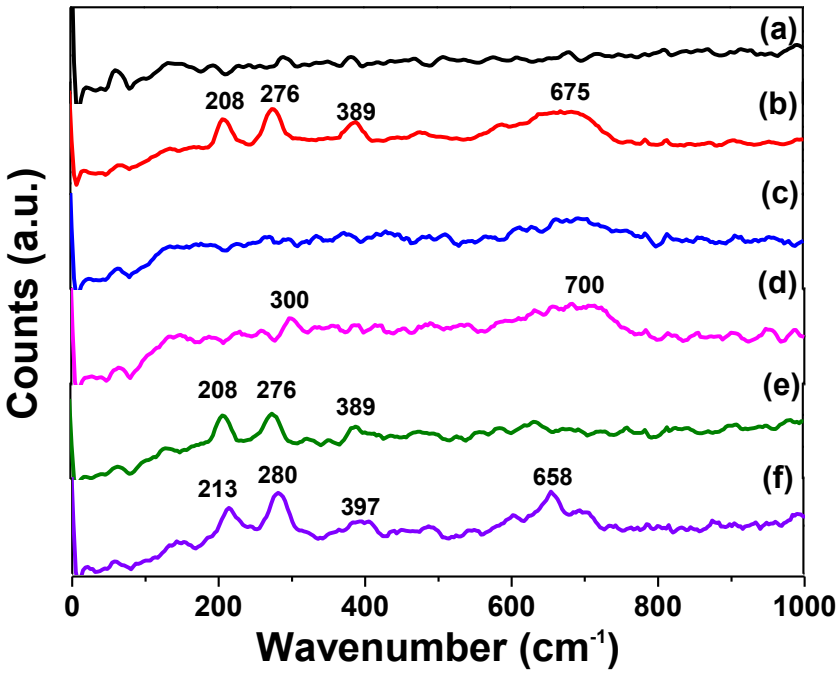

Figure 4.16: Raman spectra of (a) Al_2O_3, (b) Fe_3O_4@Fe_2O_3, (c) 5% Fe_3O_4@Fe_2O_3/Al_2O_3, (d) 10% Fe_3O_4@Fe_2O_3/Al_2O_3, (e) 20% Fe_3O_4@Fe_2O_3/Al_2O_3, and (f) 40% Fe_3O_4@Fe_2O_3/Al_2O_3.

Surface oxidation of Fe_3O_4 was further studied using Raman spectroscopy, which is a powerful technique to reveal the surface composition. Fig. 4.16 shows the Raman spectra of commercial Al_2O_3 and the synthesized photocatalysts. The commercial Al_2O_3 did not show any significant Raman peak, indicating the absence of any significant Raman active mode in Al_2O_3. On the other hand, the Fe_3O_4@Fe_2O_3 obtained by the calcination of Fe_3O_4 synthesized by the co-precipitation method exhibited characteristic peaks of α-Fe_2O_3. The peaks at 208, 276, 389 and 675 cm^{-1} can be indexed to the $A_{1g}(1)$, $E_g(1)$, $E_g(1)$ and E_u Raman active modes

of Fe_2O_3, respectively. Importantly, there was no significant peak intensity at ~540 cm^{-1}, which is a characteristic peak of $T_{2g}(2)$ Raman active mode of Fe_3O_4.[105,118,119] This reveals that the surface of Fe_3O_4 is oxidized to Fe_2O_3 due to calcination. In case of 5 and 10% Fe_3O_4@Fe_2O_3/Al_2O_3, no significant peak of Fe_2O_3 was observed in the Raman spectrum that additionally corroborates the fine dispersion of the active material over the support. Starting from 20% of active material loading, the characteristic Fe_2O_3 Raman peaks were visible and the spectra were matching with that of Fe_3O_4@Fe_2O_3.

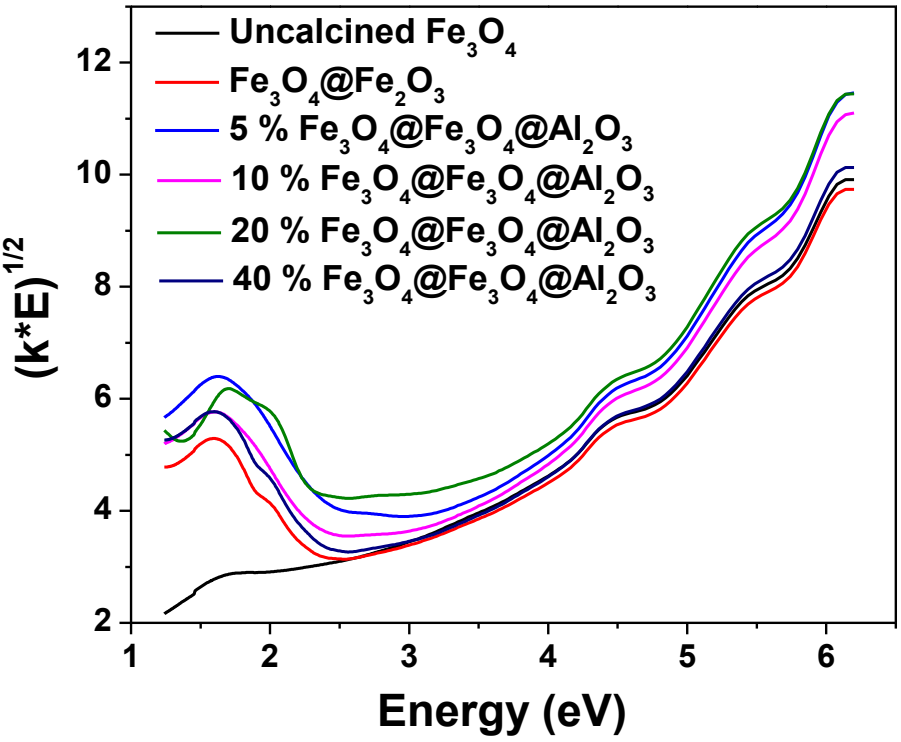

Figure 4.17: Plot (Kubelka Munk factor $(K=(1-R)^2/2R)$ * Energy)$^{1/2}$ vs Energy.

$(K \times E)^{1/2}$ vs E plots, obtained from diffuse reflectance spectra of 5, 10, 20, 40% Fe_3O_4@Fe_2O_3/Al_2O_3, Fe_3O_4@Fe_2O_3 and uncalcined Fe_3O_4 are plotted in Fig. 4.17 in order to understand the optical band gap of the materials.[102] Both Al_2O_3 and uncalcined Fe_3O_4 did not show any semiconducting band gap, which is a typical of these materials. Interestingly, the calcined Fe_3O_4 showed the band gap of ~ 2.4 eV, which is a characteristic of semiconducting Fe_2O_3. The band gap of ~ 2.4 eV is suitable for photocatalytic activity in visible light range (up to ~ 515 nm) of the electromagnetic spectrum. With increasing the loading of Fe_3O_4 over Al_2O_3 from 5 to 40%, the band gap decreased from 2.6 to 2.4 eV. The higher band gap observed with lower amount of loading could be attributed to the high dispersion of the active material, and the consequent quantum confinement[35]. However, in case of 40% Fe_3O_4

loading, the band gap was found to approach the value of the bulk. Additionally, in case of 40% Fe_3O_4/Al_2O_3 and also in calcined Fe_3O_4, the transitions corresponding to metal-ligand charge transfer, ligand-metal charge transfer and magnetically coupled Fe^{3+} adjacent site transition were also observed as a shoulder at ~ 1.9 eV.[112] This further confirms the surface oxidation of Fe_3O_4 to Fe_2O_3, which corroborates the observation from XPS and Raman. Due to the high dispersion and the lower amount of the active material, in case of 5 and 10% Fe_3O_4/Al_2O_3 the shoulder was obscured.

(ii) Photocatalysis

The efficiency of the synthesized photocatalytic materials towards Cr(VI) visible light (simulated) photoreduction was explored and the results are plotted in Fig. 4.18 (a). The complete photoreduction of 50 ppm Cr(VI) solution over $Fe_3O_4@Fe_2O_3$, which was used as a control photocatalyst, was observed in 35 minutes. The rate of photoreduction over $Fe_3O_4@Fe_2O_3$ calculated at 10% conversion of Cr(VI) was found to be 0.47 mol L^{-1} min^{-1} g^{-1}. Also, in case of 5% $Fe_3O_4@Fe_2O_3/Al_2O_3$ the complete photoreduction was achieved in 35 minutes, however the calculated rate of the photoreduction was found to be 10 mol L^{-1} min^{-1} g^{-1}. It has to be noted that the rate has been calculated with respect to the amount of active material. The high rate of photoreduction could be attributed to the high dispersion of $Fe_3O_4@Fe_2O_3$ over Al_2O_3. It should be noted that with 5% $Fe_3O_4@Fe_2O_3$ loading over Al_2O_3 support, the surface area of the composite has significantly increased than that of the individual components (*vide* Table 4.2). When the loading of $Fe_3O_4@Fe_2O_3$ was doubled (10% $Fe_3O_4@Fe_2O_3/Al_2O_3$), the complete photoreduction was achieved in 25 minutes and the rate was found to be 8.5 mol L^{-1} min^{-1} g^{-1}. In these two cases of 5 and 10% $Fe_3O_4@Fe_2O_3$ loading the rate was found to be comparable, however, with the increase in loading of the active material, the time required for the complete photoreduction was lowered. It is interesting to observe that the surface areas of these two materials are also comparable. When the loading was increased to 40% $Fe_3O_4@Fe_2O_3$ over Al_2O_3, the time required for complete photoreduction was similar to the bulk $Fe_3O_4@Fe_2O_3$, and the rate was calculated to be 1.3 mol L^{-1} min^{-1} g^{-1}. This shows that the rate of photoreduction of Cr(VI) decreased with higher loading of $Fe_3O_4@Fe_2O_3$. This could be due to formation of larger $Fe_3O_4@Fe_2O_3$ particles over Al_2O_3, which is also reflected from the surface area study. Interestingly, when 10% $Fe_3O_4@Fe_2O_3$-Al_2O_3 physical blend was used as a control, the rate of the reaction was very poor and found to be 1.7 mol L^{-1} min^{-1} g^{-1} and only 50% photoreduction of Cr(VI) was

observed in 45 minutes. This clearly emphasizes the significance of dispersing the active material over a support to enhance the photoreduction efficiency by manifold.

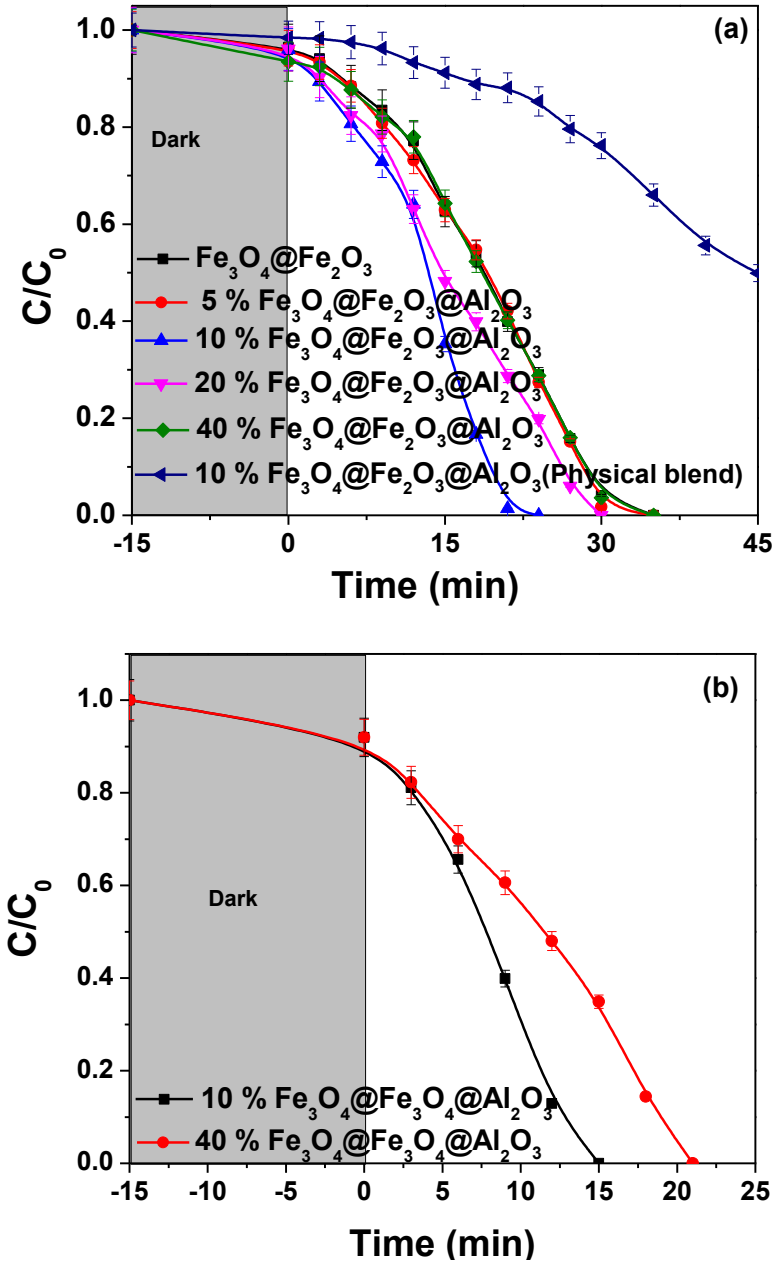

Figure 4.18: Photoreduction of Cr(VI) (a) simulated visible light, (b) direct sunlight.

For practical applicability of the synthesized materials, the Cr(VI) photoreduction was carried out under direct sunlight. For this, we have selected 10 and 40% Fe_3O_4@Fe_2O_3/Al_2O_3, which showed a similar trend as observed in simulated visible light study (Fig. 4.18 (b)). Interestingly, the Cr(VI) photoreduction was found be faster under direct sunlight than the simulated visible light. The rate calculated from 5% Fe_3O_4@Fe_2O_3/Al_2O_3 under direct sunlight was 14.2 mol L^{-1} min^{-1} g^{-1}. We speculate that this could be due to the presence of high energy UV radiation in the sun light. The required time for Cr(VI) photocatalytic

reduction was compared with the reported values in literature and presented in Table 4.4. For comparison, the light source, concentration of Cr(VI), hole scavengers, amount of photocatalyst, and required time for photoreduction are taken into account. It can be noted from the table that our catalyst outperformed the reported ones for complete Cr(VI) photoreduction.

Table 4.4: Comparison of literature on Cr(VI) photoreduction

Catalyst[Reference]	**Conc. of Cr (VI) (ppm)**	**Catalyst loading (gm/L)**	**Source**	**Hole Scavenger**	**Time (min)**	**Cr(VI) reduction (%)**
TiO_2 (P25)[24]	10	1	UV (14W)	---	300	70
ZnO[25]	50	3	UV (125W Hg lamp)	Methanol	75	90
TiO_2(P25)[26]	160	2	UV(450 W Xe lamp)	Formic acid	60	95
TiO_2(P25)[26]	160	2	UV(450 W Xe lamp)	Formic acid	60	90
ZnO[26]	160	2	UV(450 W Xe lamp)	Formic acid	60	60
CdS-RGO (1.5 wt%)[27]	10	1	Visible	---	240	92
ZnO-RGO (1.0 wt%)[28]	10	1	UV (500W Hg lamp)	---	60	96
Ti-PTA/TiO_2 nanowires[31]	160	1	UV (300W Hg lamp)	Isopropanol	50	90
α-Fe_2O_3/aMEGO (8 mol%)[44]	10	1	Visible (300W Xe lamp	---	160	95

2 mol% α-Fe_2O_3/Algerian clay[20]	100	1	Visible (200W W lamp)	Oxalic acid	300	80
2 mol % α-Fe_2O_3/Algerian clay[20]	100	1	Sunlight	Oxalic acid	40	100
CdS/α-Fe_2O_3 (20mol %)[43]	50	0.25	Visible (500W Xe lamp)	Formic acid	60	100
Fe_3O_4/ rGO[51]	25	0.5	Sunlight (3-6KWh/m^2/day)	---	25	96
ZrO_2/Fe_3O_4/Chitosan[53]	70	0.5	Sunlight	Ethanol	120	90
30 wt% TiO_2/Fe_3O_4[120]	10	0.3	UV (125W Hg lamp)	Oxalic acid	30	100
Ag@Fe_3O_4@SiO_2@TiO_2[121]	22.3	1	Sunlight	----	180	100
γ-Fe_2O_3-Alginate beads[122]	50	100	Sunlight	---	50	100
γ-Fe_2O_3-PVA-Alginate beads[123]	50	100	Sunlight	---	30	100
0.4mol% La^{+3}-TiO_2[124]	20	1	Sunlight (800W/m^2)	---	240	94
Carbon Modified-n-TiO_2[125]	3	2	Sunlight (1200W/m^2)	Phenol (e^- donor)	10	100
0.5wt % α-	10	2	Visible	Oxalic	20	99

Fe_2O_3/g-C_3N_4[126]			(300W Xe lamp)	acid		
α-FeOOH nanorods/RGO (3wt%)[127]	10	1	Visible (300W Xe lamp)	---	180	94
10% Fe_3O_4@Fe_2O_3/Al_2O_3 This work	50	0.3	Visible (250W)	Oxalic acid	25	100

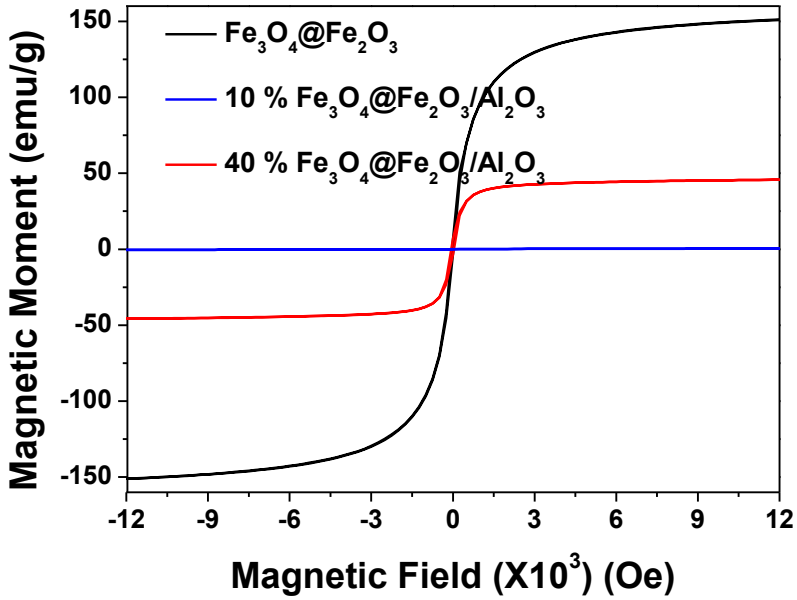

Figure 4.19: Magnetic hysteresis of Fe_3O_4@Fe_2O_3, 10% Fe_3O_4@Fe_2O_3/Al_2O_3 and 40% Fe_3O_4@Fe_2O_3/Al_2O_3.

To explore the possibility of magnetic recoverability, the saturation magnetization (M_s) of Fe_3O_4@Fe_2O_3, 10 and 40% Fe_3O_4@Fe_2O_3/Al_2O_3 was studied using vibrating sample magnetometer (Fig. 4.19). The Fe_3O_4@Fe_2O_3 was found to possess an M_s of 145 emu g^{-1}. In case of 10% Fe_3O_4@Fe_2O_3/Al_2O_3, the M_s approached a near zero value of 1.34 emu g^{-1}, which could be due to the reason that the Fe_3O_4 was highly dispersed over the support and thereby did not form any significant magnetic domain. In addition, Fe_3O_4 was also partially oxidized to non-magnetic Fe_2O_3. However, in case of 40% Fe_3O_4@Fe_2O_3/Al_2O_3 the M_s was retained at 110 emu g^{-1}. This prompts the material to be a magnetically recoverable catalyst and therefore further recyclability studies were carried out with 40% Fe_3O_4@Fe_2O_3/Al_2O_3.

Fig. 4.20 shows the recyclability of Cr(VI) photoreduction under simulated visible light up to 4 cycles. After every cycle, the catalyst was recovered using a magnet, washed with water and dried. There was a marginal decrease of rate from 1st cycle to the consecutive cycles, however, the overall performance was retained till four cycles.

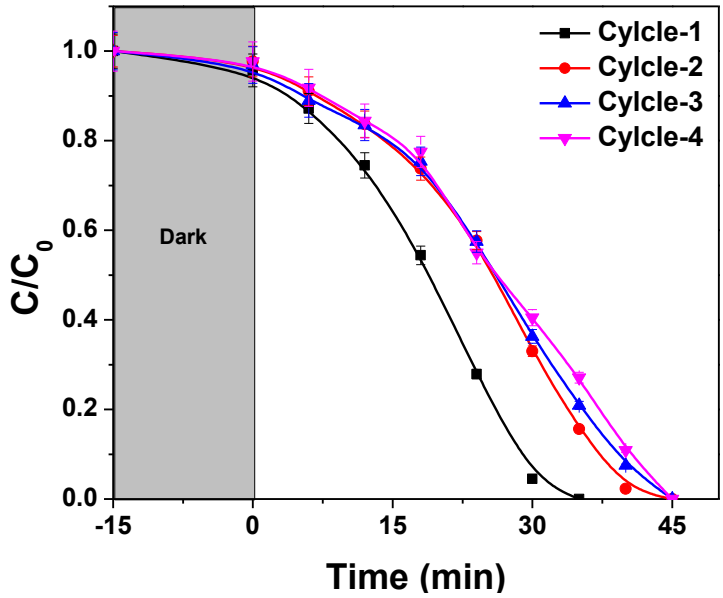

Figure 4.20: Recyclability of Cr(VI) photoreduction with 40% Fe_3O_4@Fe_2O_3/Al_2O_3 under simulated visible light.

4.4 WO_3

44.1 Methods

(i) Synthesis of WO_3

The acrylate-functionalized tungsten monomer was synthesized by complexation between tungsten (V) ethoxide (0.5 mmol) and MAEAA (1 mmol).[128] To this W-MAEAA complex, EDMA (0.75 mmol) as crosslinker and BPO (2-wt% with respect to MAEAA and EDMA) in acetone as free-radical initiator were added to constitute a polymerizable sol-gel precursor resin. This solution was subjected to heating at 120 ºC for 1 h to carry out free-radical polymerization, which yielded a yellow colored powder. The powder was grounded well and subjected to calcination at various temperatures such as 450, 650 and 850 ºC for 4 h in order to obtain WO_3 that are coded as WO_3-450, WO_3-650, and WO_3-850, respectively.

(ii) Photocatalytic studies

Photocatalytic reduction of Cr(VI) was performed by taking 100 mL of 20 ppm $K_2Cr_2O_7$ in 5 mM solution of oxalic acid at pH 3 with 30 mg of catalyst in a batch reactor housing a simulated visible light (HPS 250 visible lamp of 250 W), and the total maximum intensity of

the light was 250 mW cm^{-2}. The pH was maintained at 3, because the formation of neutral chromic acid, H_2CrO_4 takes place at lower pH and shows higher affinity towards positively charged WO_3 (PZC of WO_3 ~ 4 - 5).[24] The Cr(VI) concentration was monitored by UV-Vis spectrophotometer (JASCO V-650) after complexation with 1,5-diphenyl carbazide (DPC). The Cr(VI) reacts with DPC to produce a reddish purple colored Cr-diphenyl carbazone complex in acidic solution and quantified by measuring its absorbance at 540 nm.[129]

4.4.2 Results and Discussion

In a typical polymerizable sol–gel synthesis of metal oxides, a polymerizable functional group such as acrylate is functionalized on to the metal. Such metal complexes, depending on the chelating monomers, can exhibit enhanced stability against hydrolytic attack on the metal center.[128] These metal complexes along with the necessary cross-linker and polymerization initiator constitute the polymerizable sol–gel resin, which can be coated over flat substrates and ceramic supports. Polymerization followed by calcination of such systems would yield thin film and supported oxides.[102]

In this work, a stable W-MAEAA complex has been made by treating tungsten (V) ethoxide with MAEAA, the alkoxide otherwise is highly susceptible to hydrolysis. After mixing of MAEAA with tungsten (V) ethoxide, the resulting solution was warmed up to 50 °C for 10 min to induce chelation between the metal and the acetoacetate functionality. The results of IR analysis on the chelation of W-MAEAA complex and polymerization of sol-gel precursor resin are presented in Fig. 4.21. After chelation of tungsten with MAEAA, the carbon-carbon double bond stretching peak at 1635 cm^{-1} was observed to be broadened, while a new peak at ~1545 cm^{-1} appeared. These peaks are attributed to the carbon-oxygen double bond and carbon-carbon double bond vibrations of the chelate rings.[128] These stretching peaks were found to be present in the post-polymerization of the polymerizable precursor resin, indicating the stable chelation between the metal and the ligand even after polymerization.

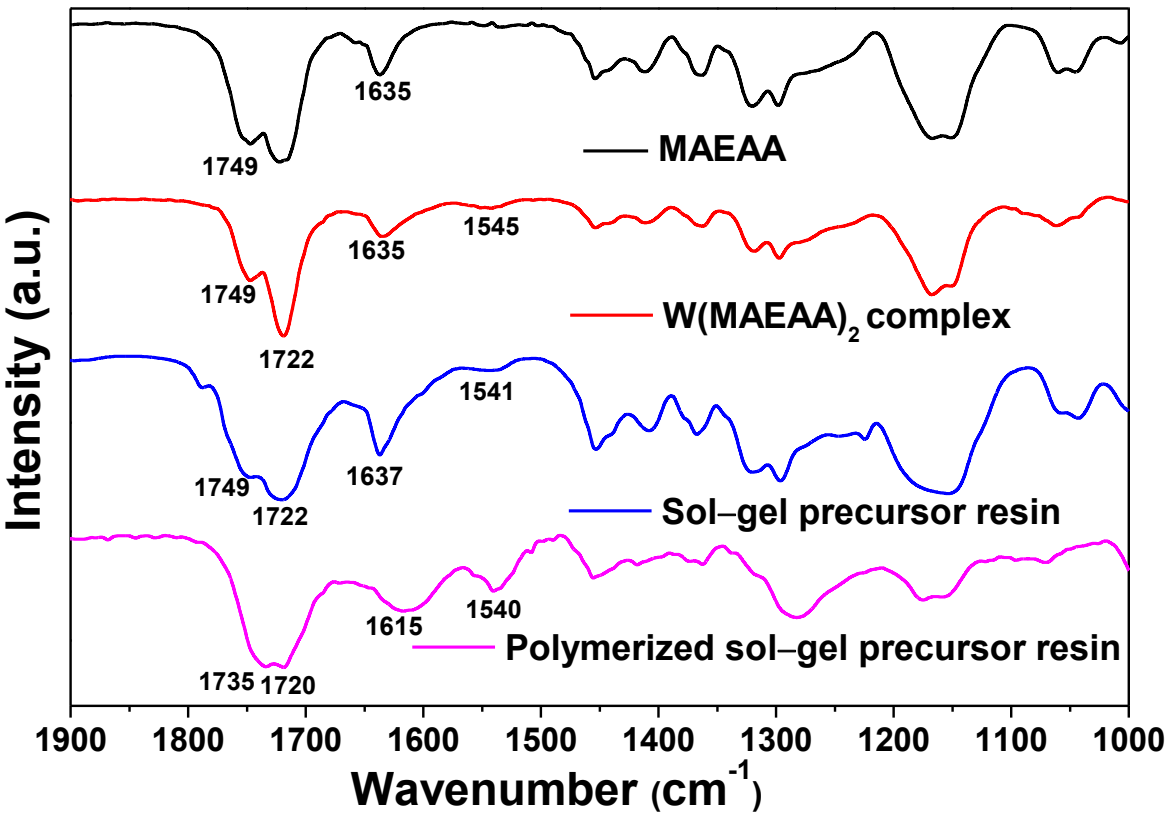

Figure 4.21: Infrared spectra of the polymerizable sol–gel precursor resin before and after subjecting to free-radical polymerization.

Thermal analysis of the sol–gel precursor resin was performed in order to understand the thermal degradation pattern (Fig. 4.22). The mass loss profile can be majorly divided into two parts. The first step mass loss up to 200 °C can be attributed to the lower molecular weight species such as solvent and uncured monomers, while the remaining mass loss can be attributed to the polymerized precursor resin. The analysis has revealed ~18% of residual WO_3 above ~550 °C. However, the isothermal TGA analysis at 450 °C showed complete loss of organics, indicating the feasibility of obtaining WO_3 even at lower calcination temperature.[130] The difference in the residual mass loss between the continuous and isothermal run experiments could be due to the different amounts of initial solvent and uncured monomers at the onset of the measurement. Based on the possibility of lower calcination temperature ascertained by the thermal analysis, the polymerized powder was calcined at 450 °C and subsequent higher temperatures of 650 and 850 ºC to synthesize WO_3.

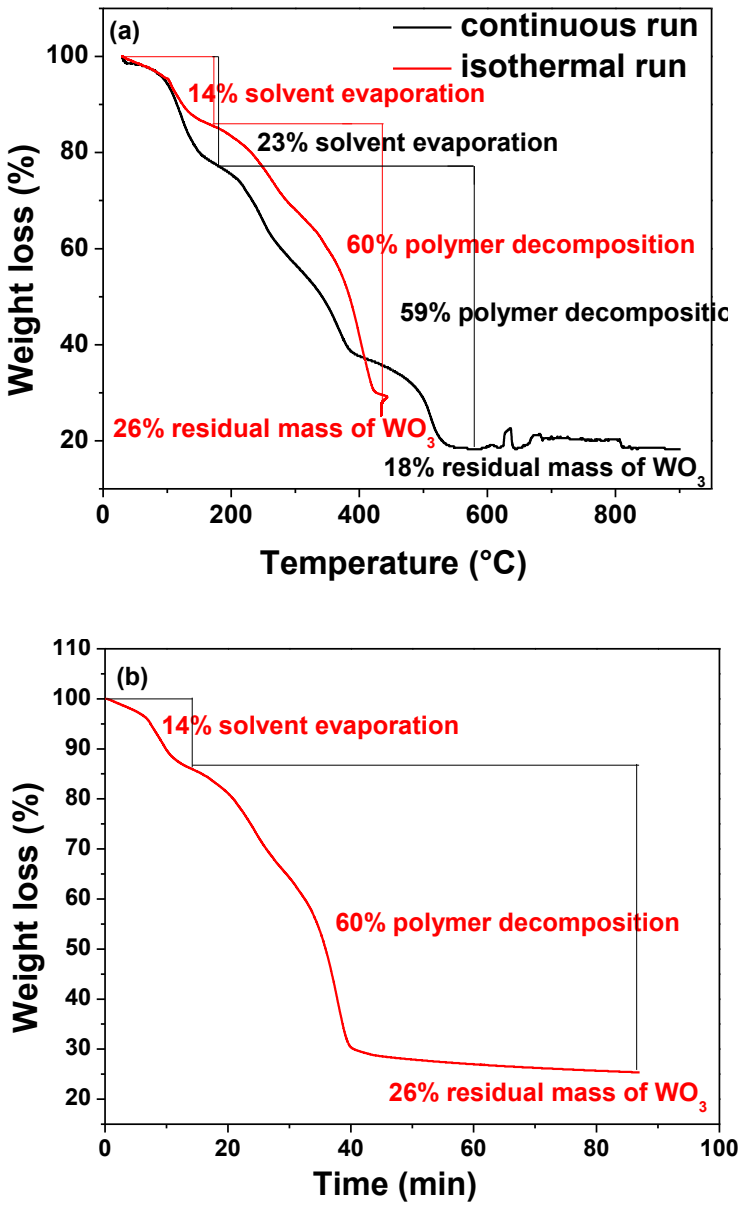

Figure 4.22: Thermogravimetric analyses of tungsten-containing sol–gel precursor resin. (a) Continuous and isothermal runs against temperature; For the isothermal case, the temperature was ramped up to 450 °C and the assembly was held at the same temperature for another 45 min. (b) Isothermal run shown against time.

Depending on the above experimental observations, we pictorially represented the synthetic strategy in Scheme 4.1. In the first step, W-MAEAA complex has been made by treating tungsten (V) ethoxide with MAEAA. The W-MAEAA complex was administered towards polymerization with the help of the cross linker (EDMA) and the free radical initiator (BPO in acetone). The calcination at 450 ^{o}C removed the organic part to form nano-crystalline WO_3.

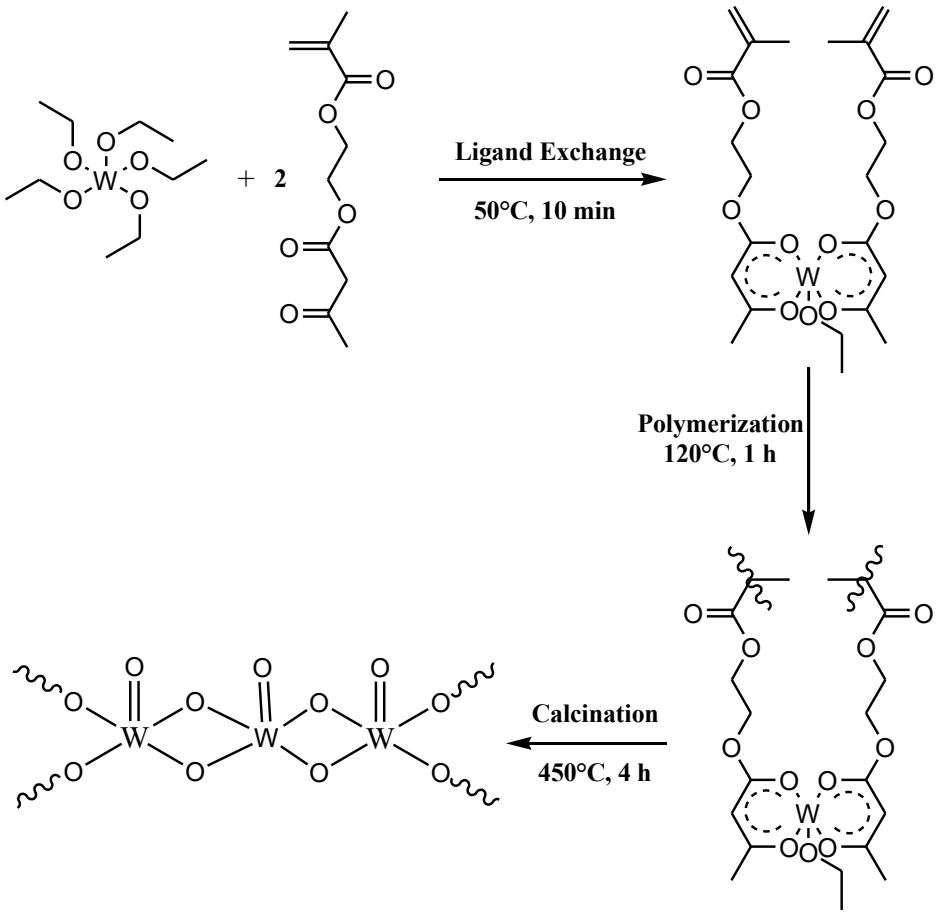

Scheme 4.1: Schematic representation of polymerization and calcination for the synthesis of WO_3 by polymerizable sol-gel approach.

The XRD patterns of WO_3 calcined at three different temperatures are shown in Fig. 4.23. The WO_3-450 crystallized in a pure phase without any impure peak. However, the peaks were found to be broad and overlapping. This clearly tells that the oxide material calcined at 450 °C is nano-crystalline in nature. When temperature was increased to 650 °C, the peaks were resolved further. However, the nano-crystallinity was partially retained. Further increase in temperature to 850 °C resulted in highly crystalline WO_3 with well resolved characteristic peaks (JCPDS #89-4476, space group $P2_1/n$).[131] The crystallite size for WO_3-450, WO_3-650 and WO_3-850 from Scherrer's formula was calculated with the help of (002) peak positioned at $2\theta = 23.1^o$ and was found to be 10.9, 15.9, and 70.2 nm, apparently showing the effect of calcination on the degree of crystallinity. These observations are in correlation with the solution-combustion synthesized nano-crystalline WO_3 reported in the literature.[79]

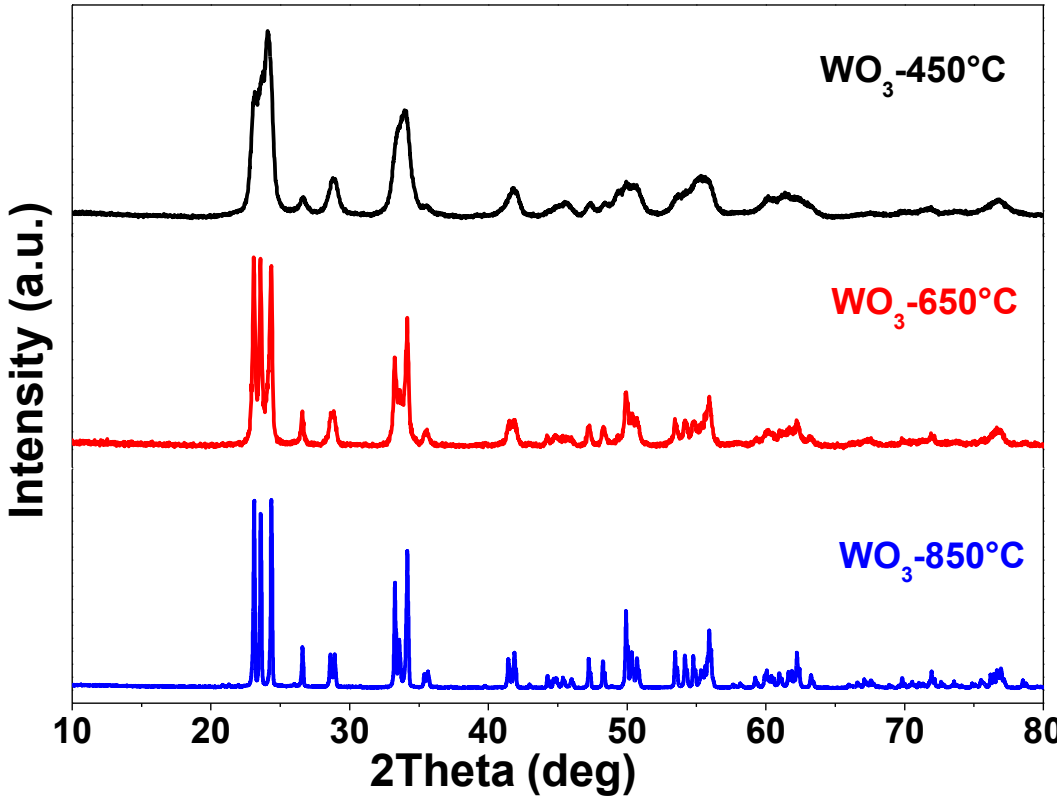

Figure 4.23: XRD patterns of WO_3 calcined at 450, 650, and 850 °C.

FE-SEM was employed to analyze the surface morphology of the synthesized catalysts and the results are given in Fig. 4.24. The WO_3-450 was found to be grainy microparticles having the sizes in the range of micrometer to few tens of micrometers. The agglomerates seem to be similar to other oxide compounds formed at comparatively low temperature, when grain intergrowth is not active.[132-134] A closer look at the particles revealed the surface to be aggregates of granular species possessing nano-crystalline domains. When the temperature of the synthesis was elevated to 650 °C, the resultant WO_3-650 was found to possess fused spherical-shaped nanoparticles. The fused grain morphology is typical when active grain interdiffusion is activated. Several examples could be found elsewhere.[135-137] However, the nanocrystalline domains were visible over the fused spheres. The WO_3-850 was found to be well-formed microcrystals that were polyhedral in shape. The faceted grains form when temperature is high enough for surface diffusion activation and surface atom ordering. Several examples could be found in the literature.[138-140] The characteristic temperatures are different for different oxides. Thus, the interpretation of the FE-SEM patterns could be drastically developed. A closer look at the particles revealed the surfaces and edges to be relatively smoother when compared to the WO_3-450 and WO_3-650. These results clearly revealed the increasing crystal growth with increase in calcination temperature.

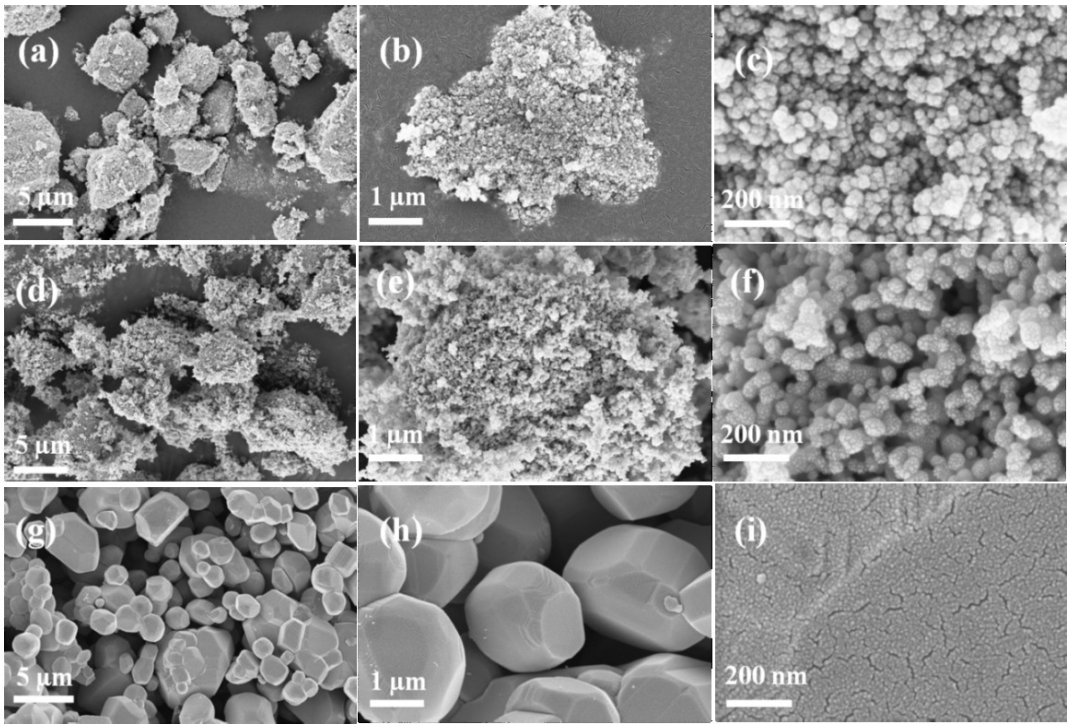

Figure 4.24: FE-SEM images of WO_3-450 (a-c), WO_3-650 (d-f), and WO_3-850 (g-i) at various magnifications.

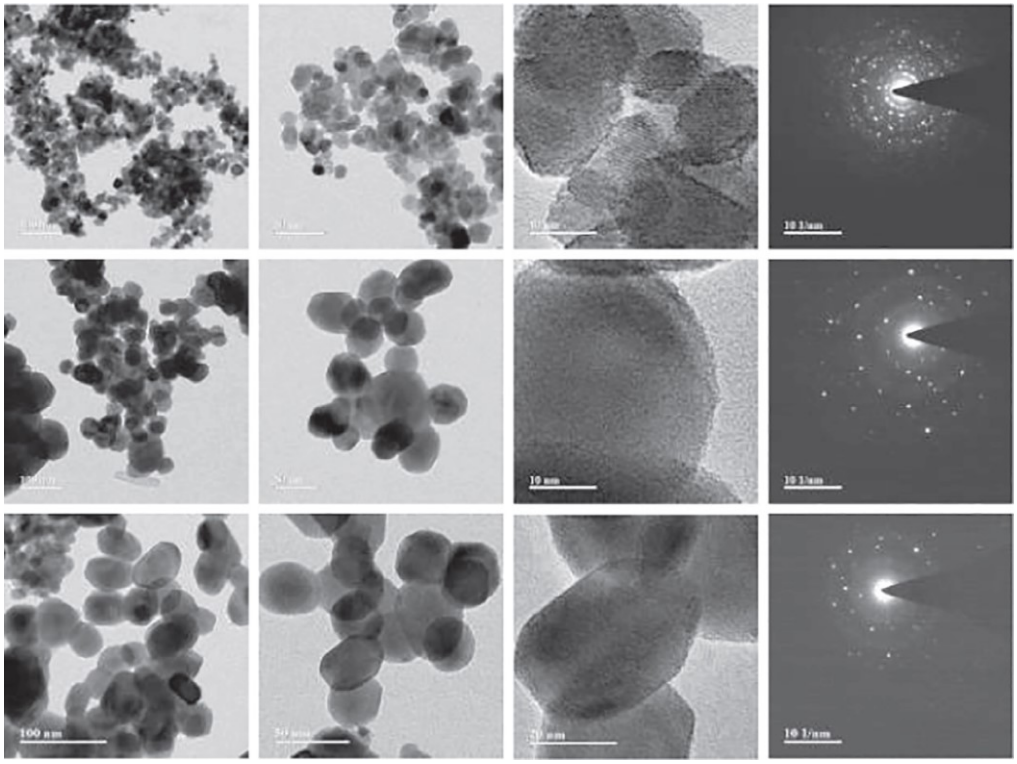

Figure 4.25: TEM images of WO3-450 (a–c), WO3-650 (e–g), and WO3-850 (i–k) at various magnifications and (d, h, l) are their corresponding SAED patterns.

The observation also been corroborated with the HR-TEM results shown in Fig. 4.25. The HR-TEM images shows the morphology of WO_3 nanoparticles, which clearly appeared in polyhedral shape with an average particle size of 10-20 nm for WO_3-450, and 30-50 nm for both WO_3-650 and WO_3-850. The lattice fringes were well resolved, indicating its crystalline nature. The Selected Area Electron Diffraction (SAED) patterns of WO_3 nanoparticles were shown in Fig. 5 (d), 5 (h), and 5 (l). The crystallinity was increased with increasing the calcination temperature from 450 to 850 °C. The lattice distance was found to be ~ 0.38 nm which corresponds to (002) plane of monoclinic WO_3.[141]

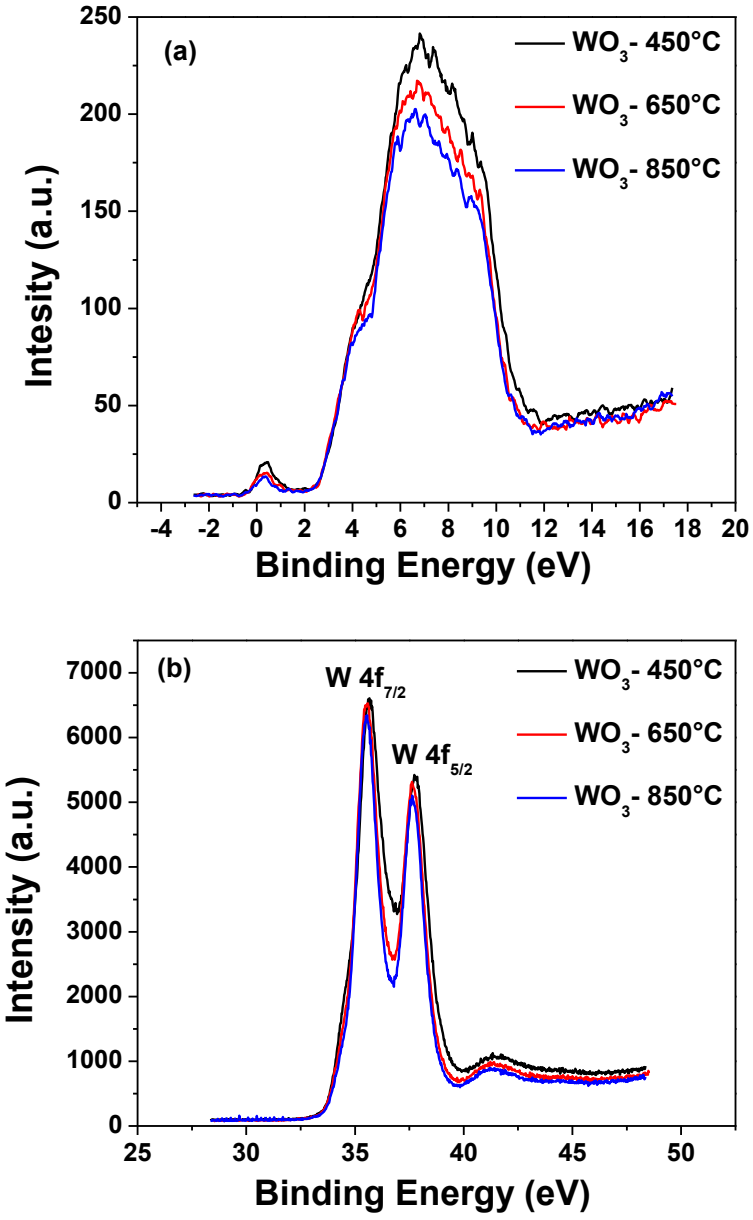

Figure 4.26: XPS analyses over WO_3-450, WO_3-650 and WO_3-850 revealing (a) valence band edge and (b) W 4*f* core level scan.

The electronic properties of WO_3 were studied by XPS and DRS. The valence band spectra of WO_3 calcined at three different temperatures are plotted in Fig. 4.26. For all practical purpose, the valance band spectra more or less coincide with the density of states. Apparently evident from Fig. 4.26 (a) that the valence bands of all the three WO_3 samples initiate at around 2.9 eV and also there is an additional sub-band near the Fermi level. The near-Fermi sub-band is believed due to the W 5d-like and W 6s-like states taking part in the formation of the shortened W-W bonds in the nonstoichiometric WO_3.[142,143] WO_3-450 has the highest intensity sub-band followed by WO_3-650, and WO_3-850. Though the all valence bands start at the same position, the valence band of WO_3-850 has a kink in the profile and the full width at half maxima of the valence band is more for WO_3-450 than that of WO_3-850. The higher intensity of near Fermi sub-band and wider valence band indicates that the oxygen stoichiometry in WO_3-450 could be lesser than 3, and calcination at higher temperatures may lead to the formation of stoichiometric WO_3. The core level spectra of W $4f_{7/2}$ and W $4f_{5/2}$ (Fig. 4.26 (b)) for all the three samples indicated W in +6 oxidation state and the profiles did not show any significant difference. It would be valuable to see also the O 1s core level recorded for the samples prepared at all three temperatures. Then, the binding energy difference method could be applied for comparison.[144,145]

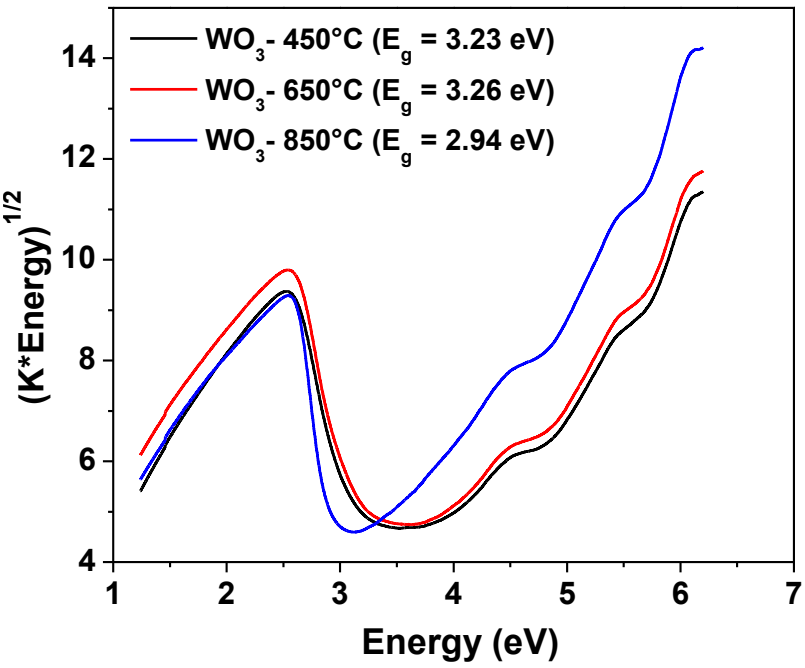

Figure 4.27: Kubelka-Munk plots derived from the diffuse reflectance spectra of WO_3 synthesized at 450, 650 and 850 °C. K represents the Kubelka-Munk factor, which is calculated by using $K = (1-R)^2/2R$, where R is the % reflectance.

The Optical band gaps of WO_3 calcined at different temperatures are obtained from the Kubelka-Munk method and the plots are shown in Fig. 4.27. The Kubelka–Munk method is based on the following equation $F(R) = \frac{(1-R)^2}{2R}$, where R is the % reflectance; F(R) is proportional to the molar extinction coefficient. This equation is usually applied to highly light scattering materials and absorbing particles in a matrix. By plotting $(F(R)\times h\nu)^n$ as a function of the energy in eV, the band gap of semiconductor particles can be obtained. As WO_3 is believed to be an indirect optical band gap semiconductor, the band gap was obtained by considering n = 2. Indirect band gap WO_3 also exhibits a long lifetime of photoexcited electrons. The optical band gaps of WO_3-450, WO_3-650 and WO_3-850 were found to be 3.1, 3.1, and 2.9 eV respectively. The higher band gap of the low temperature calcined oxides could be due to the quantum confinement of the excitons in the nano-crystalline domains, which corroborate the XRD and SEM analyses.

The BET surface area measurements of WO_3-450, WO_3-650 and WO_3-850 were recorded to follow the effect of calcination. As expected, there was a clear trend of decrease in the surface area with increase in calcination temperature. The WO_3-450 was found to possess a surface area of ~35 m^2/g, which decreased to 8.6 m^2/g for WO_3-650 and 1.6 m^2/g for WO_3-850. The enormous decrease in the surface area for WO_3-850 can be easily correlated with the FE-SEM and XRD analyses, which showed a tremendous growth in the WO_3 particles and crystallite size.

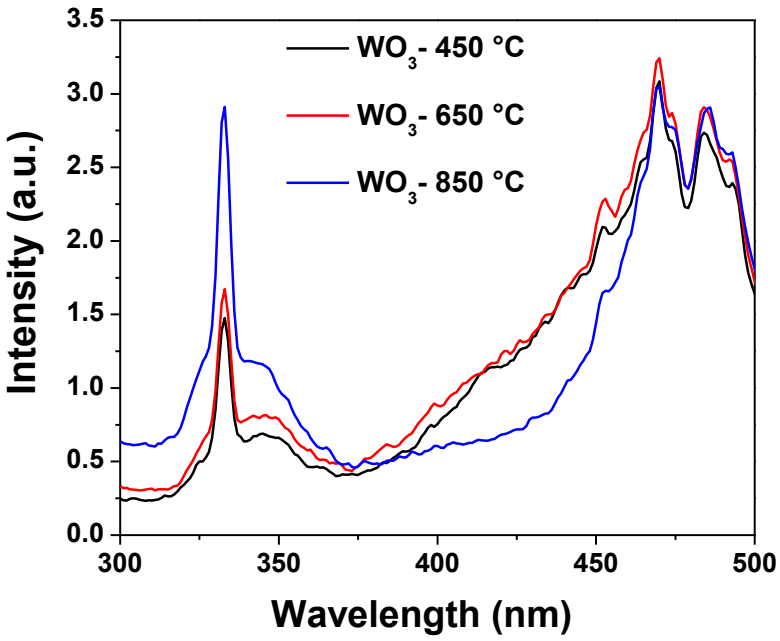

Figure 4.28: Photoluminescence spectra of WO_3 synthesized at 450, 650 and 850 °C. In all cases, the excitation was done at 270 nm.

Photoluminescence (PL) of the synthesized materials were recorded to obtain additional information on the electron-hole recombination process (Fig. 4.28). Generally, it is accepted that a higher PL efficiency would indicate higher electron-hole recombination and *vice versa*. Thus, for an efficient photocatalytic reaction, lower PL efficiency is desirable, as the recombination of the photogenerated electrons and holes would be less and, therefore, the carriers could be utilized for the reaction. In our study, the PL profiles of WO_3-450 and WO_3-650 were looking almost identical, indicating that there was no much difference in the electron-hole recombination process. However, the PL profile of WO_3-850 showed higher intensity than the other two materials in the near UV region, whilst a modestly lesser intensity in 400 to 450 nm range.

The synthesized nano-crystalline WO_3 was explored towards photoreduction of Cr(VI) as a function of calcination temperature (Fig. 4.29 (a)). Initially, till 15 min, the samples were stirred in dark to attain the adsorption-desorption equilibrium. Apparently, the adsorption rates of Cr(VI) over WO_3-450 and WO_3-650 were similar and higher compared to WO_3-850, which could be attributed to the difference in the surface area. After 120 min of visible light exposure, WO_3-450 and WO_3-650 could reduce up to 50 and 35% of Cr(VI) respectively, whereas WO_3-850 could reduce only 7% of Cr(VI). The rate of reduction calculated after 10 min of initiation of the reduction are 1.67×10^{-5}, 1.33×10^{-5} and 1.67×10^{-6} mol L^{-1} g^{-1} min^{-1} over WO_3-450, WO_3-650 and WO_3-850, respectively. To ascertain the role of photogenerated electrons and holes in the photocatalytic reduction of Cr(VI), the control experiments were done without a hole scavenger and with an electron scavenger (Fig. 4.29b). The hole scavenger is used in the photocatalytic reduction in order to scavenge the photogenerated hole and thereby making the electrons available for the reaction through minimizing the recombination. As seen in the figure, when the oxalic acid hole scavenger was not used in the reaction, the Cr(VI) photoreduction was insignificant, which clearly demonstrated the beneficial role of hole scavenger. With periodate electron scavenger, the Cr(VI) photoreduction was also insignificant, thus proving that the photogenerated electrons are responsible for the catalytic reduction of Cr(VI).

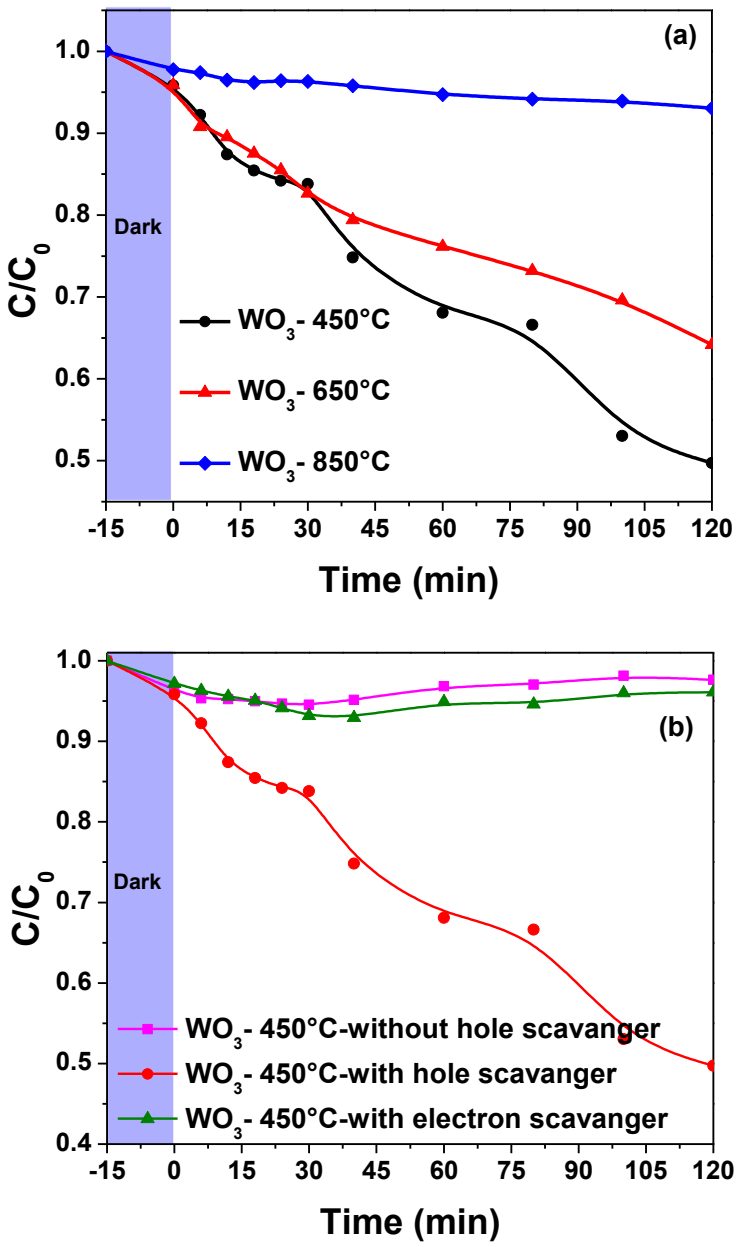

Figure 4.29: (a) Visible light photocatalytic reduction of Cr(VI) over WO_3-450, WO_3-650, and WO_3-850. (b) Role of hole scavenger and electron scavenger in the visible light photoreduction of Cr(VI) using WO_3-450.

The higher photocatalytic efficiency of WO_3-450 could be attributed to the following factors. First, WO_3-450 being nano-crystalline in nature found out from XRD, and electron microscope, possesses more catalytic active sites, which may help to catalytically outperform WO_3-650 and WO_3-850. This is also supported by the high surface area of WO_3-450. The oxygen non-stoichiometry in WO_3-450 could also be a beneficial factor for higher efficacy of the material. However, despite the optical band gap and visible range PL intensity of WO_3-850 were lower than that in WO_3-450, the higher photocatalytic activity of the latter

prompted us to take a closer view of the valence band of these materials. Therefore, with the help of valence band spectra obtained from XPS and the band gap obtained from DRS, we have constructed the conduction band edge of WO_3, and clubbed with the Cr(VI)/Cr(III) reduction potential, (1.33 V) with respect to NHE in Figure 10.[146,147] Upon irradiation of UV light, the electrons move from the VB of WO_3 to its CB leaving the holes behind. As the conduction band of WO_3 lies well above the reduction potential of Cr(VI)/Cr(III), the photogenerated electrons from the conduction band may easily hop down the hill to reduce Cr(VI). As evident from Figure 10, the over population of electrons at the edge of valence band maxima for WO_3-450 along with the higher intensity of the near-Fermi level sub band due to the oxygen non-stoichiometry can be attributed as the second aspect to the higher photocatalytic efficiency.

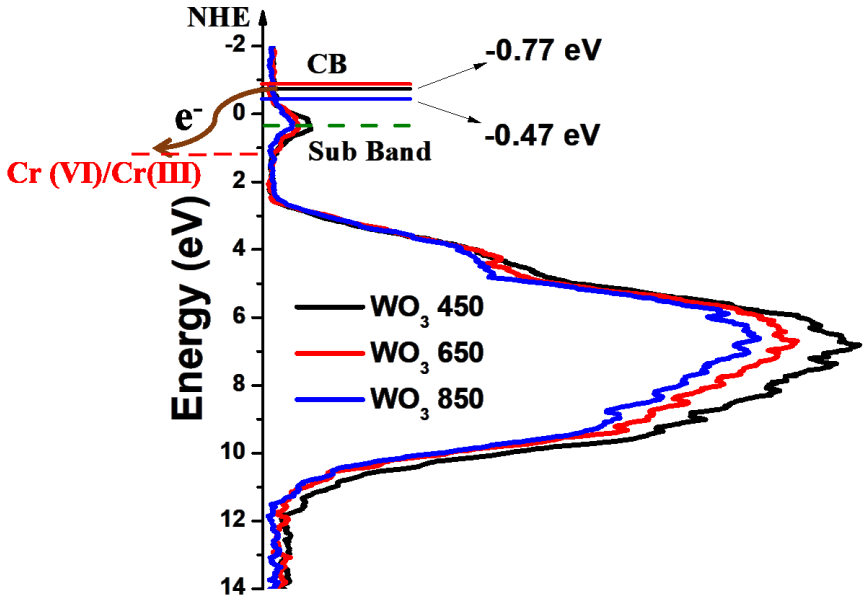

Figure 4.30: Schematic illustration of band energies of WO_3 obtained from XPS and DRS measurements with respect to the reduction potential of Cr(VI)/Cr(III).

4.5 Conclusions

TiO_2/Fe_3O_4 catalysts with various loading of TiO_2 were synthesized by the polymerizable sol–gel route. The XRD and SEM characterization revealed high dispersion of TiO_2 over Fe_3O_4. BET surface area measurements revealed increase in surface area with increase in TiO_2 loading. The surface of the Fe_3O_4 was found to be partially oxidized to Fe_2O_3 during the

calcination step. The diffuse reflectance spectra showed the semiconducting band gaps of TiO_2 and calcined Fe_3O_4. The TiO_2/Fe_3O_4 composite catalysts showed higher rate of photoreduction of Cr(VI) than the non-supported bulk TiO_2 as well as calcined Fe_3O_4. The photoreduction mechanism was probed by using hole as well as electron scavengers. The photocatalytic studies show that the anchoring of TiO_2 over Fe_3O_4 results in three-fold advantage. First, when the TiO_2 is anchored over Fe_3O_4, the dispersion of the active site was higher. This is a crucial one for achieving higher reaction rate. Second, the significant band overlap of TiO_2 and Fe_3O_4 helped decreasing the electron-hole recombination reaction, thus enhancing the photoreduction rate. Third, Fe_3O_4 being a magnetic nanoparticle, the magnetic recyclability of the catalyst was convenient.

To extend the photocatalytic activity towards visible light from UV light, the suitable $Fe_3O_4@Fe_2O_3/Al_2O_3$ catalysts were synthesized by the customized co-precipitation method. XRD and TEM analyses showed that the calcined Fe_3O_4 crystals, which were of inverse spinel structure, were highly dispersed over nano γ-Al_2O_3 support and the surface area of the composite was significantly higher than that of the individual components. XPS and Raman studies confirmed that Fe_3O_4 was partially oxidized to Fe_2O_3 due to calcination step during post co-precipitation synthesis. The Kubelka-Munk plot obtained from diffuse reflectance spectra showed the semiconducting band gap of Fe_2O_3, which was suitable for visible light photoreduction activity. The rate of Cr(VI) photoreduction over 5% $Fe_3O_4@Fe_2O_3/Al_2O_3$ was as high as 14.2 mol L^{-1} min^{-1} g^{-1} under direct sunlight. The 40% $Fe_3O_4@Fe_2O_3/Al_2O_3$ retained the magnetic property as in bulk Fe_3O_4 and the composite was magnetically recovered to show unaffected high rate of photoreduction till four cycles. The current investigation is a proof of concept towards enhanced environmental catalytic application of highly dispersed active semiconducting nanomaterials.

Another metal oxide suitable for the photocatalytic reduction of Cr (VI) in visible radiation is WO_3. Hence, WO_3 was synthesized at three different temperatures through a facile polymerizable sol–gel approach. The isothermal thermogravimetric analysis revealed that the calcination temperature to obtain nano-crystalline WO_3 can be as low as 450 °C. The XRD and FE-SEM analyses showed the presence of nano-crystalline domains in WO_3-450, whereas the raise in calcination temperature resulted in increased crystallinity. The diffuse reflectance analysis showed higher band gap value for WO_3-450 and WO_3-650 as compared to that of WO_3-850 due to the quantum confinement in the nano-crystalline domains. BET surface area measurements showed a dramatic decrease in the surface area with increasing

the calcination temperature from 450 to 850 °C. The XPS analyses revealed the presence of oxygen non-stoichiometry in the lower temperature calcined samples. The highest photocatalytic activity towards Cr(VI) reduction was reached with WO_3-450. The trend in the catalytic efficacy was explained in terms of nano-crystallinity, surface area, non-stoichiometry and valence band profile.

4.6 References

1. Lazar, M. A.; Varghese, S.; Nair, S. S., Photocatalytic water treatment by titanium dioxide: recent updates. *Catalysts* **2012,** *2* (4), 572-601.

2. Chong, M. N.; Jin, B.; Chow, C. W.; Saint, C., Recent developments in photocatalytic water treatment technology: a review. *Water Research* **2010,** *44* (10), 2997-3027.

3. Thavasi, V.; Singh, G.; Ramakrishna, S., Electrospun nanofibers in energy and environmental applications. *Energy & Environmental Science* **2008,** *1* (2), 205-221.

4. Choi, W. S.; Choi, I. S.; Lee, J. K.; Yoon, K. R., Preparation of fluorescein-functionalized electrospun fibers coated with TiO_2 and gold nanoparticles for visible-light-induced photocatalysis. *Materials Chemistry and Physics* **2015,** *163*, 213-218.

5. Bissen, M.; Frimmel, F. H., Arsenic—a review. Part II: oxidation of arsenic and its removal in water treatment. *Acta Hydrochimica et Hydrobiologica* **2003,** *31* (2), 97-107.

6. Matilainen, A.; Vepsalainen, M.; Sillanpaa, M., Natural organic matter removal by coagulation during drinking water treatment: a review. *Advances in Colloid and Iinterface Science* **2010,** *159* (2), 189-197.

7. Imamura, K.; Yoshikawa, T.; Hashimoto, K.; Kominami, H., Stoichiometric production of aminobenzenes and ketones by photocatalytic reduction of nitrobenzenes in secondary alcoholic suspension of titanium(IV)oxide under metal-free conditions. *Applied Catalysis B: Environmental* **2013,** *134*, 193-197.

8. Khin, M. M.; Nair, A. S.; Babu, V. J.; Murugan, R.; Ramakrishna, S., A review on nanomaterials for environmental remediation. *Energy & Environmental Science* **2012,** *5* (8), 8075-8109.

9. Mohan, D.; Pittman Jr, C. U., Activated carbons and low cost adsorbents for remediation of tri-and hexavalent chromium from water. *Journal of Hazardous Materials* **2006,** *137* (2), 762-811.

10. Ai, Z.; Cheng, Y.; Zhang, L.; Qiu, J., Efficient removal of Cr(VI) from aqueous solution with Fe@Fe_2O_3 core−shell nanowires. *Environmental Science & Technology* **2008,** *42* (18), 6955-6960.

11. Ali, I., New generation adsorbents for water treatment. *Chemical Reviews* **2012,** *112* (10), 5073-5091.

12. Guo, X.; Fei, G. T.; Su, H.; De Zhang, L., High-performance and reproducible polyaniline nanowire/tubes for removal of Cr(VI) in aqueous solution. *The Journal of Physical Chemistry C* **2011,** *115* (5), 1608-1613.

13. Ke, Z.; Huang, Q.; Zhang, H.; Yu, Z., Reduction and removal of aqueous Cr(VI) by glow discharge plasma at the gas–solution interface. *Environmental Science & Technology* **2011,** *45* (18), 7841-7847.

14. Gaberell, M.; Chin, Y. P.; Hug, S. J.; Sulzberger, B., Role of dissolved organic matter composition on the photoreduction of Cr(VI) to Cr(III) in the presence of iron. *Environmental Science & Technology* **2003,** *37* (19), 4403-4409.

15. Marouani, N.; Tebourbi, O.; Mokni, M.; Yacoubi, M. T.; Sakly, M.; Benkhalifa, M.; Rhouma, K. B., Embryotoxicity and fetotoxicity following intraperitoneal administrations of hexavalent chromium to pregnant rats. *Zygote* **2011,** *19* (3), 229-235.

16. Samuel, J. B.; Stanley, J. A.; Sekar, P.; Princess, R. A.; Sebastian, M. S.; Aruldhas, M. M., Persistent hexavalent chromium exposure impaired the pubertal development and ovarian histoarchitecture in wistar rat offspring. *Environmental Toxicology* **2014,** *29* (7), 814-828.

17. Blowes, D. W.; Ptacek, C. J.; Jambor, J. L., In-situ remediation of Cr(VI)-contaminated groundwater using permeable reactive walls: laboratory studies. *Environmental Science & Technology* **1997,** *31* (12), 3348-3357.

18. Weckhuysen, B. M.; Wachs, I. E.; Schoonheydt, R. A., Surface chemistry and spectroscopy of chromium in inorganic oxides. *Chemical Reviews* **1996,** *96* (8), 3327-3350.

19. Dong, G.; Zhang, L., Synthesis and enhanced Cr(VI) photoreduction property of formate anion containing graphitic carbon nitride. *The Journal of Physical Chemistry C* **2013,** *117* (8), 4062-4068.

20. Mekatel, H.; Amokrane, S.; Bellal, B.; Trari, M.; Nibou, D., Photocatalytic reduction of Cr(VI) on nanosized Fe_2O_3 supported on natural algerian clay: characteristics, kinetic and thermodynamic study. *Chemical Engineering Journal* **2012,** *200*, 611-618.

21. Yang, C.; Choi, C. H.; Lee, C. S.; Yi, H., A facile synthesis–fabrication strategy for integration of catalytically active viral-palladium nanostructures into polymeric hydrogel microparticles via replica molding. *ACS Nano* **2013,** *7* (6), 5032-5044.

22. Yang, C.; Meldon, J. H.; Lee, B.; Yi, H., Investigation on the catalytic reduction kinetics of hexavalent chromium by viral-templated palladium nanocatalysts. *Catalysis Today* **2014,** *233*, 108-116.

23. Cappelletti, G.; Bianchi, C.; Ardizzone, S., Nano-titania assisted photoreduction of Cr(VI): the role of the different TiO_2 polymorphs. *Applied Catalysis B: Environmental* **2008,** *78* (3-4), 193-201.

24. Ku, Y.; Jung, I. L., Photocatalytic reduction of Cr(VI) in aqueous solutions by UV irradiation with the presence of titanium dioxide. *Water Research* **2001,** *35* (1), 135-142.

25. Chakrabarti, S.; Chaudhuri, B.; Bhattacharjee, S.; Ray, A. K.; Dutta, B. K., Photo-reduction of hexavalent chromium in aqueous solution in the presence of zinc oxide as semiconductor catalyst. *Chemical Engineering Journal* **2009,** *153* (1-3), 86-93.

26. Wang, X.; Pehkonen, S.; Ray, A. K., Removal of aqueous Cr(VI) by a combination of photocatalytic reduction and coprecipitation. *Industrial & Engineering Chemistry Research* **2004,** *43* (7), 1665-1672.

27. Liu, X.; Pan, L.; Lv, T.; Zhu, G.; Sun, Z.; Sun, C., Microwave-assisted synthesis of CdS–reduced graphene oxide composites for photocatalytic reduction of Cr(VI). *Chemical Communications* **2011,** *47* (43), 11984-11986.

28. Liu, X.; Pan, L.; Zhao, Q.; Lv, T.; Zhu, G.; Chen, T.; Lu, T.; Sun, Z.; Sun, C., UV-assisted photocatalytic synthesis of ZnO–reduced graphene oxide composites with enhanced photocatalytic activity in reduction of Cr(VI). *Chemical Engineering Journal* **2012,** *183*, 238-243.

29. Khalil, L.; Mourad, W.; Rophael, M., Photocatalytic reduction of environmental pollutant Cr(VI) over some semiconductors under UV/visible light illumination. *Applied Catalysis B: Environmental* **1998,** *17* (3), 267-273.

30. Yang, L.; Xiao, Y.; Liu, S.; Li, Y.; Cai, Q.; Luo, S.; Zeng, G., Photocatalytic reduction of Cr(VI) on WO_3 doped long TiO_2 nanotube arrays in the presence of citric acid. *Applied Catalysis B: Environmental* **2010,** *94* (1-2), 142-149.

31. Zhang, D.; Li, X.; Tan, H.; Zhang, G.; Zhao, Z.; Shi, H.; Zhang, L.; Yu, W.; Sun, Z., Photocatalytic reduction of Cr(VI) by polyoxometalates/TiO_2 electrospun nanofiber composites. *RSC Advances* **2014,** *4* (84), 44322-44326.

32. Wee, L. H.; Meledina, M.; Turner, S.; Custers, K.; Kerkhofs, S.; Sree, S.; Gobechiya, E.; Kirschhock, C.; Van Tendeloo, G.; Martens, J., Anatase TiO_2 nanoparticle coating on porous COK-12 platelets as highly active and reusable photocatalysts. *RSC Advances* **2016,** *6* (52), 46678-46685.

33. Mahanta, D.; Manna, U.; Madras, G.; Patil, S., Multilayer self-assembly of TiO_2 nanoparticles and polyaniline-grafted-chitosan copolymer (CPANI) for photocatalysis. *ACS Applied Materials & Interfaces* **2010,** *3* (1), 84-92.

34. He, Z.; Cai, Q.; Wu, M.; Shi, Y.; Fang, H.; Li, L.; Chen, J.; Chen, J.; Song, S., Photocatalytic reduction of Cr(VI) in an aqueous suspension of surface-fluorinated anatase TiO_2 nanosheets with exposed {001} facets. *Industrial & Engineering Chemistry Research* **2013,** *52* (28), 9556-9565.

35. Nagarjuna, R.; Roy, S.; Ganesan, R., Polymerizable sol–gel precursor mediated synthesis of TiO_2 supported zeolite-4A and its photodegradation of methylene blue. *Microporous and Mesoporous Materials* **2015,** *211*, 1-8.

36. Challagulla, S.; Nagarjuna, R.; Ganesan, R.; Roy, S., Role of solvents on photocatalytic reduction of nitroarenes by sol–gel synthesized TiO_2/zeolite-4A. *Journal of Porous Materials* **2015,** *22* (4), 1105-1110.

37. Nagarjuna, R.; Challagulla, S.; Alla, N.; Ganesan, R.; Roy, S., Synthesis and characterization of reduced-graphene oxide/TiO_2/zeolite-4A: A bifunctional nanocomposite for abatement of methylene blue. *Materials & Design* **2015,** *86*, 621-626.

38. Polshettiwar, V.; Varma, R. S., Green chemistry by nano-catalysis. *Green Chemistry* **2010,** *12* (5), 743-754.

39. Gelbrich, T.; Feyen, M.; Schmidt, A. M., Magnetic thermoresponsive core−shell nanoparticles. *Macromolecules* **2006,** *39* (9), 3469-3472.

40. Baig, R. N.; Varma, R. S., Magnetically retrievable catalysts for organic synthesis. *Chemical Communications* **2013,** *49* (8), 752-770.

41. Yang, X.; Chen, W.; Huang, J.; Zhou, Y.; Zhu, Y.; Li, C., Rapid degradation of methylene blue in a novel heterogeneous Fe_3O_4@rGO@TiO_2-catalyzed photo-fenton system. *Scientific Reports* **2015,** *5*, 10632.

42. Wu, W.; Jiang, C.; Roy, V. A., Recent progress in magnetic iron oxide–semiconductor composite nanomaterials as promising photocatalysts. *Nanoscale* **2015,** *7* (1), 38-58.

43. Zhang, S.; Xu, W.; Zeng, M.; Li, J.; Xu, J.; Wang, X., Hierarchically grown CdS/α-Fe_2O_3 heterojunction nanocomposites with enhanced visible-light-driven photocatalytic performance. *Dalton Transactions* **2013,** *42* (37), 13417-13424.

44. Du, Y.; Tao, Z.; Guan, J.; Sun, Z.; Zeng, W.; Wen, P.; Ni, K.; Ye, J.; Yang, S.; Du, P., Microwave-assisted synthesis of hematite/activated graphene composites with superior performance for photocatalytic reduction of Cr(VI). *RSC Advances* **2015,** *5* (99), 81438-81444.

45. Wee, L. H.; Meledina, M.; Turner, S.; Custers, K.; Kerkhofs, S.; Van Tendeloo, G.; Martens, J., Hematite iron oxide nanorod patterning inside COK-12 mesochannels as an efficient visible light photocatalyst. *Journal of Materials Chemistry A* **2015,** *3* (39), 19884-19891.

46. Smith, Y. R.; Raj, K. J. A.; Subramanian, V. R.; Viswanathan, B., Sulfated Fe_2O_3–TiO_2 synthesized from ilmenite ore: a visible light active photocatalyst. *Colloids and Surfaces A: Physicochemical and Engineering Aspects* **2010,** *367* (1-3), 140-147.

47. McDonald, K. J.; Choi, K. S., Synthesis and photoelectrochemical properties of Fe_2O_3/$ZnFe_2O_4$ composite photoanodes for use in solar water oxidation. *Chemistry of Materials* **2011,** *23* (21), 4863-4869.

48. Zhong, D. K.; Sun, J.; Inumaru, H.; Gamelin, D. R., Solar water oxidation by composite catalyst/α-Fe_2O_3 photoanodes. *Journal of the American Chemical Society* **2009,** *131* (17), 6086-6087.

49. Xu, Y.; Schoonen, M. A., The absolute energy positions of conduction and valence bands of selected semiconducting minerals. *American Mineralogist* **2000,** *85* (3-4), 543-556.

50. Zhang, W.; Chen, Y., Experimental determination of conduction and valence bands of semiconductor nanoparticles using Kelvin probe force microscopy. *Journal of Nanoparticle Research* **2013,** *15* (1), 1334.

51. Boruah, P. K.; Borthakur, P.; Darabdhara, G.; Kamaja, C. K.; Karbhal, I.; Shelke, M. V.; Phukan, P.; Saikia, D.; Das, M. R., Sunlight assisted degradation of dye molecules and reduction of toxic Cr(VI) in aqueous medium using magnetically recoverable Fe_3O_4/reduced graphene oxide nanocomposite. *RSC Advances* **2016,** *6* (13), 11049-11063.

52. Hudson, R.; Feng, Y.; Varma, R. S.; Moores, A., Bare magnetic nanoparticles: sustainable synthesis and applications in catalytic organic transformations. *Green Chemistry* **2014,** *16* (10), 4493-4505.

53. Kumar, A.; Guo, C.; Sharma, G.; Pathania, D.; Naushad, M.; Kalia, S.; Dhiman, P., Magnetically recoverable ZrO_2/Fe_3O_4/chitosan nanomaterials for enhanced sunlight driven photoreduction of carcinogenic Cr(VI) and dechlorination & mineralization of 4-chlorophenol from simulated waste water. *RSC Advances* **2016,** *6* (16), 13251-13263.

54. Sharma, A.; Lee, B. K., Rapid photo-degradation of 2-chlorophenol under visible light irradiation using cobalt oxide-loaded TiO_2/reduced graphene oxide nanocomposite from aqueous media. *Journal of Environmental Management* **2016,** *165*, 1-10.

55. Sivula, K.; Formal, F. L.; Gratzel, M., WO_3−Fe_2O_3 photoanodes for water splitting: A host scaffold, guest absorber approach. *Chemistry of Materials* **2009,** *21* (13), 2862-2867.

56. Wang, F.; Di Valentin, C.; Pacchioni, G., Rational band gap engineering of WO_3 photocatalyst for visible light water splitting. *ChemCatChem* **2012,** *4* (4), 476-478.

57. Vattikuti, S. P.; Byon, C.; Ngo, I. L., Highly crystalline multi-layered WO_3 sheets for photodegradation of Congo red under visible light irradiation. *Materials Research Bulletin* **2016,** *84*, 288-297.

58. Xin, G.; Guo, W.; Ma, T., Effect of annealing temperature on the photocatalytic activity of WO_3 for O_2 evolution. *Applied Surface Science* **2009,** *256* (1), 165-169.

59. Woodward, P.; Sleight, A.; Vogt, T., Ferroelectric tungsten trioxide. *Journal of Solid State Chemistry* **1997,** *131* (1), 9-17.

60. Vogt, T.; Woodward, P. M.; Hunter, B. A., The high-temperature phases of WO_3. *Journal of Solid State Chemistry* **1999,** *144* (1), 209-215.

61. Magneli, A., Crystal structure studies on beta-tungsten oxide. *Arkiv For Kemi* **1950,** *1* (6), 513-523.

62. Sundberg, M.; Tilley, R., An electron microscope study of some nonstoichiometric tungsten oxides. *Journal of Solid State Chemistry* **1974,** *11* (2), 150-160.

63. De Angelis, B.; Schiavello, M., X-ray photoelectron spectroscopy study of nonstoichiometric tungsten oxides. *Journal of Solid State Chemistry* **1977,** *21* (1), 67-72.

64. Iguchi, E.; Salje, E.; Tilley, R., Polaron interaction energies in reduced tungsten trioxide. *Journal of Solid State Chemistry* **1981,** *38* (3), 342-359.

65. Braun, A.; Erat, S.; Zhang, X.; Chen, Q.; Huang, T. W.; Aksoy, F.; Lohnert, R.; Liu, Z.; Mao, S. S.; Graule, T., Surface and bulk oxygen vacancy defect states near the fermi level in 125 nm $WO_{3-\delta}/TiO_2$ (110) films: a resonant valence band photoemission spectroscopy study. *The Journal of Physical Chemistry C* **2011,** *115* (33), 16411-16417.

66. Kudo, T.; Oi, J.; Kishimoto, A.; Hiratani, M., Three kinds of framework structures of corner-sharing WO_6 octahedra derived from peroxo-polytungstates as a precursor. *Materials Research Bulletin* **1991,** *26* (8), 779-787.

67. Siciliano, T.; Tepore, A.; Micocci, G.; Serra, A.; Manno, D.; Filippo, E., WO_3 gas sensors prepared by thermal oxidization of tungsten. *Sensors and Actuators B: Chemical* **2008,** *133* (1), 321-326.

68. Gao, G.; Zhang, Z.; Wu, G.; Jin, X., Engineering of coloration responses of porous WO_3 gasochromic films by ultraviolet irradiation. *RSC Advances* **2014,** *4* (57), 30300-30307.

69. Kuroki, T.; Matsushima, Y.; Unuma, H., Electrochromic response of WO_3 and WO_3-TiO_2 thin films prepared from water-soluble precursors and a block copolymer template. *Journal of Asian Ceramic Societies* **2016,** *4* (4), 367-370.

70. Dalavi, D. S.; Devan, R. S.; Patil, R. A.; Patil, R. S.; Ma, Y.-R.; Sadale, S. B.; Kim, I.; Kim, J. H.; Patil, P. S., Efficient electrochromic performance of nanoparticulate WO_3 thin films. *Journal of Materials Chemistry C* **2013,** *1* (23), 3722-3728.

71. Ng, K. H.; Minggu, L. J.; Mark-Lee, W. F.; Arifin, K.; Jumali, M. H. H.; Kassim, M. B., A new method for the fabrication of a bilayer WO_3/Fe_2O_3 photoelectrode for enhanced photoelectrochemical performance. *Materials Research Bulletin* **2018,** *98*, 47-52.

72. Miseki, Y.; Sayama, K., High-efficiency water oxidation and energy storage utilizing various reversible redox mediators under visible light over surface-modified WO_3. *RSC Advances* **2014,** *4* (16), 8308-8316.

73. Lin, J.; Hu, P.; Zhang, Y.; Fan, M.; He, Z.; Ngaw, C. K.; Loo, J. S. C.; Liao, D.; Tan, T. T. Y., Understanding the photoelectrochemical properties of a reduced graphene oxide–WO_3 heterojunction photoanode for efficient solar-light-driven overall water splitting. *RSC Advances* **2013,** *3* (24), 9330-9336.

74. Szilagyi, I. M.; Forizs, B.; Rosseler, O.; Szegedi, A.; Nemeth, P.; Kiraly, P.; Tarkanyi, G.; Vajna, B.; Varga-Josepovits, K.; Laszlo, K., WO_3 photocatalysts: Influence of structure and composition. *Journal of catalysis* **2012,** *294*, 119-127.

75. Supothina, S.; Seeharaj, P.; Yoriya, S.; Sriyudthsak, M., Synthesis of tungsten oxide nanoparticles by acid precipitation method. *Ceramics International* **2007,** *33* (6), 931-936.

76. Santato, C.; Odziemkowski, M.; Ulmann, M.; Augustynski, J., Crystallographically oriented mesoporous WO_3 films: synthesis, characterization, and applications. *Journal of the American Chemical Society* **2001,** *123* (43), 10639-10649.

77. Song, X.; Zhao, Y.; Zheng, Y., Hydrothermal synthesis of tungsten oxide nanobelts. *Materials Letters* **2006,** *60* (28), 3405-3408.

78. Joshi, U. A.; Darwent, J. R.; Yiu, H. H.; Rosseinsky, M. J., The effect of platinum on the performance of WO_3 nanocrystal photocatalysts for the oxidation of methyl orange and iso-propanol. *Journal of Chemical Technology & Biotechnology* **2011,** *86* (8), 1018-1023.

79. Morales, W.; Cason, M.; Aina, O.; de Tacconi, N. R.; Rajeshwar, K., Combustion synthesis and characterization of nanocrystalline WO_3. *Journal of the American Chemical Society* **2008,** *130* (20), 6318-6319.

80. Natile, M. M.; Tomaello, F.; Glisenti, A., WO_3/CeO_2 nanocomposite powders: synthesis, characterization, and reactivity. *Chemistry of Materials* **2006,** *18* (14), 3270-3280.

81. Atuchin, V.; Troitskaia, I.; Khyzhun, O. Y.; Bekenev, V.; Solonin, Y. M. In *Electronic structure of h-WO_3 and $CuWO_4$ nanocrystals, harvesting materials for renewable energy systems and functional devices*, *Applied Mechanics and Materials, Trans Tech Publ:* **2012,** 2188-2193.

82. Szekely, I.; Kovacs, G.; Baia, L.; Danciu, V.; Pap, Z., Synthesis of shape-tailored WO_3 micro-/nanocrystals and the photocatalytic activity of WO_3/TiO_2 composites. *Materials* **2016,** *9* (4), 258.

83. Nayak, A. K.; Lee, S.; Choi, Y. I.; Yoon, H. J.; Sohn, Y.; Pradhan, D., Crystal phase and size-controlled synthesis of tungsten trioxide hydrate nanoplates at room temperature: enhanced Cr(VI) photoreduction and methylene blue adsorption properties. *ACS Sustainable Chemistry & Engineering* **2017,** *5* (3), 2741-2750.

84. Nagy, D.; Nagy, D.; Szilagyi, I. M.; Fan, X., Effect of the morphology and phases of WO_3 nanocrystals on their photocatalytic efficiency. *RSC Advances* **2016,** *6* (40), 33743-33754.

85. Long, H.; Zeng, W.; Zhang, H., Synthesis of WO_3 and its gas sensing: a review. *Journal of Materials Science: Materials in Electronics* **2015,** *26* (7), 4698-4707.

86. Zheng, H.; Ou, J. Z.; Strano, M. S.; Kaner, R. B.; Mitchell, A.; Kalantar-zadeh, K., Nanostructured tungsten oxide–properties, synthesis, and applications. *Advanced Functional Materials* **2011,** *21* (12), 2175-2196.

87. Lu, X.; Liu, X.; Zhang, W.; Wang, C.; Wei, Y., Large-scale synthesis of tungsten oxide nanofibers by electrospinning. *Journal of Colloid and Interface Science* **2006,** *298* (2), 996-999.

88. Wang, J.; Khoo, E.; Lee, P. S.; Ma, J., Synthesis, assembly, and electrochromic properties of uniform crystalline WO_3 nanorods. *The Journal of Physical Chemistry C* **2008,** *112* (37), 14306-14312.

89. Le Houx, N.; Pourroy, G.; Camerel, F.; Comet, M.; Spitzer, D., WO_3 nanoparticles in the 5−30 nm range by solvothermal synthesis under microwave or resistive heating. *The Journal of Physical Chemistry C* **2009,** *114* (1), 155-161.

90. Meng, D.; Yamazaki, T.; Shen, Y.; Liu, Z.; Kikuta, T., Preparation of WO_3 nanoparticles and application to NO_2 sensor. *Applied Surface Science* **2009,** *256* (4), 1050-1053.

91. Zhang, H.; Liu, Z.; Yang, J.; Guo, W.; Zhu, L.; Zheng, W., Temperature and acidity effects on WO_3 nanostructures and gas-sensing properties of WO_3 nanoplates. *Materials Research Bulletin* **2014,** *57*, 260-267.

92. Martinez-de la Cruz, A.; Martínez, D. S.; Cuellar, E. L., Synthesis and characterization of WO_3 nanoparticles prepared by the precipitation method: evaluation of photocatalytic activity under vis-irradiation. *Solid State Sciences* **2010,** *12* (1), 88-94.

93. Ahmadi, M.; Younesi, R.; Guinel, M. J., Synthesis of tungsten oxide nanoparticles using a hydrothermal method at ambient pressure. *Journal of Materials Research* **2014,** *29* (13), 1424-1430.

94. Hariharan, V.; Radhakrishnan, S.; Parthibavarman, M.; Dhilipkumar, R.; Sekar, C., Synthesis of polyethylene glycol (PEG) assisted tungsten oxide (WO_3) nanoparticles for L-dopa bio-sensing applications. *Talanta* **2011,** *85* (4), 2166-2174.

95. Amini, M.; Heydarloo, D. B.; Rahimi, M.; Kim, M. G.; Gautam, S.; Chae, K. H., Mizoroki Heck reaction over palladium nanoparticles supported on WO_3. *Materials Research Bulletin* **2016,** *83*, 179-185.

96. Wang, F.; Di Valentin, C.; Pacchioni, G., Doping of WO_3 for photocatalytic water splitting: hints from density functional theory. *The Journal of Physical Chemistry C* **2012,** *116* (16), 8901-8909.

97. Aslam, M.; Qamar, M. T.; Soomro, M. T.; Ismail, I. M.; Rehan, Z. A.; Ashraf, M. W.; Hameed, A., The effect of cerium alteration on the photocatalytic performance of WO_3 in sunlight exposure for water decontamination. *RSC Advances* **2016,** *6* (3), 2436-2449.

98. Zhu, S.; Liu, X.; Chen, Z.; Liu, C.; Feng, C.; Gu, J.; Liu, Q.; Zhang, D., Synthesis of Cu-doped WO_3 materials with photonic structures for high performance sensors. *Journal of Materials Chemistry* **2010,** *20* (41), 9126-9132.

99. Nagy, D.; Firkala, T.; Drotar, E.; Szegedi, A.; Laszlo, K.; Szilagyi, I. M., Photocatalytic WO_3/TiO_2 nanowires: WO_3 polymorphs influencing the atomic layer deposition of TiO_2. *RSC Advances* **2016,** *6* (98), 95369-95377.

100. Adhikari, S.; Sarkar, D.; Madras, G., Highly efficient WO_3–ZnO mixed oxides for photocatalysis. *RSC Advances* **2015,** *5* (16), 11895-11904.

101. Yao, S.; Xue, S.; Zhang, J.; Shen, X., Characterization and mechanism analysis of AgBr mixed cuboid WO_3 rods with enhanced photocatalytic activity. *RSC Advances* **2016,** *6* (96), 93436-93444.

102. Challagulla, S.; Nagarjuna, R.; Ganesan, R.; Roy, S., Acrylate-based polymerizable sol–gel synthesis of magnetically recoverable TiO_2 Supported Fe_3O_4 for Cr(VI) photoreduction in aerobic atmosphere. *ACS Sustainable Chemistry & Engineering* **2016,** *4* (3), 974-982.

103. Nagarjuna, R.; Challagulla, S.; Ganesan, R.; Roy, S., High rates of Cr(VI) photoreduction with magnetically recoverable nano-Fe_3O_4@Fe_2O_3/Al_2O_3 catalyst under visible light. *Chemical Engineering Journal* **2017,** *308*, 59-66.

104. Su, W.; Zhang, J.; Feng, Z.; Chen, T.; Ying, P.; Li, C., Surface phases of TiO_2 nanoparticles studied by UV Raman spectroscopy and FT-IR spectroscopy. *The Journal of Physical Chemistry C* **2008,** *112* (20), 7710-7716.

105. El Mendili, Y.; Bardeau, J. F.; Randrianantoandro, N.; Gourbil, A.; Greneche, J. M.; Mercier, A. M.; Grasset, F., New evidences of in situ laser irradiation effects on γ-Fe_2O_3 nanoparticles: a Raman spectroscopic study. *Journal of Raman Spectroscopy* **2011,** *42* (2), 239-242.

106. Shim, S. H.; Duffy, T. S., Raman spectroscopy of Fe_2O_3 to 62 GPa. *American Mineralogist* **2002,** *87* (2-3), 318-326.

107. Benjwal, P.; Kumar, M.; Chamoli, P.; Kar, K. K., Enhanced photocatalytic degradation of methylene blue and adsorption of arsenic (III) by reduced graphene oxide (rGO)–metal oxide (TiO_2/Fe_3O_4) based nanocomposites. *RSC Advances* **2015,** *5* (89), 73249-73260.

108. Roy, S.; Viswanath, B.; Hegde, M.; Madras, G., Low-temperature selective catalytic reduction of NO with NH_3 over $Ti_{0.9}M_{0.1}O_{2-\delta}$ (M= Cr, Mn, Fe, Co, Cu). *The Journal of Physical Chemistry C* **2008,** *112* (15), 6002-6012.

109. Yamashita, T.; Hayes, P., Analysis of XPS spectra of Fe^{2+} and Fe^{3+} ions in oxide materials. *Applied Surface Science* **2008,** *254* (8), 2441-2449.

110. Wang, J. C.; Zhang, L.; Fang, W. X.; Ren, J.; Li, Y. Y.; Yao, H. C.; Wang, J. S.; Li, Z. J., Enhanced photoreduction CO_2 activity over direct Z-scheme α-Fe_2O_3/Cu_2O heterostructures under visible light irradiation. *ACS Applied Materials & Interfaces* **2015,** *7* (16), 8631-8639.

111. Vayssieres, L.; Sathe, C.; Butorin, S. M.; Shuh, D. K.; Nordgren, J.; Guo, J., One-dimensional quantum-confinement effect in α-Fe_2O_3 ultrafine nanorod arrays. *Advanced Materials* **2005,** *17* (19), 2320-2323.

112. Mallick, P.; Dash, B., X-ray diffraction and UV-visible characterizations of α-Fe_2O_3 nanoparticles annealed at different temperature. *Nanoscience and Nanotechnology* **2013,** *3* (5), 130-134.

113. Chen, Z.; Naidu, R.; Subramanian, A., Separation of chromium(III) and chromium(VI) by capillary electrophoresis using 2,6-pyridinedicarboxylic acid as a pre-column complexation agent. *Journal of Chromatography A* **2001,** *927* (1-2), 219-227.

114. Ji, X.; Shao, R.; Elliott, A. M.; Stafford, R. J.; Esparza-Coss, E.; Bankson, J. A.; Liang, G.; Luo, Z. P.; Park, K.; Markert, J. T., Bifunctional gold nanoshells with a superparamagnetic iron oxide−silica core suitable for both MR imaging and photothermal therapy. *The Journal of Physical Chemistry C* **2007,** *111* (17), 6245-6251.

115. Kandpal, N.; Sah, N.; Loshali, R.; Joshi, R.; Prasad, J., Co-precipitation method of synthesis and characterization of iron oxide nanoparticles. *Journal of Scientific.and Industria. Research* **2014,** *73*, 87-90.

116. Berger, P.; Adelman, N. B.; Beckman, K. J.; Campbell, D. J.; Ellis, A. B.; Lisensky, G. C., Preparation and properties of an aqueous ferrofluid. *Journal of Chemical Education* **1999,** *76* (7), 943.

117. Wei, Y.; Han, B.; Hu, X.; Lin, Y.; Wang, X.; Deng, X., Procedia Engineering. 27 (2012) 632-637. *Rec. 04/03/2015, Ac. 30/04/2015*.

118. Shebanova, O. N.; Lazor, P., Raman spectroscopic study of magnetite ($FeFe_2O_4$): a new assignment for the vibrational spectrum. *Journal of Solid State Chemistry* **2003,** *174* (2), 424-430.

119. Shebanova, O. N.; Lazor, P., Raman study of magnetite (Fe_3O_4): laser-induced thermal effects and oxidation. *Journal of Raman spectroscopy* **2003,** *34* (11), 845-852.

120. Challagulla, S.; Nagarjuna, R.; Ganesan, R.; Roy, S., Acrylate-based polymerizable sol–gel synthesis of magnetically recoverable TiO_2 supported Fe_3O_4 for Cr(VI) photoreduction in aerobic atmosphere. *ACS Sustainable Chemistry & Engineering* **2016,** *4* (3), 974-982.

121. Su, J.; Zhang, Y.; Xu, S.; Wang, S.; Ding, H.; Pan, S.; Wang, G.; Li, G.; Zhao, H., Highly efficient and recyclable triple-shelled $Ag@Fe_3O_4@SiO_2@TiO_2$ photocatalysts for degradation of organic pollutants and reduction of hexavalent chromium ions. *Nanoscale* **2014,** *6* (10), 5181-5192.

122. Idris, A.; Hassan, N.; Ismail, N. S. M.; Misran, E.; Yusof, N. M.; Ngomsik, A. F.; Bee, A., Photocatalytic magnetic separable beads for chromium(VI) reduction. *Water Research* **2010,** *44* (6), 1683-1688.

123. Idris, A.; Misran, E.; Yusof, N. M., Photocatalytic reduction of Cr(VI) by PVA-alginate encapsulated γFe_2O_3 magnetic beads using different types of illumination lamp and light. *Journal of Industrial and Engineering Chemistry* **2012,** *18* (6), 2151-2156.

124. Parida, K.; Sahu, N., Visible light induced photocatalytic activity of rare earth titania nanocomposites. *Journal of Molecular Catalysis A: Chemical* **2008,** *287* (1-2), 151-158.

125. Shaban, Y. A., Effective photocatalytic reduction of Cr(VI) by carbon modified (CM)-n-TiO_2 nanoparticles under solar irradiation. *World Journal of Nano Science and Engineering* **2013,** *3* (04), 154.

126. Xiao, D.; Dai, K.; Qu, Y.; Yin, Y.; Chen, H., Hydrothermal synthesis of α-Fe_2O_3/g-C_3N_4 composite and its efficient photocatalytic reduction of Cr(VI) under visible light. *Applied Surface Science* **2015,** *358*, 181-187.

127. Padhi, D. K.; Parida, K., Facile fabrication of α-FeOOH nanorod/RGO composite: a robust photocatalyst for reduction of Cr(VI) under visible light irradiation. *Journal of Materials Chemistry A* **2014,** *2* (26), 10300-10312.

128. Dinachali, S. S.; Saifullah, M. S.; Ganesan, R.; Thian, E. S.; He, C., A universal scheme for patterning of oxides via thermal nanoimprint lithography. *Advanced Functional Materials* **2013,** *23* (17), 2201-2211.

129. Tayonea, J., Spectrophotometric determination of chromium(VI) in canned fruit juices. *International Journal of Sciences: Basic and Applied Researchm* **2015,** *19*, 426-432.

130. Dinachali, S. S.; Dumond, J.; Saifullah, M. S.; Ansah-Antwi, K. K.; Ganesan, R.; Thian, E. S.; He, C., Large area, facile oxide nanofabrication via step-and-flash imprint lithography of metal–organic hybrid resins. *ACS Applied Materials & Interfaces* **2013,** *5* (24), 13113-13123.

131. Wang, Z.; Sun, P.; Yang, T.; Gao, Y.; Li, X.; Lu, G.; Du, Y., Flower-like WO_3 architectures synthesized via a microwave-assisted method and their gas sensing properties. *Sensors and Actuators B: Chemical* **2013,** *186*, 734-740.

132. Ramana, C.; Carbajal-Franco, G.; Vemuri, R.; Troitskaia, I.; Gromilov, S.; Atuchin, V., Optical properties and thermal stability of germanium oxide (GeO_2) nanocrystals with α-quartz structure. *Materials Science and Engineering: B* **2010,** *174* (1-3), 279-284.

133. Atuchin, V.; Andreeva, O.; Korolkov, I.; Maximovskiy, E.; Lim, C., Low-temperature synthesis and structural properties of $PbMoO_4$ nanocrystals. *Asian Journal of Chemistry* **2014,** *26* (5).

134. Atuchin, V. V.; Molokeev, M. S.; Yurkin, G. Y.; Gavrilova, T. A.; Kesler, V. G.; Laptash, N. M.; Flerov, I. N.; Patrin, G. S., Synthesis, structural, magnetic, and electronic properties of cubic $CsMnMoO_3F_3$ oxyfluoride. *The Journal of Physical Chemistry C* **2012,** *116* (18), 10162-10170.

135. Atuchin, V.; Gavrilova, T.; Grivel, J. C.; Kesler, V.; Troitskaia, I., Electronic structure of layered ferroelectric high-k titanate $Pr_2Ti_2O_7$. *Journal of Solid State Chemistry* **2012,** *195*, 125-131.

136. Lim, C. S.; Aleksandrovsky, A.; Molokeev, M.; Oreshonkov, A.; Atuchin, V., Microwave sol–gel synthesis and upconversion photoluminescence properties of $CaGd_2(WO_4)_4:Er^{3+}/Yb^{3+}$ phosphors with incommensurately modulated structure. *Journal of Solid State Chemistry* **2015,** *228*, 160-166.

137. Galashov, E.; Atuchin, V.; Gavrilova, T.; Korolkov, I.; Mandrik, Y.; Yelisseyev, A.; Xia, Z., Synthesis of $Y_3Al_5O_{12}:Ce^{3+}$ phosphor in the Y_2O_3–Al metal–CeO_2 ternary system. *Journal of Materials Science* **2017,** *52* (22), 13033-13039.

138. Atuchin, V.; Chimitova, O.; Gavrilova, T.; Molokeev, M.; Kim, S. J.; Surovtsev, N.; Bazarov, B., Synthesis, structural and vibrational properties of microcrystalline RbNd $(MoO_4)_2$. *Journal of Crystal Growth* **2011,** *318* (1), 683-686.

139. Atuchin, V. V.; Beisel, N. F.; Galashov, E. N.; Mandrik, E. M.; Molokeev, M. S.; Yelisseyev, A. P.; Yusuf, A. A.; Xia, Z., Pressure-stimulated synthesis and luminescence properties of microcrystalline $(Lu,Y)_3Al_5O_{12}:Ce_{3+}$ garnet phosphors. *ACS Applied Materials & Interfaces* **2015,** *7* (47), 26235-26243.

140. Ji, H.; Wang, L.; Molokeev, M. S.; Hirosaki, N.; Xie, R.; Huang, Z.; Xia, Z.; Otmar, M.; Liu, L.; Atuchin, V. V., Structure evolution and photoluminescence of $Lu_3(Al,Mg)_2(Al,Si)_3O_{12}:Ce^{3+}$ phosphors: new yellow-color converters for blue LED-driven solid state lighting. *Journal of Materials Chemistry C* **2016,** *4* (28), 6855-6863.

141. Adhikari, S.; Sarkar, D., Hydrothermal synthesis and electrochromism of WO_3 nanocuboids. *RSC Advances* **2014,** *4* (39), 20145-20153.

142. Khyzhun, O. Y., XPS, XES and XAS studies of the electronic structure of tungsten oxides. *Journal of Alloys and Compounds* **2000,** *305* (1-2), 1-6.

143. Nalwa, H. S., Handbook of advanced electronic and photonic materials and devices. *Academic Press:* **2000,** 1.

144. Atuchin, V.; Pokrovsky, L.; Khyzhun, O. Y.; Sinelnichenko, A.; Ramana, C., Surface crystallography and electronic structure of potassium yttrium tungstate. *Journal of Applied Physics* **2008,** *104* (3), 033518.

145. Atuchin, V. V.; Galashov, E. N.; Khyzhun, O. Y.; Kozhukhov, A. S.; Pokrovsky, L. D.; Shlegel, V. N., Structural and electronic properties of $ZnWO_4$ (010) cleaved surface. *Crystal Growth & Design* **2011,** *11* (6), 2479-2484.

146. Bledowski, M.; Wang, L.; Ramakrishnan, A.; Khavryuchenko, O. V.; Khavryuchenko, V. D.; Ricci, P. C.; Strunk, J.; Cremer, T.; Kolbeck, C.; Beranek, R., Visible-light photocurrent response of TiO_2–polyheptazine hybrids: evidence for interfacial charge-transfer absorption. *Physical Chemistry Chemical Physics* **2011,** *13* (48), 21511-21519.

147. Cheng, Q.; Wang, C.; Doudrick, K.; Chan, C. K., Hexavalent chromium removal using metal oxide photocatalysts. *Applied Catalysis B: Environmental* **2015,** *176*, 740-748.

Chapter 5

Effective adsorption of precious metal palladium over polyethyleneimine-functionalized alumina nanopowder and its reusability as a catalyst for energy and environmental applications

Chapter 5: Effective adsorption of precious metal palladium over polyethyleneimine-functionalized alumina nanopowder and its reusability as a catalyst for energy and environmental applications

5.1 Introduction

Palladium is one of the important heavy metals that find extensive usage in various catalytic applications such as coupling, hydrogenation, hydrogen generation, oxidation, decarbonylation etc.[1-4] Several organic transformations that find widespread implications in pharmaceutical and other chemical industries primarily use palladium as one of the main catalysts. Albeit enormous efforts to find alternatives are being pursued, palladium is still considered to be a dominant candidate in many catalytic reactions till date. Some of the limitations of palladium include its high cost, environmental toxicity at higher concentrations and limited natural availability.[5,6] From both environmental and cost perspectives, it is necessary to bring the amount of palladium in the final effluents below 5 mg L^{-1}.[5,6] Although, toxicity of palladium is not substantial, at higher concentrations the kidney tissues are more likely to be affected and recent facts testify that it perturbs the mitochondrial respiratory chain leading to cell death by depleting cellular glutathione levels.[7] Also, palladium has the ability to be transported through plant roots and later could enter into the food chain.[8] Thus, it is imperative to effectively utilize the available palladium in a sustainable fashion and recover it successfully. The recovery of palladium could be accomplished through liquid-liquid extraction, and solid phase extraction processes. Among these, the solid phase extraction is known to be an economical and effectual strategy for the recovery of palladium and other metal species.[9-11]

Development of efficient adsorbents to recover palladium from the spent catalysts and industrial wastes provides economical and sustainable opportunities. In this regard, activated carbon, and biopolymer modified activated carbon are reported for palladium and platinum removal.[12] Precious metals such as Au(III), Pd(II), and Pt(IV) are shown to be well adsorbed onto native graphene oxide.[13] The interaction of sulfur ligands such as mercaptobenzothiazole[14] and mercaptobenzimidazole[15] with biopolymers such as cellulose and chitosan show good ability to adsorb and recover palladium. Impregnation of ionic liquid (Aliquat-336) onto a mesoporous silica matrix (SBA-15) is another versatile adsorbent that has been utilized to recover palladium from an industrial catalyst.[16]

Recently, there is an increasing trend in using amine functionality such as polyethyleneimine (PEI) towards environmental remediation as it is a biocompatible polymer that has been widely used in various biological applications including tissue engineering and drug delivery.[17-20] While the linear PEI is mainly consisted of secondary amines, the branched PEI possesses primary, secondary and tertiary amine groups. Because of the abundant nitrogen, PEI is also known for its polycationic behavior. On a different note, alumina is an inert, cost-effective and non-toxic substance. The surface of alumina can be easily functionalized with amines, carboxylic acid, thiols etc. in order to obtain the desired property. The commercial availability of high surface area alumina nanopowder makes it interesting to be used as a cost-effective support.[21] PEI coated onto alumina was used as a sorbent with an adsorption capacity of 13 mg g^{-1}.[22] PEI-coated polysulfone/*Escherichia coli* has been studied recently as a biosorbent for the sorption of Pd(II). Here, polysulfone was used as a polymer matrix for immobilization of *Escherichia coli* biomass and to enhance the adsorption capacity.[23] Polyallylamine hydrochloride-modified *Escherichia coli* also has been studied for its Pd(II) sorption efficiency.[24] The utility of PEI-modified *Corynebacterium glutamicum* biomass as a sorbent[25] has been reported for palladium recovery. Alumina combined with (5-bromo-2-pyridylazo)-5-diethylaminophenol) shows good potential for the adsorptive removal of Pd(II) from different water samples with the sorption capacity of 11.0 mg g^{-1}.[26] *N,N*-bis(salicylidene)1,2-bis(2-aminophenylthio)ethane anchored over mesoporous silica was found to be efficient in adsorbing and sensing Pd(II).[27] Amine-functionalized TiO_2 nanofibers obtained through electrospinning has been found to effectively perform as a membrane for recovery of precious metals such as Pd, Pt and Rh.[28] Palladium supported onto amine-functionalized montmorillonite has also been used as a catalyst towards regioselective synthesis of aurones and flavones.[29] In this effort, we chose high surface area alumina nanopowder and functionalized it with PEI. It is with the aim that the nitrogen moieties present in PEI can effectively interact with palladium and thereby leading to efficient palladium recovery and its reusability in catalytic applications. Furthermore, the surface functionalization and the catalytic applications were carried out entirely in aqueous medium, and thereby offering an environmentally benign methodology. The methodology of preparation of adsorbent and application towards catalysis are well documented in chapter 5.

4.2 Experimental Section

(i) Carboxyl-functionalization of AO

In a typical reaction, 1.0 g of AO was added to 100 mL of Millipore water in a 250 mL round bottom flask. To this, about 20 wt.-% (w.r.t. AO) of sodium citrate was added and the mixture was sonicated for 30 min in an ultra-sonication bath to disperse the particles in the media. The temperature of the reaction medium was raised to 90 °C in an oil bath and allowed to stand for 8 h under stirring.[30] Subsequently, the mixture was cooled to room temperature and centrifuged. The resultant product (SC-AO) was acidified by adding 50% (v/v) aqueous acetic acid solution and incubated for 10 min. The citrate-functionalized alumina nanopowder (CA-AO) thus obtained was centrifuged, washed with Millipore water three times, and then dried in a vacuum oven for overnight at room temperature.

(ii) Polyethylenimine-functionalization of CA-AO

The amine functionalization was carried out by covalently anchoring PEI onto CA-AO through amide coupling.[31] To achieve this, about 1.0 g of CA-AO in 20 mL of water was treated with a solution containing 0.6 g of EDC and 0.2 g of NHS. The resulting suspension was stirred for 3 h at room temperature. After this time, the suspension was added dropwise into a beaker containing 1.2 g of PEI dissolved in 500 mL of water and the pH of the mixture was adjusted to 5 and stirred for 24 h at room temperature. Finally, the PEI-anchored alumina nanopowder (PEI-AO) was obtained by centrifugation, washing and drying in a similar manner to CA-AO.

(iii) Batch adsorption experiments

The batch adsorption studies were carried out by taking 0.1 g of adsorbent (PEI-AO) in 30 mL of 10 mg L^{-1} Pd(II) solution prepared in HCl medium and the parameters like pH, adsorbent amount, adsorption time and temperature were optimized at room temperature (25 °C) for the desired time interval in an orbital incubator shaker at 120 rpm. The optimized pH was 6.0. Various initial concentrations of Pd(II) ranging from 40 to 300 mg L^{-1} were used to study the isotherms. The adsorbed palladium (II) at equilibrium (q_e) is calculated using the following relation:

$$q_e = (C_0 - C_e) \times \frac{V}{W} \qquad (1)$$

where, C_0 and C_e are the initial and final liquid phase concentrations of palladium, V is the volume (in L) of the solution, and W is the weight (in g) of the PEI-AO adsorbent used,

respectively. The adsorption process was studied using first-order and second-order kinetics and the isotherms were evaluated using Langmuir and Freundlich models.

(iv) Characterization and catalysis studies of Pd-adsorbed PEI-AO

For the characterization studies, 300 mg L^{-1} of palladium chloride solution was stirred with 0.1 g of PEI-AO to ensure maximum palladium adsorption. The resultant material was coded as Pd-PEI-AO and used for catalytic studies. The reduction of 4-NP was carried out by taking catalytic quantity (~5 mg) of Pd-PEI-AO in 10 mL of solution containing 0.143 mM of 4-NP and 14.3 mM of $NaBH_4$. The reaction progress was monitored using UV-visible spectrophotometer. After the complete reduction of 4-NP, the Pd-PEI-AO was recovered through centrifugation and reconstituted for recyclability studies. To perform Cr(VI) reduction, the Pd-PEI-AO was subjected to reduction using $NaBH_4$ solution in order to reduce the adsorbed palladium, referred hereafter as rPd-PEI-AO. A stock solution of 20 mg L^{-1} potassium dichromate containing 0.33 M of oxalic acid was prepared and the pH was adjusted to 3.0. To a 3 mL of this solution, 5 mg of the rPd-PEI-AO was added and the UV-Vis absorbance of the resultant solution was recorded as a function of time. After the complete reduction of Cr(VI), the solution was centrifuged to recover the catalyst, which was utilized for the recyclability studies. For hydrogen generation experiments, 100 mg of rPd-PEI-AO was added to a 20 mL of 64.8 mM AB solution and stirred. The evolved hydrogen gas was measured using gas burette method. In all the catalytic reactions, the reusability was studied up to 5 cycles.

5.3 Results and discussion

The functionalization of AO nano-support with PEI was accomplished in a two-step synthesis, as depicted in Scheme 5.1. First, sodium citrate was chemically anchored over alumina nano-support, followed by acidification with acetic acid, in order to achieve carboxyl surface functionalization. It is envisaged that one of the carboxylate arms of the citrate gets anchored onto the alumina surface, while the remaining two carboxylates are free that can be converted to carboxylic acid upon acidification. In the second step, these carboxyl groups on the surface of AO were activated using well-known EDC/NHS coupling reagents, which facilitated covalent immobilization of PEI through amide bond formation. This was accomplished by the dropwise addition of CA-AO nanopowder suspension to the PEI solution. The surface functionalization was monitored through IR, XPS, TGA, surface area and zeta potential measurements.

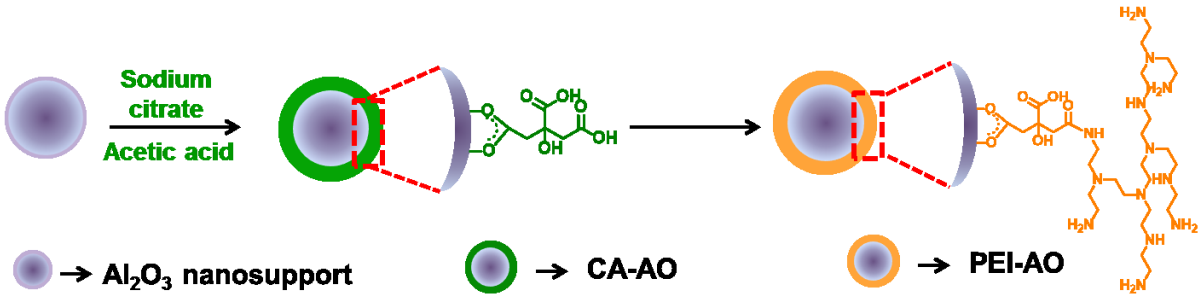

Scheme 5.1: Pictorial representation of citrate-mediated amine-functionalization of alumina nanopowder.

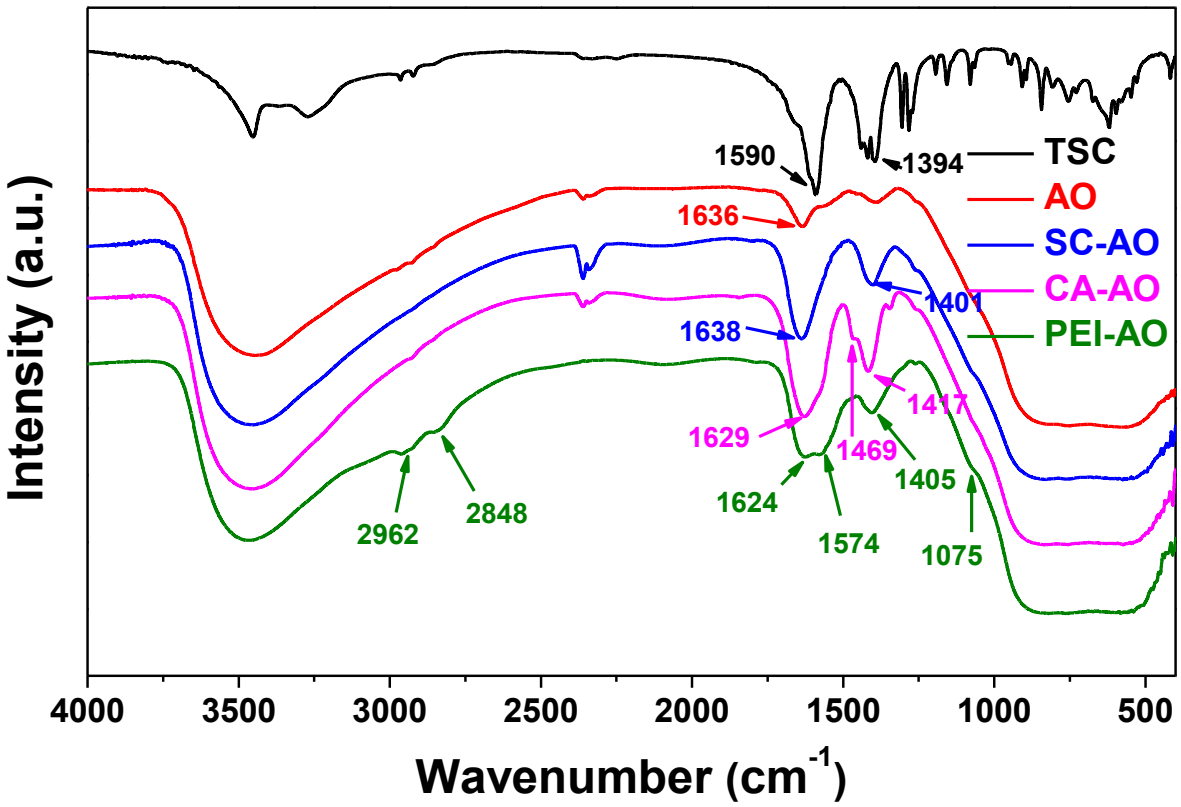

Figure 5.1: FT-IR spectra of the pristine TSC, AO, SC-AO, CA-AO and PEI-AO.

The IR measurement of pristine AO, SC-AO, CA-AO, and PEI-AO were recorded to follow the surface functionalization and the spectra are plotted in Fig. 5.1. As seen from the figure, the pristine AO exhibited a broad band in the range of 400 to 1000 cm^{-1}. A peak at 1636 cm^{-1} was found in the commercial AO, which may be attributed to the AlOOH layer on the surface.[32] After functionalization with sodium citrate (before acidification), the obtained SC-AO exhibited characteristic asymmetric $\nu_{as}(COO^{-})$ and symmetric $\nu_{s}(COO^{-})$ vibrational stretching frequencies of surface bound carboxylate at 1638 and 1401 cm^{-1}, respectively. The separation of 237 cm^{-1} between these two peaks indicate the bridging type of chelation of the

–(COO^-) groups over the adjacent metal centers in the AO support. After acidification, the peak maxima in CA-AO are observed at 1629, 1469, and 1417 cm^{-1}. The narrowing of separation between the $\nu_{as}(COO^-)$ and symmetric $\nu_s(COO^-)$ with an additional peak formation at 1468 cm^{-1} indicates successful acidification.[32-34] After immobilizing PEI onto CA-AO, the $\nu_{as}(COO^-)$ and $\nu_s(COO^-)$ stretching peaks were found to be slightly shifted to 1624 and 1405 cm^{-1}, respectively. This is indicative of amide bond formation through free –COOH groups, while the remaining carboxylate groups remain chelated to the AO support. The new peak at 1574 cm^{-1} due to N-H stretching, and a weak shoulder at 1075 cm^{-1} due to C-N stretching of PEI indicate that the surface is covered with amine-functionalities due to the reaction between PEI and the alumina surface.[35] One may not exclude the possibility of PEI getting coated over CA-AO through electrostatic interaction. Thus, PEI could be immobilized partially through amide bond as well as electrostatic interaction over CA-AO.[22]

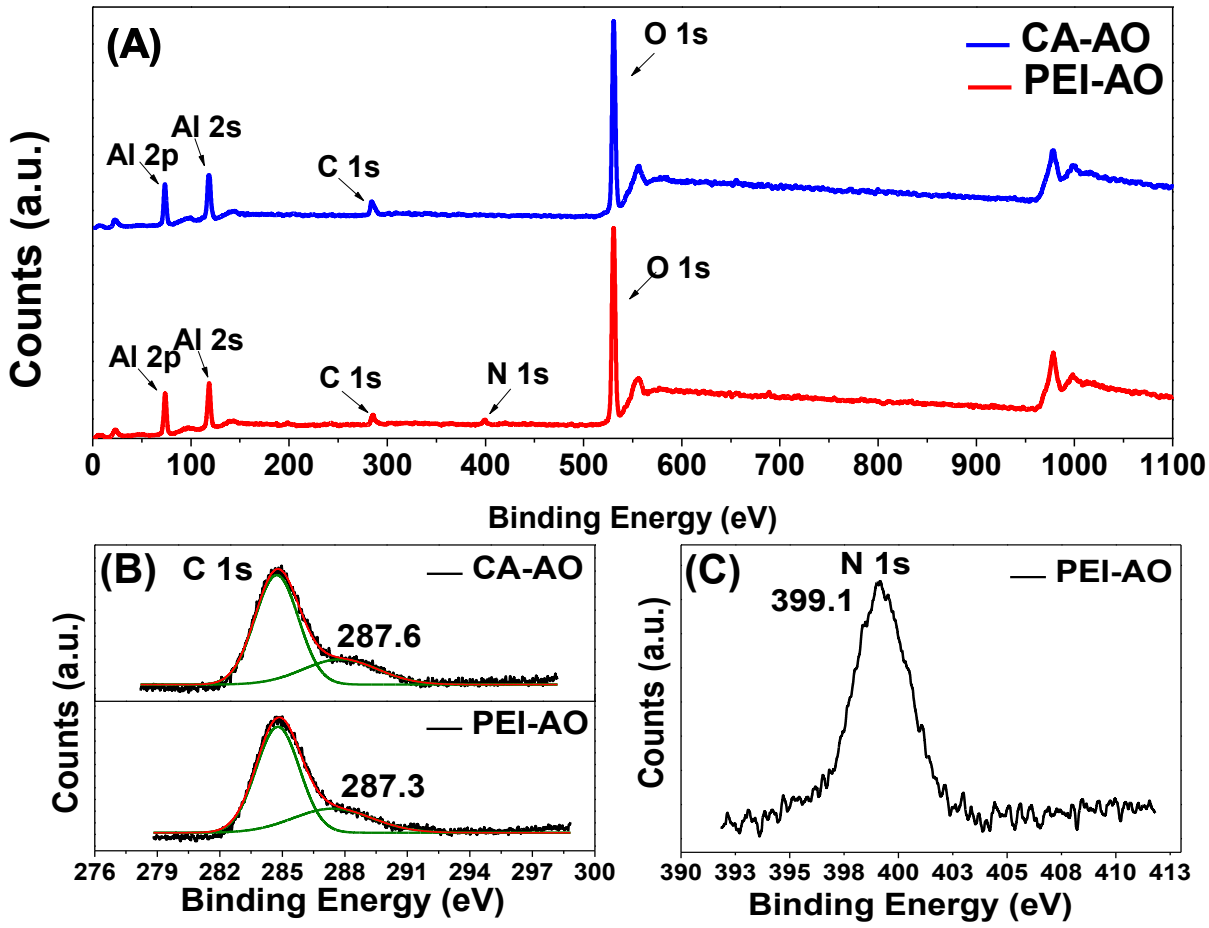

Figure 5.2: XPS survey scan measurements on CA-AO and PEI-AO (A), C 1*s* narrow scan measurements on C-AO and PEI-AO (B), and N 1*s* narrow scan measurement on PEI-AO (C).

To corroborate the observation from IR, we performed XPS measurements on CA-AO and PEI-AO (Fig. 5.2). The survey scan spectrum of CA-AO revealed the presence of characteristic Al 2*p*, Al 2*s*, C 1*s*, and O 1*s* peaks at the binding energies correspond to 73.5, 118.2, 285.0, and 530.7 eV, respectively.[36] The C 1*s* narrow scan further revealed that a significant portion of the carbon was possessing higher binding energy due to the bonding with the electronegative oxygen atoms. The deconvolution of the C 1*s* narrow scan showed a peak at 288 eV that can be attributed to the –C=O(O) of the carboxyl group.[37] This has clearly indicated the presence of carboxylic acids on the surface of alumina nanopowder. The survey scan spectrum of PEI-AO, in addition to the peaks observed with CA-AO, revealed an additional N 1*s* peak at 399.1 eV, which was further resolved in the narrow scan. These observations additionally substantiated the successful surface functionalization of AO with PEI.

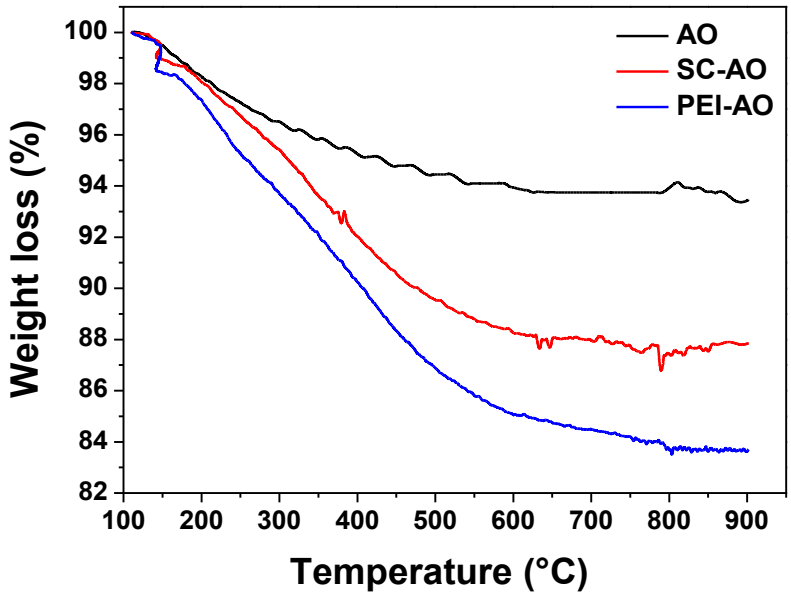

Figure 5.3: Mass loss study on AO, SC-AO, and PEI-AO using thermogravimetric analysis

TGA analyses of pristine AO, CA-AO, and PEI-AO were performed in order to understand the degradation profile of the organics present in the functionalized alumina nanoparticles (Fig. 5.3). The pristine AO exhibited a gradual mass loss up to 600 °C, the temperature at which the total mass loss was found to be ~6%. The mass loss study of the functionalized materials revealed that the CA-AO possessed ~11% of organics, while the amount of organics present in the PEI-AO was in the range of ~15%. In both the cases, the major degradation started from ~250 °C, which was nearly completed at ~600 °C. The

difference in mass loss between the pristine AO and the functionalized-AO indicates the increment in the overall proportion of organics with each functionalization step.

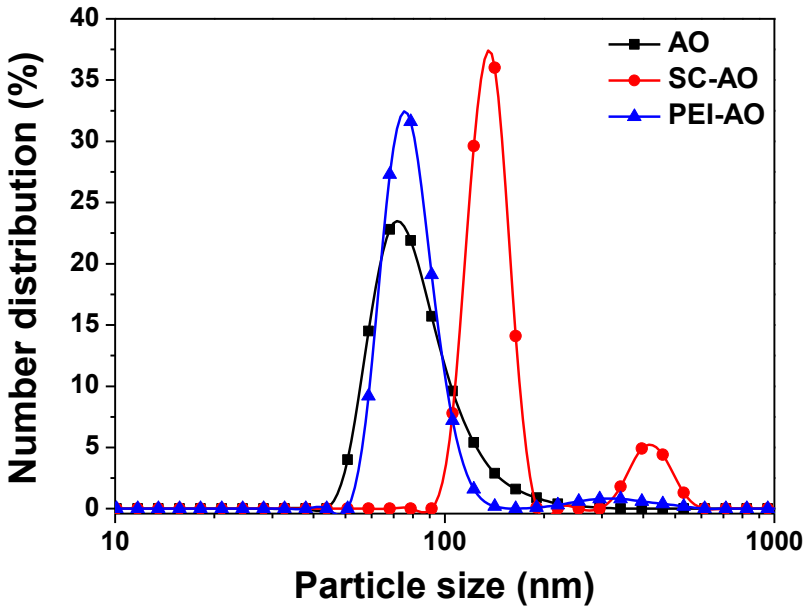

Figure 5.4: Size distribution analysis of AO, CA-AO, and PEI-AO using DLS.

The particle size analysis of AO, CA-AO, and PEI-AO were performed by dynamic light scattering (DLS) technique to understand the effect of surface functionalization in the particles' hydrodynamic radius. As seen in Fig. 5.4, the pristine AO possessed a size of ~80 nm, which was increased to ~135 nm for CA-AO. This increase in particle size indicates some aggregation among the CA-AO. After functionalization of CA-AO with PEI, the hydrodynamic radius of the resultant PEI-AO was found to be ~79 nm, which indicates that the particles regained their original surface after this step. Zeta potential measurements of these materials were carried out to understand the change in surface charge with each surface functionalization (Fig. 5.5). It is well known that the high acidic conditions would protonate the surfaces that would give rise to positive zeta potential, while the high alkaline conditions would render the surfaces negatively charged and therefore lead to negative zeta potential. As expected, in all the three samples, at ~pH 2 the surfaces possessed a positive zeta potential that was switched to negative at ~pH 12, however, their respective magnitudes were found to be different, additionally corroborating the functionalization. The isoelectric pH values of pristine AO, CA-AO and PEI-AO were found to be 6.3, 6.5, and 7.3, respectively.

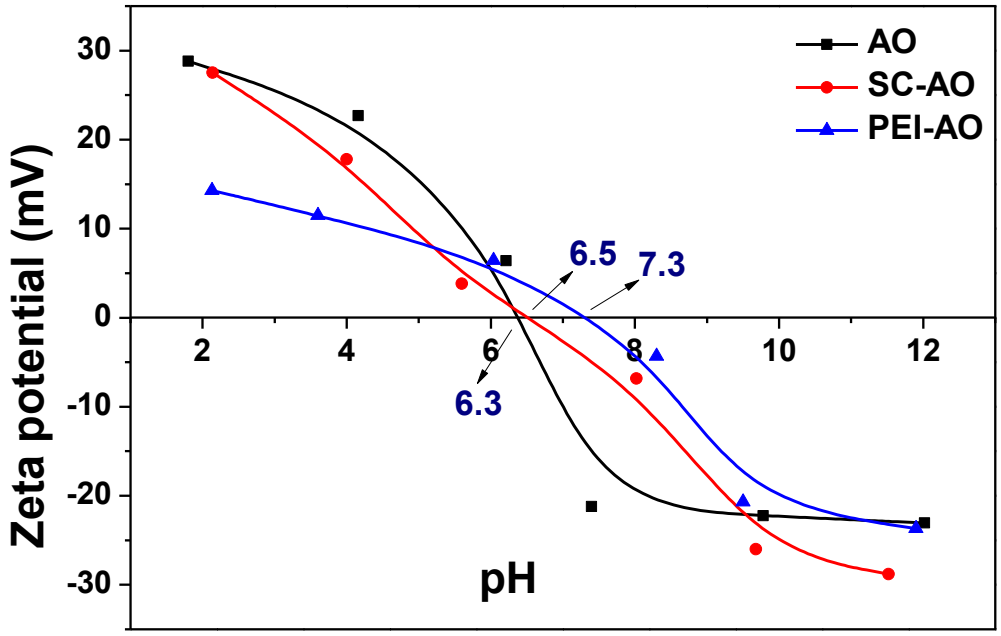

Figure 5.5: Zeta potential analysis of AO, SC-AO, and PEI-AO as a function of pH.

The BET surface area of the pristine AO, CA-AO, and PEI-AO was measured to follow the change in surface area as a function of surface functionalization. The surface area of the pristine AO was found to be ~141 m^2/g, while that of the CA-AO was found to be ~104 m^2/g. The reduction in surface area could be attributed to the aggregation of carboxyl-functionalized alumina nanopowder during the acidification step. The surface area of PEI-AO was found to be ~155 m^2/g. The high value of surface area obtained after the PEI-functionalization step indicates that the PEI chains did not suffer aggregation, possibly due to the electrostatic repulsions between the amine groups. These results are in line with the DLS observation.

The PEI-AO thus obtained was studied for its palladium sorption properties. The Pd(II) adsorption as a function of pH and amount of adsorbent revealed the optimal values to be 6.0 and 0.1 g, respectively (Fig. 5.6). Fig. 5.6 showed that with the increase in the amount of adsorbent, the % adsorption of Pd(II) significantly decreases. This unique behavior could be attributed to the following reason. Generally, it is well-known that the adsorption-desorption is an equilibrium process. When an adsorbate is strongly anchored over an adsorbent, the equilibrium will be shifted towards adsorption and therefore desorption will be suppressed. The nature of adsorption is determined through the magnitude of enthalpy of adsorption. In our case, the ΔH^0 was found to be -103.63 kJ mol^{-1} (*vide infra*), which lies in the boundary between physisorption and chemisorption. With increase in the adsorbent dosage, there exists

a competition for Pd(II) between the PEI-AO nanopowders that shifts the equilibrium towards desorption. Hence, at higher adsorbent dosage the % Pd adsorption decreases.

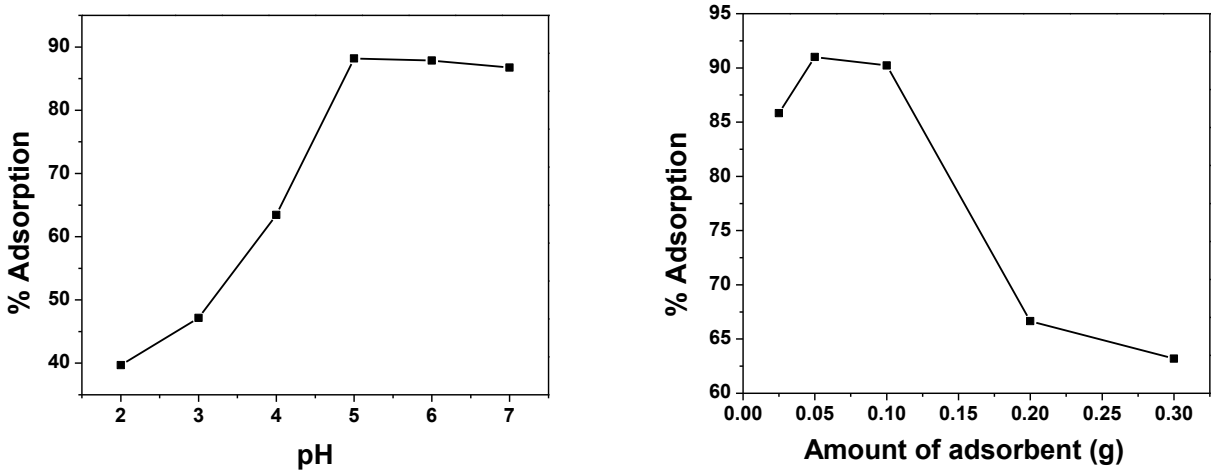

Figure 5.6: Optimization studies for pH (A) and amount of adsorbent (B) using 10 mg L^{-1} of Pd(II) ions.

For the isotherm studies, the initial concentrations of Pd(II) were varied from 40 to 300 mg L^{-1}. The equilibrium adsorption data was applied to two important isotherms (Langmuir and Freundlich) from which we could obtain the various isotherm parameters.

The Langmuir isotherm model was used to comprehend the monolayer adsorption on homogeneous surface containing a limited number of identical sites and to calculate the maximum adsorption capacity of adsorbent.[38,39] This isotherm explains the relation between the equilibrium concentration of palladium (C_e) and the amount adsorbed at equilibrium (q_e) on the surface of PEI-AO. The maximum adsorption capacity, q_o (amount of Pd(II) adsorbed per unit weight of the adsorbent) and constant b were obtained from the linear plot (Fig. 5.7 (A)). The linearized form for Langmuir isotherm is shown in equation (1).

$$\frac{C_e}{q_e} = \frac{1}{q_0 b} + \frac{C_e}{q_0} \qquad (1)$$

Using the above equation, the maximum adsorption capacity, q_o was found to be 97.7 mg g^{-1} ($R^2 = 0.91$). Suitability of a particular adsorption isotherm could be inferred through an important parameter called the dimensionless separation factor R_L. This is given by the equation ($R_L = 1/(1 + bC_o)$, where C_o is the initial concentration of Pd(II) in mg L^{-1} and b is the Langmuir constant (L mg^{-1}). The value of b was found to be 0.03 L mg^{-1}. The value of R_L less than 1 relates to satisfactory adsorption, while the same when greater than 1 indicates reduced or unfavourable adsorption.[40] The value of R_L for the adsorption of palladium over PEI-AO adsorbent was found to be 0.77, indicating the usefulness of Langmuir isotherm in this system.

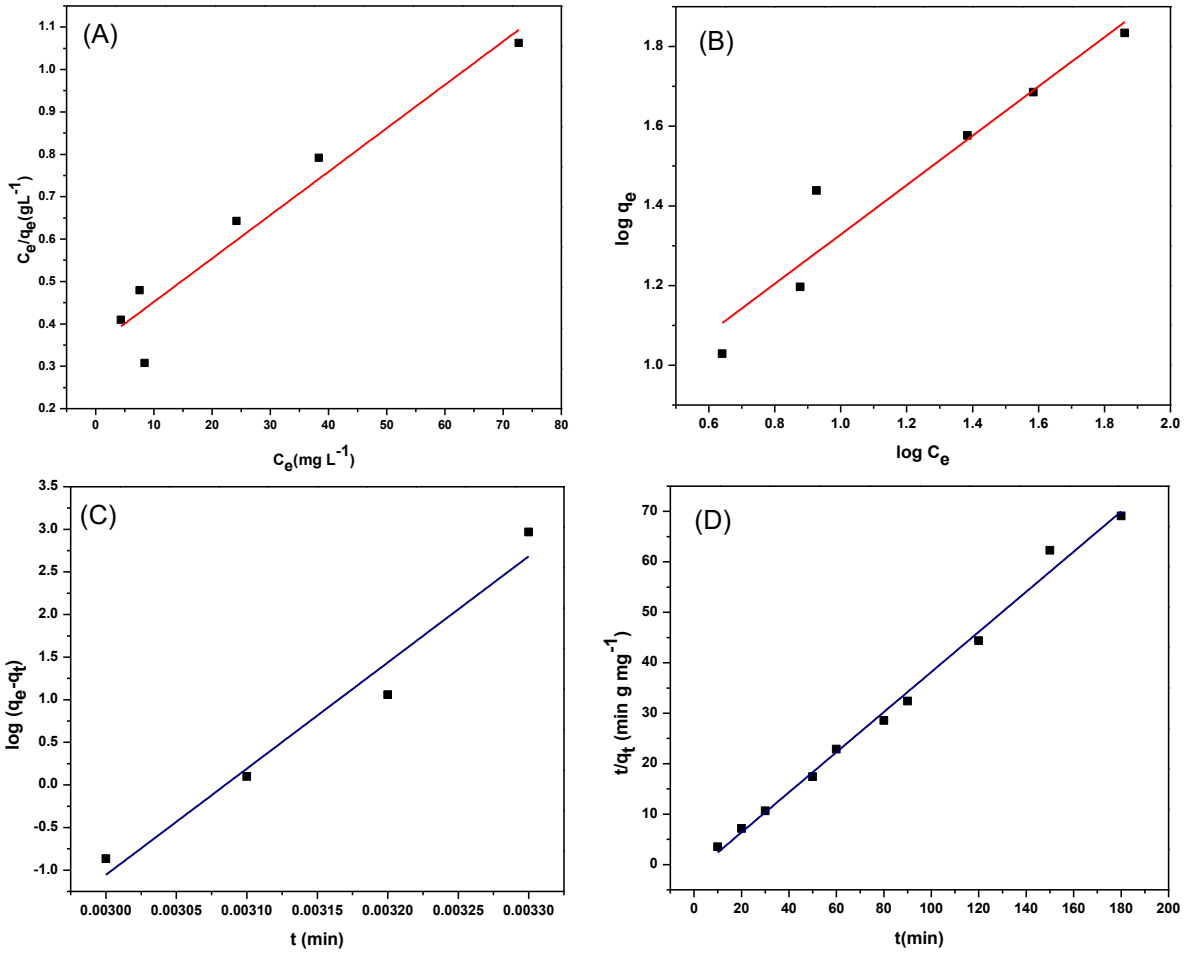

Figure 5.7: Langmuir (A) and Freundlich (B) isotherms for the adsorption of Pd(II) over PEI-AO. Pseudo first-order (C) and pseudo second-order (D) kinetics for the adsorption of Pd(II) over PEI-AO.

The Freundlich isotherm, based on sorption on a heterogeneous surface, is an alternative useful model to gauge the adsorption phenomena occurring in dilute solutions.[41,42] The linearized form for Freundlich isotherm is given as

$$\log q_e = \log K_F + \frac{1}{n}\log C_e \qquad (2)$$

In this particular model, C_e is the equilibrium concentration of the Pd(II) in mg L^{-1}, q_e is the amount of Pd(II) adsorbed at equilibrium in mg g^{-1}, and K_F and n are the Freundlich constants for adsorption capacity and adsorption intensity, respectively. K_F and n were obtained from the slope and intercept of the Freundlich isotherm plots (Fig. 5.7 (B)). The regression coefficient R^2 was found to be 0.90. The Freundlich exponent n should fall in the range of 1-10 so as to predict the suitability of this isotherm[16] for a particular adsorption process. The respective values of n and K_F were calculated to be 1.61 and 5.12, implying the favourable adsorption process. The Langmuir and Freundlich isotherm parameters are given in Table 5.1.

Table 5.1: Parameters of Langmuir and Freundlich isotherm models

Isotherm model	Parameters	Values
Langmuir	q_o (mg g^{-1})	97.7
	b (L mg^{-1})	0.03
	R_L	0.77
Freundlich	K_F (mg $^{1-1/n}$ g^{-1} $L^{1/n}$)	5.12
	n	1.61
	R^2	0.90

The kinetics of the palladium adsorption onto the PEI-AO surface was studied using first-order[43] and pseudo-second order[44] models and the linearized equations are expressed as given by eqns. (4) and (5), respectively.

$$\log(q_e - q_t) = \log q_e - \frac{k_1 t}{2.303} \qquad (3)$$

$$\frac{t}{q_t} = \frac{1}{k_2 {q_e}^2} + \frac{t}{q_e} \qquad (4)$$

where q_e and q_t refers to the amount of palladium adsorbed at equilibrium and time t with the first and second-order rate constants k_1 and k_2, respectively. By fitting the experimental data through the plots of log (q_e-q_t) and t/q_t against t (Fig. 5.7 (C) and 7 (D)), we obtain the kinetic

parameters for the above two models. The adsorption data follows well with the pseudo-second-order model as indicated by the higher regression coefficient (Table 4.2). Further, the q_e values obtained experimentally and from the pseudo second-order kinetic model were found to be 2.6362 and 2.5159 mg g^{-1}, respectively. With the experimental and calculated q_e values being quite agreeable, it proves the applicability of pseudo second-order model in understanding the adsorption kinetics of palladium onto the PEI-AO adsorbent. Also, the kinetics data revealed the optimal equilibration time to be 50 min.

Table 5.2: Kinetic parameters for the adsorption of Pd(II)

Concentration of Pd (II) solution ($mg\ L^{-1}$)	q_e $mg\ g^{-1}$	Pseudo second order kinetic model		
		k_2 $g\ mg\ min^{-1}$	q_2 $mg\ g^{-1}$	R^2
10	2.6362	0.1004	2.5159	0.99

The sorption of Pd(II) onto PEI-AO surface was evaluated through the thermodynamic studies involving Gibbs free energy (ΔG^0), standard enthalpy change (ΔH^0), and standard entropy change (ΔS^0). These parameters were calculated (Table 5.3) from the temperature-dependent adsorption data using the Van't Hoff equations[45,46] as shown in eqns. (5) and (6).

$$\Delta G^0 = -RT\ln K_c \qquad (5)$$

$$\ln K = \frac{-\Delta H^0}{RT} + \frac{\Delta S^0}{R} \qquad (6)$$

The K_c values were obtained from the ratio of concentration of tetrachloropalladate (II) anion adsorbed onto PEI-AO adsorbent to that in the liquid phase at equilibrium. The standard enthalpy and entropy changes were obtained through the lnK against 1/T (Fig. 5.8) plot. The negative ΔG^0 substantiates the spontaneity of adsorption of Pd(II) onto PEI-AO. The decrease in ΔG^0 values with increase in temperature shows that palladium adsorption does not proceed well at higher temperatures. The negative ΔH^0 (-103.63 kJ mol^{-1}) points the exothermic adsorption behaviour and also its magnitude gives vital information on the adsorption type, which could be either physical or chemical. When there is physical adsorption, ΔH^0 would generally be less than 80 kJ mol^{-1} and for chemical adsorption ΔH^0 has a range 80-400 kJ mol^{-1}.[47] The negative ΔS^0 (-319.67 J $mol^{-1}K^{-1}$) is indicative of decreased randomness at the Pd(II)-PEI-AO interface. The negative activation energy (E_a) at different temperatures (E_a =

ΔH^0_{ads} + RT) is also an indicator of the exothermic nature of adsorption of Pd(II) on to the PEI-AO adsorbent surface.[14]

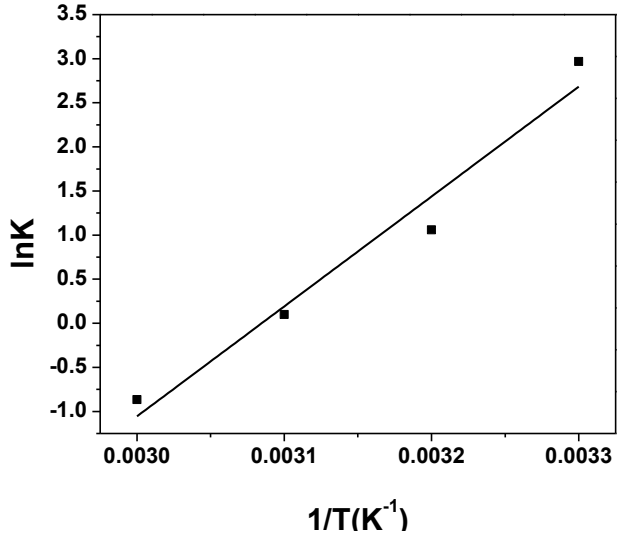

Figure 5.8: Van't Hoff plot for the palladium adsorption over PEI-AO.

Table 5.3: Thermodynamic parameters for the adsorption of Pd(II) ions

Temperature (Kelvin)	ΔG^0 (kJ mol^{-1})	ΔS^0 (J mol^{-1} K^{-1})	ΔH^0 (kJ mol^{-1})	E_a (kJ mol^{-1})
298	-8.3683	-319.67	-103.63	-101.02
308	-5.1716			
318	-1.9749			
328	-1.2217			

For the recovery of adsorbed palladium, the fixed bed column studies were performed on a glass column packed with 1.0 g of the PEI-AO adsorbent. A 10 mg L^{-1} Pd(II) was poured onto the adsorbent column (flow rate 5 mL min^{-1}) and the concentration of palladium in the solution phase was measured using AAS. Thiourea that contains sulfur and nitrogen as coordinating atoms was used as a desorbing agent. Desorption of palladium was found to be effective with a 9 mL volume of 0.2 mol L^{-1} aqueous thiourea. This could be elucidated through the formation of palladium-thiourea yellow colored complex, which considerably lowers the interaction between the adsorbent (PEI-AO) and Pd(II) ions and thereby facilitating palladium desorption from the adsorbent surface. After 3 cycles of regeneration,

the percentage adsorption of palladium was slightly decreased from 91.4% to 90.8%, while the 4th cycle showed the percentage adsorption as 84.6%. This shows that the adsorbent could be regenerated and reused for 3 cycles using thiourea without any significant loss in adsorption capability. This has additionally proven the robustness and stability of the PEI surface functionalization.

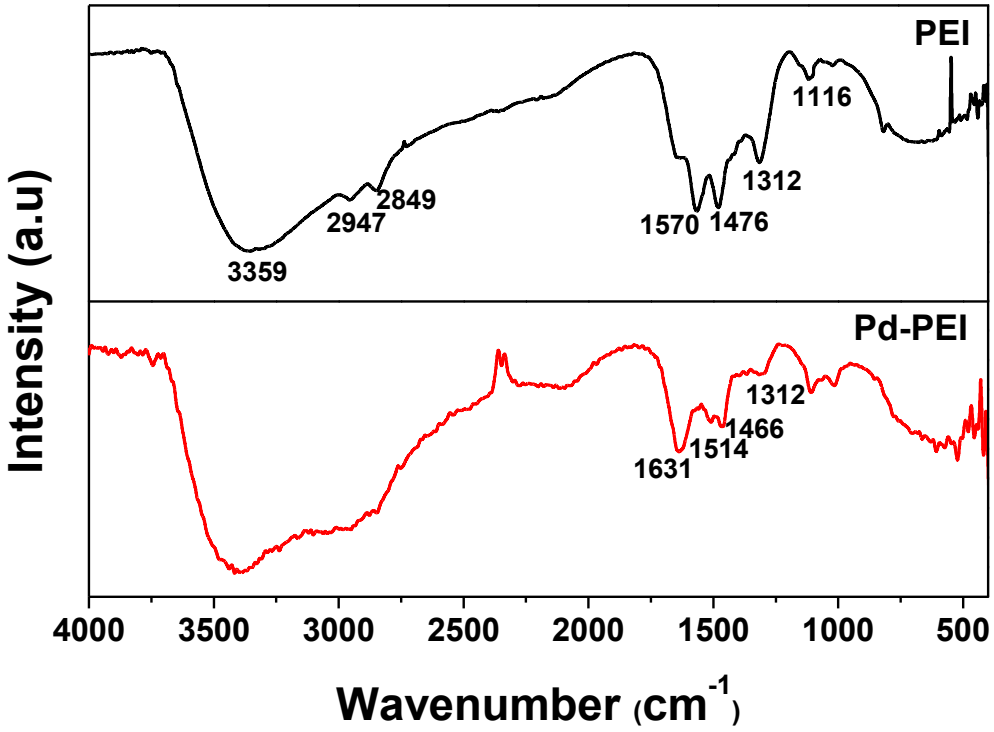

Figure 5.9: FT-IR spectra of neat PEI before and after adsorption of Pd(II).

The interaction between Pd(II) and PEI was probed using IR spectroscopy (Fig. 5.9). The IR spectrum of polyethyleneimine (PEI) shows characteristic peaks at 3359 cm^{-1} (–N–H stretching), 2947, 2849 cm^{-1} (–C–H stretching), 1570 cm^{-1} (–N–H bending), 1476 cm^{-1} (–C–H bending) and 1312, 1116 cm^{-1} (–C–N stretching).[48-50] After loading Pd(II) onto PEI, the N-H bending peak at 1570 cm^{-1} and the –C–N stretching and 1312 cm^{-1} were vastly suppressed, while new peaks were prominent at 1631, 1514, and 1466 cm^{-1}. This shows that the electrostatic interaction through N-H group is certainly accountable for palladium sorption. In case of PEI-AO, the N-H stretching peak at 1567 cm^{-1} was suppressed after palladium sorption, confirming the role of nitrogen in the adsorption of palladium (Fig. 5.10).

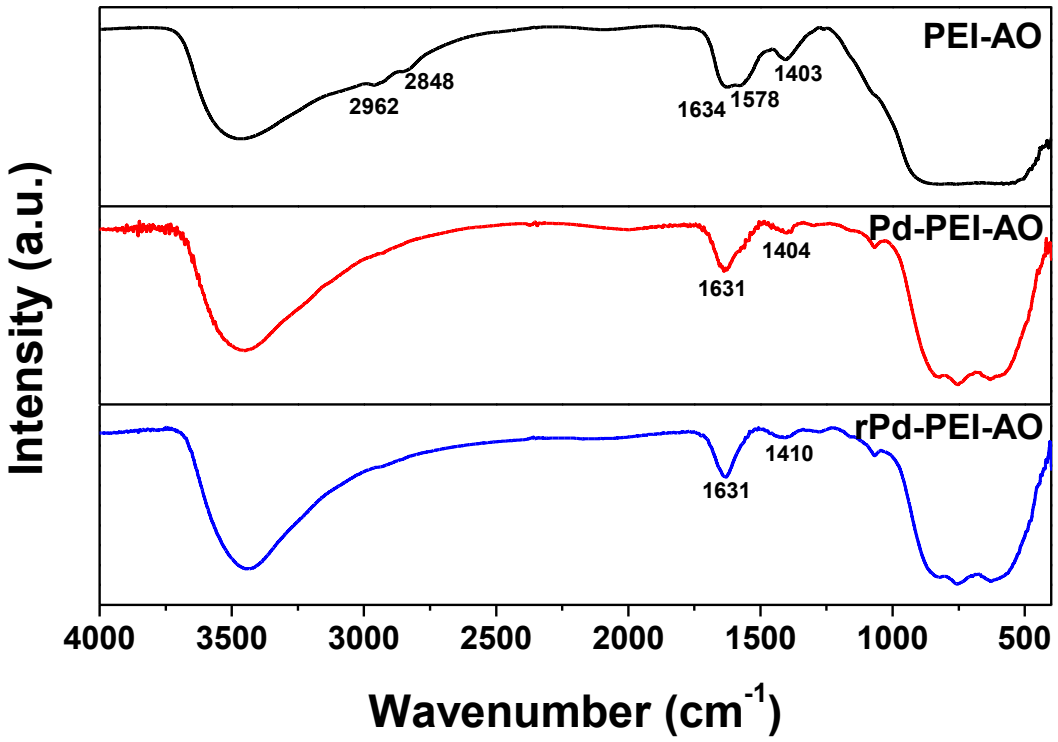

Figure 5.10: FT-IR spectra of neat PEI-AO, Pd-PEI-AO, and rPd-PEI-AO.

The Pd-PEI-AO and rPd-PEI-AO were characterized using XPS to gain additional insight to the interaction between palladium and the adsorbent (Fig. 5.11). In both the cases, the survey scan revealed the presence of N 1*s* and Pd 3*d* peaks. The N 1*s* narrow scan revealed that the nitrogen peak of PEI-AO at 399.1 eV was shifted to 399.8 eV after Pd adsorption, indicating that the electron density surrounding nitrogen was decreased due to the interaction with Pd(II).[50] After reduction of palladium, the N 1*s* peak at 399.5 eV was appeared to be broader and less in intensity, which indicates that the palladium linked to the nitrogen, is reduced, as a consequence the nitrogen has partially regained its electron density. The Pd 3*d* narrow scan revealed that the Pd-PEI-AO exhibited the characteristic Pd $3d_{5/2}$ and Pd $3d_{3/2}$ peaks at 335.5 and 340.7 eV, respectively. The deconvolution of the curve reveals that the palladium mostly exists in its +2-oxidation state when adsorbed over PEI-AO. After reduction, the peaks have become much sharper and shifted to a lower binding energy value, which substantiated that the Pd present in rPd-PEI-AO was successfully reduced to zero-valent oxidation state.[51]

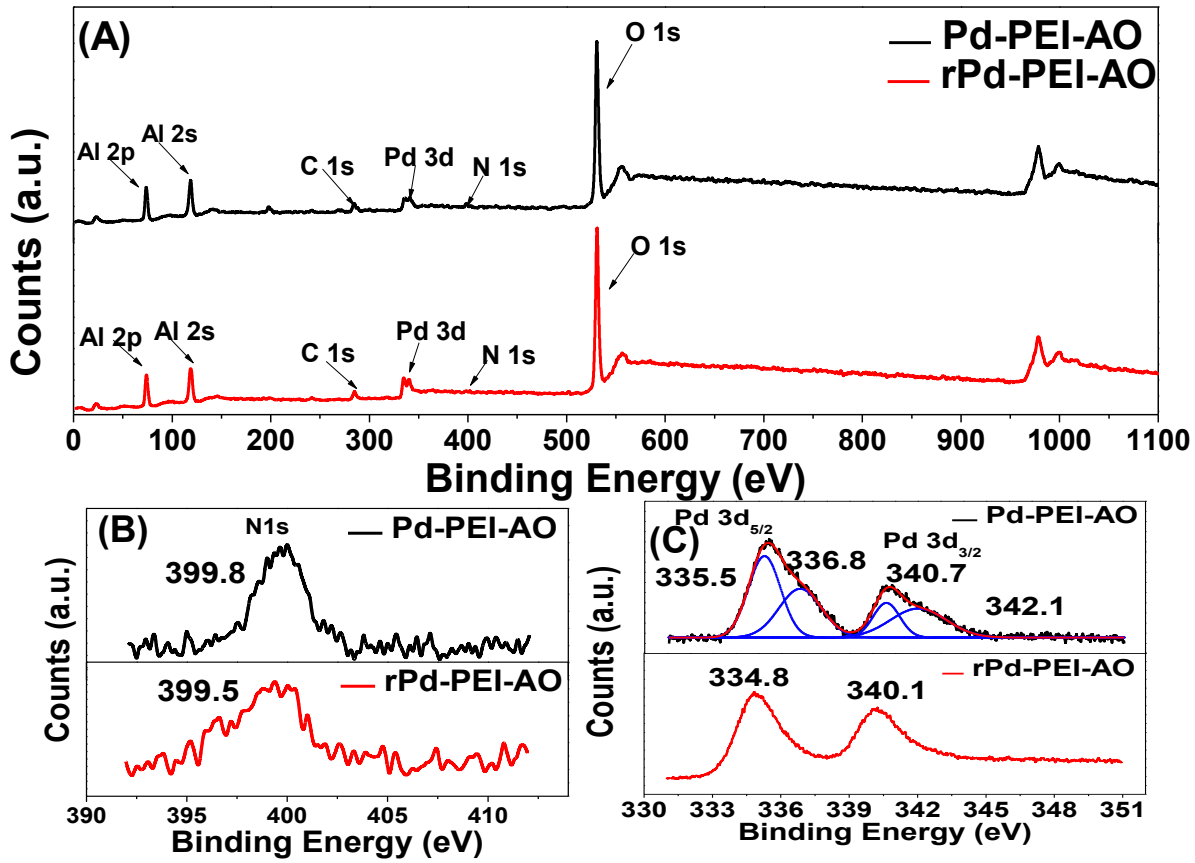

Figure 5.11: XPS survey scan (A), N 1*s* narrow scan (B), and Pd *3d* narrow scan (C) of Pd-PEI-AO and rPd-PEI-AO.

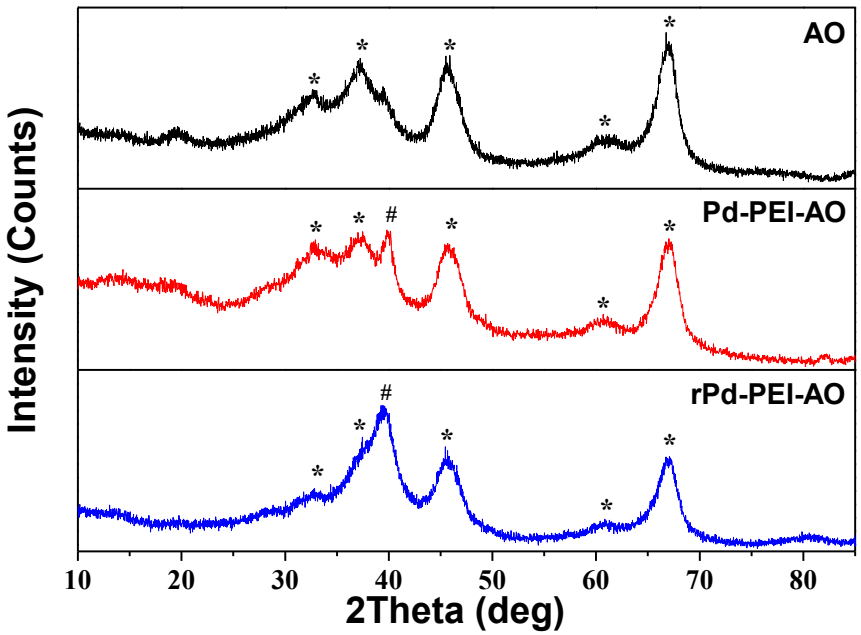

Figure 5.12: XRD patterns of pristine AO, Pd-PEI-AO, and rPd-PEI-AO (* and # indicates the planes corresponding to alumina and palladium, respectively).

XRD patterns were recorded for pristine AO, Pd-PEI-AO and rPd-PEI-AO and presented in Fig. 5.12. The pristine AO exhibited broad peaks, indicating the amorphous nature of alumina possessing a certain amount of nanocrystalline domains. The XRD pattern of Pd-PEI-AO was found to be almost identical to the pristine AO (JCPDS # 77-0396) except the peak at 39.9° corresponding to the (111) plane of palladium (JCPDS # 89-4897) was appeared. After reduction, the intensity of (111) plane of palladium in rPd-PEI-AO was increased, while the planes correspond to AO were relatively suppressed. This could be attributed to the increased crystallinity of palladium, facilitated by the reduction process.

FE-SEM imaging and EDS analysis for PEI-AO, Pd-PEI-AO and rPd-PEI-AO were performed and the results are shown in Fig. 5.13. In all the samples, the surface morphology of the AO was found to be almost identical. The samples were vastly found to possess flat plate-like particles, which were comprised of nano granules. The EDS analysis of PEI-AO revealed the presence of elements such as C, O, and Al. It is known that nitrogen is less sensitive and susceptible for interference in EDS and therefore excluded. In case of Pd-PEI-AO, in addition to C, O, and Al, about 0.8 at.% of Pd and 1.3 at.% of Cl were also detected. This could be attributed to the $PdCl_4^{2-}$ adsorbed over the Pd-PEI-AO. After reduction of palladium, the rPd-PEI-AO showed an increased amount of Pd (~1.1 at.%), while the Cl was completely absent. The loss of chlorine has additionally confirmed that the $PdCl_4^{2-}$ was successfully reduced to metallic palladium.

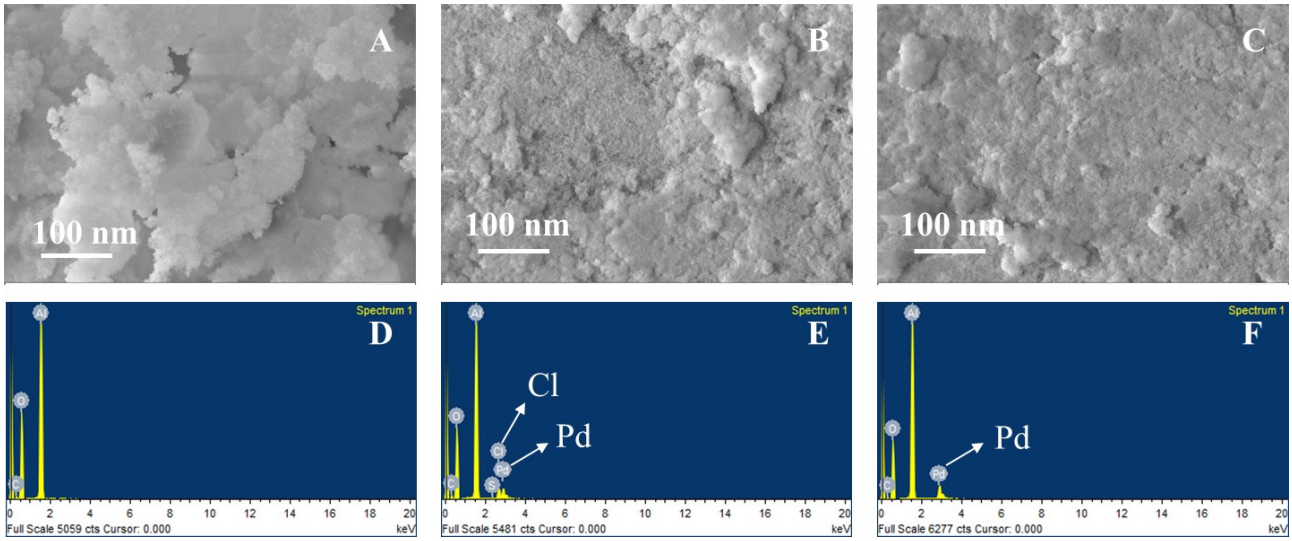

Figure 5.13: FE-SEM and EDS images of pristine AO (A and D), PEI-AO (B and E), and Pd-PEI-AO (C and F).

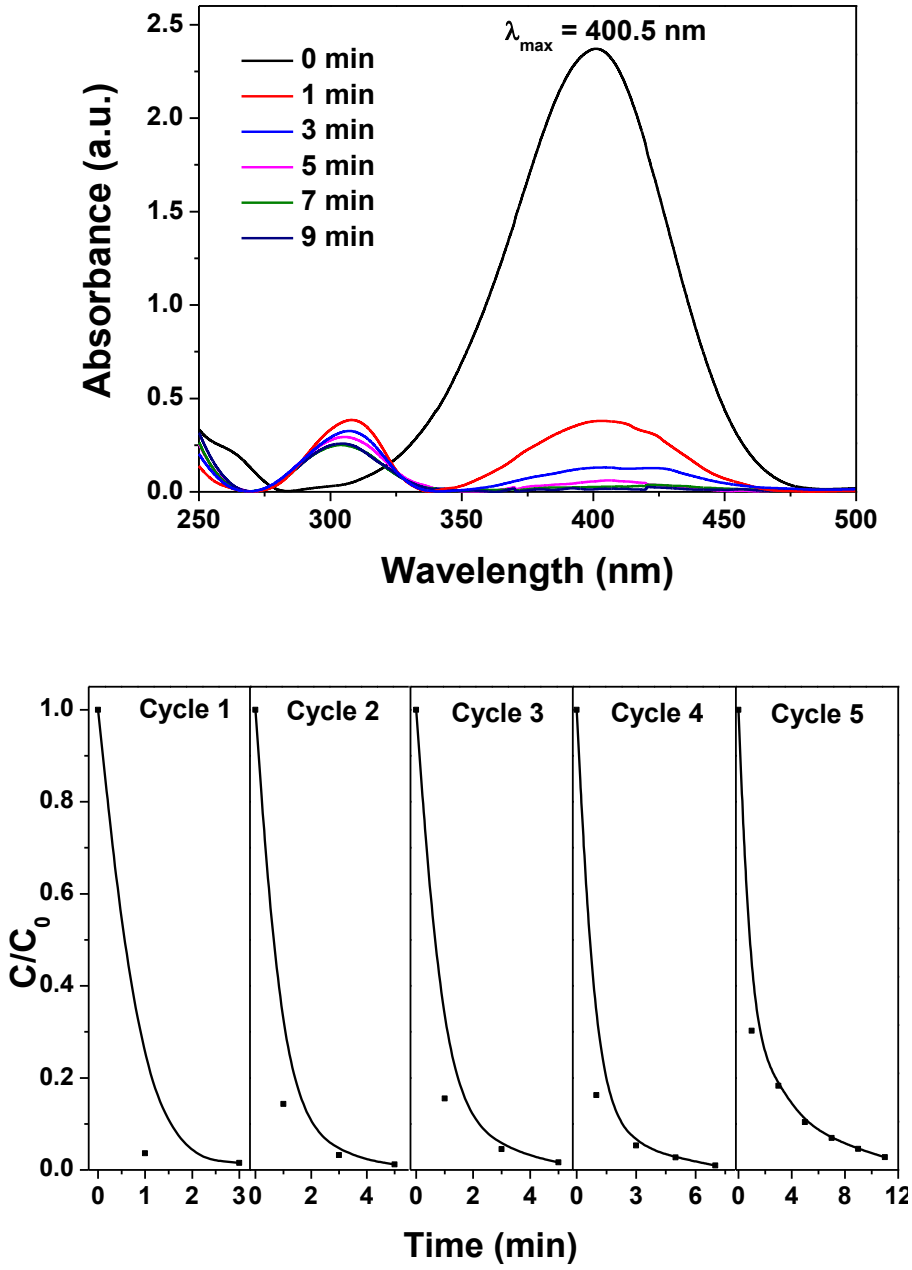

Figure 5.14: UV-Vis absorption spectra of 4-NP reduction (4th cycle) by Pd-PEI-AO (top) and the recyclability data for the reaction up to 5 cycles (bottom).

One of the popular catalytic performance evaluations of a noble metal catalyst is the conversion of 4-NP to 4-aminophenol (4-AP).[52] This conversion has practical significance that an endocrine disruptor (4-NP) chemical is converted to its corresponding amino derivative. In this case, the product 4-AP is a precursor for the synthesis of *paracetamol*, thus signifying the valorization of a potential hazardous chemical. The conversion of 4-NP to 4-AP was followed using UV-visible spectroscopy. The original yellow color of 4-NP was intensified to dark yellow upon addition of $NaBH_4$ due to the formation of phenolate ion, which exhibited an absorption maximum at 400.5 nm. When the catalyst was added, the color

of the solution was faded and became colorless on complete reduction of 4-NP. This was witnessed by the gradual decrease in the absorption band at 400.5 nm and formation of a new band at 307 nm, corresponding to the 4-AP. The representative UV-vis spectrum and the recyclability data are shown in Fig. 5.14. In the first cycle, 98% reduction of 4-NP was achieved in 3 minutes, while the fifth cycle required 11 min to accomplish the same. The gradual decrease in the activity could be due to the loss of small amount of palladium during each cycle and/or catalyst poisoning. Therefore, we quantified the total palladium content leached into the solution phase over 3 cycles using AAS and it was found that less than 1% of palladium got leached into the solution phase, while that desorbed using thiourea from the spent catalyst was found to be ~96%. The rate of 4-NP reduction at 10% conversion in the first cycle was found to be 125 mmol L^{-1} min^{-1} g^{-1}.

A representative inorganic polluting species is Cr(VI), which is considered to be potentially carcinogenic, while Cr(III) is known to be an essential metabolite for the function of insulin.[53] Hence, it is essential to convert Cr(VI) to the less toxic Cr(III) through a simple and facile process. The catalytic reduction of Cr(VI) to Cr(III) was chosen as a model system to explore the potential of Pd-PEI-AO towards environmental remediation. In an attempt towards Cr(VI) reduction, no significant reaction occurred when the Pd-PEI-AO was directly used as the catalyst. This is because the catalytic property of Pd(II) towards Cr(VI) reduction under the experimental conditions was poor. Therefore, the Pd-PEI-AO was subjected to reduction to yield rPd-PEI-AO, which was further used for Cr(VI) reduction. Oxalic acid was used as a sacrificial agent in this case. The reduction of Cr(VI) was followed using UV spectrometry at a wavelength maximum of 350 nm. About 95% reduction was attained within 3 min in the first cycle, while the fifth cycle required 7 min to accomplish the same (Fig. 5.14). This has revealed that the catalyst possessed adequate activity even after multiple times of regeneration. The rate of Cr(VI) reduction at 10% conversion in the first cycle was found to be 67 mmol L^{-1} min^{-1} g^{-1}. The palladium leaching studies revealed that ~7% of the metal was leached into the solution phase over 3 cycles of the reaction and ~88% of palladium was desorbed using thiourea solution. The little excess of palladium leaching as compared to the 4-NP reduction could be due to the oxalic acid used in the catalytic reaction, which could have interacted with the basic amine groups in PEI and caused liberation of small quantity of the bound metal.

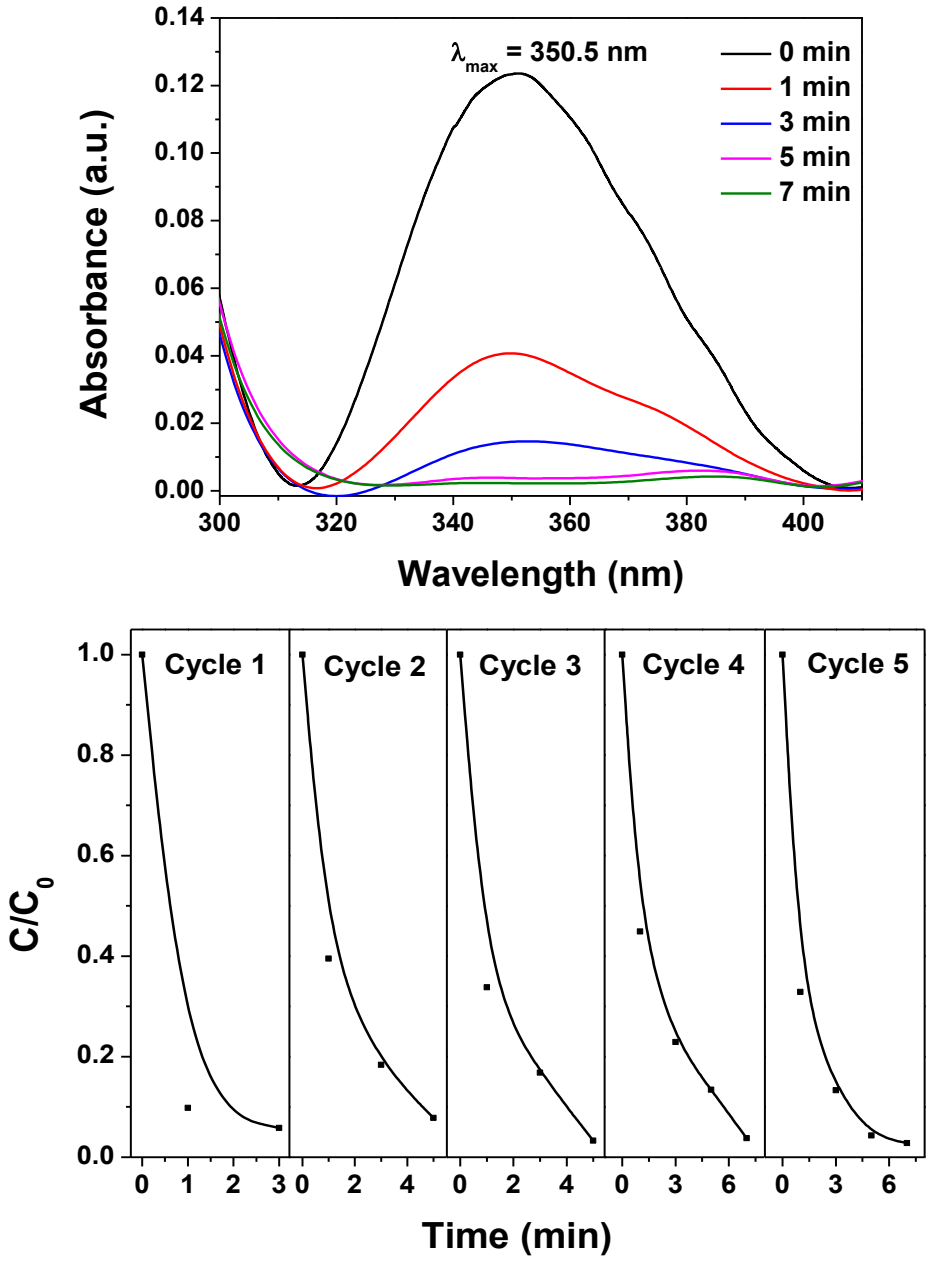

Figure 5.15: UV-Vis absorption spectra of Cr(VI) reduction (5th cycle) by rPd-PEI-AO (top) and the recyclability data for the reaction up to 5 cycles (bottom).

Sustainable hydrogen production is considered to be one of the important avenues to meet the growing energy demand. Among the various hydrogen sources, ammonia borane is considered to be one of the safest and green compounds that possess high density of hydrogen.[54] On-demand catalytic hydrogen generation is therefore considered to be an important reaction. The Pd-PEI-AO was tested for its catalytic activity towards hydrogen evolution from ammonia borane in aqueous medium. The first cycle produced the maximum amount (~52 mL) of hydrogen in about 2 min, while the successive cycles up to 5 times required 3 to 4 min of duration to produce similar quantity of hydrogen (Fig. 5.16). This has

additionally proven the high catalytic performance of Pd-PEI-AO even after multiple cycles with a minimal to moderate loss in activity. The rate of hydrogen production at 10% conversion in the first cycle was found to be 10.5 mol min^{-1} g^{-1}. The stability of the adsorbed palladium over 3 cycles was studied through estimation of the palladium content in the solution phase and solid phase before and after the reaction. AAS studies revealed that the total palladium content leached into the solution phase over 3 cycles was less than 1%, while that desorbed using thiourea from the spent catalyst was found to be ~96%.

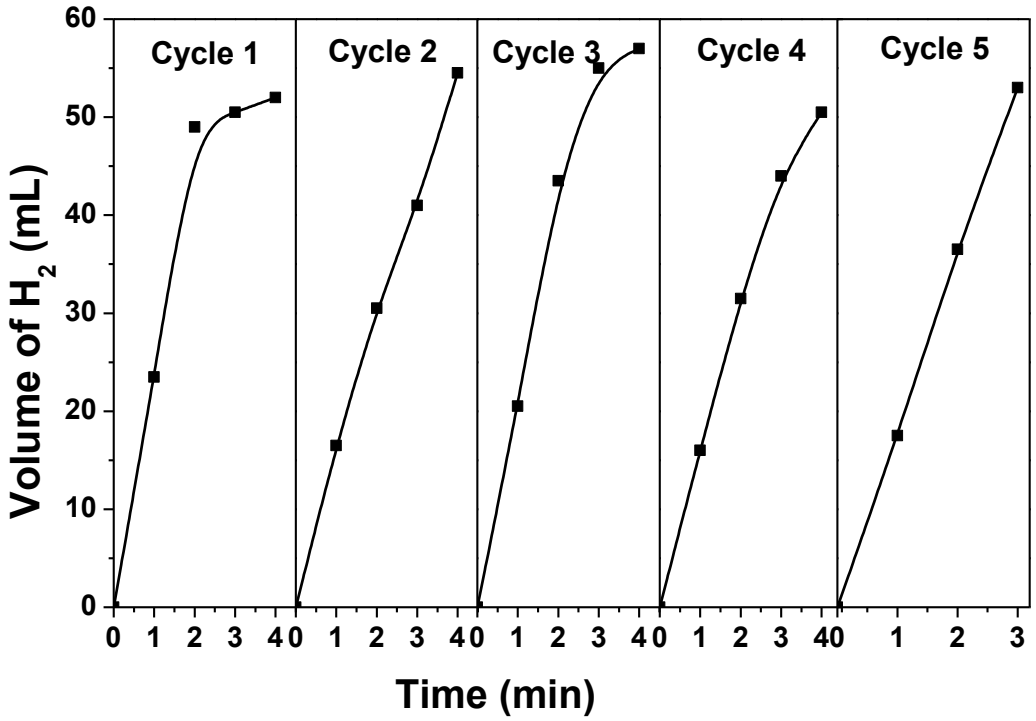

Figure 5.16: Hydrogen generation studies from ammonia borane up to 5 cycles using Pd-PEI-AO.

5.4 Conclusions

Facile surface functionalization of PEI over alumina nanopowder was accomplished in a two-step approach, which was confirmed using IR, XPS, TGA, and zeta potential measurements. The present work showed the utility of the PEI-coated alumina nanopowder towards effective adsorption of palladium. The sorption parameters of palladium were studied through pH effect, contact time, amount of adsorbent, concentrations and temperature. The optimum pH for the adsorption of Pd(II) was found to be 6.0 and the adsorption adhered to the pseudo second-order kinetics. While the native alumina showed an adsorption capacity of 35.08 mg g^{-1}, the PEI-AO exhibited a high adsorption capacity of 97.7 mg g^{-1}, obtained through Langmuir adsorption isotherm. The exothermic nature of adsorption process and the negative

free energy obtained at various temperatures confirm the spontaneity of adsorption. XPS analysis of Pd-PEI-AO, and rPd-PEI-AO revealed the favorable interaction of $PdCl_4^{2-}$ with nitrogen moieties of PEI. XRD studies on these samples revealed an increase in the crystallinity of palladium after reduction. The catalytic reduction of 4-NP and Cr(VI) using Pd-PEI-AO was found to proceed with rates as high as 125 mmol L^{-1} min^{-1} g^{-1} and 67 mmol L^{-1} min^{-1} g^{-1}, respectively. Hydrogen generation from ammonia borane was found to be efficient with Pd-PEI-AO with a rate of 10.5 mol min^{-1} g^{-1} at 10% conversion. Recyclability of Pd-PEI-AO was studied up to 5 cycles in all the three catalytic reactions, which revealed the potential of the sorbent for efficient reusability. The amine-functionalization strategy presented in this work could also show potential in recovering and reusing other precious metals such as gold, platinum, and rhodium.[28]

5.5 References

1. Ruiz-Castillo, P.; Buchwald, S. L., Applications of palladium-catalyzed C–N cross-coupling reactions. *Chemical Reviews* **2016,** *116* (19), 12564-12649.

2. Johansson Seechurn, C. C.; Kitching, M. O.; Colacot, T. J.; Snieckus, V., Palladium-catalyzed cross-coupling: a historical contextual perspective to the 2010 Nobel Prize. *Angewandte Chemie International Edition* **2012,** *51* (21), 5062-5085.

3. Huang, Y. B.; Yang, Z.; Chen, M. Y.; Dai, J. J.; Guo, Q. X.; Fu, Y., Heterogeneous palladium catalysts for decarbonylation of biomass-derived molecules under mild conditions. *ChemSusChem* **2013,** *6* (8), 1348-1351.

4. Suresh Kumar, B.; Amali, A. J.; Pitchumani, K., Mesoporous microcapsules through d-glucose promoted hydrothermal self-assembly of colloidal silica: reusable catalytic containers for palladium catalyzed hydrogenation reactions. *ACS Sustainable Chemistry & Engineering* **2016,** *5* (1), 667-674.

5. Garrett, C. E.; Prasad, K., The art of meeting palladium specifications in active pharmaceutical ingredients produced by Pd-catalyzed reactions. *Advanced Synthesis & Catalysis* **2004,** *346* (8), 889-900.

6. Kohler, K.; Heidenreich, R. G.; Soomro, S. S.; Prockl, S. S., Supported palladium catalysts for suzuki reactions: structure-property relationships, optimized reaction protocol and control of palladium leaching. *Advanced Synthesis & Catalysis* **2008,** *350* (18), 2930-2936.

7. Hosseini, M. J.; Jafarian, I.; Farahani, S.; Khodadadi, R.; Tagavi, S.; Naserzadeh, P.; Mohammadi-Bardbori, A.; Arghavanifard, N., New mechanistic approach of inorganic palladium toxicity: impairment in mitochondrial electron transfer. *Metallomics* **2016,** *8* (2), 252-259.

8. Shultz, M. D.; Lassig, J. P.; Gooch, M. G.; Evans, B. R.; Woodward, J., Palladium-a new inhibitor of cellulase activities. *Biochemical and Biophysical Research Communications* **1995,** *209* (3), 1046-1052.

9. Katal, R.; Hasani, E.; Farnam, M.; Baei, M. S.; Ghayyem, M. A., Charcoal ash as an adsorbent for Ni(II) adsorption and its application for wastewater treatment. *Journal of Chemical & Engineering Data* **2012,** *57* (2), 374-383.

10. Ruiz, M.; Sastre, A. M.; Guibal, E., Palladium sorption on glutaraldehyde-crosslinked chitosan. *Reactive and Functional Polymers* **2000,** *45* (3), 155-173.

11. Yamada, M.; Gandhi, M. R.; Kondo, Y.; Haga, K.; Shibayama, A.; Hamada, F., Selective sorption of palladium by thiocarbamoyl-substituted thiacalix[n]arene derivatives immobilized on amberlite resin: application to leach liquors of automotive catalysts. *RSC Advances* **2015,** *5* (74), 60506-60517.

12. Sharififard, H.; Soleimani, M.; Ashtiani, F. Z., Evaluation of activated carbon and bio-polymer modified activated carbon performance for palladium and platinum removal. *Journal of the Taiwan Institute of Chemical Engineers* **2012,** *43* (5), 696-703.

13. Liu, L.; Liu, S.; Zhang, Q.; Li, C.; Bao, C.; Liu, X.; Xiao, P., Adsorption of Au(III), Pd(II), and Pt(IV) from aqueous solution onto graphene oxide. *Journal of Chemical & Engineering Data* **2012,** *58* (2), 209-216.

14. Sharma, S.; Rajesh, N., 2-Mercaptobenzothiazole impregnated cellulose prepared by ultrasonication for the effective adsorption of precious metal palladium. *Chemical Engineering Journal* **2014,** *241*, 112-121.

15. Sharma, S.; Barathi, M.; Rajesh, N., Efficacy of a heterocyclic ligand anchored biopolymer adsorbent for the sequestration of palladium. *Chemical Engineering Journal* **2015,** *259*, 457-466.

16. Sharma, S.; Wu, C. M.; Koodali, R. T.; Rajesh, N., An ionic liquid-mesoporous silica blend as a novel adsorbent for the adsorption and recovery of palladium ions, and its

applications in continuous flow study and as an industrial catalyst. *RSC Advances* **2016,** *6* (32), 26668-26678.

17. Wen, Y.; Pan, S.; Luo, X.; Zhang, X.; Zhang, W.; Feng, M., A biodegradable low molecular weight polyethylenimine derivative as low toxicity and efficient gene vector. *Bioconjugate Chemistry* **2009,** *20* (2), 322-332.

18. Moghimi, S. M.; Symonds, P.; Murray, J. C.; Hunter, A. C.; Debska, G.; Szewczyk, A., A two-stage poly(ethylenimine)-mediated cytotoxicity: implications for gene transfer/therapy. *Molecular Therapy* **2005,** *11* (6), 990-995.

19. Kim, J. H.; Choung, P. H.; Kim, I. Y.; Lim, K. T.; Son, H. M.; Choung, Y. H.; Cho, C. S.; Chung, J. H., Electrospun nanofibers composed of poly(ε-caprolactone) and polyethylenimine for tissue engineering applications. *Materials Science and Engineering: C* **2009,** *29* (5), 1725-1731.

20. Kuo, Y. C.; Ku, I. N., Application of polyethyleneimine-modified scaffolds to the regeneration of cartilaginous tissue. *Biotechnology Progress* **2009,** *25* (5), 1459-1467.

21. Nagarjuna, R.; Challagulla, S.; Ganesan, R.; Roy, S., High rates of Cr(VI) photoreduction with magnetically recoverable nano-Fe_3O_4@Fe_2O_3/Al_2O_3 catalyst under visible light. *Chemical Engineering Journal* **2017,** *308*, 59-66.

22. Sabermahani, F.; Taher, M. A., Flame atomic absorption determination of palladium after separation and preconcentration using polyethyleneimine water-soluble polymer/alumina as a new sorbent. *Journal of Analytical Atomic Spectrometry* **2010,** *25* (7), 1102-1106.

23. Cho, C. W.; Kang, S. B.; Kim, S.; Yun, Y. S.; Won, S. W., Reusable polyethylenimine-coated polysulfone/bacterial biomass composite fiber biosorbent for recovery of Pd(II) from acidic solutions. *Chemical Engineering Journal* **2016,** *302*, 545-551.

24. Park, J.; Won, S. W.; Mao, J.; Kwak, I. S.; Yun, Y. S., Recovery of Pd(II) from hydrochloric solution using polyallylamine hydrochloride-modified Escherichia coli biomass. *Journal of Hazardous Materials* **2010,** *181* (1-3), 794-800.

25. Won, S. W.; Park, J.; Mao, J.; Yun, Y. S., Utilization of PEI-modified corynebacterium glutamicum biomass for the recovery of Pd(II) in hydrochloric solution. *Bioresource Technology* **2011,** *102* (4), 3888-3893.

26. Sabermahani, F.; Saeidi, M.; Sharifzade, V., Removal of nickel(II) and palladium(II) from surface waters. *Bulletin of the Chemical Society of Ethiopia* **2013,** *27* (1), 15-23.

27. Awual, M. R.; Yaita, T., Rapid sensing and recovery of palladium(II) using N,N-bis(salicylidene)1,2-bis(2-aminophenylthio)ethane modified sensor ensemble adsorbent. *Sensors and Actuators B: Chemical* **2013,** *183*, 332-341.

28. Dai, Y.; Formo, E.; Li, H.; Xue, J.; Xia, Y., Surface-functionalized electrospun titania nanofibers for the scavenging and recycling of precious metal ions. *ChemSusChem* **2016,** *9* (20), 2912-2916.

29. Chavan, S. P.; Bishwa Bidita Varadwaj, G.; Parida, K. M.; Bhanage, B. M., Solvent-switchable regioselective synthesis of aurones and flavones using palladium-supported amine-functionalized montmorillonite as a heterogeneous catalyst. *ChemCatChem* **2016,** *8* (16), 2649-2658.

30. Bertazzo, S.; Rezwan, K., Control of α-alumina surface charge with carboxylic acids. *Langmuir* **2009,** *26* (5), 3364-3371.

31. Ganesan, R.; Yoo, S. Y.; Choi, J. H.; Lee, S. Y.; Kim, J. B., Simple micropatterning of biomolecules on a diazoketo-functionalized photoresist. *Journal of Materials Chemistry* **2008,** *18* (6), 703-709.

32. Lewis, W. K.; Rosenberger, A. T.; Gord, J. R.; Crouse, C. A.; Harruff, B. A.; Fernando, K. S.; Smith, M. J.; Phelps, D. K.; Spowart, J. E.; Guliants, E. A., Multispectroscopic (FTIR, XPS, and TOFMS−TPD) investigation of the core−shell bonding in sonochemically prepared aluminum nanoparticles capped with oleic acid. *The Journal of Physical Chemistry C* **2010,** *114* (14), 6377-6380.

33. Van den Brand, J.; Blajiev, O.; Beentjes, P.; Terryn, H.; De Wit, J., Interaction of anhydride and carboxylic acid compounds with aluminum oxide surfaces studied using infrared reflection absorption spectroscopy. *Langmuir* **2004,** *20* (15), 6308-6317.

34. Pletincx, S.; Trotochaud, L.; Fockaert, L. L.; Mol, J. M.; Head, A. R.; Karslıoglu, O.; Bluhm, H.; Terryn, H.; Hauffman, T., In situ characterization of the initial effect of water on molecular interactions at the interface of organic/inorganic hybrid systems. *Scientific Reports* **2017,** *7*, 45123.

35. Shen, L.; Zhang, L.; Chen, M.; Chen, X.; Wang, J., The production of pH-sensitive photoluminescent carbon nanoparticles by the carbonization of polyethylenimine and their use for bioimaging. *Carbon* **2013,** *55*, 343-349.

36. Rotole, J. A.; Sherwood, P. M., Gamma-alumina (γ-Al_2O_3) by XPS. *Surface Science Spectra* **1998,** *5* (1), 18-24.

37. Choi, J. H.; Ganesan, R.; Kim, D. K.; Jung, C. H.; Hwang, I. T.; Nho, Y. C.; Yun, J. M.; Kim, J. B., Patterned immobilization of biomolecules by using ion irradiation-induced graft polymerization. *Journal of Polymer Science Part A: Polymer Chemistry* **2009,** *47* (22), 6124-6134.

38. Langmuir, I., The adsorption of gases on plane surfaces of glass, mica and platinum. *Journal of the American Chemical Society* **1918,** *40* (9), 1361-1403.

39. Hubicki, Z.; Wołowicz, A., A comparative study of chelating and cationic ion exchange resins for the removal of palladium(II) complexes from acidic chloride media. *Journal of Hazardous Materials* **2009,** *164* (2-3), 1414-1419.

40. Baki, M. H.; Shemirani, F.; Khani, R.; Bayat, M., Applicability of diclofenac–montmorillonite as a selective sorbent for adsorption of palladium(II); kinetic and thermodynamic studies. *Analytical Methods* **2014,** *6* (6), 1875-1883.

41. Freundlich, H., Over the Adsorption in Solution. *Journal of Physical Chemistry* **1907,** *57* (1), 385-470.

42. Singh, K. K.; Ruhela, R.; Das, A.; Kumar, M.; Singh, A. K.; Hubli, R. C.; Bajaj, P. N., Separation and recovery of palladium from spent automobile catalyst dissolver solution using dithiodiglycolamide encapsulated polymeric beads. *Journal of Environmental Chemical Engineering* **2015,** *3* (1), 95-103.

43. Lagergren, S., About the theory of so-called adsorption of soluble substances. *Sven. Vetenskapsakad. Handingarl* **1898,** *24*, 1-39.

44. Ho, Y.; McKay, G., A multi-stage batch sorption design with experimental data. *Adsorption Science & Technology* **1999,** *17* (4), 233-243.

45. Krishna Kumar, A. S.; Kalidhasan, S.; Rajesh, V.; Rajesh, N., Adsorptive demercuration by virtue of an appealing interaction involving biopolymer cellulose and

mercaptobenzothiazole. *Industrial & Engineering Chemistry Research* **2013,** *52* (34), 11838-11849.

46. Li, K.; Wang, X., Adsorptive removal of Pb(II) by activated carbon prepared from Spartina alterniflora: equilibrium, kinetics and thermodynamics. *Bioresource Technology* **2009,** *100* (11), 2810-2815.

47. Shen, X. E.; Shan, X. Q.; Dong, D. M.; Hua, X. Y.; Owens, G., Kinetics and thermodynamics of sorption of nitroaromatic compounds to as-grown and oxidized multiwalled carbon nanotubes. *Journal of Colloid and Interface Science* **2009,** *330* (1), 1-8.

48. Li, J.; Tang, W.; Huang, J.; Jin, J.; Ma, J., Polyethyleneimine decorated graphene oxide-supported $Ni_{1-x}Fe_x$ bimetallic nanoparticles as efficient and robust electrocatalysts for hydrazine fuel cells. *Catalysis Science & Technology* **2013,** *3* (12), 3155-3162.

49. Wang, F.; Liu, P.; Nie, T.; Wei, H.; Cui, Z., Characterization of a polyamine microsphere and its adsorption for protein. *International Journal of Molecular Sciences* **2012,** *14* (1), 17-29.

50. Tang, H.; Zhou, C.; Wu, R.; Mao, M.; Shen, H.; Li, L. S., The enhanced fluorescence properties & colloid stability of aqueous CdSe/ZnS QDs modified with N-alkylated poly(ethyleneimine). *New Journal of Chemistry* **2015,** *39* (6), 4334-4342.

51. Saifullah, M. S.; Ganesan, R.; Lim, S. H.; Hussain, H.; Low, H. Y., Large area sub-100 nm direct nanoimprinting of palladium nanostructures. *RSC Advances* **2016,** *6* (26), 21940-21947.

52. Mallampati, R.; Valiyaveettil, S., Eggshell membrane-supported recyclable catalytic noble metal nanoparticles for organic reactions. *ACS Sustainable Chemistry & Engineering* **2014,** *2* (4), 855-859.

53. Challagulla, S.; Nagarjuna, R.; Ganesan, R.; Roy, S., Acrylate-based polymerizable sol–gel synthesis of magnetically recoverable TiO_2 supported Fe_3O_4 for Cr(VI) photoreduction in aerobic atmosphere. *ACS Sustainable Chemistry & Engineering* **2016,** *4* (3), 974-982.

54. Stephens, F. H.; Pons, V.; Baker, R. T., Ammonia–borane: the hydrogen source par excellence? *Dalton Transactions* **2007,** (25), 2613-2626.

Chapter 6

Design and synthesis of photocurable precursors for direct nanoimprinting of metal oxide micro/nano structures

Chapter 6: Design and synthesis of photocurable precursors for direct nanoimprinting of metal oxide micro/nano structures

6.1 Introduction

Fabrication of micro/nanostructures of oxides is of paramount importance in various applications including photoelectrochemical cells,[1] photovoltaic cells,[2] sensors,[3] and catalysis.[4] Several techniques including photolithography,[5,6] electron-beam lithography,[7,8] electro-hydrodynamic lithography,[9,10] direct write assembly,[11] selective surface wetting,[12] dip-pen nanolithography,[13,14] nanoimprint lithography (NIL)[15-17] among others[18,19] have been utilized towards fabrication of metal oxide micro/nanostructures. Each of these techniques has its own merits as well as limitations. Among the various available techniques, NIL has been regarded as the next generation fabrication approach due to its advantages such as simplicity, low-cost, high-fidelity, high-resolution, non-dependence on the optical diffraction limit, compatibility with various substrates and ability to imprint arbitrary structures over flat and curved surfaces.[20-23] The descendants of NIL like step-and-flash,[24-26] roll-to-roll[27] and roll-to-flat[28] imprint lithography techniques have augmented its high-throughput capability while maintaining high-precision. The NIL process can be broadly classified into two categories: thermal and UV. Thermal NIL requires temperature cycling, which reduces the throughput, affects the mold life, and leads to line-width variation owing to the differences in thermal expansion coefficients of the mold, substrate, and resist.[29] On the other hand, UV-NIL is an attractive room temperature process that does not require any temperature cycling, and thereby allows high-throughput patterning. As opposed to the fabrication of polymeric micro/nanostructures, fabrication of oxides has inherent challenges in the materials design as the metal-containing polymers and ceramics do not possess workable characteristics for direct patterning. Therefore, the material design has to be customized as per the requirement of each technique. In the case of nanoimprinting, sol–gel approach was initially employed that utilized hydrolysis followed by condensation of metal alkoxides or halides.[16,30-32] The conventional sol–gel approach suffered low yield due to the lack of mechanical strength of the imprints during the demolding step. Nanoparticle suspensions have also been used for direct nanoimprinting with a soft PDMS mold.[33] This approach has been used to directly fabricate three-dimensional structures of multicomponent oxides like indium tin oxide and nickel ferrite.[34,35] Photosensitive ethylhexanoate-based oxide patterning has been reported that utilizes photo-breakable precursors rather than photo-curable monomers.[17] In this concern, the polymerizable sol–gel approach (PSG) has emerged as a promising method for

rapid direct nanoimprinting of a host of metal oxides such as TiO_2, ZrO_2, Hf_2O_5 amongst others.[29,36,37] The PSG approach utilizes metal-methacrylate liquid precursors that undergo *in situ* thermal- or photo-induced free radical polymerization during the nanoimprinting step. One of the major advantages of this approach is the spin-coatable liquid phase metal-containing resin that can easily fill up the pattern features of the mold at near-ambient pressure due to capillary action. Polymerization solidifies the metal-containing precursor and decreases the surface energy to facilitate easy and clean demolding. This approach has been found to harness the advantages and obviates the limitations of the conventional sol–gel approach. The PSG approach has been shown to be suitable for high-throughput step-and-flash imprint lithography for various oxides[38] and to synthesize supported oxide photo-catalysts.[39,40] Despite the high potential, the PSG approach based on free radical polymerization of methacrylates is vulnerable to radical scavenging by oxygen that could affect the degree of polymerization, which in turn could effect on the quality of imprinting. This warrants purging/bubbling of inert gas into the metal-containing resin before patterning in order to eliminate any dissolved oxygen.

6.1.1 Thiol-ene photo click chemistry

Due to its simplicity, versatility, and specific reactivity, click chemistry has gained significant interest in various fields including organic transformations, surface functionalization, polymeric materials, and biological applications.[41-46] Several reactions including alkyne-azide, Diels-Alder reactions, thiol-ene, thiol-yne, etc., have been classified under click chemistry, as these reactions directly yield an adduct without giving any other byproduct.[47] Among them, thiol-ene click is an interesting reaction occurring between commonly available reactive alkenes and thiol groups, which are known to be tolerant to the presence of oxygen and moisture when the oxygen concentration is less than that of thiol.[48-52] Thiol-ene reaction is also called as hydrothiolation, in which the thiol group adds across the carbon-carbon double bond in anti-Markovnikov orientation. Generally, the hydrothiolation reaction can proceed under a variety of conditions such as thermal catalytic processes, and photo-addition.[53-56] Hydrothiolation *via* photo-clicking is attractive as it proceeds well at room temperature reaction conditions. In a typical thiol-ene click reaction, the photo-generated electron from a photo-initiator is transferred to the thiol group to produce a thiyl radical, which adds across a carbon-carbon double bond and thus transferring the radical to the alkene. Abstraction of a hydrogen radical from the neighborhood thiol to this carbon radical accomplishes the hydrothiolation, while simultaneously propagating the chain reaction.[49,57]

As thiol-ene click chemistry can fulfil the requirements such as oxygen-insensitivity, spin-coatability, and room temperature photo-crosslinking, it is deemed to be attractive for UV-NIL.[58-60] This chemistry has recently been shown for its potential for imprinting polymeric structures over flat and curved surfaces.[61] However, the merits of the thiol-ene photo-click chemistry have so far not been realized for oxide nanoimprinting. Here, we show the augmentation of the PSG approach by employing the oxygen-insensitive thiol-ene click chemistry towards fabrication of metal oxide micro/nanostructures (Scheme 6.1). The design of the photo-curable metal-containing resin, its photo-curability and patternability are discussed by choosing titanium alkoxide as the precursor to fabricate TiO_2 nanostructures. TiO_2 was chosen as the principal oxide candidate, as it is one of the most studied semiconducting oxides that possesses huge potential for various applications including energy, health, and environment.[62-64] Finally, the thiol-ene approach was also studied for patterning Ta_2O_5 in order to ascertain its potential towards structuring other metal oxides.

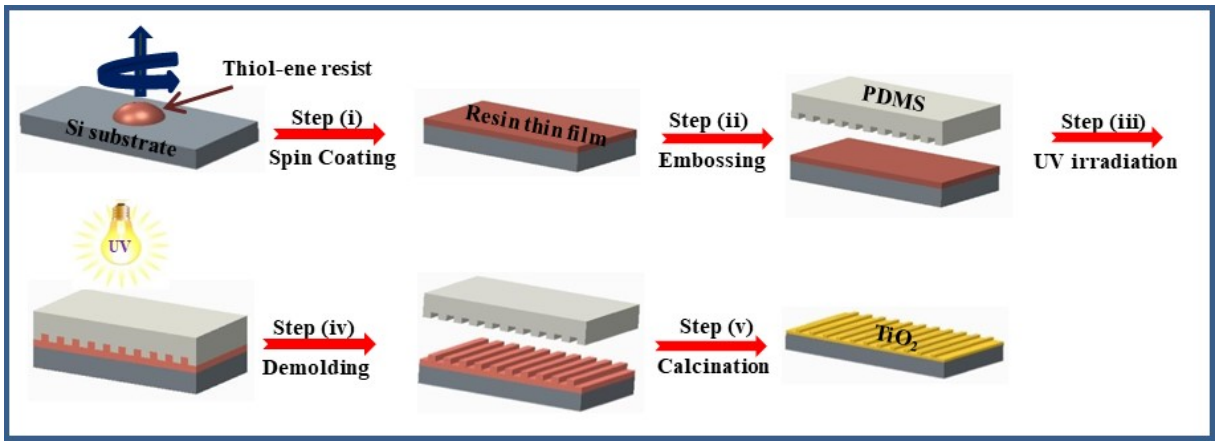

Scheme 6.1: Schematic representation of the overall process involving thiol-ene click chemistry for imprinting of metal oxides.

6.1.2 Ring opening polymerization chemistry

Direct nanoimprinting of oxides typically uses metal-containing polymerizable precursors that are synthesized by reacting the corresponding metal alkoxides with polymerizable chelating agent such as acetoacetate-functionalized acrylate. Imprintable resin formulations are prepared by mixing suitable proportions of the precursor with a reactive diluent, which typically enhances the spin-coatability and increases the crosslinking density. Although, this strategy was very successful in direct imprinting of several oxides and found to be compatible with the high throughput technique like step-and-flash imprint lithography, due to lesser metal content the final oxide patterns were shrunk ~70-80% during the calcination step.

Increasing of metal content increases the challenge, as the resin needs to fulfil the requirements of spin-coatability and high crosslinking density for direct imprintability, which are mainly governed by the organics present in it. This results in a tradeoff between the imprintability and the pattern shrinkage. In this work, we aim to decrease the pattern size reduction by not including any reactive diluents in the imprintable resin. We have taken TiO_2 as the candidate due to the reasons mentioned above. Instead of titanium *iso*-propoxide, we chose titanium ethoxide in this work, the ethoxy group possesses one carbon lesser than the *iso*-propoxy group. To obtain well-cured resin, we selected epoxy group and its analogous oxetane group for their high cross-linkability through ring opening polymerization.

By designing the appropriate monomers, for the first time, we augment the capability of the PSG approach with epoxy- and oxetane-functionalized metal-containing resin that falls under the category of chemically amplified resists (CARs). The CARs, which are very popular in the photolithography process of semiconductor industries, typically utilize photoacid generator (PAG) that generates a strong acid upon UV exposure.[65,66]In a typical negative tone resist, the reactive functional group such as epoxy consumes a photogenerated acid and undergoes ring opening during a subsequent post-exposure bake (PEB) step and generate an acid at the end of the ring opening step. Thus, the photogenerated acid is generated back after every ring opening and such resists are therefore called as CARs. The CARs have the advantages such as very short UV exposure duration (typically less than 1 min) and short PEB time (typically less than 2 min). Thus, CARs are considered to be high potential resists under optimized conditions. Additionally, the epoxy- and oxetane-based resists are known to be oxygen insensitive and therefore do not require inert processing conditions.[65-67] Few literature have reported the application of epoxy chemistry in NIL, wherein epoxy-functionalized silicon was used. [65,68] Another work by Wu et al., used epoxy/inorganic hybrid resist for the imprinting of SiO_2 and TiO_2 nanoparticles, in which the diglycidyl ether of bisphenol A (DGEBA) resin is mixed with tetraethyl orthotitanate ($Ti(OEt)_4$) and tetraethyl orthosilicate $Si(OEt)_4$) with the help of coupling agent (3-glycidyloxypropyltrimethoxysilane (GLYMO)). The TiO_2 and SiO_2 nanoparticles were formed by sol–gel processing and enhanced the thermal properties and etching resistability of the epoxy resin.[69] However, a metal-containing epoxy/oxetane functionalized single source precursor has not been reported so far for the fabrication of oxide patterns through NIL.

In the present work, we synthesized epoxy- and oxetane-functionalized acetoacetate derivatives and complexed them with titanium ethoxide to formulate imprintable resits. The design of the metal-containing CAR, and its patternability are discussed (Scheme 6.2).

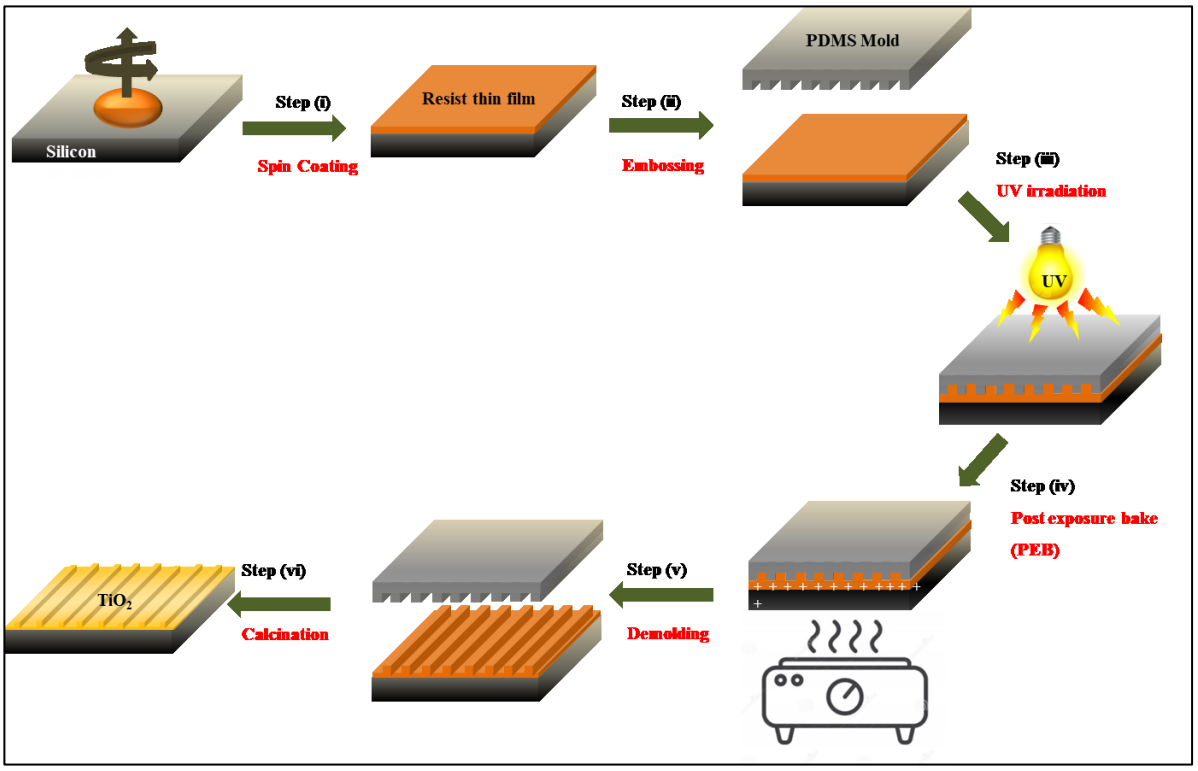

Scheme 6.2: Schematic representation of the overall process involving ring opening polymerization chemistry for imprinting of metal oxides.

6.2 Thiol-ene photo click chemistry

6.2.1 Experimental section

(i) Resin formulation

The TiO_2 resists were prepared using requisite amounts of precursors as mentioned in Table 6.1. Briefly, one equivalent of Ti(*i*-PrO)$_4$ was added and thoroughly stirred with 4 equivalents of AAAc in a glass vial inside a nitrogen glove box. The color of the solution rapidly turned into red that indicated the formation of Ti(AAA)$_4$ complex. To this complex, either half equivalent or one equivalent of the PETMP cross-linker was added and the resultant mixture was shaken well on a vortex stirrer for 2 min to obtain a clear solution. To this mixture, 3 wt% (with respect to the AAAc and PETMP) of HMP photo-initiator was added to formulate the imprintable resin, which was diluted with toluene in 1:1 (wt.:wt.) ratio to decrease the viscosity. The Ta_2O_5 resist was also prepared in a similar manner by taking tantalum (V) ethoxide as the alkoxide source.

Table 6.1: Proportions of various components used in the different formulations

Sample code	TIPO (mmol)	AAAc (mmol)	PETMP (mmol)	HMP (mmol)
TA	1.0	4.0	0.0	0.156
TAP-0.5	1.0	4.0	0.50	0.208
TAP-1	1.0	4.0	1.00	0.277

(ii) Imprinting of metal oxide

First, PDMS stamps were fabricated following the standard procedure from Sylgard 184. Briefly, the silicon rubber base pre-polymer and cross-linker of Sylgard 184 were thoroughly mixed in 10:1 weight ratio and the resulting mixture was poured over polycarbonate master mold kept in a petri dish. This assembly was degassed in a vacuum desiccator to remove any trapped air bubbles. The assembly was the subjected to 70 °C for 1 h to induce cross-linking of the precursor. Finally, the PDMS elastomeric stamp was peeled off from the master mold. The fabricated PDMS stamps were treated with 1H,1H,2H,2H–perfluorodecyltrichlorosilane for 5 h inside an evacuated desiccator in order to decrease the surface energy that facilitates easy demolding. The water contact angle of the fluorinated PDMS stamp was found to be ~130° as opposed to 105° of freshly prepared PDMS, indicating the reduction in surface energy.

In a typical nanoimprinting process, the metal-containing resin solution was spin-coated over a silicon wafer (20 mm × 20 mm) at 1000 rpm for 45 s. The PDMS mold was then placed on top of the wet thin film and a slight pressure was applied. This assembly was subjected to UV irradiation with a Hg vapor lamp (125 W) for 20 min to induce crosslinking of the monomers. After UV exposure, the PDMS stamp was carefully demolded and the imprints were subjected to calcination at designated temperatures for 1 h to obtain metal oxide micro/nanostructures.

6.2.2 Results and Discussion

A judicious choice of precursors is the key to successful implementation of the thiol-ene click chemistry to realize oxide nanofabrication. In this regard, we chose pentaerythritol tetrakis(3-mercaptopropionate) (PETMP) as the cross-linker that has four thiol arms. Allyl acetoacetate (AAAc) was chosen as the bifunctional reagent that on one hand chelates with the metal

center through the acetoacetate group and on the other hand possesses the reactive alkene group for the click reaction. When the metal center is chelated with more than one AAAc, it could also act as a cross-linker, which would lead to the formation of highly branched polymeric network. The chemical structures of the various components used in this study are shown in Fig. 6.1.

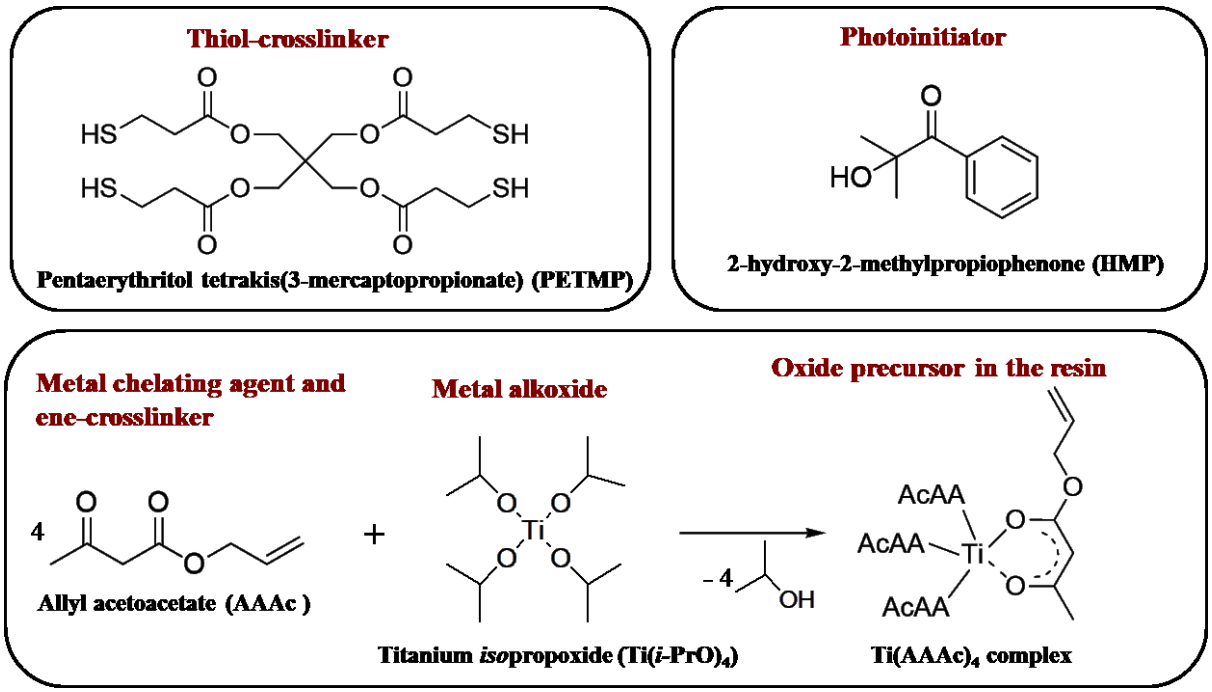

Figure 6.1: Chemical structures of the various components used for imprinting of metal oxides.

To probe the thiol-ene click reaction under UV irradiation, we formulated a resin containing PETMP and AAAc in 1:4 ratio mixed with 3 wt% of 2-hydroxy-2-methylpropiophenone (HMP) photo-initiator. This metal-free resin was spin-coated over a pre-cleaned silicon wafer and studied with the Fourier transform infrared (FT-IR) spectroscopy to follow the thiol-ene photo-click chemistry (Fig. 6.2 (a)). As seen from the figure, the characteristic –SH stretching peak was observed at 2570 cm^{-1}, confirming the presence of free thiol groups in the resin formulation. In addition, an intense peak at 1738 cm^{-1} due to the carbonyl group stretching and a weak peak at 1632 cm^{-1} due to the alkene group were also observed. After subjecting the film to 20 min of UV irradiation, it remained wet, indicating poor efficiency of the thiol-ene click-reaction in this system. The FT-IR spectrum obtained after irradiation was almost identical to that before UV irradiation. We postulated that this could be due to the unfavorably positioned functional groups or reduced probability of stoichiometric encountering of the allyl and thiol groups in the thin film. Therefore, we

decreased the amount of PETMP to half (PETMP and AAAc in 1:8 ratio) to provide more alkene double bonds per –SH group so as to enhance the probability of the reaction at the thiol group sites. Interestingly, the irradiated film became dry to yield a smooth photo-cured film. The FT-IR corresponding to this composition revealed the complete disappearance of the –SH stretching peak, strongly corroborating the occurrence of thiol-ene click reaction (Fig. 6.2 (b)).

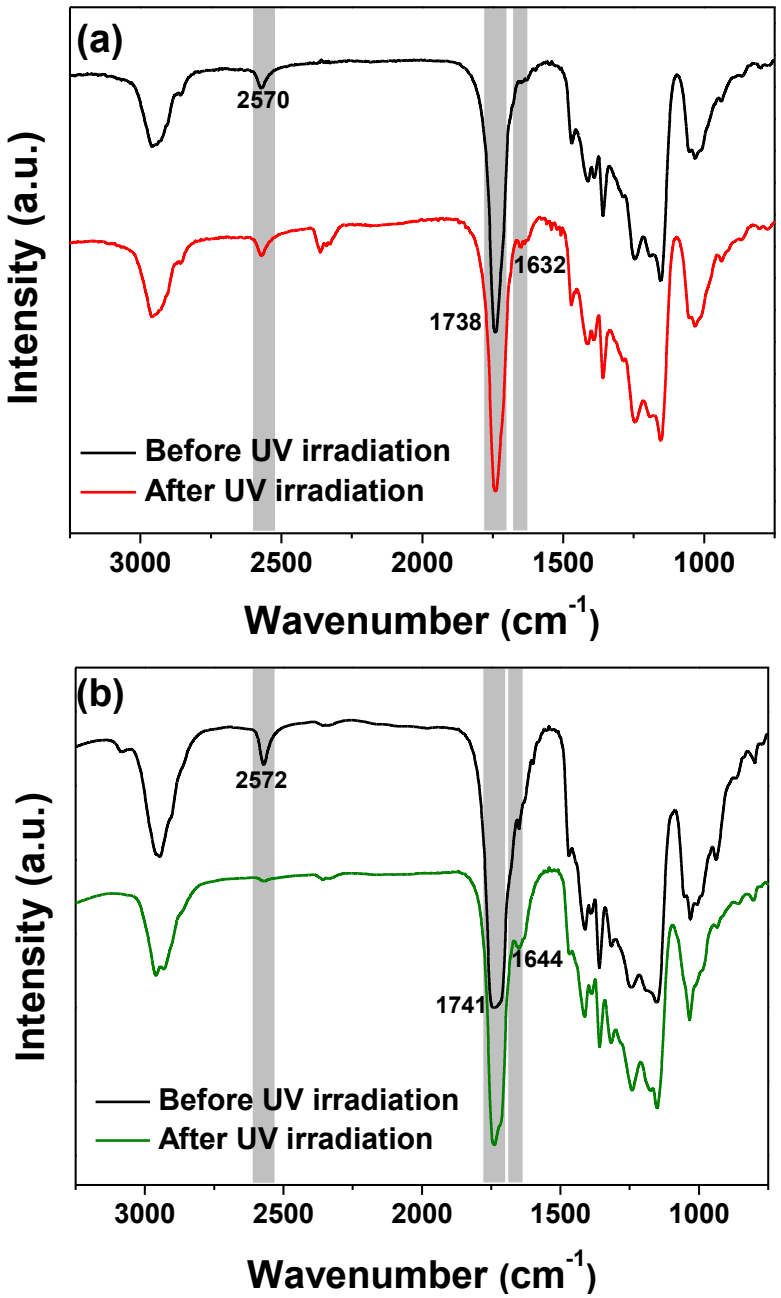

Figure 6.2: FT-IR analyses of thiol-ene photo-curing of resins containing PETMP and AAAc in the ratio of (a) 1:4 (TAP-1) and (b) 1:8 (TAP-0.5) showing that the latter composition is amenable to the click chemistry.

To enable the thiol-ene chemistry for oxide nanoimprinting, a photo-curable metal-containing resin formulation was prepared by mixing titanium-allyl acetoacetate complex [$Ti(AAAc)_4$] with PETMP and HMP. Table 6.1 shows the three resin formulations that were used for photo-curability studies. The first composition (TA), which does not contain PETMP could undergo [2 + 2] photo-addition of alkene double bonds to yield cyclobutane derivative. This composition yielded a dry film after UV irradiation. However, the film was found to be brittle and easily flaked off of the silicon wafer. This could be due to the excessive photo-curing of the four-arm alkene-functionalized $Ti(AAAc)_4$ that caused residual stress in the thin film.[36] In the second composition (TAP-0.5), 1/8 equivalent of PETMP with respect to $Ti(AAAc)_4$ was introduced to keep the effective available thiol groups per alkene as 0.5. This formulation after UV irradiation was found to yield a dry and smooth film that did not suffer any peeling off behaviour. This could be attributed to the cushioning effect provided by the optimum cross-linking of PETMP that circumvented cracking of the film.

In the third composition (TAP-1), 1/4 equivalent of PETMP with respect to $Ti(AAAc)_4$ was used in order to keep the thiol to alkene ratio 1:1. Interestingly, the film obtained with this composition was found not fully dry after 20 min of UV irradiation. This is similar to the poor photo-curing observed with the metal-free resin containing stoichiometric ratio of allyl to thiol. Thus, for the remaining characterization and imprinting studies, we utilized the optimized composition of TAP-0.5.

Fig. 6.3 shows the FT-IR analyses using TAP-0.5 to probe the thiol-ene photo-click reaction. As seen from the spectra, the characteristic ester and *keto* carbonyl groups are observed at 1745 and 1718 cm^{-1}, respectively. Compared to the metal-free resin, pristine $Ti(AAA)_4$ showed two additional characteristic peaks at 1610 and 1532 cm^{-1} that can be attributed to the bidendate chelation of the enol form of AAAc.[37] In addition, the carbon-carbon double bond of allyl group appeared at 1633 cm^{-1}. In the case of TAP-0.5, in addition to the above mentioned stretching peaks, a new peak at 2572 cm^{-1} corresponding to the thiol appeared. After UV light irradiation, the thiol peak became nearly invisible, while the intensity of allyl double bond peak diminished. These changes clearly indicate the occurrence of click reaction between the thiol and allyl groups in this system. It is noteworthy that the chelation with the metal remains intact even after the UV irradiation, which confirms that the metal is entrapped inside the cross-linked polymeric network.

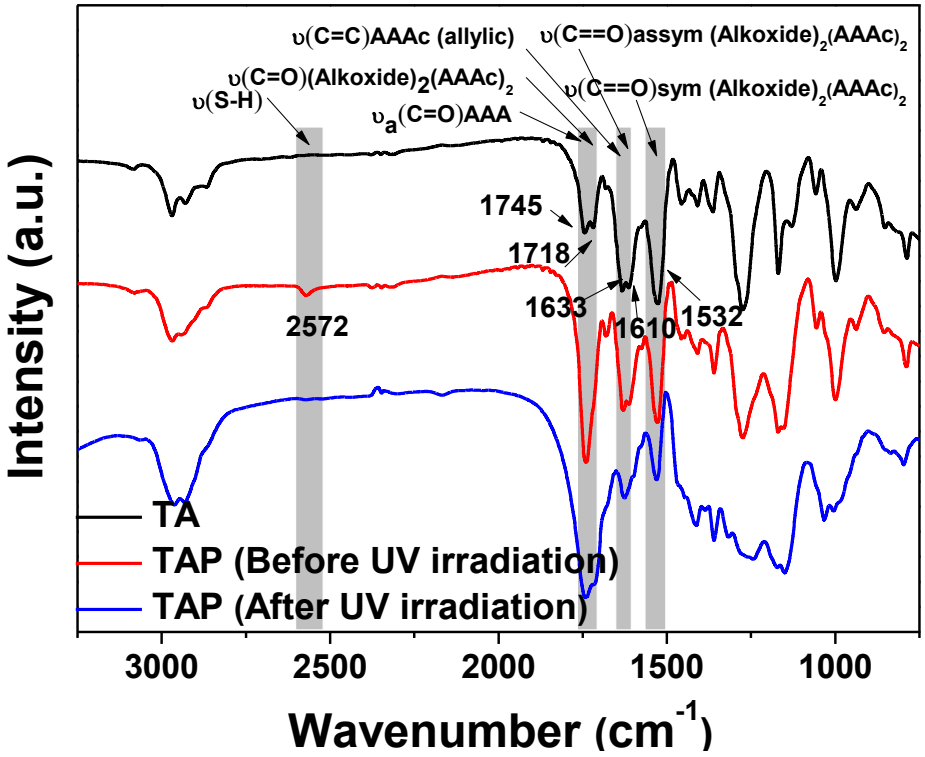

Figure 6.3: FT-IR study of thiol-ene photo-addition in the titanium-containing resin TAP-0.5.

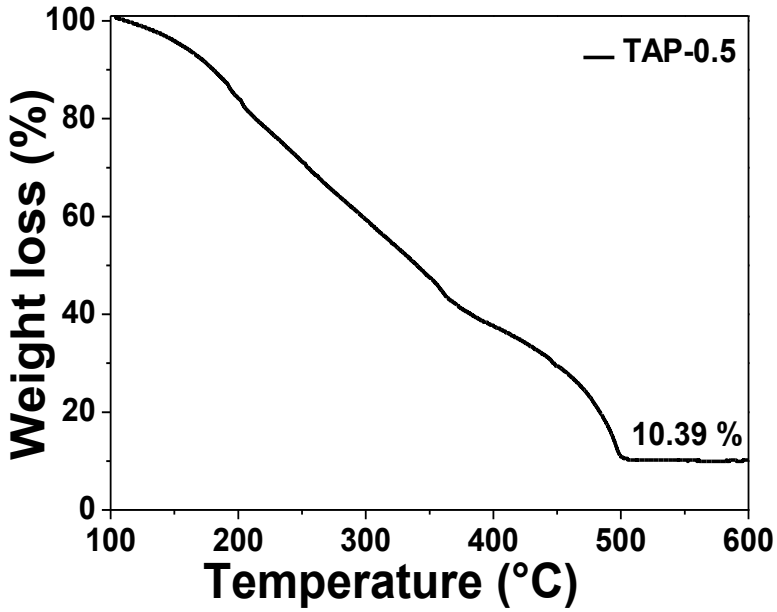

Figure 6.4: Thermogravimetric analysis of TAP-0.5 resin.

Fig. 6.4 shows the thermogravimetric analysis (TGA) of TAP-0.5 performed in air. A steady mass loss was observed between 100 and 500 °C due to the removal of residual solvent, low molecular weight monomers, and polymers. No further mass loss was observed above 500 °C, suggesting the complete removal of organics present in the resin. The residual inorganic mass corresponding to TiO_2 at 500 °C was found to be 10.4% which is in close agreement with the theoretical estimated value of 11.9%.

To confirm the phases obtained after calcination of the UV-cured TAP-0.5 films, x-ray diffraction (XRD) and Raman spectroscopy were performed. The calcination temperature was varied from 450 to 650 °C at a constant duration of 1 h to monitor the evolution of the phases and the corresponding XRD patterns are presented in Fig. 6.5. As seen from the figure, the TAP-0.5 films heat-treated at 450 and 500 °C revealed the formation of phase pure anatase. The broad peaks indicate the nanocrystalline nature of TiO_2 obtained at these temperatures. Above 500 °C, the (101) anatase peak was found to intensify with narrowing of the peak, indicating the growth of nanocrystallites to larger crystals (JCPDS 89-4921). At and above 600 °C, formation of a small amount of rutile phase is indicated by the appearance of (110) plane at $2\theta = 27.4°$. Applying the Scherrer's formula to the (101) plane of anatase TiO_2, the crystallite size of the samples calcined at 450, 500, 550, 600 and 650 °C are calculated to be 6.7, 7.1, 12.0, 15.7, and 15.6 nm, respectively.

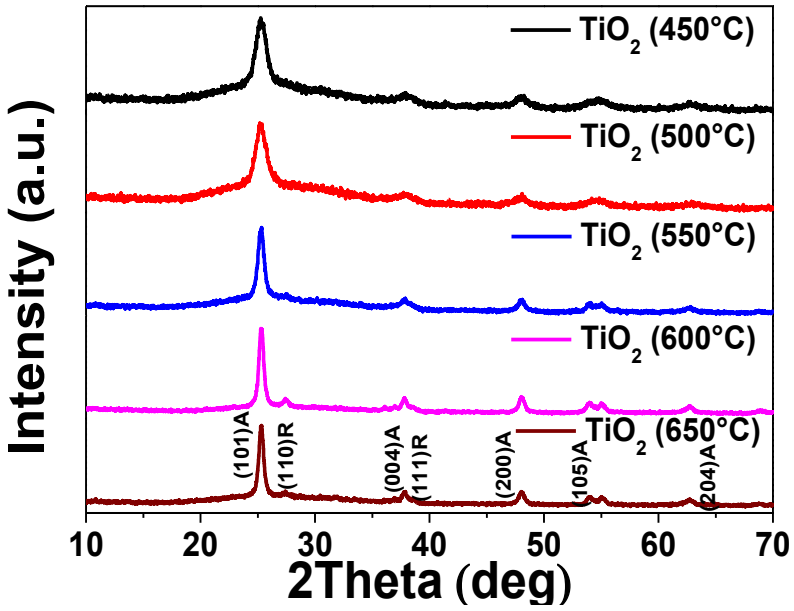

Figure 6.5: XRD patterns of TiO_2 obtained by calcination of photo-cured TAP-0.5 thin films at various temperatures.

The Raman spectra of the TiO_2 samples calcined at different temperatures looked identical (Fig. 6.6). A major peak at 121 cm^{-1} along with weak peaks at 365, 482, and 603 cm^{-1} were observed in all cases that can be attributed to the respective vibrational symmetries of E_g, B_{1g}, A_{1g}, and E_g Raman-active modes of anatase TiO_2.[40,70] Due to the presence in minute quantity, the Raman peaks of rutile TiO_2 were not observed in the samples calcined at 600 and 650 °C.

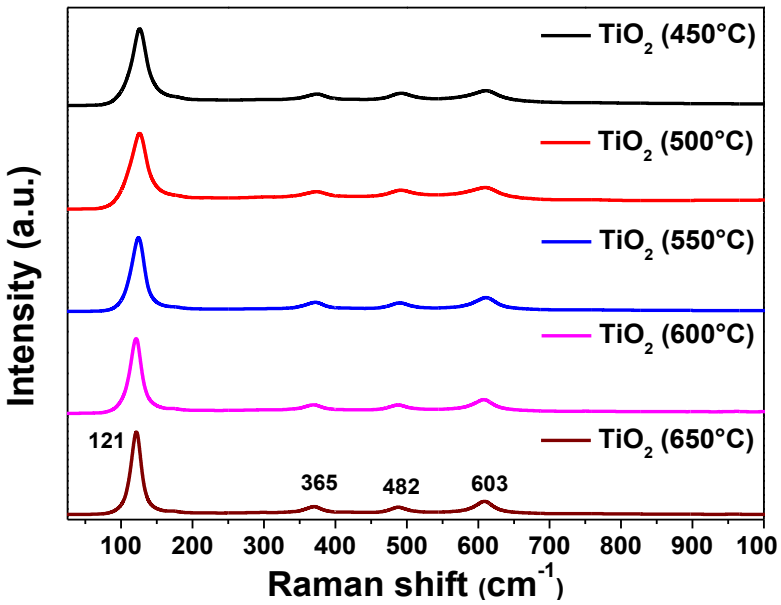

Figure 6.6: Raman spectra of TiO_2 obtained by calcination of photo-cured TAP-0.5 thin films at various temperatures.

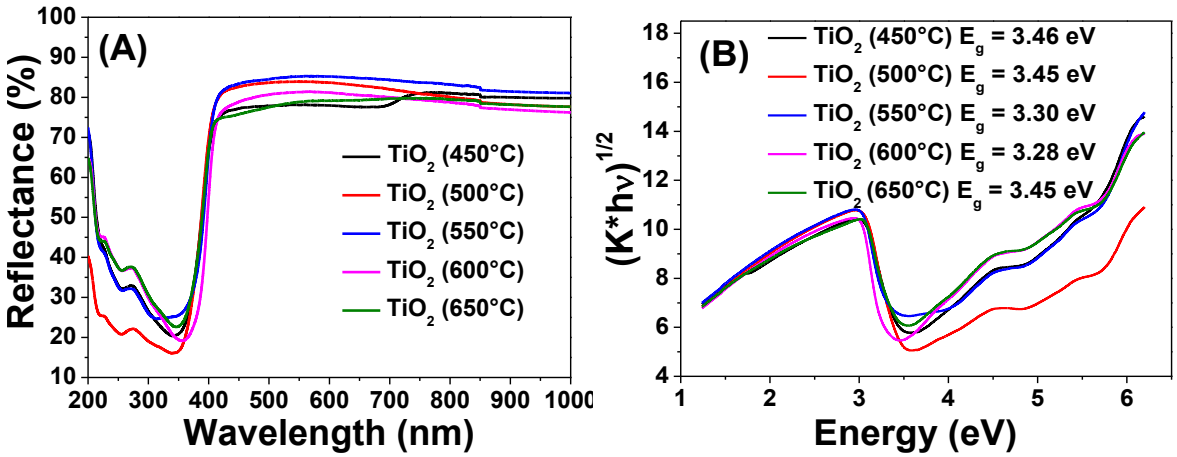

Figure 6.7: (a) Diffuse reflectance spectra and (b) the corresponding Kubelka-Munk plots of TiO_2 thin films prepared at different temperatures.

The semiconducting nature of the oxide thin films obtained through the thiol-ene approach has been studied using diffuse reflectance spectroscopy. The percentage reflectance and their corresponding Kubelka-Munk plots of TiO_2 calcined at various temperatures are shown in Fig. 6.7 (a) and Fig. 6.7 (b), respectively. The Kubelka-Munk factor (K) is given by $K = (1–R)^2/2R$, where R is the % reflectance. The intersection of the extrapolated linear portion of the curve in $(K \times \text{energy})^n$ *versus* energy plot with the energy axis yields the band gap of the semiconductor material. For direct band gap materials, the value of n is taken as 2, while for indirect band gap material the value is taken as ½. Since TiO_2 is an indirect band gap material, the value of 'n' used was ½. The Kubelka-Munk plots show the band gaps of

TiO_2 calcined at various temperatures to be in the range of 3.3 to 3.45 eV. These values agree well with the band gap of anatase TiO_2 reported in the literature (3.2 to 3.4 eV) and thereby confirming the semiconducting nature of the obtained thin films.[71,72]

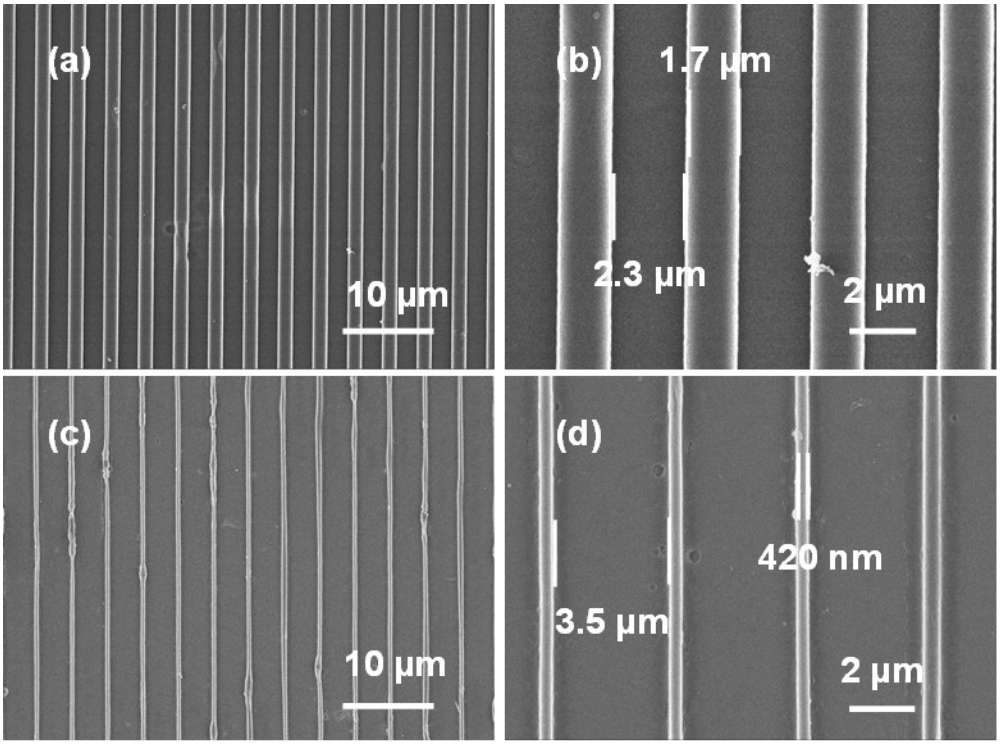

Figure 6.8: FE-SEM images of imprinted lines of TAP-0.5 (a and b) before and (c and d) after calcination.

The metal-containing resin formulations were studied for their suitability for imprinting under laboratory conditions. A polydimethylsiloxane (PDMS) stamp was pressed over the spin-coated TAP-0.5 film and irradiated with UV light. After demolding, the morphology of the photo-cured imprints before and after calcination was characterized using field-emission scanning electron microscopy (FE-SEM) and the images are shown in Figure 6.8. The PDMS soft mold used in this study possessed a feature size of ~2.1 µm line and ~1.8 µm space (Fig. 6.9). After patterning of TAP-0.5, the width of the imprinted line and space was found to be ~1.7 and ~2.3 µm, respectively. The shrinkage of the imprinted lines may be attributed to the absorption of the residual solvent by PDMS mold and polymerization. Post-calcination, the lines were further shrunk to ~420 nm and the spaces widened to ~3.5 µm. On the whole, the TiO_2 lines were shrunk to ~25% compared to the as-imprinted lines, which is similar to the values previously reported PSG-based literature on TiO_2 nanoimprinting.[29,36-38]. The shelf-life of the AAAc-based titanium resin was poor and thereby warrants immediate imprinting of the formulation. We speculated that this could be due to the vulnerability of titanium for

hydrolysis, which was not averted by the chelated AAAc. Therefore, we briefly studied the shelf-life and imprintability of a titanium resin in which AAAc was replaced with 2-(methacryloyloxy)ethyl acetoacetate (MAEAA). This formulation was found to have a good shelf life of more than a month. Furthermore, the successful direct imprinting using this MAEAA-based thiol-ene resin confirmed that the approach can be extended to other chelating monomers as well (Fig. 6.10).

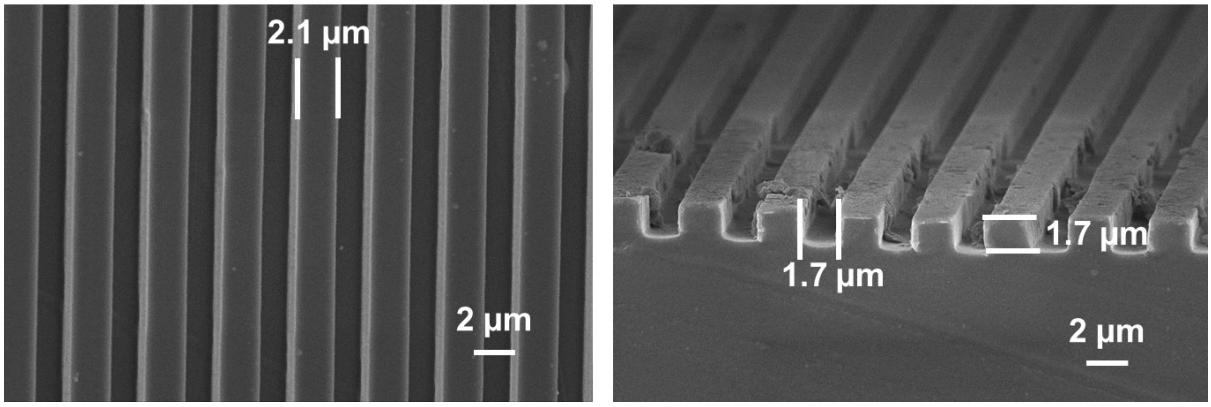

Figure 6.9: Arial and cross-sectional views of the PDMS mold used in this study.

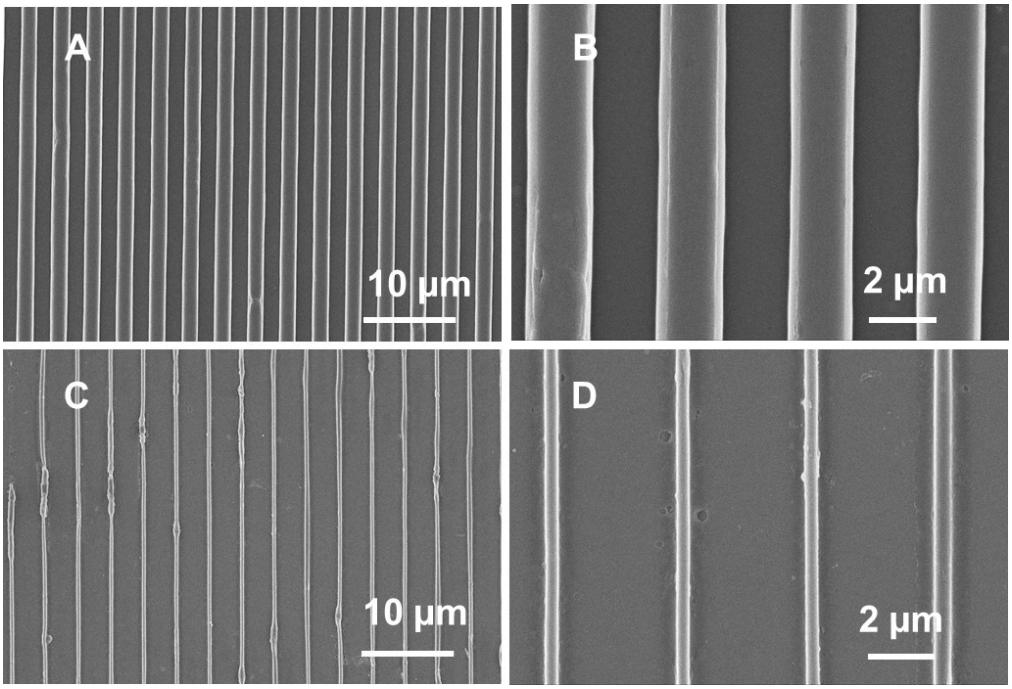

Figure 6.10: FE-SEM images of imprinted lines of $Ti(MAEAA)_4$-based resin (A and B) before and (C and D) after calcination.

To substantiate the applicability of this thiol-ene approach for patterning other oxides, Ta_2O_5 was chosen as the candidate due to its potential applications in semiconducting devices.[73,74] Although tantalum is a pentavalent metal, we used 4 equivalents of AAAc in

order to match with the corresponding titanium precursor. The resultant resin was found to have a good shelf life of more than a month. The PETMP ratio to the AAAc was fixed in the similar fashion to that used in TAP-0.5 and the FT-IR analyses before and after UV light exposure were performed (Fig. 6.11). The results revealed the disappearance of the –SH stretching peak, indicating the occurrence of thiol-ene photo-click chemistry.

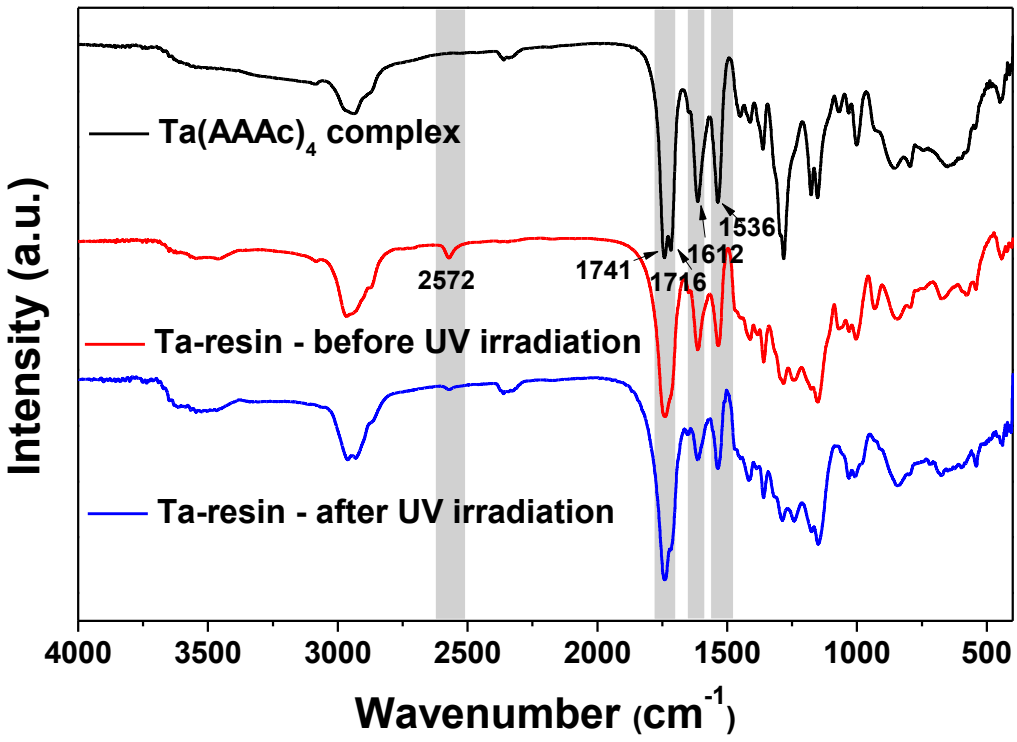

Figure 6.11: FT-IR analysis of $Ta(AAAc)_4$ complex, and tantalum-containing resin before and after UV irradiation to probe the thiol-ene click reaction.

Fig. 6.12 shows the TGA, XRD and diffuse reflectance spectra of the tantalum-containing resin. The TGA profile was observed to be in similar nature to that of TAP-0.5. The complete mass loss was found to occur at ~530 °C and the residual inorganic mass corresponding to Ta_2O_5 was observed to be 20.1%. The XRD pattern of Ta_2O_5 was found to be broad, indicating its amorphous nature at this temperature. Therefore, the UV-cured film was calcined at 700 °C to obtain crystalline Ta_2O_5. The XRD analysis of this sample revealed well-defined orthorhombic crystalline phase of Ta_2O_5 (JCPDS No. 79-1375).[75] The diffuse reflectance and the corresponding Kubelka-Munk plots revealed a shallow spectrum for the 450 °C calcined sample, confirming the amorphous nature of the Ta_2O_5. The thin film calcined at 700 °C was found to exhibit a band gap of 4.26 eV, which is similar to that reported in the literature.[76]

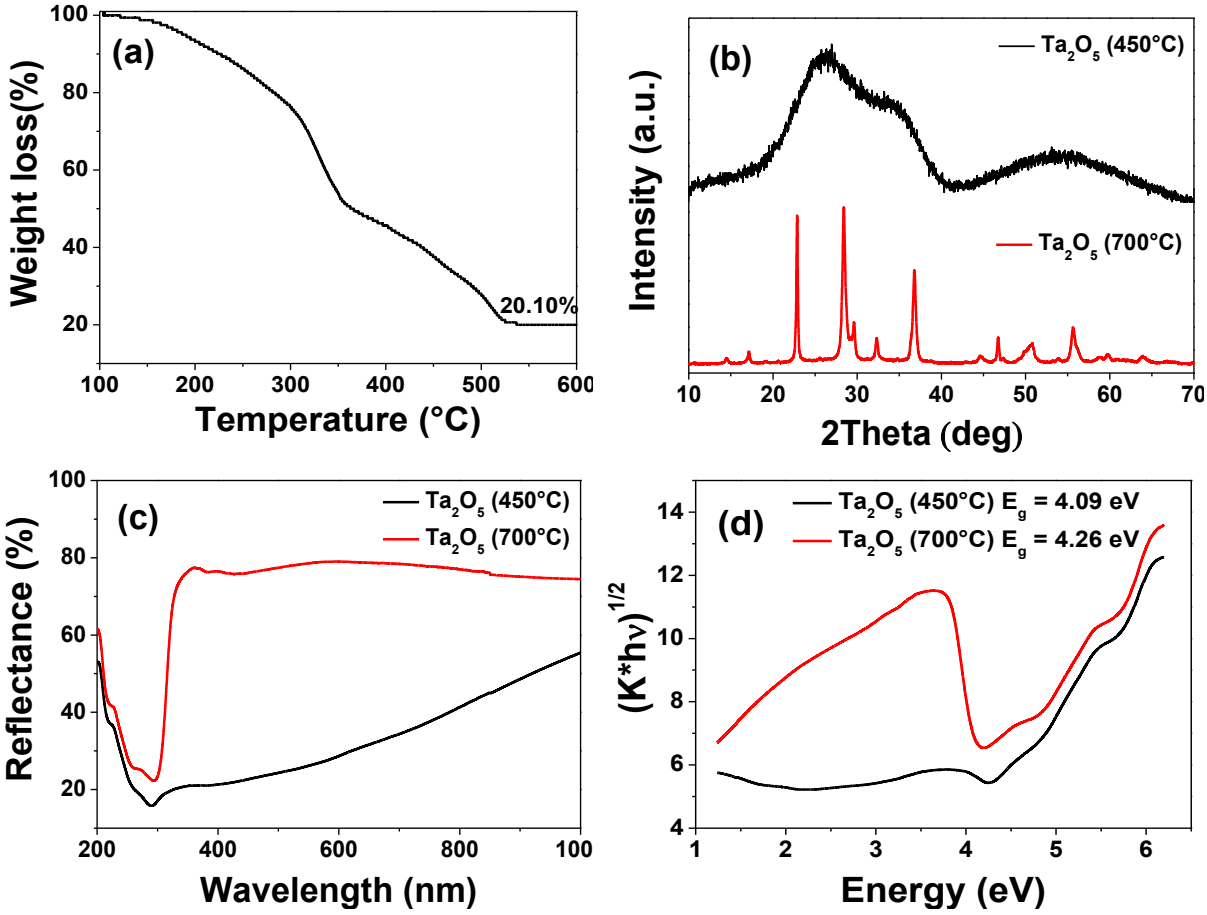

Figure 6.12: (a) Thermogravimetric analysis of tantalum-containing resin. (b) XRD patterns, (c) diffuse reflectance spectra and (d) Kubelka-Munk plots of Ta_2O_5 obtained at 450 and 700 °C.

UV imprint lithography of the tantalum-containing resin was performed and the FE-SEM images corresponding to the as-imprinted and calcined samples are shown in Fig. 6.13. The line and space feature sizes of the as-imprinted patterns were found to be ~1.7 and ~2.1 µm, respectively. After calcination, the lines were shrunk to ~470 nm and the spaces extended to ~3.4 µm. The cross-sectional view of FE-SEM images of the as-imprinted and calcined samples showed the heights to be ~1.7 µm and 410 nm, respectively. Thus, the lateral and vertical shrinkages were found to be ~75% that is similar to the case of TiO_2. The very similar imprinting behaviour of tantalum-containing resin shows the capability of the thiol-ene approach to be a potential route for fabricating nanostructures of a host of oxides that could find applications in various devices.

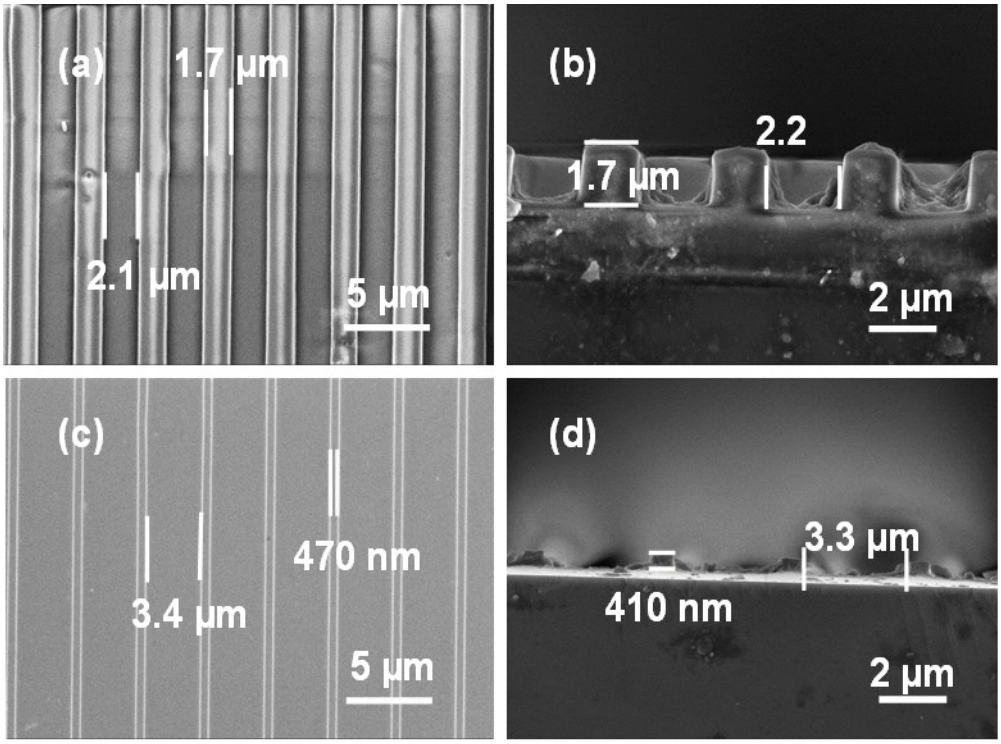

Figure 6.13: Areal (a and c) and cross-sectional (b and d) FE-SEM images of as-imprinted (a and b) and post-calcined (c and d) imprints of tantalum-containing resin.

6.3 Ring opening polymerization chemistry

6.3.1 Experimental section

(i) Synthesis of Oxirane-2-ylmethyl 3-oxobutanoate (Glycidyl acetoacetate or Epoxy-functionalized acetoacetate (EAA))

EAA was synthesized by following the literature report on *trans*-esterification reaction between alcohol and ester.[77] Here the ester, 0.86 mmol t-BAA was taken in 12 mL toluene and heated to 85 °C. To the pre heated ester, 0.1 mmol glycidol in 2 mL toluene solution was slowly added using syringe. The reaction was stirred under inert atmosphere for 3 hours at 110 °C. After the completion of the reaction, the toluene solvent was evaporated and the product was purified by column chromatography using neutral alumina as stationary phase. The solvent system used for the purification was 10% of ethylacetane in hexane. In the similar way, 3-methyloxetane-3-ylmethyl 3-oxobutanoate (Oxetane-functionalized acetoacetate (OAA)) was also prepared and purified.

(ii) Resist formulation

The polymerizable TiO_2 resist materials were prepared by the addition of precursor materials. Table 5.2 shows the feed ratios and amounts of the precursor materials for the resist formulations. Briefly, to make $Ti(EAA)_4$ complex, 1 equivalent of $Ti(OEt)_4$ was added to 4 equivalents of EAA in a glass vial and stirred for sufficient time to form a homogeneous solution. The colour of the resist solution rapidly turned to red, indicating the chelation of the EAA with the metal. To this complex, 2 wt% (with respect to EAA) of DPHFP was added to induce the photoacid generation upon UV light irradiation. The above formulated resist was diluted in 1:1 (wt/wt) ratio with toluene to decrease the viscosity. In a similar way, titanium alkoxide treated with different equivalents of EAA were also made and studied for their imprintability.

Table 6.2: Proportions of the components used in the different formulations

Sample code	Titanium (IV) ethoxide (mmol)	EAA/OAA (mmol)	PAG (mmol)
$Ti(EAA)_1$	1	1	0.0075
$Ti(EAA)_2$	1	2	0.0150
$Ti(EAA)_3$	1	3	0.0225
$Ti(EAA)_4$	1	4	0.0300
$Ti(OAA)_1$	1	1	0.0873
$Ti(OAA)_2$	1	2	0.0174
$Ti(OAA)_3$	1	3	0.0262
$Ti(OAA)_4$	1	4	0.0350

(iii) Imprinting of metal oxide

From a polycarbonate mold containing ~2.3 and ~1.7 μm line and space, respectively, PDMS stamps were fabricated following the standard procedure as discussed in 6.2.1. In a typical nanoimprinting process, the metal-containing resist solution was spin-coated over a silicon wafer (20 mm x 20 mm) at 1200 rpm for 60 s. The PDMS mold was then placed on top of the wet thin film and a slight pressure was applied. This assembly was subjected to UV irradiation with a Hg vapour lamp (125 W) for 1 min to induce the formation of photoacids in

the resist matrix. After UV exposure, the assembly was subjected to post exposure baking (PEB) by placing on hot plate at 110 °C for 3-5 min. After PEB, the PDMS stamp was carefully demolded and the imprints were subjected to calcination at designated temperatures for 1 h to obtain metal oxide patterns.

6.3.2 Results and discussions

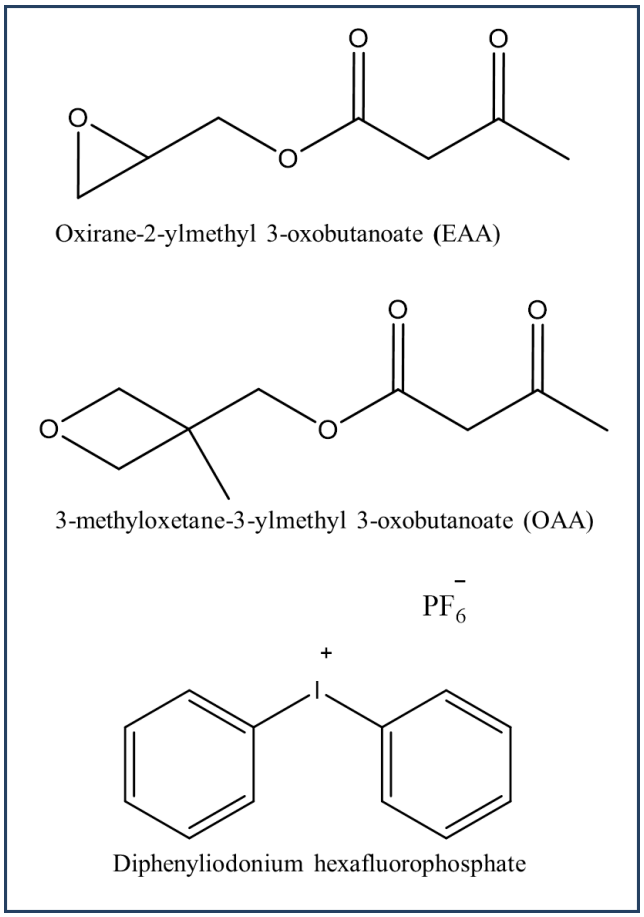

Figure 6.14: Chemical structures of EAA, OAA and PAG.

In order to successfully fabricate metal oxides, the choice of the resist materials is the foremost criterion. So far, the reported polymerizable approach using methacrylate and thiol-ene chemistry used reactive diluents, due to which the metal content in the final resin formulation was relatively lesser, which led to ~75% shrinkage after nanoimprinting followed by calcination. Keeping this in mind, we aimed to increase the metal content in the resin formulation in order to increase the ceramic yield and thereby to decrease the shrinkage. In this context, we designed two low molecular monomers that contain epoxy/oxetane group at one end that could undergo cationic ring opening polymerization and acetoacetate group on the other end to facilitate chelation with the metal of interest. Among the two monomers,

epoxy acetoacetate (EAA) was synthesized by a *trans*-esterification reaction reported in the literature. However, there is no literature report on the synthesis of OAA. Following the synthetic route of EAA, we have successfully synthesized OAA as well. The chemical structures of the monomers and photo-acid generator (PAG) are shown in Fig.6.14. The resist formulation reactions are shown in Fig. 6.15.

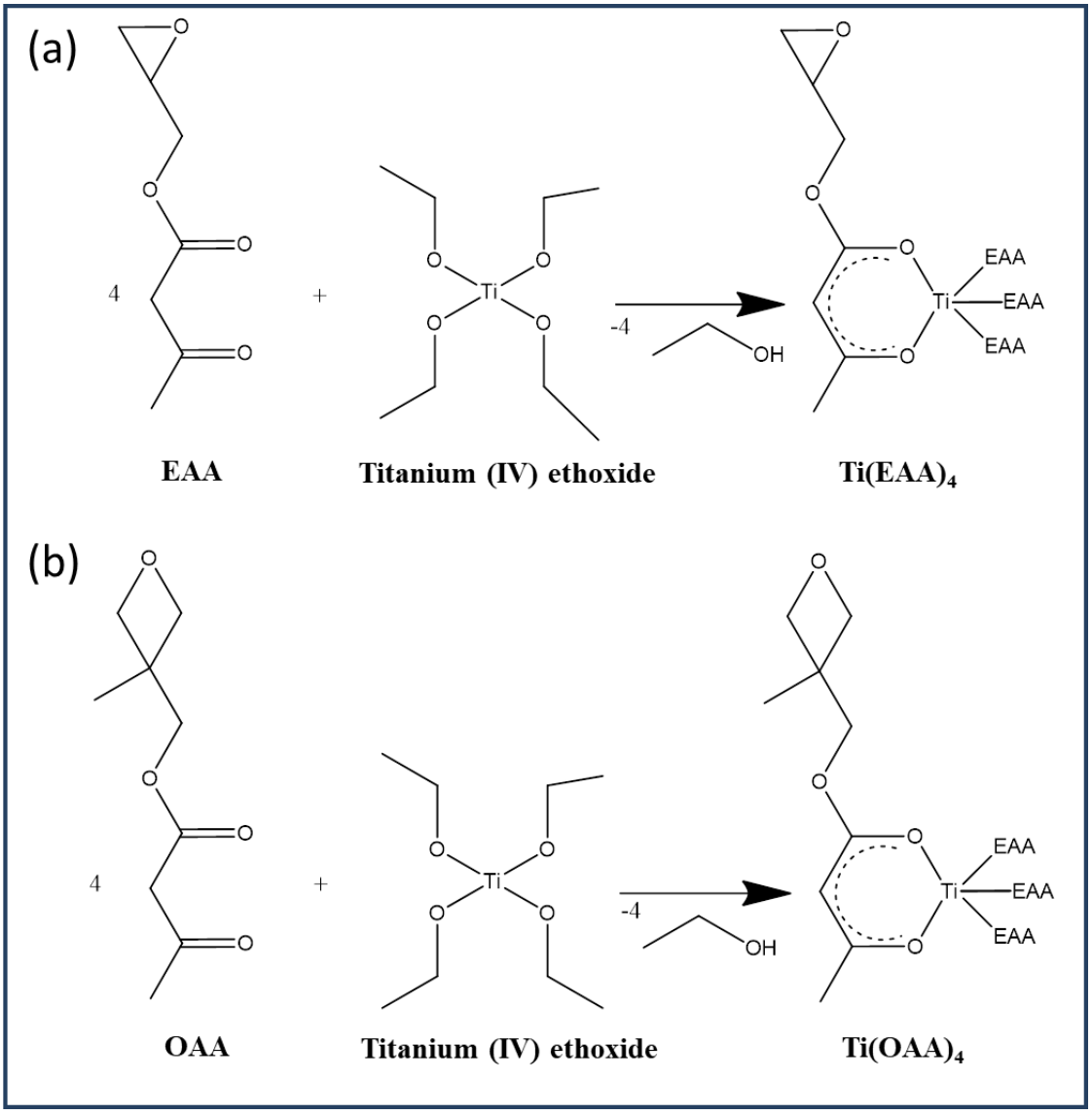

Figure 6.15: Resist formulation reactions of (a) $Ti(EAA)_4$ and (b) $Ti(OAA)_4$.

The synthesized monomers were characterized using NMR spectroscopy. Fig. 6.16 (a) shows the ^1H NMR spectra of the EAA. ^1H NMR spectra of EAA shows characteristic peaks at δ values (ppm) 2.28 (s, 3 H_a), 2.67 (dd, 1 H_f), 2.86 (dd, 1 H_g), 3.23 (m, 1 H_e), 3.53 (s, 2 H_b), 4.0 (dd, 1 H_c), and 4.42 (dd, 1 H_d). Further, ^{13}C NMR spectrum shows the peaks with δ values (ppm) 30.12 (C_7), 44.53 (C_1), 49.06 (C_5), 49.57 (C_2), 65.59 (C_3), 166.80 (C_4), 200.27

(C_6) (Fig. 6.16 (b)). The both spectra were found to be matching with the reported values and thus confirmed the successful synthesis of the compound.[77]

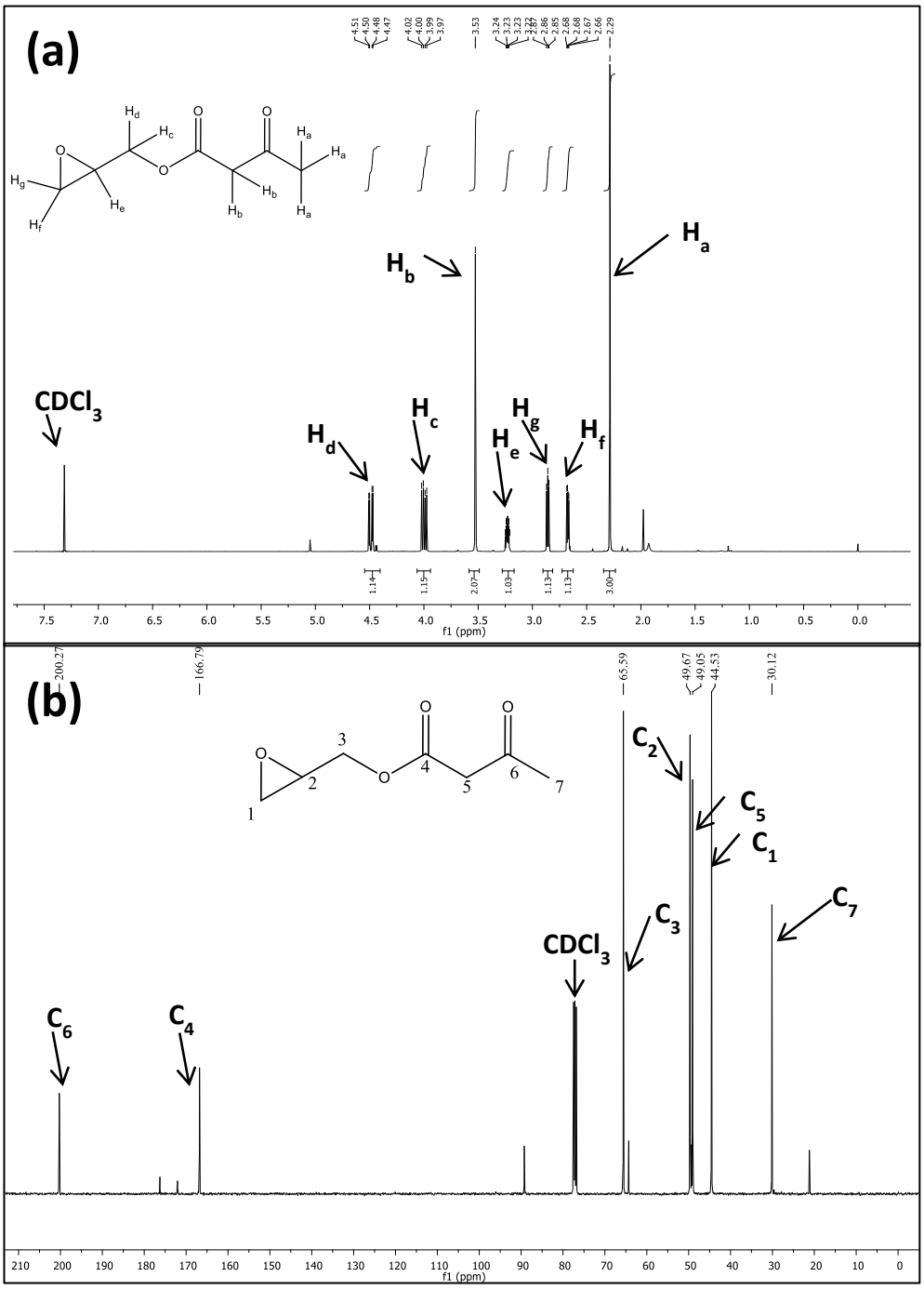

Figure 6.16: (a) ^{1}H-NMR and (b) ^{13}C-NMR spectra of the synthesized EAA in $CDCl_3$ solvent.

Fig. 6.17 (a) shows the ^{1}H NMR of OAA with peaks δ 1.34 (s, 3H_d), 2.28 (s, 3 H_a), 3.54 (s, 2 H_b), 4.24 (d, 2 H_e), 4.39 (d, 2H_f), 4.52 (d, 2 H_c). ^{13}C NMR spectrum of OAA shows the peaks with δ values (ppm) 21.09 (C_3), 30.18 (C_8), 39.02 (C_2), 49.84 (C_6), 69.37 (C_4),

77.46 (C_1), 167.15 (C_5), 200.32 (C_7) (Fig. 6.17b). The chemical shift, splitting pattern and the integral values have proved the successful synthesis of OAA. Fig. 6.18 shows the ^{1}H NMR spectrum of the as-procured Titanium (IV) ethoxide. The peaks at δ 1.25 and δ 4.35 are corresponding to (C***H***$_3$) and (C***H***$_2$) protons of the ethoxide group. The peaks appear to be broader due to the linkage of ethoxide group to the metal centre.

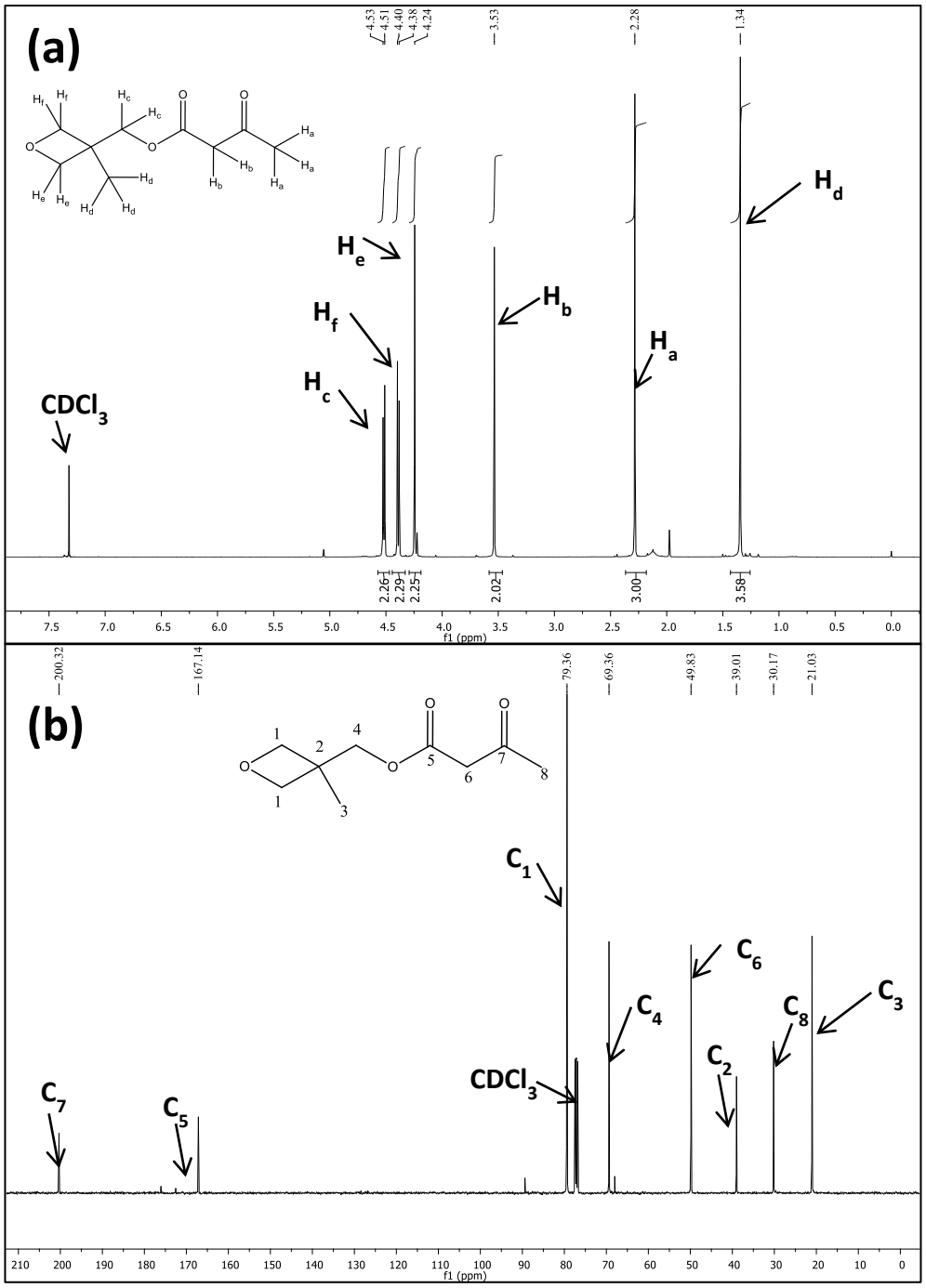

Figure 6.17: (a) ^{1}H-NMR and (b) ^{13}C-NMR spectra of the synthesized OAA in $CDCl_3$ solvent.

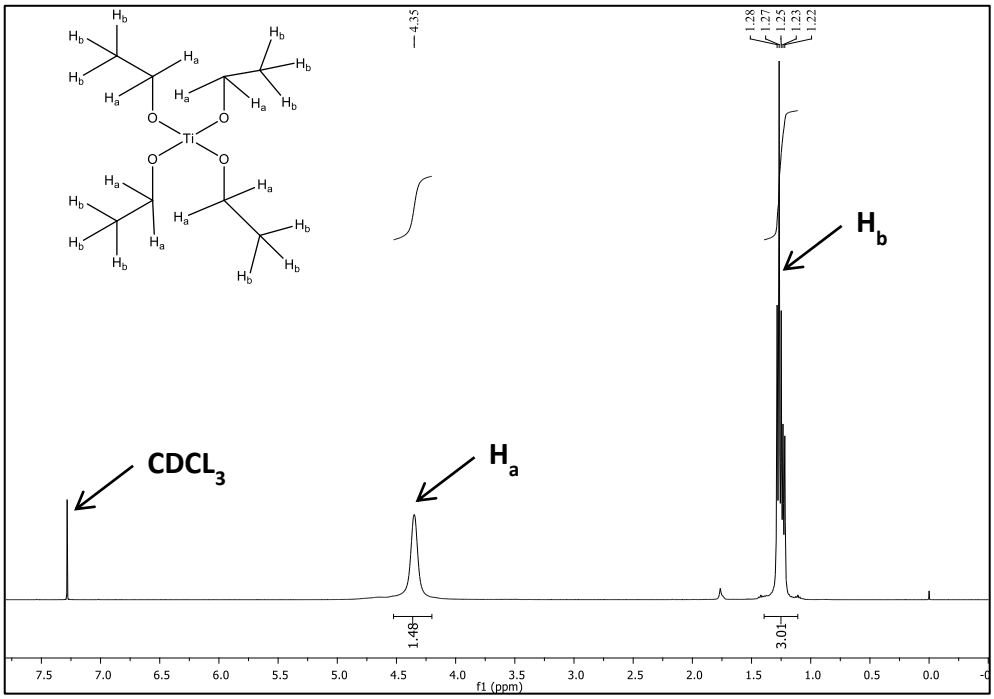

Figure 6.18: ^{1}H-NMR spectrum of as procured $Ti(OEt)_4$ in $CDCl_3$ solvent.

After the successful preparation of the monomers, the metal containing resist solutions were prepared by mixing EAA and OAA separately with titanium (IV) ethoxide in different proportions. Initially, to probe the metal-monomer chelation, the synthesized monomers were mixed with titanium ethoxide in 4:1 ratio and the ^{1}H NMR spectra of the obtained products, $Ti(EAA)_4$ and $Ti(OAA)_4$, were recorded (Fig. 6.19). After chelation, characteristic peaks of free ethanol at δ values 1.22 (m, C**H**$_3$), 3.71 (m, C**H**$_2$), 1.98 (s, O**H**) were found, which confirmed the successful replacement of ethoxy groups by the acetoacetate moieties (Fig. 6.19 (a)). Apart from this, the spectrum of $Ti(EAA)_4$ was largely found to match with the spectrum of EAA, expect the peak at δ = 5.05, which corresponds to the proton of the (COC***H***CO).[78] The integral value of the number of protons at this δ was 0.43, instead of the expected 1.00. This could be because of the incomplete or reversible chelation of the monomer to the metal. The previous literature on the metal-acetoacetate chelation reported high yield complexation reaction. However, the occurrence of partial chelation indicates that the lone pair of oxygen in the epoxy group might be interacting with the electropositive central metal ion (Ti^{4+}). It is also speculated that such an interaction could have shifted the equilibrium of the chelation reaction modestly towards the left. The similar behaviour in the ^{1}H NMR was also observed with $Ti(OAA)_4$ (Fig. 6.19 (b)).

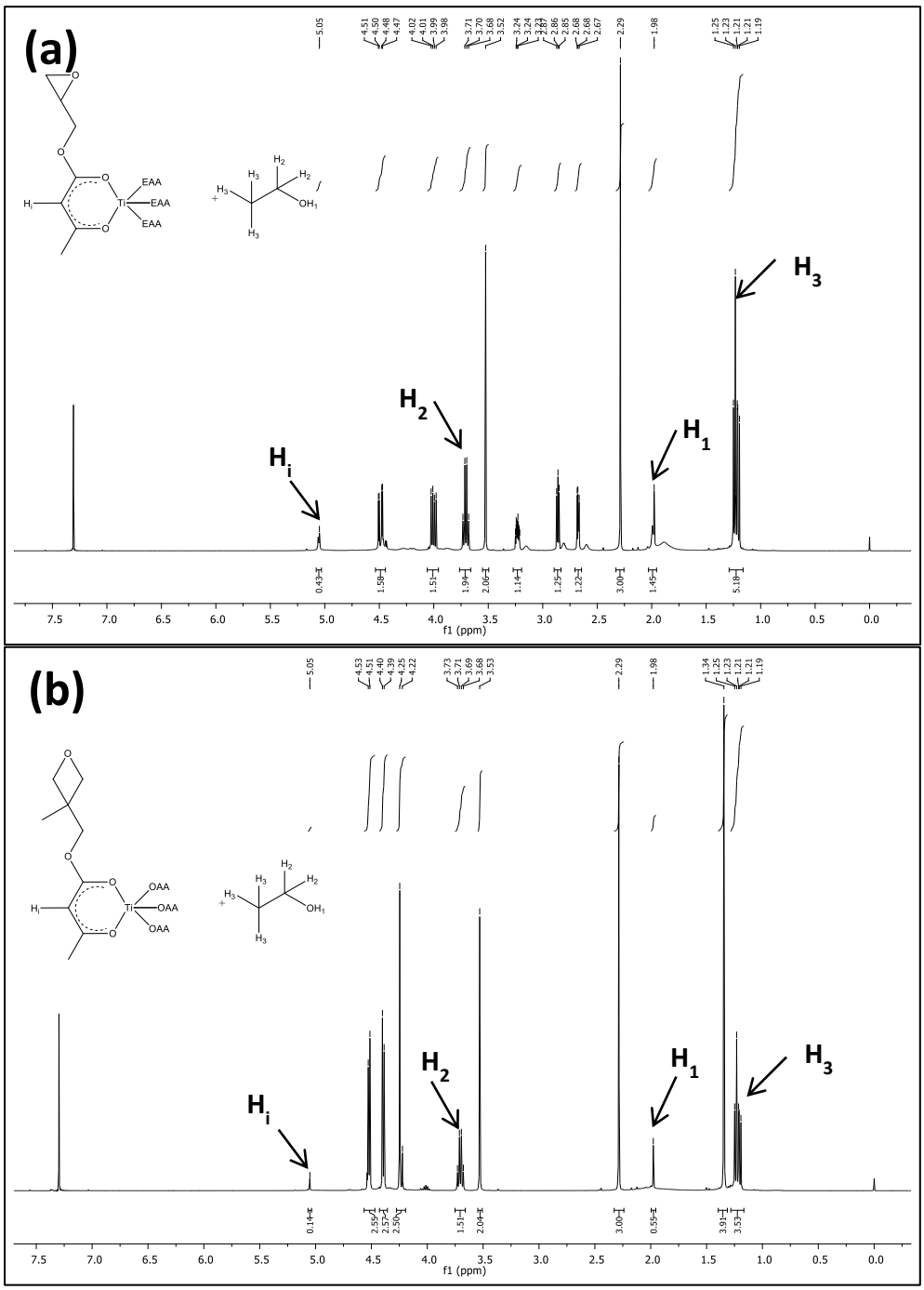

Figure 6.19: ^{1}H-NMR spectra of formulated (a) $Ti(EAA)_4$ and (b) $Ti(OAA)_4$ in $CDCl_3$ solvent.

To further probe the extent of chelation of the metal with acetoacetate group of the monomers, FT-IR studies were performed on the above mentioned resist formulations. Fig 6.20 (a) shows the IR spectra of EAA and $Ti(EAA)_4$ before and after ring opening polymerization. EAA showed the prominent peaks at 1746 cm^{-1} and 1712 cm^{-1} corresponding to the ester and keto carbonyl groups, respectively. In addition, the characteristic epoxy signature peak at 914 cm^{-1} was also observed.[79,80]

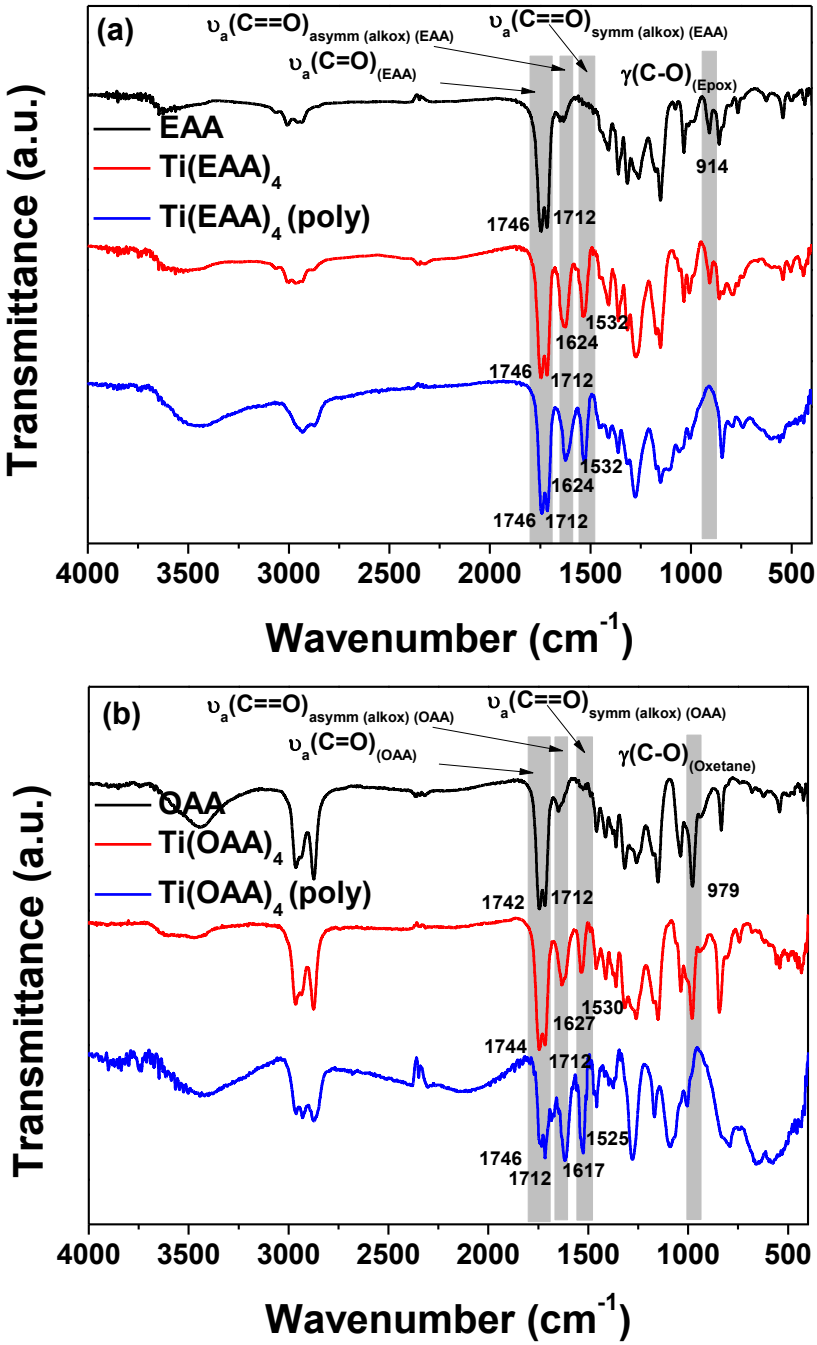

Figure 6.20: FT-IR analysis of titanium containing (a) EAA and (b) OAA resist formulations.

$Ti(EAA)_4$ resist showed new peaks at 1624 and 1532 cm^{-1}, which correspond to the bidendate chelation of the enol form of EAA with the metal center.[37] However, the intensity of the ester and keto peaks was found to be higher than that of symmetric and asymmetric stretching peaks of the chelated carbonyl group. This observation is in line with the ^1H NMR analysis and indicate incomplete or reversible chelation between EAA and metal centre. After UV exposure followed by PEB, the spectrum remained almost similar to the metal containing

resist, except the epoxy peak. The signature epoxy functional group peak at 914 cm^{-1} was found to be disappeared after PEB, indicating the participation of epoxy functional group in the ring opening polymerization. The intensity of peaks corresponding to the chelation was unchanged after the polymerization, indicating the stability of the metal-monomer chelation. Similar trend was observed with the Ti-containing OAA resist (Fig. 6.20 (b)). In this case, the characteristic oxetane ring breathing at 979 cm^{-1} was found to disappear after curing, which confirmed the occurrence of cationic ring opening polymerization in this system as well.[81]

To monitor the chelation further, UV-Vis absorption spectra was recorded for the as-synthesized EAA and $Ti(EAA)_4$ in $CHCl_3$ solvent and the results are shown in Fig. 6.21 (a). It can be seen from the figure that EAA shows λ_{max} at 245.5 nm due to the keto functional groups of acetoacetate. On addition of Ti-ethoxide, the intensity of the peak at 245.5 nm is increased due to the formation of six membered ring between the metal and EAA. The similar trend was observed with OAA and $Ti(OAA)_4$ (Fig. 6.21 (b)).

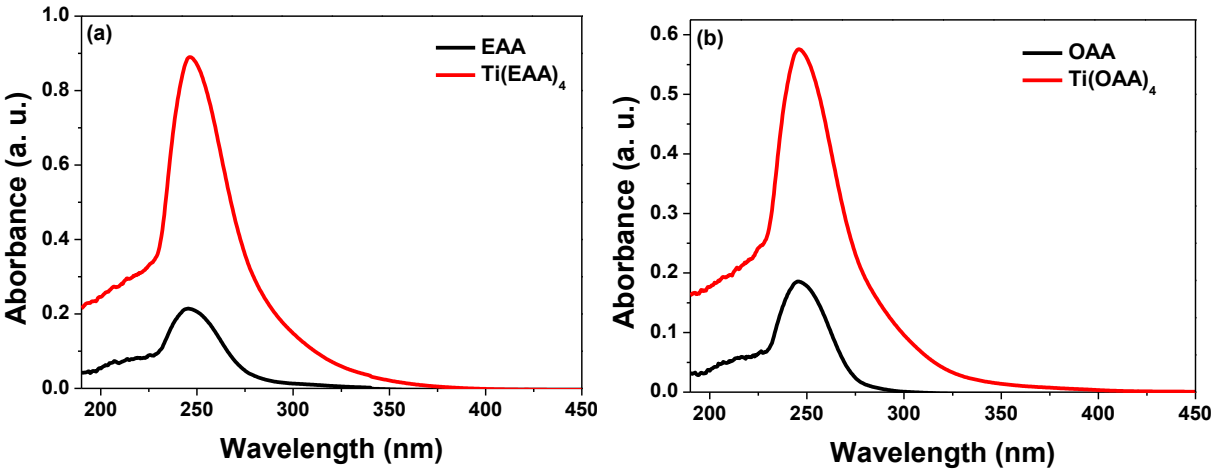

Figure 6.21: UV-Vis absorption spectra (a) EAA and $Ti(EAA)_4$ and (b) OAA and $Ti(OAA)_4$ resist formulations in $CHCl_3$ solvent.

The $Ti(EAA)_4$ resin was spin coated over the quartz plates and recorded the UV-Vis spectra (Fig. 6.22). The spectrum of $Ti(EAA)_4$ shows the absorption below 250 nm is due to the chelation of the metal to the monomer. The spectrum after UV irradiation is almost similar and the absorption decreases after the polymerization step. Considerable amount of absorption is remained even after the polymerization, indicates that the metal is still is intact with the monomer. Hence the polymerization step did not interference the chelation of the metal with monomer and provided the metal containing polymer thin film post imprinting.

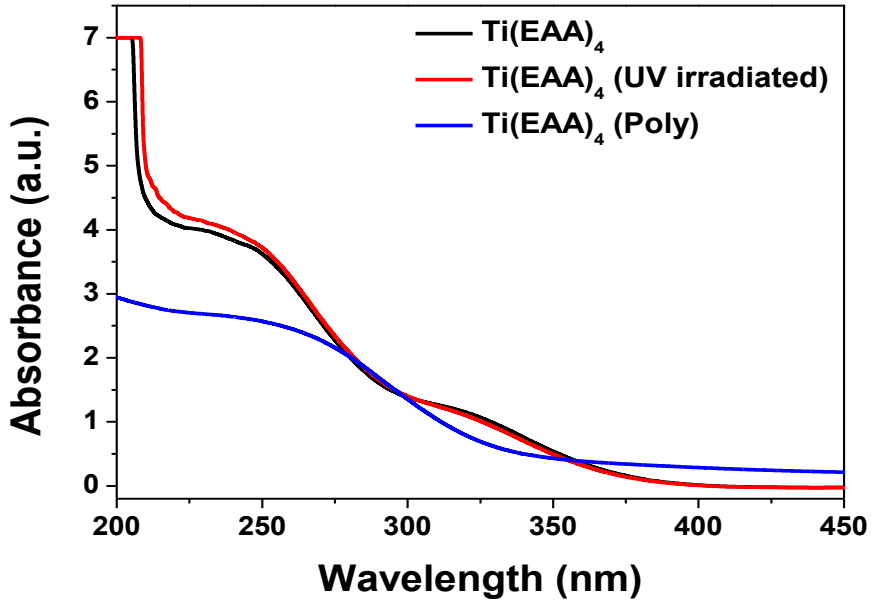

Figure 6.22: UV-visible absorbance spectra of $Ti(EAA)_4$ thin film (coated over quartz substrate).

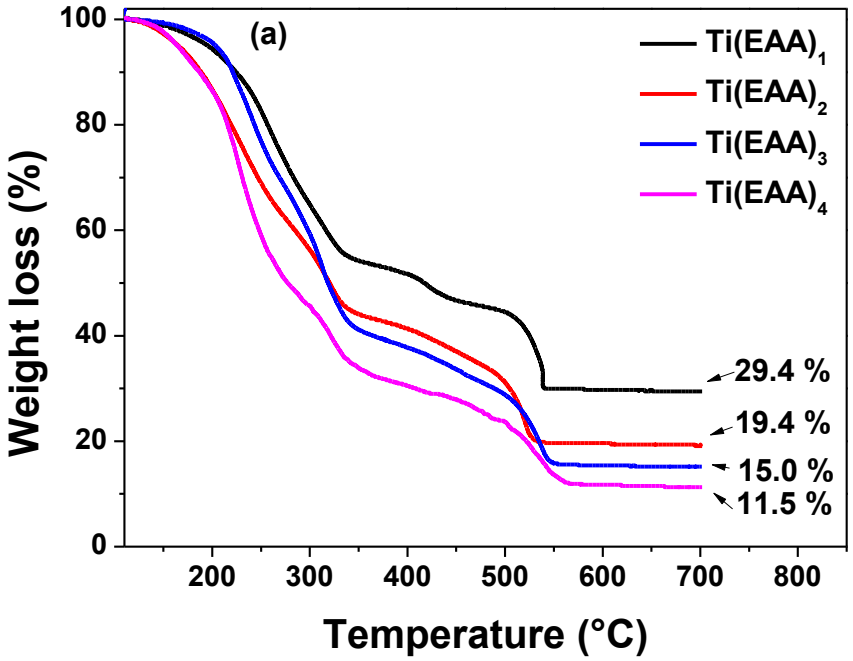

Figure 6.23: (a) Thermogravimetric analysis (TGA) of different Ti-EAA formulations.

The thermogravimetric analysis (TGA) of EAA-based formulations was performed in air (Fig. 6.23 (a)). It can be seen from the figure that the first step of mass loss occurred between 100 and 350 °C corresponding to the loss of solvent and unreacted monomers. The second step of mass loss between 350 and 550 °C was observed that could be attributed to the thermal decomposition of the polymer. No mass loss was observed above 550 °C, resulting in a stable residual mass corresponding to the formation of TiO_2. The residual mass of TiO_2 was

observed to be 11.5% with $Ti(EAA)_4$. As expected, the mass loss was increased as the content of monomer in the resin formulation was increased. The similar trend was observed with OAA-based formulation and the results are shown in Fig. 6.23 (b). The residual mass of the materials after calcination step were tabulated in Table 6.3.

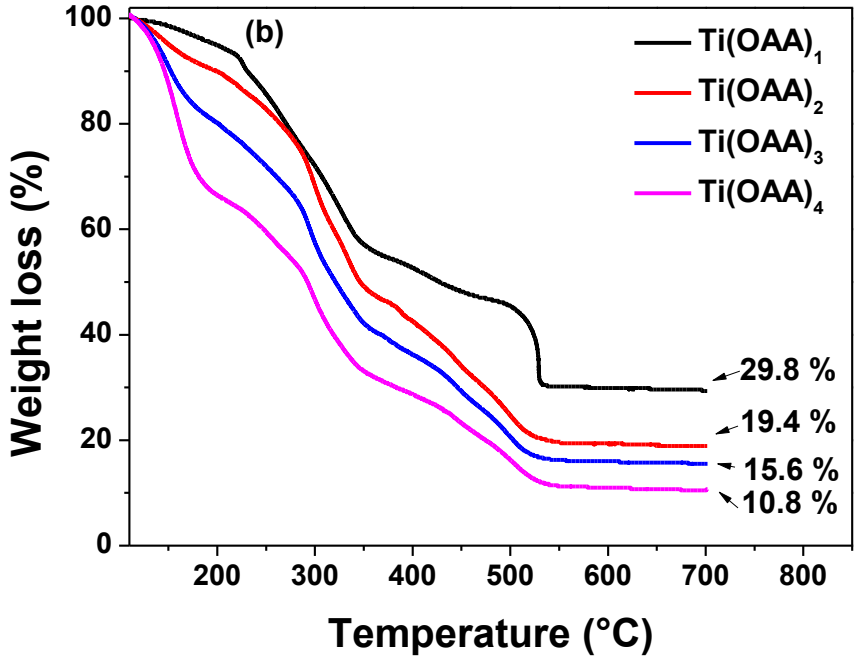

Figure 6.23: (b) Thermogravimetric analysis (TGA) of different Ti-OAA formulations.

Table 6.3: Theoretical and experimental mass of residual TiO_2 of different formulations

Sample code	Residual mass (%)	
	Theoretical	Experimental
$Ti(EAA)_1$	23.6	29.4
$Ti(EAA)_2$	17.8	19.4
$Ti(EAA)_3$	14.3	15.0
$Ti(EAA)_4$	11.9	11.5
$Ti(OAA)_1$	21.7	29.8
$Ti(OAA)_2$	15.7	19.4
$Ti(OAA)_3$	12.3	15.6
$Ti(OAA)_4$	10.1	10.8

As mentioned in the Table 6.2, four resist formulations with respect to each monomer were made and studied for their imprintability.. The morphology of the imprints before and after calcination were analysed using FE-SEM. The PDMS mold used for the imprinting was having the pattern line width of ~2.1 µm and space width of ~1.8 µm. The patterns were successfully transferred onto the film with the line size of ~1.6 µm and space of ~2.33 µm. The thin films of $Ti(EAA)_1$ and $Ti(OAA)_1$ were found to be brittle and peeled off on demolding (data not shown). This could be due to the lesser monomer content that could have resulted in poorer degree of polymerization. With $Ti(EAA)_2$ and $Ti(OAA)_2$, the imprints were obtained with cracks at the macroscopic scale (Fig. 6.24). However, these imprints also suffered poorer stability and flaked off during calcination. When the metal to monomer ratio was increased to 1:3 and 1:4, the obtained imprints were smoother and mechanically stable even after the calcination. Thus, the good quality imprints was obtained with the resist materials containing three and four equivalents of monomers.

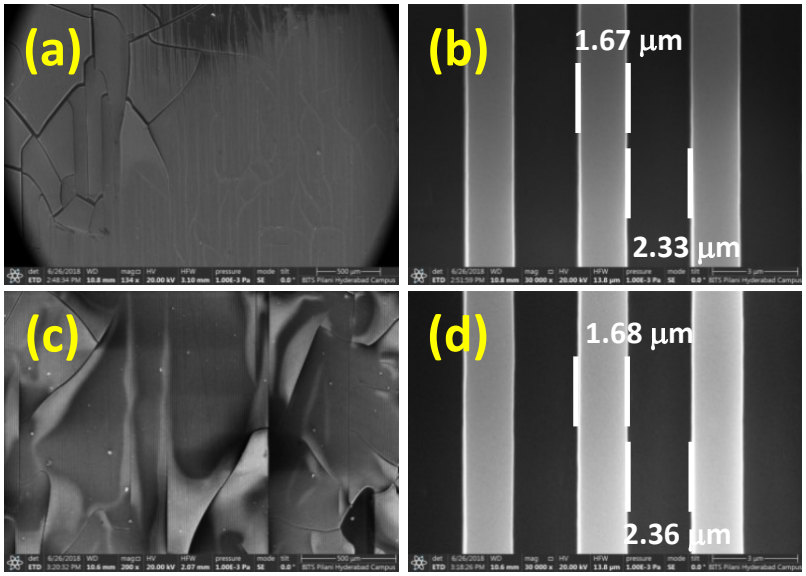

Figure 6.24: FE-SEM images of the imprints using resist formulations of (a, b) $Ti(EAA)_2$ and (c, d) $Ti(OAA)_2$.

Fig. 6.25 and 6.26 shows the area and cross sectional morphology of the imprinted films of $Ti(EAA)_3$ and $Ti(OAA)_3$. The imprints before calcination contain the line of ~1.55 µm and space of 2.5 µm. After calcination, the patterns shrunk to ~52% of the original size in of the polymer film and thus exhibited ~48% pattern shrinkage. Whereas, the shrinkage increased and the patterns retained ~40% of original size in case of $Ti(EAA)_4$ and $Ti(OAA)_4$, which corresponds to ~60% pattern shriknage(Fig. 6.27 and 6.28). The increased shrinkage is because of the high amount of monomer, which will be burnt off during heat treatment.

Hence the optimum condition to overcome the shrinkage is 1:3 ratios of the metal alkoxide to the monomer. Furthermore, this composition has resulted in ~48% of pattern shrinkage, as opposed to the previously reported 70-80% shrinkage using PSG approach. Both the monomers EAA and OAA were suitable for better imprinting and retainable patterns as the thin films.

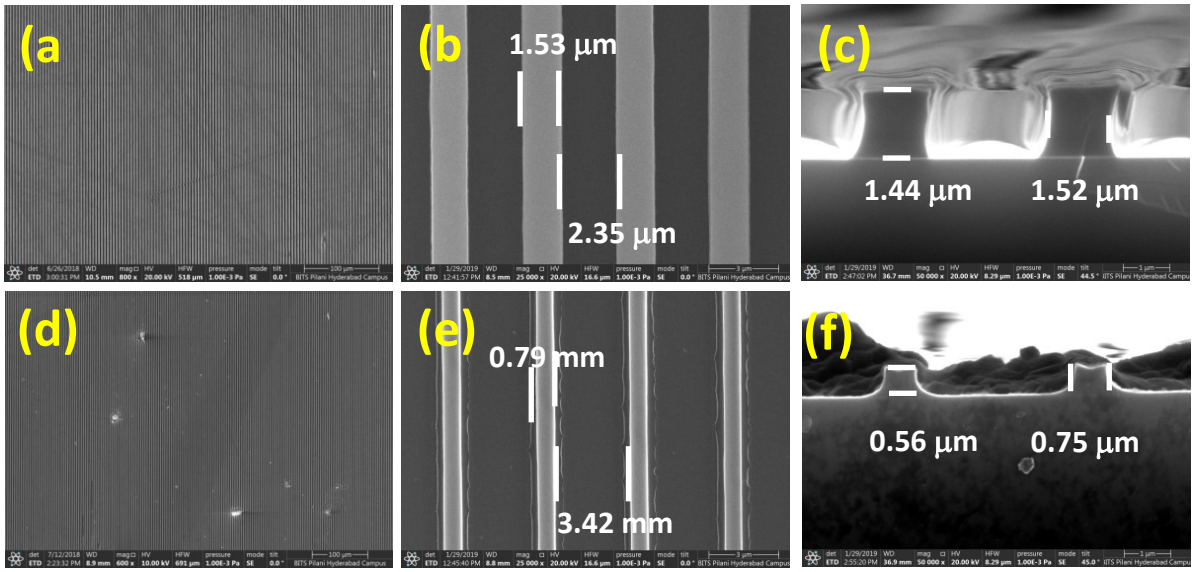

Figure 6.25: Areal and cross sectional FE-SEM images of the imprints of $Ti(EAA)_3$ (a-c) before and (d-f) after calcination.

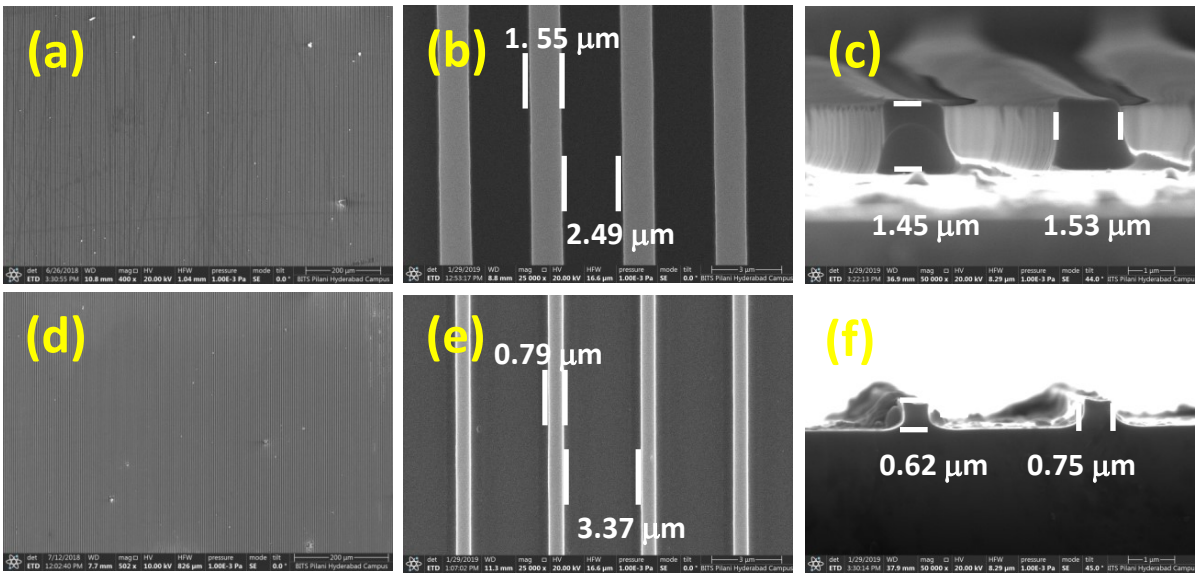

Figure 6.26: Areal and cross sectional FE-SEM images of the imprints of $Ti(OAA)_3$ (a-c) before and (d-f) after calcination.

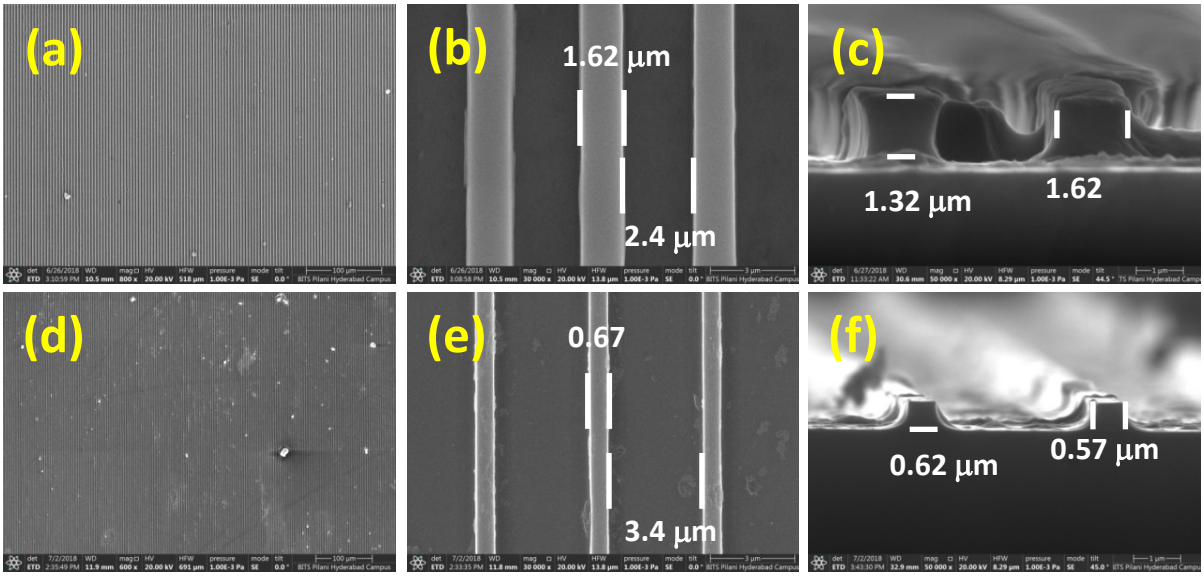

Figure 6.27: Areal and cross sectional FE-SEM images of the imprints of $Ti(EAA)_4$ (a-c) before and (d-f) after calcination.

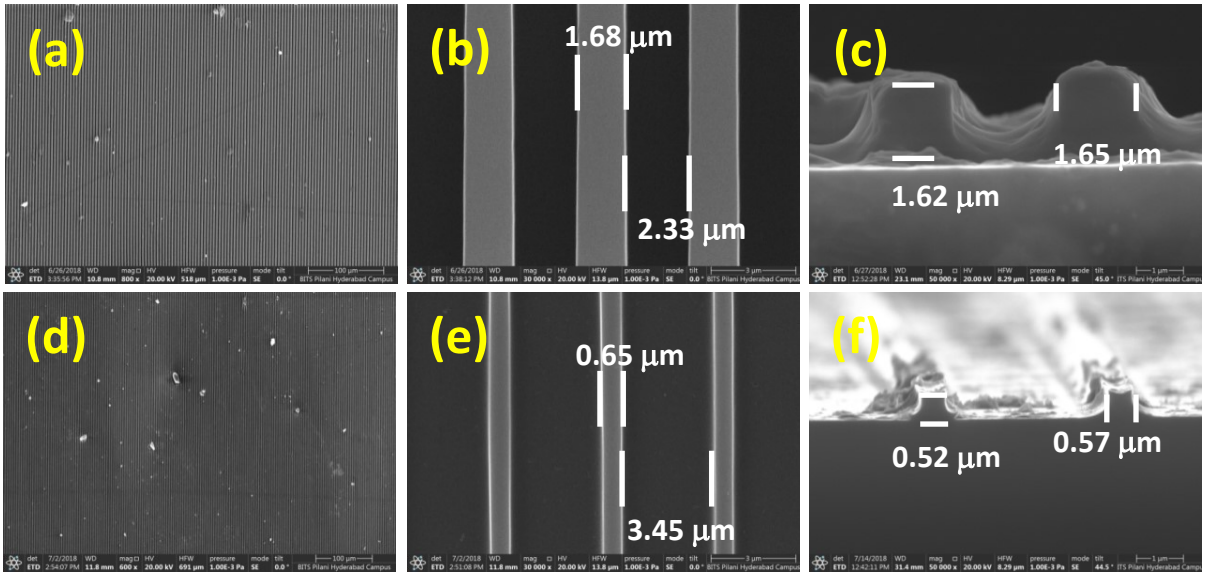

Figure 6.28: Areal and cross sectional FE-SEM images of the imprints of $Ti(OAA)_4$ (a-c) before and (d-f) after calcination.

The imprinted thin films were calcined at 450 °C and the phase of TiO_2 was analysed using X-ray diffraction (XRD). Fig. 6.29 shows the XRD pattern of the thin films of TiO_2 prepared from $Ti(EAA)_4$ and $Ti(OAA)_4$. In both the cases phase pure form of anatase TiO_2 (JCPDS 89-4921) was after calcination. The broad peaks are due to nanocrystalline nature of the material. The crystallite size of the materials was calculated using Scherrer's formula and the values are found to be 6.5 and 8.2 nm for TiO_2 thin films formed from $Ti(EAA)_4$ and $Ti(OAA)_4$ respectively. The calcined thin films were analysed with diffuse reflectance

spectroscopy to calculate the band gap of the material (Fig. 6.30). The band gap was calculated from Kubelka-Munk plot and the band gap varies from 3.9 to 4.2 eV which is in accordance with UV region of the spectrum. The high band gaps could be attributed to the quantum confinement in the nanocrystalline TiO_2 thin films.

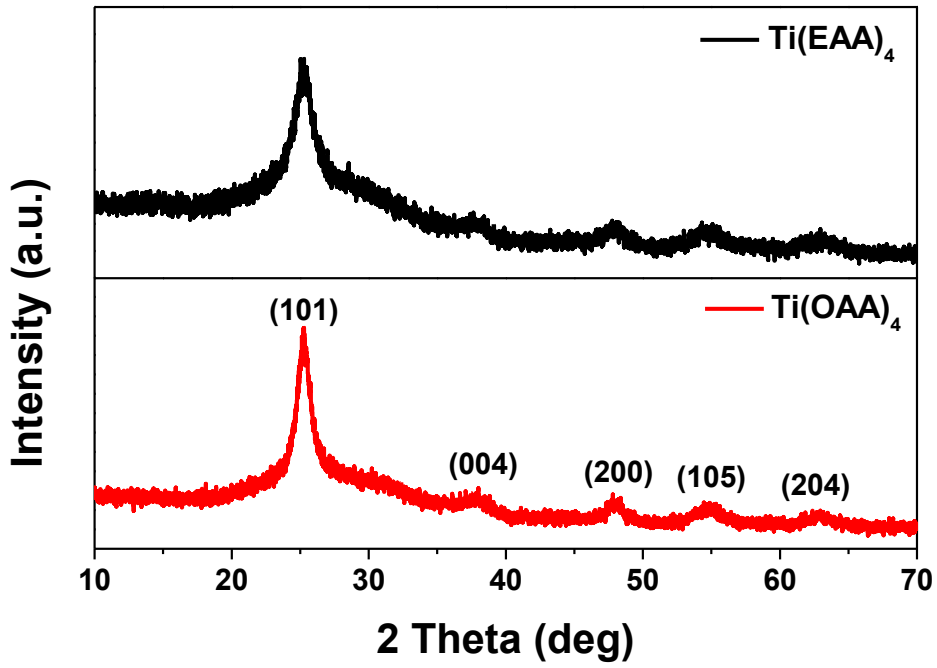

Figure 6.29: X-ray diffraction of the thin films of TiO_2 prepared from $Ti(EAA)_4$ and $Ti(OAA)_4$.

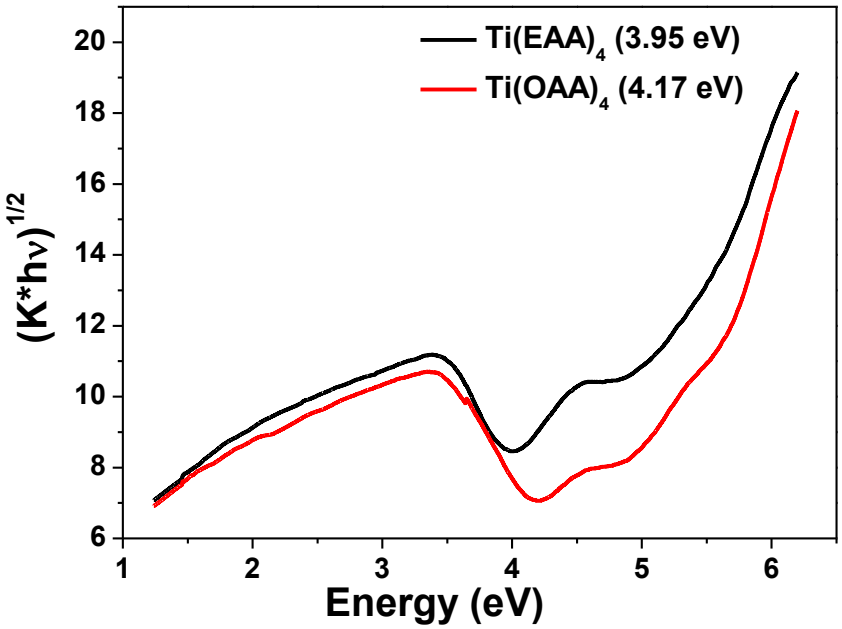

Figure 6.30: Kubelka-Munk plot of thin films of TiO_2 prepared from $Ti(EAA)_4$ and $Ti(OAA)_4$.

5.4 Conclusions

In summary, thiol-ene photo-click chemistry has been successfully applied to the fabrication of metal oxide micro/nanostructures *via* imprinting. When PETMP and AAAc were mixed to keep the allyl to thiol ratio as 1:1, the FT-IR studies revealed poor efficiency of the thiol-ene photo-click chemistry. When allyl to thiol ratio was kept as 1:0.5, the thiol-ene photo-click chemistry was found to be efficient under ambient conditions, possibly due to the enhanced probability of the reaction between –SH group and the abundant alkene. The metal-containing resin consisted of chelated titanium alkoxide with AAAc (or MAEAA) with suitable proportion of PETMP cross-linker, and HMP photo-initiator. With the optimal amount of allyl to thiol ratio as 1:0.5 (TAP-0.5), the resin exhibited excellent photo-curability to yield stable, crack-free, and dry thin film. The XRD and Raman analyses revealed the formation of anatase TiO_2 phase at temperatures below 550 °C, above which a small amount of rutile formation was confirmed with XRD. The diffuse reflectance spectroscopy revealed the semiconducting nature of the thin film TiO_2. The imprinting studies demonstrated the patternability of the titanium-containing resin to fabricate micro/nanostructures of TiO_2. Successful extension of this thiol-ene photo-click chemistry for patterning Ta_2O_5 confirmed the leeway of this approach towards fabrication of various functional oxide nanostructures.

Afterwards this polymerizable sol-gel approach was effectively extended to imprint the metal oxide nanostructures in NIL using epoxy and oxetane based resist materials. Two monomers, EAA and OAA, have been successfully synthesized and chelated with titanium to obtain metal-containing resist. UV exposure followed by PEB during the imprinting of the metal-containing containing resist resulted in cationic ring opening polymerization. The occurrence of the epoxy and oxetane ring opening was confirmed by FT-IR analyses. In this approach, the usage of reactive diluents was completely avoided and thereby increased the residual metal content in this resist. This was found to result in higher ceramic yield, due to which the net shrinkage was decreased, when compared to the previous sol-gel polymerizable approach. The optimum ratio of the metal alkoxide to the monomer was found to be 1:3, which exhibited a pattern shrinkage of ~48%, as opposed to the previously reported 70-80% size reduction in TiO_2. The results show that the epoxy and oxetane based resins can be promising candidates for creating functional patterned oxides with high pattern density that would be suitable for several semiconducting, catalytic and sensing applications.

5.5 References

1. Xu, Z.; Yin, M.; Sun, J.; Ding, G.; Lu, L.; Chang, P.; Chen, X.; Li, D., 3D periodic multiscale TiO_2 architecture: a platform decorated with graphene quantum dots for enhanced photoelectrochemical water splitting. *Nanotechnology* **2016,** *27* (11), 115401.

2. Na, J.; Kim, Y.; Park, C.; Kim, E., Multi-layering of a nanopatterned TiO_2 layer for highly efficient solid-state solar cells. *NPG Asia Materials* **2015,** *7*, e217.

3. Hu, P.; Du, G.; Zhou, W.; Cui, J.; Lin, J.; Liu, H.; Liu, D.; Wang, J.; Chen, S., Enhancement of ethanol vapor sensing of TiO_2 nanobelts by surface engineering. *ACS Applied Materials & Interfaces* **2010,** *2* (11), 3263-3269.

4. Kumar, S. G.; Devi, L. G., Review on modified TiO_2 photocatalysis under UV/visible light: selected results and related mechanisms on interfacial charge carrier transfer dynamics. *The Journal of Physical Chemistry A* **2011,** *115* (46), 13211-13241.

5. Tohge, N.; Ueno, R.; Chiba, F.; Kintaka, K.; Nishii, J., Characteristics of diffraction gratings fabricated by the two-beam interference method using photosensitive hybrid gel films. *Journal of Sol-Gel Science and Technology* **2000,** *19* (1), 119-123.

6. Li, L.; Chakrabarty, S.; Spyrou, K.; Ober, C. K.; Giannelis, E. P., Studying the mechanism of hybrid nanoparticle photoresists: effect of particle size on photopatterning. *Chemistry of Materials* **2015,** *27* (14), 5027-5031.

7. Saifullah, M.; Subramanian, K.; Tapley, E.; Kang, D. J.; Welland, M.; Butler, M., Sub-10 nm electron beam nanolithography using spin-coatable TiO_2 resists. *Nano Letters* **2003,** *3* (11), 1587-1591.

8. Garoli, D.; Della Giustina, G., Directly patternable high refractive index ferroelectric sol–gel resist. *Materials Chemistry and Physics* **2015,** *164*, 63-70.

9. Voicu, N. E.; Saifullah, M.; Subramanian, K.; Welland, M. E.; Steiner, U., TiO_2 patterning using electro-hydrodynamic lithography. *Soft Matter* **2007,** *3* (5), 554-557.

10. Lee, S.; Jung, S. H.; Kang, D. J.; Lee, J., Fabrication of a nano-scale pattern with various functional materials using electrohydrodynamic lithography and functionalization. *RSC Advances* **2016,** *6* (7), 5944-5948.

11. Duoss, E. B.; Twardowski, M.; Lewis, J. A., Sol-gel inks for direct-write assembly of functional oxides. *Advanced Materials* **2007,** *19* (21), 3485-3489.

12. Sung, S.; Park, S.; Cha, S.; Lee, W. J.; Kim, C. H.; Yoon, M. H., Direct patterning of sol–gel metal oxide semiconductor and dielectric films via selective surface wetting. *RSC Advances* **2015,** *5* (48), 38125-38129.

13. Fu, L.; Liu, X.; Zhang, Y.; Dravid, V. P.; Mirkin, C. A., Nanopatterning of "hard" magnetic nanostructures via dip-pen nanolithography and a sol-based ink. *Nano Letters* **2003,** *3* (6), 757-760.

14. Su, M.; Liu, X.; Li, S. Y.; Dravid, V. P.; Mirkin, C. A., Moving beyond molecules: patterning solid-state features via dip-pen nanolithography with sol-based inks. *Journal of the American Chemical Society* **2002,** *124* (8), 1560-1561.

15. Lim, S. H.; Saifullah, M.; Hussain, H.; Loh, W. W.; Low, H. Y., Direct imprinting of high resolution TiO_2 nanostructures. *Nanotechnology* **2010,** *21* (28), 285303.

16. Li, M.; Tan, H.; Chen, L.; Wang, J.; Chou, S. Y., Large area direct nanoimprinting of SiO_2–TiO_2 gel gratings for optical applications. *Journal of Vacuum Science & Technology B: Microelectronics and Nanometer Structures Processing, Measurement, and Phenomena* **2003,** *21* (2), 660-663.

17. Park, H. H.; Choi, D. G.; Zhang, X.; Jeon, S.; Park, S. J.; Lee, S. W.; Kim, S.; Kim, K. D.; Choi, J. H.; Lee, J., Photo-induced hybrid nanopatterning of titanium dioxide via direct imprint lithography. *Journal of Materials Chemistry* **2010,** *20* (10), 1921-1926.

18. Azimi, S.; Song, J.; Li, C.; Mathew, S.; Breese, M.; Venkatesan, T., Nanoscale lithography of $LaAlO_3/SrTiO_3$ wires using silicon stencil masks. *Nanotechnology* **2014,** *25* (44), 445301.

19. Faustini, M.; Boissiere, C.; Nicole, L.; Grosso, D., From chemical solutions to inorganic nanostructured materials: a journey into evaporation-driven processes. *Chemistry of Materials* **2013,** *26* (1), 709-723.

20. Costner, E. A.; Lin, M. W.; Jen, W. L.; Willson, C. G., Nanoimprint lithography materials development for semiconductor device fabrication. *Annual Review of Materials Research* **2009,** *39*, 155-180.

21. Byeon, K. J.; Lee, H., Recent progress in direct patterning technologies based on nano-imprint lithography. *The European Physical Journal Applied Physics* **2012,** *59* (1), 10001.

22. Ok, J. G.; Shin, Y. J.; Park, H. J.; Guo, L. J., A step toward next-generation nanoimprint lithography: extending productivity and applicability. *Applied Physics A* **2015,** *121* (2), 343-356.

23. Choi, D. G.; Lee, K. J.; Kim, S.; Lee, E. S.; Jeong, J. H.; Lee, J.; Choi, J. H., Rapid nanopatterning of zirconium dioxide via nanoprinting and microwave-assisted annealing. *RSC Advances* **2012,** *2* (29), 11035-11039.

24. Resnick, D. J.; Sreenivasan, S.; Willson, C. G., Step & flash imprint lithography. *Materials Today* **2005,** *8* (2), 34-42.

25. Kustandi, T. S.; Loh, W. W.; Gao, H.; Low, H. Y., Wafer-scale near-perfect ordered porous alumina on substrates by step and flash imprint lithography. *ACS Nano* **2010,** *4* (5), 2561-2568.

26. Takei, S.; Ogawa, T.; Deschner, R.; Willson, C. G., Reduction of pattern peeling in step-and-flash imprint lithography. *Microelectronic Engineering* **2014,** *116*, 44-50.

27. Kooy, N.; Mohamed, K.; Pin, L. T.; Guan, O. S., A review of roll-to-roll nanoimprint lithography. *Nanoscale Research Letters* **2014,** *9* (1), 320.

28. Ahn, S. H.; Guo, L. J., Large-area roll-to-roll and roll-to-plate nanoimprint lithography: a step toward high-throughput application of continuous nanoimprinting. *ACS Nano* **2009,** *3* (8), 2304-2310.

29. Ganesan, R.; Dumond, J.; Saifullah, M. S.; Lim, S. H.; Hussain, H.; Low, H. Y., Direct patterning of TiO_2 using step-and-flash imprint lithography. *ACS Nano* **2012,** *6* (2), 1494-1502.

30. Gobel, O. F.; Nedelcu, M.; Steiner, U., Soft lithography of ceramic patterns. *Advanced Functional Materials* **2007,** *17* (7), 1131-1136.

31. Kwon, S. J.; Park, J. H.; Park, J. G., Selective growth of ZnO nanorods by patterning of sol-gel-derived thin film. *Journal of Electroceramics* **2006,** *17* (2), 455-459.

32. Zanchetta, E.; Auzelyte, V.; Brugger, J.; Savegnago, A. V.; Della Giustina, G.; Brusatin, G., Highly inorganic titania based sol–gel as directly patternable resist for micro-and nano-structured surfaces. *Microelectronic Engineering* **2012,** *98*, 176-179.

33. Choi, J. H.; Jo, H. B.; Choi, H. J.; Lee, H., Fabrication of TiO_2 nano-to-microscale structures using UV nanoimprint lithography. *Nanotechnology* **2013,** *24* (19), 195301.

34. Kothari, R.; Beaulieu, M. R.; Hendricks, N. R.; Li, S.; Watkins, J. J., Direct patterning of robust one-dimensional, two-dimensional, and three-dimensional crystalline metal oxide nanostructures using imprint lithography and nanoparticle dispersion inks. *Chemistry of Materials* **2017,** *29* (9), 3908-3918.

35. Rasic, G.; Schwartz, J., Nanoimprint lithographic surface patterning of sol–gel fabricated nickel ferrite (NiFe 2 O 4). *MRS Communications* **2013,** *3* (04), 207-211.

36. Ganesan, R.; Lim, S. H.; Saifullah, M.; Hussain, H.; Kwok, J. X.; Ryan, L.; Bo, H. A.; Low, H. Y., Direct nanoimprinting of metal oxides by in situ thermal co-polymerization of their methacrylates. *Journal of Materials Chemistry* **2011,** *21* (12), 4484-4492.

37. Dinachali, S. S.; Saifullah, M. S.; Ganesan, R.; Thian, E. S.; He, C., A universal scheme for patterning of oxides via thermal nanoimprint lithography. *Advanced Functional Materials* **2013,** *23* (17), 2201-2211.

38. Dinachali, S. S.; Dumond, J.; Saifullah, M. S. M.; Ansah-Antwi, K. K.; Ganesan, R.; Thian, E. S.; He, C., Large area, facile oxide nanofabrication via step-and-flash imprint lithography of metal–organic hybrid resins. *ACS Applied Materials & Interfaces* **2013,** *5* (24), 13113-13123.

39. Nagarjuna, R.; Roy, S.; Ganesan, R., Polymerizable sol–gel precursor mediated synthesis of TiO_2 supported zeolite-4A and its photodegradation of methylene blue. *Microporous and Mesoporous Materials* **2015,** *211*, 1-8.

40. Challagulla, S.; Nagarjuna, R.; Ganesan, R.; Roy, S., Acrylate-based polymerizable sol–gel synthesis of magnetically recoverable TiO_2 Supported Fe_3O_4 for Cr(VI) photoreduction in aerobic atmosphere. *ACS Sustainable Chemistry & Engineering* **2016,** *4* (3), 974-982.

41. Ramirez, L. M. S.; He, M.; Mailloux, S.; George, J.; Wang, J., Facile and high-throughput synthesis of functional microparticles with quick response codes. *Small* **2016,** *12* (24), 3259-3269.

42. Kolb, H. C.; Sharpless, K. B., The growing impact of click chemistry on drug discovery. *Drug Discovery Today* **2003,** *8* (24), 1128-1137.

43. Kim, C. H.; Bang, J. H.; Hong, K. B.; Park, M. H., Fabrication of highly photoluminescent quantum dot-polymer composite micropatterned surface using thiol-ene chemistry. *RSC Advances* **2016,** *6* (99), 96700-96705.

44. Ruizendaal, L.; Pujari, S. P.; Gevaerts, V.; Paulusse, J. M.; Zuilhof, H., Biofunctional silicon nanoparticles by means of thiol-ene click chemistry. *Chemistry–An Asian Journal* **2011,** *6* (10), 2776-2786.

45. Durham, O. Z.; Norton, H. R.; Shipp, D. A., Functional polymer particles via thiol–ene and thiol–yne suspension "click" polymerization. *RSC Advances* **2015,** *5* (82), 66757-66766.

46. Modjinou, T.; Rodriguez-Tobias, H.; Morales, G.; Versace, D. L.; Langlois, V.; Grande, D.; Renard, E., UV-cured thiol–ene eugenol/ZnO composite materials with antibacterial properties. *RSC Advances* **2016,** *6* (91), 88135-88142.

47. Zhou, Y. B.; Zhan, Z. P., Conjugated microporous polymers for heterogeneous catalysis. *Chemistry–An Asian Journal* **2018,** *13* (1), 9-19.

48. Hoyle, C. E.; Bowman, C. N., Thiol–ene click chemistry. *Angewandte Chemie International Edition* **2010,** *49* (9), 1540-1573.

49. Lowe, A. B., Thiol-ene "click" reactions and recent applications in polymer and materials synthesis. *Polymer Chemistry* **2010,** *1* (1), 17-36.

50. Lowe, A. B., Thiol–ene "click" reactions and recent applications in polymer and materials synthesis: a first update. *Polymer Chemistry* **2014,** *5* (17), 4820-4870.

51. Kade, M. J.; Burke, D. J.; Hawker, C. J., The power of thiol-ene chemistry. *Journal of Polymer Science Part A: Polymer Chemistry* **2010,** *48* (4), 743-750.

52. Tan, J.; Li, C.; Zhou, J.; Yin, C.; Zhang, B.; Gu, J.; Zhang, Q., Fast and facile fabrication of porous polymer particles via thiol–ene suspension photopolymerization. *RSC Advances* **2014,** *4* (26), 13334-13339.

53. Campos, L. M.; Killops, K. L.; Sakai, R.; Paulusse, J. M.; Damiron, D.; Drockenmuller, E.; Messmore, B. W.; Hawker, C. J., Development of thermal and photochemical strategies for thiol−ene click polymer functionalization. *Macromolecules* **2008,** *41* (19), 7063-7070.

54. Hayes, T. R.; Lyon, P. A.; Silva-Lopez, E.; Twamley, B.; Benny, P. D., Photo-initiated thiol-ene click reactions as a potential strategy for incorporation of $[MI(CO)_3]^+$(M= Re, 99mTc) complexes. *Inorganic chemistry* **2013,** *52* (6), 3259-3267.

55. Connal, L. A.; Kinnane, C. R.; Zelikin, A. N.; Caruso, F., Stabilization and functionalization of polymer multilayers and capsules via thiol−ene click chemistry. *Chemistry of Materials* **2009,** *21* (4), 576-578.

56. Xu, J.; Boyer, C., Visible light photocatalytic thiol–ene reaction: an elegant approach for fast polymer postfunctionalization and step-growth polymerization. *Macromolecules* **2015,** *48* (3), 520-529.

57. Bordoni, A. V.; Lombardo, M. V.; Wolosiuk, A., Photochemical radical thiol–ene click-based methodologies for silica and transition metal oxides materials chemical modification: a mini-review. *RSC Advances* **2016,** *6* (81), 77410-77426.

58. Hagberg, E. C.; Malkoch, M.; Ling, Y.; Hawker, C. J.; Carter, K. R., Effects of modulus and surface chemistry of thiol-ene photopolymers in nanoimprinting. *Nano Letters* **2007,** *7* (2), 233-237.

59. Campos, L. M.; Meinel, I.; Guino, R. G.; Schierhorn, M.; Gupta, N.; Stucky, G. D.; Hawker, C. J., Highly versatile and robust materials for soft imprint lithography based on thiol-ene click chemistry. *Advanced Materials* **2008,** *20* (19), 3728-3733.

60. Lin, H.; Wan, X.; Jiang, X.; Wang, Q.; Yin, J., A nanoimprint lithography hybrid photoresist based on the thiol–ene system. *Advanced Functional Materials* **2011,** *21* (15), 2960-2967.

61. Hu, X.; Huang, S.; Gu, R.; Yuan, C.; Ge, H.; Chen, Y., An Oxygen-insensitive degradable resist for fabricating metallic patterns on highly curved surfaces by uv-nanoimprint lithography. *Macromolecular Rapid Communications* **2014,** *35* (19), 1712-1718.

62. Pelaez, M.; Nolan, N. T.; Pillai, S. C.; Seery, M. K.; Falaras, P.; Kontos, A. G.; Dunlop, P. S.; Hamilton, J. W.; Byrne, J. A.; O'shea, K., A review on the visible light active titanium dioxide photocatalysts for environmental applications. *Applied Catalysis B: Environmental* **2012,** *125*, 331-349.

63. Song, L.; Abdelsamie, A.; Schaffer, C. J.; Körstgens, V.; Wang, W.; Wang, T.; Indari, E. D.; Froschl, T.; Husing, N.; Haeberle, T., A low temperature route toward

hierarchically structured titania films for thin hybrid solar cells. *Advanced Functional Materials* **2016,** *26* (39), 7084-7093.

64. Pina-Hernandez, C.; Lacatena, V.; Calafiore, G.; Dhuey, S.; Kravtsov, K.; Goltsov, A.; Olynick, D.; Yankov, V.; Cabrini, S.; Peroz, C., A route for fabricating printable photonic devices with sub-10 nm resolution. *Nanotechnology* **2013,** *24* (6), 065301.

65. Zhang, J.; Hu, X.; Zhang, J.; Cui, Y.; Yuan, C.; Ge, H.; Chen, Y.; Wu, W.; Xia, Q., A fast thermal-curing nanoimprint resist based on cationic polymerizable epoxysiloxane. *Nanoscale Research Letters* **2012,** *7* (1), 380.

66. Stewart, M. D.; Willson, C. G., Imprint materials for nanoscale devices. *MRS Bulletin* **2005,** *30* (12), 947-951.

67. Decker, C.; Viet, T. N. T.; Decker, D.; Weber-Koehl, E., UV-radiation curing of acrylate/epoxide systems. *Polymer* **2001,** *42* (13), 5531-5541.

68. Cheng, X.; Guo, L. J.; Fu, P. F., Room-temperature, low-pressure nanoimprinting based on cationic photopolymerization of novel epoxysilicone monomers. *Advanced Materials* **2005,** *17* (11), 1419-1424.

69. Wu, C. C.; Hsu, S. L. C., Preparation of epoxy/silica and epoxy/titania hybrid resists via a sol−gel process for nanoimprint lithography. *The Journal of Physical Chemistry C* **2010,** *114* (5), 2179-2183.

70. Su, W.; Zhang, J.; Feng, Z.; Chen, T.; Ying, P.; Li, C., Surface phases of TiO_2 nanoparticles studied by UV Raman Spectroscopy and FT-IR Spectroscopy. *The Journal of Physical Chemistry C* **2008,** *112* (20), 7710-7716.

71. Linsebigler, A. L.; Lu, G.; Yates Jr, J. T., Photocatalysis on TiO2 surfaces: principles, mechanisms, and selected results. *Chemical Reviews* **1995,** *95* (3), 735-758.

72. Challagulla, S.; Tarafder, K.; Ganesan, R.; Roy, S., Structure sensitive photocatalytic reduction of nitroarenes over TiO_2. *Scientific Reports* **2017,** *7* (1), 8783.

73. Lü, X.; Ding, S.; Lin, T.; Mou, X.; Hong, Z.; Huang, F., Ta_2O_5 Nanowires: a novel synthetic method and their solar energy utilization. *Dalton Transactions* **2012,** *41* (2), 622-627.

74. Zhao, D.; Zhang, C.; Kim, H.; Guo, L. J., High-performance Ta_2O_5/Al-doped Ag electrode for resonant light harvesting in efficient organic solar cells. *Advanced Energy Materials* **2015,** *5* (17).

75. Dhawan, S.; Dhawan, T.; Vedeshwar, A. G., Crystalline to amorphous phase transformation of Ta_2O_5 quantum dots driven by residual stress. *Journal of Alloys and Compounds* **2016,** *657*, 366-371.

76. Chun, W. J.; Ishikawa, A.; Fujisawa, H.; Takata, T.; Kondo, J. N.; Hara, M.; Kawai, M.; Matsumoto, Y.; Domen, K., Conduction and valence band positions of Ta_2O_5, TaON, and Ta_3N_5 by UPS and electrochemical methods. *The Journal of Physical Chemistry B* **2003,** *107* (8), 1798-1803.

77. Witzeman, J. S.; Nottingham, W. D., Transacetoacetylation with tert-butyl acetoacetate: synthetic applications. *The Journal of Organic Chemistry* **1991,** *56* (5), 1713-1718.

78. Ganesan, R.; Dinachali, S. S.; Lim, S. H.; Saifullah, M.; Chong, W. T.; Lim, A. H.; Yong, J. J.; San Thian, E.; He, C.; Low, H. Y., Direct nanoimprint lithography of Al_2O_3 using a chelated monomer-based precursor. *Nanotechnology* **2012,** *23* (31), 315304.

79. Nikolic, G.; Zlatkovic, S.; Cakic, M.; Cakic, S.; Lacnjevac, C.; Rajic, Z., Fast fourier transform IR characterization of epoxy GY systems crosslinked with aliphatic and cycloaliphatic EH polyamine adducts. *Sensors* **2010,** *10* (1), 684-696.

80. Evtushenko, Y. M.; Ivanov, V.; Zaitsev, B., Determination of epoxide and hydroxyl groups in epoxide resins by IR spectrometry. *Journal of Analytical Chemistry* **2003,** *58* (4), 347-350.

81. Zhan, F.; Cheng, X. E.; Shi, W., Cationic UV curing behavior and thermal properties of oxetane-modified polysiloxane prepared from tetraethyl orthosilicate. *Journal of Applied Polymer Science* **2012,** *123* (2), 717-724.

Chapter 7

Conclusions and future perceptive

Chapter 7: Conclusions and future perspective

7.1 Conclusions

Synthesis of various supported and non-supported metal oxide nanomaterials such as TiO_2, Fe_2O_3 and WO_3 through polymerizable sol-gel (PSG) route have been studied systematically in this thesis. In addition, the surface functionalization and fabrication of metal oxide nano-structures have been discussed.

Briefly, the chapter 1 provides a broad introduction to the metal oxide nanomaterials and various synthetic approaches to achieve them. Several characterization techniques and applications of the metal oxide nanomaterials were also explained in this chapter. In the subsequent chapter 2, the chemicals and characterization tools were listed, which were utilized for the synthesis and analysis of the materials.

Chapter 3 describes the design and synthesis of TiO_2 supported zeolite-4A by tailored polymerizable sol-gel method. The hydrolysis of the precursor blend of Ti-*di*methacrylate *diiso*propoxide and the industrial grade zeolite-4A under vigorous shaking produced a homogeneously mixed polymerizable gel in the zeolite matrix. Upon inducing the free radical polymerization at 125 °C, this gel produced a polymer coating on the top of the support. Further calcination at 450 °C for 4 hours yielded highly dispersed TiO_2 anchored on the zeolite-4A. DRS revealed a clear trend in decreasing the band gap from 3.81 to 3.66 eV when TiO_2 content in the matrix was increased from 10 to 30 wt% indicating the nano-crystallinity of TiO_2 particle. Surface area measurement disclosed an enhancement of surface area by ~2.5 times for the customized sol-gel synthesized 20 % TiO_2/zeolite-4A than that of the physical blend of 20 % TiO_2 and zeolite-4A. The photocatalytic activities of the catalysts were studied by measuring the photodegradation of methylene blue. The catalysts showed pH dependence, and the rate was faster in alkaline medium. The polymerizable sol-gel synthesized catalyst was found to have superior catalytic activity to the physical blend of TiO_2 and zeolite-4A. To improve the adsorption capacity of the catalyst, GO was anchored on to TiO_2 and zeolite-4A. This investigation deals in detail with the synthesis of GO by an improved oxidation method from graphite flakes, and pure TiO_2 by the polymerizable sol–gel route. The GO was partially photoreduced in alcoholic medium in the presence of TiO_2 and in the process the RGO was anchored onto the TiO_2 surface. The RGO/TiO_2 was dispersed on zeolite-4A for better adsorption efficiency. The partial reduction of GO to RGO over TiO_2 was evidenced from XRD, FT-IR and Raman spectroscopy. The adsorption of methylene blue over RGO/TiO_2/zeolite-4A was found to be following the Langmuir isotherm model. The

adsorption kinetics was fitted well with the pseudo first order kinetic model. The high adsorption as well as photocatalytic degradation efficiency of RGO/TiO_2/zeolite-4A towards MB paves the way for new advanced bifunctional materials for environmental applications.

Since the route offered facile reaction conditions and enhanced material properties, it can be considered as a potential approach to synthesize other supported metal oxides for environmental remediation. The materials can be applied for degradation of other dyes and antibiotics.

In chapter 4, TiO_2/Fe_3O_4 catalysts with various loading of TiO_2 were synthesized by the polymerizable sol–gel route. The XRD and SEM characterization revealed high dispersion of TiO_2 over Fe_3O_4. BET surface area measurements revealed increase in surface area with increase in TiO_2 loading. The surface of the Fe_3O_4 was found to be partially oxidized to Fe_2O_3 during the calcination step. The DRS showed the semiconducting band gaps of TiO_2 and calcined Fe_3O_4. The TiO_2/Fe_3O_4 composite catalysts showed higher rate of photoreduction of Cr(VI) than the non-supported bulk TiO_2 as well as calcined Fe_3O_4. The photoreduction mechanism was probed by using hole as well as electron scavengers. The photocatalytic studies show that the anchoring of TiO_2 over Fe_3O_4 results in three-fold advantage. First, when the TiO_2 is anchored over Fe_3O_4, the dispersion of the active site was higher. This is a crucial one for achieving higher reaction rate. Second, the significant band overlap of TiO_2 and Fe_3O_4 helped decreasing the electron-hole recombination reaction, thus enhancing the photoreduction rate. Third, Fe_3O_4 being a magnetic nanoparticle, the magnetic recyclability of the catalyst was convenient.

To extend the photocatalytic activity towards visible light from UV light, the suitable Fe_3O_4@Fe_2O_3/Al_2O_3 catalysts were synthesized by the customized co-precipitation method. XRD and TEM analyses showed that the calcined Fe_3O_4 crystals, which were of inverse spinel structure, were highly dispersed over nano γ-Al_2O_3 support and the surface area of the composite was significantly higher than that of the individual components. XPS and Raman studies confirmed that Fe_3O_4 was partially oxidized to Fe_2O_3 due to calcination step during post co-precipitation synthesis. The Kubelka-Munk plot obtained from diffuse reflectance spectra showed the semiconducting band gap of Fe_2O_3, which was suitable for visible light photoreduction activity. The rate of Cr(VI) photoreduction over 5% Fe_3O_4@Fe_2O_3/Al_2O_3 was as high as 14.2 mol L^{-1} min^{-1} g^{-1} under direct sunlight. The 40% Fe_3O_4@Fe_2O_3/Al_2O_3 retained the magnetic property as in bulk Fe_3O_4 and the composite was magnetically recovered to show unaffected high rate of photoreduction till four cycles. The current investigation is a

proof of concept towards enhanced environmental catalytic application of highly dispersed active semiconducting nanomaterials.

Another metal oxide suitable for the photocatalytic reduction of Cr(VI) in visible radiation is WO_3. Therefore, WO_3 was synthesized at three different temperatures through a facile polymerizable sol–gel approach. The isothermal thermogravimetric analysis revealed that the calcination temperature to obtain nano-crystalline WO_3 can be as low as 450 °C. The XRD and FE-SEM analyses showed the presence of nano-crystalline domains in WO_3-450, whereas the raise in calcination temperature resulted in increased crystallinity. The diffuse reflectance analysis showed higher band gap value for WO_3-450 and WO_3-650 as compared to that of WO_3-850 due to the quantum confinement in the nano-crystalline domains. The XPS analyses revealed the presence of oxygen non-stoichiometry in the lower temperature calcined samples. The highest photocatalytic activity towards Cr(VI) reduction was reached with WO_3-450. The trend in the catalytic efficacy was explained in terms of nano-crystallinity, surface area, non-stoichiometry and valence band profile.

In chapter 5, facile surface functionalization of PEI over alumina nanopowder was accomplished in a two-step approach and showed the utility of the PEI-coated alumina nanopowder towards effective adsorption of palladium. The sorption parameters of palladium were studied through pH effect, contact time, amount of adsorbent, concentrations and temperature. The optimum pH for the adsorption of Pd(II) was found to be 6.0 and the adsorption adhered to the pseudo second-order kinetics. While the native alumina showed an adsorption capacity of 35.08 mg g^{-1}, the PEI-AO exhibited a high adsorption capacity of 97.7 mg g^{-1}, obtained through Langmuir adsorption isotherm. The exothermic nature of adsorption process and the negative free energy obtained at various temperatures confirm the spontaneity of adsorption. XPS analysis of Pd-PEI-AO, and rPd-PEI-AO revealed the favourable interaction of $PdCl_4^{2-}$ with nitrogen moieties of PEI. XRD studies on these samples revealed an increase in the crystallinity of palladium after reduction. The catalytic reduction of 4-NP and Cr(VI) using Pd-PEI-AO was found to proceed with rates as high as 125 mmol L^{-1} min^{-1} g^{-1} and 67 mmol L^{-1} min^{-1} g^{-1}, respectively. Hydrogen generation from ammonia borane was found to be efficient with Pd-PEI-AO with a rate of 10.5 mol min^{-1} g^{-1} at 10% conversion. Recyclability of Pd-PEI-AO was studied up to 5 cycles in all the three catalytic reactions, which revealed the potential of the sorbent for efficient reusability. The amine-functionalization strategy presented in this work could also show potential in recovering and reusing other precious metals such as gold, platinum, and rhodium. The functionalization

procedure can be transferred for other functional groups on different support materials such as SiO_2, TiO_2 etc.

In chapter 6, thiol-ene photo-click chemistry has been successfully applied to the fabrication of metal oxide micro/nanostructures *via* imprinting. When PETMP and AAAc were mixed to keep the allyl to thiol ratio as 1:1, the FT-IR studies revealed poor efficiency of the thiol-ene photo-click chemistry. When allyl to thiol ratio was kept as 1:0.5, the thiol-ene photo-click chemistry was found to be efficient under ambient conditions, possibly due to the enhanced probability of the reaction between –SH group and the abundant alkene. The metal-containing resin consisted of chelated titanium alkoxide with AAAc (or MAEAA) with suitable proportion of PETMP cross-linker, and HMP photo-initiator. With the optimal amount of allyl to thiol ratio as 1:0.5 (TAP-0.5), the resin exhibited excellent photo-curability to yield stable, crack-free, and dry thin film. The XRD and Raman analyses revealed the formation of anatase TiO_2 phase at temperatures below 550 °C, above which a small amount of rutile formation was confirmed with XRD. The diffuse reflectance spectroscopy revealed the semiconducting nature of the thin film TiO_2. The imprinting studies demonstrated the patternability of the titanium-containing resin to fabricate micro/nanostructures of TiO_2. Successful extension of this thiol-ene photo-click chemistry for patterning Ta_2O_5 confirmed the scope of this approach towards fabrication of various functional oxide nanostructures. Afterwards, this polymerizable sol-gel approach was effectively extended to imprint the metal oxide nanostructures in NIL using epoxy and oxetane based resist materials. Two monomers, EAA and OAA, have been successfully synthesized and chelated with titanium to obtain metal-containing resist. UV exposure followed by PEB during the imprinting of the metal-containing containing resist resulted in cationic ring opening polymerization. In this approach, the usage of reactive diluents was completely avoided and thereby increased the residual metal content in this resist. This was found to result in higher ceramic yield, due to which the net shrinkage was decreased, when compared to the previously reported polymerizable sol-gel approach. The optimum ratio of the metal alkoxide to the monomer was found to be 1:3. The patterns were retained even after the annealing and formed crystalline TiO_2.

7.2 Future Perspective

Development of novel photoresist materials is a continually evolving field. In this thesis, a polymerizable sol-gel approach, which is highly scalable, has been used for the bulk synthesis of various oxides and supported oxides. Though only a limited number of oxides have been demonstrated by this approach, a numerous other oxides and mixed oxides are also possible to be designed and synthesized. Furthermore, different support candidates that vary in their role towards catalysis/environmental remediation can also be used. The synthetic strategy can evolve to introduce a variety of dopant into the active semiconductor. All these variants can be explored for their photocatalytic behaviour. In particular, several industrially used dyes such as congo red, indigo etc., and active pharmaceutical ingredients that are released into the aquatic environment can be studied for their photodegradation. Another important avenue is the application of these materials in photovoltaics, wherein the active semiconductor material is made into an integral part of the semiconducting device. Such devices are highly useful in solar energy harvesting through photovoltaics and photoelectrochemical cells.

Nanoimprinting of oxides is fundamentally important as the nanostructured materials exhibit enhanced properties. The photo-click chemistry and ring opening polymerization approaches reported in this thesis can be extrapolated to various oxides. In particular, the epoxy and oxetane based ring opening polymerization chemistry is found to be highly promising in obtaining the oxide nanostructures with less shrinkage. It would be interesting to design and imprint doped and multicomponent oxides through this approach. All such functional nanoimprints can be studied directly for their semiconducting and catalytic applications.

List of publications

From this work

1. **Ravikiran Nagarjuna**, Sounak Roy, Ramakrishnan Ganesan, Polymerizable sol-gel precursor mediated synthesis of TiO_2 supported zeolite-4A and its photodegradation of methylene blue. Microporous and Mesoporous Materials, 211 (2015) 1-8.
2. **Ravikiran Nagarjuna**, Swapna Challagulla, Navateja Alla, Ramakrishnan Ganesan, Sounak Roy, Synthesis and characterization of reduced-graphene oxide/TiO_2/zeolite-4A: A bifunctional nanocomposite for abatement of methylene blue. Materials & Design, 86 (2015) 621-626.
3. Swapna Challagulla, **Ravikiran Nagarjuna**, Ramakrishnan Ganesan, Sounak Roy, Acrylate-based polymerizable sol–gel synthesis of magnetically recoverable TiO_2 supported Fe_3O_4 for Cr(VI) photoreduction in aerobic atmosphere. ACS Sustainable Chemistry & Engineering, 4 (2016) 974–982.
4. **Ravikiran Nagarjuna**, Swapna Challagulla, Ramakrishnan Ganesan, Sounak Roy, High rates of Cr(VI) photoreduction with magnetically recoverable nano-Fe_3O_4@Fe_2O_3/Al_2O_3 catalyst under visible light. Chemical Engineering Journal, 308 (2017) 59-66.
5. **Ravikiran Nagarjuna**, Swapna Challagulla, Pooja Sahu, Sounak Roy, Ramakrishnan Ganesan, Polymerizable sol–gel synthesis of nano-crystalline WO_3 and its photocatalytic Cr(VI) reduction under visible light. Advanced Powder Technology, 28 (2017) 3265-3273.
6. **Ravikiran Nagarjuna**, Shivani Sharma, Nagaratnam Rajesh, and Ramakrishnan Ganesan, Effective adsorption of precious metal palladium over polyethyleneimine-functionalized alumina nanopowder and its reusability as a catalyst for energy and environmental applications. ACS Omega, 2 (2017) 4494-4504.
7. **Ravikiran Nagarjuna**, Mohammad S. M. Saifullah and Ramakrishnan Ganesan, Oxygen insensitive thiol–ene photo-click chemistry for direct imprint lithography of oxide. RSC Advances, 8, (2018), 11403-11411.

Other publications

1. Swapna Challagulla, **Ravikiran Nagarjuna**, Ramakrishnan Ganesan, Sounak Roy, Role of solvents on photocatalytic reduction of nitroarenes by sol-gel synthesized TiO_2/zeolite 4A. Journal of Porous Materials, 22 (2015) 1105-1110.
2. Swapna Challagulla, **Ravikiran Nagarjuna**, Ramakrishnan Ganesan, Sounak Roy, TiO_2 synthesized by various routes and its role on environmental remediation and alternate energy production. Nano-Structures & Nano-Objects, 12 (2017) 147–156.
3. Swapna Challagulla, **Ravikiran Nagarjuna**, Sounak Roy, Ramakrishnan Ganesan, Scalable free-radical polymerization based sol–gel synthesis of $SrTiO_3$ and its photocatalytic activity. Chemistry Select, 2 (2017) 4836 – 4842.
4. Imran Khan, **Ravikiran Nagarjuna**, Jayati Ray Dutta, Ramakrishnan Ganesan, Towards single crystalline, higly monodisperse and catalytically active gold nanoparticles capped with probiotic *Lactobacillus plantarum* derived lipase. Applied Nanoscience, (2018) 1-9.
5. Imran Khan, Nivetha Sivasankaran, **Ravikiran Nagarjuna**, Ramakrishnan Ganesan, Jayati Ray Dutta, Extracellular probiotic lipase capped silver nanoparticles as highly efficient broad spectrum antimicrobial agents. RSC Advances, 8 (2018) 31358-31365.
6. Imran Khan, **Ravikiran Nagarjuna**, Jayati Ray Dutta, Ramakrishnan Ganesan, Enzyme embedded degradation of poly(ε-caprolactone) using lipase derived from probiotic lactobacillus plantarum. ACS Omega 4 (2019) 2844-2852.

Patent

1. A method for preparing core-shell nanoparticles. Balaji Gopalan, Ramakrishnan Ganesan, Nalluri Srinivasa Rao, **Ravikiran Nagarjuna**, Indian Patent filed on 18th May 2016 (Ref. No. 201611017377).

List of conferences attended

1. Poster presentation entitled Polymerization mediated soft-synthesis of zeolite-4A supported TiO_2, its characterization and photodegradation of methylene blue at 13th Eurasia conference on Chemical Sciences-2014, IISC, Bangalore.
2. Poster presentation entitled Polymerizable sol–gel synthesis of reduced graphene oxide/TiO_2/zeolite-4A, its characterization and photodegradation of methylene blue at International Conference on Nascent Developments in Chemical Sciences-2015, BITS-Pilani, Pilani campus, Rajasthan.
3. Oral presentation entitled Highly efficient and magnetically recoverable TiO_2/Fe_3O_4 catalysts for photoreduction of Cr(VI) ions in aerobic environment at 1st National Workshop on Catalysis-2017, IIT(ISM) Dhanbad, Jharkhand.
4. Poster presentation entitled Polymerizable sol–gel synthesis of nano-crystalline WO_3 and its photocatalytic Cr(VI) reduction under visible light at National Symposium on Convergence of Chemistry and Materials-2017, BITS-Pilani, Hyderabad campus.
5. Poster presentation entitled oxygen insensitive thiol–ene photo-click chemistry for direct imprint lithography of oxides at Analytical Science at National Centre for Compositional Characterization of Materials (NCCCM): A journey over 25 years-2018, NFC, Hyderabad.

Biography of Prof. Ramakrishnan Ganesan

Prof. G. Ramakrishnan, Associate Professor in the Department of Chemistry, has been with Birla Institute of Technology and Science, Pilani, Hyderabad Campus, India since 2012. He obtained his Master's degree from Anna University, Chennai and Ph.D. from Korea Advanced Institute of Science and Technology (KAIST, 2006). He also served as a scientific employee at Helmholtz-Zentrum Geesthacht (HZG), Teltow, Germany from Apr, 2008 to Jan, 2010 and as a Scientist in Institute of Materials Research and Engineering (IMRE), Agency for Science Technology and Research (A*STAR) Singapore during Jan, 2010 – Jan, 2012.

Prof. Ramakrishnan's research interests include materials design, synthesis, fabrication and characterization of functional nanomaterials, thin films, and polymers. He also works on biodegradation of polymers, antimicrobial nanomaterials and nano-biotechnology based sensing of pathogeneses. He has published 44 research articles in international peer-reviewed journals. He has served as a reviewer for several reputed international journals including Polymer Chemistry, Langmuir, Journal of Materials Chemistry C, Chemical Engineering Journal etc. Currently, his group is engaged in the development of industrially important materials for environmental remediation and biosensing. He has successfully completed the Fast Track project sponsored by Department of Science and Technology, India.

Biography of Mr. Nagajuna Ravi Kiran

Mr. Nagarjuna Ravi Kiran completed his B. Sc (Botany, Zoology and Chemistry) in 2008 from Osmania University. He completed his M. Sc (Inorganic chemistry) in 2010 from Osmania University and achieved University gold medal for the first rank in respective subject domain. He also pursued B. Ed degree in 2011 from Osmania University. He started his career as Junior Lecturer in December 2010 at New Government Junior college, Malakpet, Hyderabad. Later he was appointed as Junior Research Fellow in DST project from March 2014 to February 2017 in BITS-Pilani, Hyderabad campus under the supervision of Prof. Ramakrishnan Ganesan. He is currently working as Institute Research Fellow at BITS Pilani, Hyderabad campus since March 2017. He authored/co-authored thirteen publications in international peer-reviewed journals and presented five papers at national and international conferences.